Searching for long-lived particles with the ATLAS muon spectrometer

Paul Anthony William Jones

of Girton College
and the Cavendish Laboratory

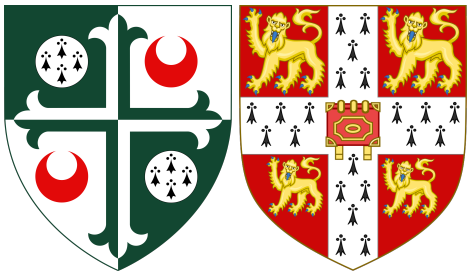

A dissertation submitted to the University of Cambridge
for the degree of Doctor of Philosophy

October 2025

Abstract

Dark matter comprises 25% of the mass-energy in the Universe, only interacting with visible matter via gravity. Many models that attempt to explain dark matter as particulate in nature also hypothesise the existence of long-lived particles beyond the Standard Model that could be produced in collider experiments and can elude detection by traversing a macroscopic distance without interacting with visible matter. A search for neutrally-charged, feebly interacting long-lived particles produced in proton-proton collisions at a centre-of-mass of $\sqrt{s} = 13$ TeV at the Large Hadron Collider of CERN is presented. 140 fb^{-1} of data collected with the ATLAS experiment is utilised to set limits on the cross-section times branching ratio of long-lived particles produced in association with a Z boson. Long-lived particles are identified through their decays into hadronic jets that are reconstructed as displaced vertices in the ATLAS muon spectrometer, and decays of the Z boson into electron or muon pairs are used to trigger the ATLAS detector. The data is found in agreement with the standard model predictions and exclusion limits are set on long-lived scalars, axion-like particles, and dark photons. The results presented are the most stringent ATLAS limits for photophobic axion-like particles with proper decay lengths greater than $\mathcal{O}(10\text{ cm})$.

Declaration

This thesis is the result of my own work and includes nothing which is the outcome of work done in collaboration except as declared in the preface and specified in the text. It is not substantially the same as any work that has already been submitted, or is being concurrently submitted, for any degree, diploma or other qualification at the University of Cambridge or any other University or similar institution except as declared in the preface and specified in the text. It does not exceed the prescribed word limit for the relevant Degree Committee.

Paul A. W. Jones

Acknowledgements

Starting a PhD in particle physics in the midst of a global pandemic may not have been my wisest decision... with all the trials and tribulations of the last 5 years, I certainly would not have succeeded in completing this PhD without the support of so many. Thank you to my friends and family for being patient with me and for still caring even when I make it hard to.

To my PhD supervisor, Oleg Brandt, I simply cannot thank you enough. Not only did you give me the opportunity to study my PhD at Cambridge on a topic that has fascinated me since I first learned about it (which was at my PhD interview when we first met), you have been an incredible teacher, a wise mentor, and a caring friend through the hardest times. I'm proud and grateful to have been your student. Likewise, to my College tutor, Sophia Shellard-von Weikersthal, thank you so much for all the support you've given me. Thanks to both of you I'm finally submitting my thesis, which on multiple occasions I believed I never would.

I am grateful to STFC for funding my PhD and the adventures that have came with it, including summer schools and conferences abroad. Thank you also to the Cavendish Laboratory, Girton College, and the University's Postgraduate Financial Assistance Fund for funding me during difficult times and allowing me to focus on finally finishing this thesis.

I'd like to thank my analysis team: Cristiano Alpigiani, Henry Lubatti, Ken Johns, Michael Schott, and Hao Zhou, for their work and guidance in developing the analysis presented in this thesis. A special thanks is owed to Julian Wack and Michael Revering for their hard work that resulted in the lepton-triggered actually getting finished, making this thesis possible. Thank you also to Jon Burr for guiding me in the early stages of the analysis and for teaching me so much.

Thank you to Carl Gwilliam and Chris Lester for agreeing to be my examiners and for your patience with the many delays!

To all the friends I've made along this crazy journey, thank you for the good times, laughs, and pub trips. A special mention to Seb, Harry, and Richard for surviving Peebles with me! To all the friends back home I've kept waiting for far too long, I appreciate you more than I can say.

To mum, you gave me everything that started me on this path and so much more. I went from a kid looking at pictures of space in books to doing my own research because of you. Sarah, thank you for believing in me and giving me a boot when I need it. Thank you to Victoria for getting through the hardest times together and for making the best. Bardzo cie kocham. Finally, to Michael... I miss you bro.

Preface

The Standard Model (SM) of particle physics has so far successfully predicted the results of all particle collider experiments and has been validated to extremely high precision. However, the SM is not yet a complete description of the Universe. Notably, the SM lacks a viable explanation for astrophysical observations of Dark Matter (DM), which does not interact with light and comprises $\sim 26\%$ of the mass-energy of the universe, whereas as visible matter comprises only 5%. DM dominates visible matter and plays a crucial role in the formation of stable galaxies and other large-scale structures.

Extensions to the SM that attempt to explain DM as a Beyond the Standard Model (BSM) particle generally predict a spectrum of additional BSM particles that could be produced at collider experiments. The lifetimes of these particles are typically free parameters not constrained by the relevant model. Hence, the particles can be long-lived and evade detection. If neutral long-lived particles (LLPs) are produced at a collider experiment, they may propagate a macroscopic distance through the detector without interacting. LLPs could escape the detector entirely or decay into charged particles inside it at a position that is significantly displaced from the hard scatter. In the latter case, standard reconstruction algorithms will often be inefficient as they are typically optimised to identify decays of heavy SM particles that occur within a a distance smaller than the detector resolution.

The ATLAS muon spectrometer (MS) is a powerful tool for LLP searches at the LHC due to its large size and precise tracking and timing capabilities. Previous searches for LLPs using the ATLAS MS typically probed models where LLPs are pair produced. However, other models predict the production of a single LLP in association with a massive SM boson.

This thesis summarises a search for long-lived axion-like particles produced in association with a Z boson using the ATLAS MS that was developed and conducted by the author. The thesis is structured as:

Part I discusses the theoretical and experimental background necessary to conduct the work carried out by the author. Chapter 1 outlines the theoretical motivation for searches for LLPs. Section 1.1 describes the SM and how it is not yet a complete theory of the Universe. Section 1.2 summarises the experimental evidence for DM. Section 1.3 introduces LLPs as an intriguing prospect in the search for a BSM DM candidate, as well as detailing the physics of the LLP model considered in this work. Chapter 2 describes the experimental setup used in this work. The Large Hadron Collider (LHC) is discussed in Section 2.1, while the ATLAS detector used to record the collision events is described in Section 2.2.

Part II discusses searches for LLPs conducted using the ATLAS MS. Chapter 3 describes previous searches for LLPs with the ATLAS muon spectrometer, on which the work of the author is based. A reinterpretation of a previous search is conducted and the results are used to develop a more efficient trigger strategy. Chapter 4 details the search performed by the author and collaborators, utilising the new trigger strategy. Further optimisation studies are presented. Finally, Chapter 5 contains concluding remarks, including prospects for future LLP searches.

The author's main contributions to the work presented in this thesis are:

- Developed the framework used to conduct the analysis, including calculating kinematic variables, applying selection criteria, and scripts for plotting and error propagation that were used by the analysis team. Produced ntuples containing variables related calculated from ALP Monte Carlo samples and data for sensitivity studies and analysis.
- Reinterpreted the partial Run 2 (36 fb^{-1}) search for displaced vertices in the MS with the ALP MC samples, as presented in Section 3.3.1, and used the results to identify that the triggering strategy was suboptimal. Then designed a more efficient trigger strategy, targeting leptonic decays of the associated Z boson and requiring the dilepton mass to be close to the Z mass.
- Implemented the prompt Z requirement in addition to the selection criteria and neural nets used in the RoI-triggered channel of the 140 fb^{-1} search for events with a single displaced vertex in the MS, which is described in Section 3.4.
- Conducted the optimisation studies presented in Section 4.2.3 and developed a final selection criteria that is is 4-8 times more efficient than the RoI-triggered channel selection, depending on the ALP mass. In particular, the new selection is

much more efficient at longer LLP decay lengths. Several additional discriminating variables were studied but not utilised in the final selection due to statistical limitations in data.

- Validated the data-driven background method using a E_T^{miss}-based validation region. Then calculated the expected number of events in the signal region, unblinded and checked for consistency between the observed and expected event counts. Additionally produced displays of the observed events in the signal region.
- Contributed to writing the ATLAS-internal analysis report and the published paper.

As experimental high energy physics is extremely collaborative in nature, many people have contributed to the work presented in this thesis. The many who designed, built, and maintain the LHC, the ATLAS experiment and its software for reconstruction and analysis have all played a part in this work.

Summarised below are the contributions from those directly involved in the search for displaced MS vertices in events with a leptonically decaying Z boson

The team working on the inclusive search for events with a single displaced MS vertex have laid down the groundwork for the search with the associated Z boson. The cutflow framework and lifetime extrapolation procedure developed by Michael Schott were implemented for the associated Z boson search and the neural nets trained by Hao Zhou were used without retraining. Major contributions of Cristiano Alpigiani, Ken Johns, and Henry Lubatti towards the RoI-triggered channel have aided the development of this work.

For a long time, the author was the only analyser directly working on the search for displaced vertices in the ATLAS muon spectrometer in events with a leptonically decaying Z boson. The addition of two more team members, Michael Revering (postdoc, Cambridge) and Julian Wack (PhD student, Cambridge) ensured the analysis wrapped up in a timely manner. The guidance of the author's supervisor, Oleg Brandt, has been critical to the success of the work presented.

Contents

"The test of all knowledge is experiment. Experiment is the sole judge of scientific 'truth'."

— Richard P. Feynman, The Feynman Lectures on Physics (1964)

Part I.

Fundamentals

Chapter 1.

Theory and motivation

The Standard Model of particle physics (SM) is the most successful and rigorously tested theory of the Universe. However, despite its success, there is much experimental evidence that indicates the SM is not a complete theory of the Universe. Notably, there is compelling evidence that only 5% of the mass-energy in the Universe is matter described by the SM, and 25% appears to be comprised of an unknown, massive substance, known as dark matter (DM). Theories that attempt to explain the observed DM often predict a plethora of additional particles, which can potentially have long lifetimes that cause them to evade searches at collider experiments.

This chapter discusses the motivation for the work in this thesis, beginning with an overview of the SM in Section 1.1. Then, the compelling evidence for DM is discussed in Section 1.2. Finally, Section 1.3 describes mechanisms that result in LLPs and discusses the LLP model investigated in this thesis.

1.1. The Standard Model

The SM is a locally gauge invariant relativistic quantum field theory that describes the fundamental forces of nature[1] and predicts the existence of 25 elementary particles, all of which have been observed experimentally and are listed in Figure 1.1. The SM has given extremely accurate, experimentally validated predictions. The structure and symmetries of the SM are described in Section 1.1.1 and spontaneous breaking of the electroweak symmetry is discussed in Section 1.1.3 – much of the information in these two Sections comes from [1]. The key successes of the SM and its remaining open questions are discussed in Sections 1.1.4 and 1.1.5, respectively.

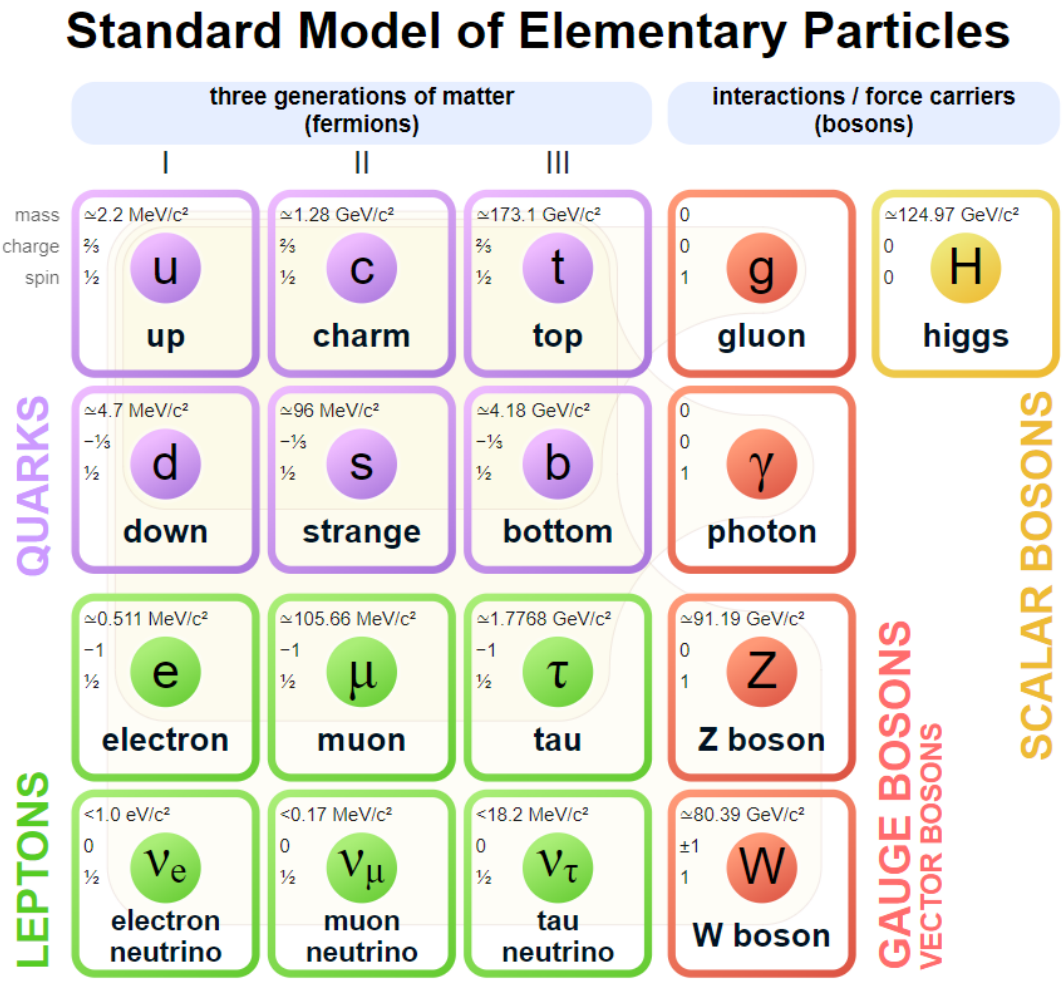

Figure 1.1.: The particles in the SM [2], grouped by type and generation. The mass, spin and electric charge of each particle are shown.

[1] With the exception of gravity.

1.1.1. Structure and symmetries

The SM is described by a Lagrangian density (henceforth referred to as simply the Lagrangian) $\mathcal{L}$ that must obey Poincaré and gauge symmetries, which constrain the model to a limited parameter space and therefore determine the allowed fields, particles and interactions. Symmetries are desirable as they imply conserved currents and therefore invariant observables, due to Noether's theorem. The Poincaré symmetry group includes space-time translations, boosts and rotations, under all of which $\mathcal{L}$ must be invariant. Gauge symmetries are local symmetries; The transformation is applied to the gauge field, and $\mathcal{L}$ is left locally invariant. The SM is a gauge field theory built from three gauge symmetry groups as

$$\mathrm{SU}(3)_C \times \mathrm{SU}(2)_L \times \mathrm{U}(1)_Y, \tag{1.1}$$

which encapsulates the physics of three fundamental interactions: electromagnetism and the strong and weak interactions, each of which has a corresponding charge that is conserved in all processes.

Quantum Electrodynamics (QED) describes electromagnetism (EM), which is the interaction of light and electrically charged particles. The strength of interactions in QED depend on the electric charge Q of particles in the interaction, which can be positive, negative. If a particle is neutrally charged it does not interact electromagnetically. The range of the EM force is infinite as its mediator, the photon γ, is massless.

The weak interaction allows transitions between particle generations, which are discussed in Section 1.1.2. It force has a very short range of $\mathcal{O}(10^{-18}\ \mathrm{m})$ as it is mediated by the very massive ($\mathcal{O}(100\ \mathrm{GeV})$) and unstable $W^{\pm}$ and Z bosons. In the SM, QED and the weak interaction are unified into the electroweak (EW) interaction, defined as $\mathrm{SU}(2)_L \times \mathrm{U}(1)_\mathrm{Y}$, where L denotes the fact that only left-handed chiral states interact via the weak force. The charge of the unified electroweak force is known as weak hypercharge $\mathrm{Y} = 2(Q - I_3)$, where is I_3 is weak isospin.

The strong nuclear interaction is described by Quantum Chromodynamics (QCD), defined by the $\mathrm{SU}(3)_C$ gauge group, where C denotes the strong interaction charge, known as colour. Colour charge is analogous to electric charge in QED, except colour charge can take three values corresponding to three orthogonal wavefunctions: red (r), blue (b) and green (g). Like electric charge, colour charge is conserved. The strong

force is mediated by massless gluons but only has a subatomic range of $\mathcal{O}(10^{-15}\text{ m})$ for reasons described in Section 1.1.2.1.

Prior to electroweak symmetry breaking (EWSB), the SM Lagrangrian is

$$\mathcal{L} = \mathcal{L}_{Gauge} + \mathcal{L}_{Dirac} \tag{1.2}$$

where the first term describes the gauge sector defining the mediators of the fundamental interactions and the second term describes how the mediators interact with matter. These two terms are discussed in Section 1.1.2. There are no mass terms in this Lagrangian as gauge symmetry forbids them. Following EWSB, the Higgs mechanism adds terms to the Lagrangian that impart mass to many elementary particles. This is discussed in Section 1.1.3.

1.1.2. Particles

The SM describes the Universe in terms of quantum fields and the particles we observe are excitations in these quantum fields. Particles have charges corresponding to the fundamental forces they can interact via. Some particles have *mass*, which is a resistance to changes in inertia, whilst others are massless and are bound to one inertial frame: the speed of light. Particles also possess an intrinsic angular momentum, known as *spin*. Particles fall into two categories based on their spin: fermions and bosons. Fermions are "matter" particles and the elementary bosons are exchanged between them to mediate the fundamental forces.

1.1.2.1. Bosons

Bosons abide by Bose-Einstein statistics and possess integer spin. The wavefunction for a pair of identical bosons (b_1 and b_2) is symmetric under exchange of the bosons: $\Psi(b_1, b_2) = \Psi(b_2, b_1)$, thus allowing any number of bosons to occupy the same quantum state[2]. The SM contains spin-0 and spin-1 bosons[3]. The only fundamental spin-0, or *scalar*, particle in the SM (and the most recently discovered) is the Higgs boson H – an electrically neutral particle with a relatively large mass of 125 GeV that is an

[2] At extremely low temperatures bosons form an exotic state known as a Bose-Einstein condensate.

[3] If gravity were to be included in the SM, the corresponding mediator would be a spin-2 (tensor) boson called the graviton.

excitation in the Higgs field which imparts mass to particles following EWSB. Scalar bosons satisfy the Klein-Gordon equation

$$(\partial_\mu \partial^\mu + m^2)\phi = 0, \tag{1.3}$$

where ϕ is the scalar field and m is the mass of the particle.

The spin-1 elementary particles in the SM are known as the *gauge* bosons since they are excitations in the gauge fields. The gauge bosons are the photon γ, $W^\pm$ boson and the Z boson of the EW interaction, as well as the 8 gluons g that mediate the strong interaction. The Lagrangian describing the gauge fields – prior to EWSB – takes the form of

$$\mathcal{L}_{Gauge} = -\frac{1}{4} F^{\mu\nu} F_{\mu\nu}, \tag{1.4}$$

where $F^{\mu\nu}$ are the gauge field strength tensors. Gauge symmetry dictates that all gauge bosons are massless. However, the $W^\pm$ and Z bosons are known to have large masses of 82 and 91 GeV, respectively. The $\mathrm{SU}(2)_L$ symmetry gives rise to three massless gauge bosons: W^1, W^2 and W^3, while $\mathrm{U}(1)_Y$ gives rise to the massless neutral B boson. Following EWSB, the physical $W^\pm$ and Z bosons are obtained by mixing of the W^i_μ and B_μ fields and corresponding mass terms are introduced in the Lagrangian, as described in Section 1.1.3.

The gluon is electrically neutral and mediates the strong nuclear force. The $\mathrm{SU}(3)_C$ symmetry gives rise to 8 gluons, each carrying a different combination of colour and anti-colour charge. The gluon fields correspond to rotations in colour space and are denoted by G^a_μ, where a=1-8 is the gluon colour index.

The $\mathrm{SU}(2)_L$ and $\mathrm{SU}(3)_C$ gauge groups are non-Abelian - their generators do not commute, resulting in cubic and quartic terms in the Lagrangian that correspond to self-interactions involving three or four bosons, as shown in Figures 1.4 and 1.5. These self-interactions cause the strength of the strong and weak nuclear forces to increase with distance. However, the strength and range of the weak interaction are limited by the large masses and very short lifetimes of the W and Z bosons. Gluons are not hindered by mass. At "large" distances, the potential of the gluon field scales linearly with distance until the energy of the interaction is large enough to pair-produce new particles, which limits the range of the strong interaction to $\mathcal{O}(1\text{ fm})$.

1.1.2.2. Fermions

Fermions abide by Fermi-Dirac statistics and have half-integer spin, which results in the wavefunction Ψ for a system of two identical fermions (f_1 and f_2) being antisymmetric under exchange of the two fermions: $\Psi(f_1, f_2) = -\Psi(f_2, f_1)$. This prohibits multiple fermions occupying the same quantum state and is known as the Pauli exclusion principle. Fermions are described by the Dirac equation, written in covariant form as

$$(i\gamma^\mu \partial_\mu - m)\psi = 0, \tag{1.5}$$

where γ^μ are the Dirac gamma matrices, ∂_μ is the four-derivative, m is the mass of the particle and ψ is the four-component wavefunction known as the Dirac spinor, given by $\psi = (\psi_1, \psi_2, \psi_3, \psi_4)$, where ψ_1 and ψ_2 are solutions to the Dirac equation with positive energy eigenvalues and respectively describe the spin-up and spin-down states of fermions, while ψ_3 and ψ_4 are negative energy solutions describing the spin-up and spin-down states of fermionic antimatter, respectively. The term "antimatter" denotes (anti)particles, which possess the same mass and spin as their 'regular' matter counterparts, but with the sign of their charges switched. For every fermion f in the SM there is a corresponding antiparticle $\bar{f}$.

There are two subcategories of fermions: leptons and quarks, both of which include three generations of particles with similar basic properties such as charge and spin, but different masses.

Leptons interact solely via the EW interaction. The charged leptons in order of ascending mass are the electron e^-, muon μ^-, and tau τ^-) all of which posses an electric charge of $-1e$, where e is the fundamental unit of electric charge. Additionally, each charged lepton has a corresponding very light, electrically neutral partner called a neutrino ($\nu_{e,\mu,\tau}$), which only interacts via the weak force. Left-handed charged leptons and their corresponding neutrinos form $\mathrm{SU}(2)_L$ doublets, whereas right-handed charged leptons are $\mathrm{SU}(2)_L$ singlets and right-handed neutrinos are not predicted by the SM. This is illustrated in Figure 1.2.

Quarks interact via the EW and strong interactions and therefore possess electric, weak charge and colour charge. The flavours of quark, as shown in Figure 1.1 and listed in order of generation, are: up u and down d, charm c and strange s, and top t and bottom b. The up-type (u, c, t) quarks have an electric charge of $+\frac{2}{3}e$, and the

$$\begin{matrix} \begin{pmatrix} \nu_e \\ e \end{pmatrix}_L & \begin{pmatrix} \nu_\mu \\ \mu \end{pmatrix}_L & \begin{pmatrix} \nu_\tau \\ \tau \end{pmatrix}_L \\ e_R & \mu_R & \tau_R \end{matrix}$$

Figure 1.2.: Representation of the left-handed and right-handed chiral states of the lepton fields, denoted by L and R, respectively.

down-type (d, s, b) quarks have a charge of $-\frac{1}{3}e$. Left-handed quarks form $\mathrm{SU}(2)_L$ doublets and the right-handed quarks are $\mathrm{SU}(2)_L$ singlets, as shown in Figure 1.3.

$$\begin{matrix} \begin{pmatrix} u \\ d \end{pmatrix}_L & \begin{pmatrix} c \\ s \end{pmatrix}_L & \begin{pmatrix} t \\ b \end{pmatrix}_L \\ u_R & c_R & t_R \\ d_R & s_R & b_R \end{matrix}$$

Figure 1.3.: Representation of the left-handed and right-handed chiral states of the quark fields, denoted by L and R, respectively.

Colour confinement dictates that hadrons (strongly bound quark states) can only exist in colour singlets (colour-neutral states), e.g. diquark states called *mesons*: $r\bar{r}/b\bar{b}/g\bar{g}$, triquark states called *baryons*: $rbg/\bar{r}\bar{b}\bar{g}$, such as the proton (uud), and tetra/pentaquark states. As gluons self-interact, if one attempts to separate bound quarks, eventually the energy in the interaction is so large that new quarks are pair-produced and hadronise with the original quarks to create new colour singlets[4].

The Lagrangian describing the interactions of fermions with the gauge fields is

$$\mathcal{L}_{Dirac} = i\bar{\psi}\gamma^\mu D_\mu \psi + h.c. \tag{1.6}$$

where D_μ is the covariant derivative and "h.c." denotes Hermitian conjugate interactions. Due to the different transformation properties of the left-handed fermion doublets ψ_L and right-handed singlets ψ_R, fermion mass terms $-m\bar{\psi}\psi = -m(\bar{\psi}_R\psi_L + \bar{\psi}_L\psi_R)$ break the $\mathrm{SU}(2)_L \times \mathrm{U}(1)_Y$ symmetry and are thus forbidden in Equation 1.6. Like the $W^\pm$ and Z bosons, fermions gain mass via EWSB, described in Section 1.1.3.

[4]The exception is the top quark, which decays via the weak interaction before hadronisation can occur.

1.1.2.3. Interaction vertices

Figure 1.4 shows the allowed interaction vertices involving the EW gauge bosons: (a) shows the interaction between the Z boson and fermions, (b) and (c) show the interactions involving the W bosons with leptons and quarks, respectively. (d) shows the interaction between electrically charged fermions $f^{\pm}$ and the photon, and (e) and (f) show the interactions between the W bosons and the other EW bosons, including W self-interactions. Figure 1.5 shows (a) the interaction vertex between gluons and quarks, and (b,c) gluon self-interaction vertices.

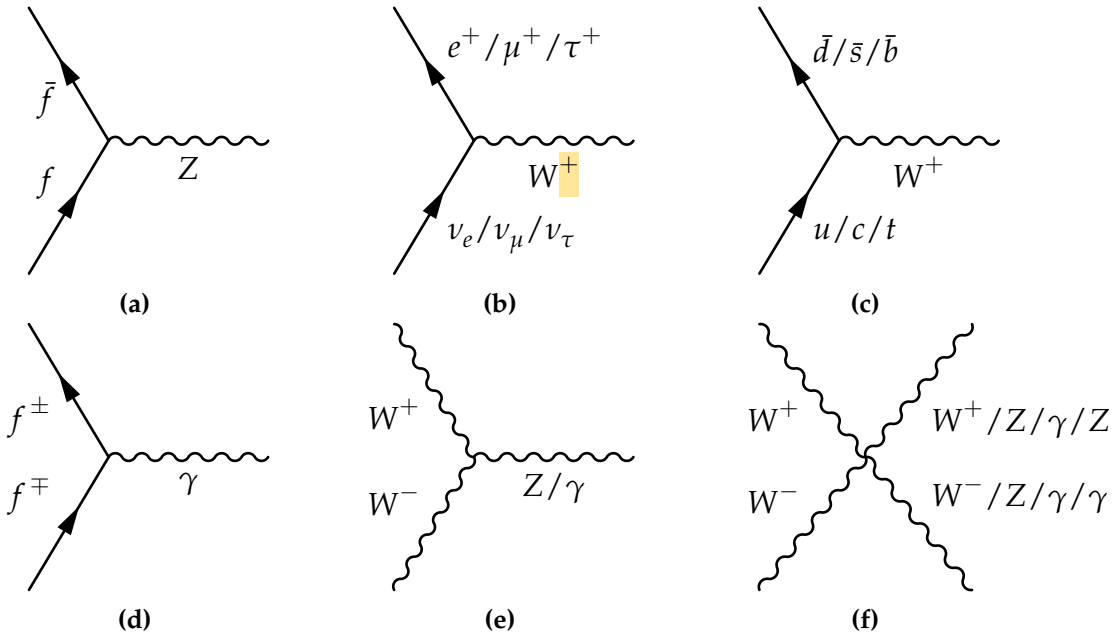

Figure 1.4.: Electroweak interaction vertices. The Hermitian conjugate process are not shown.

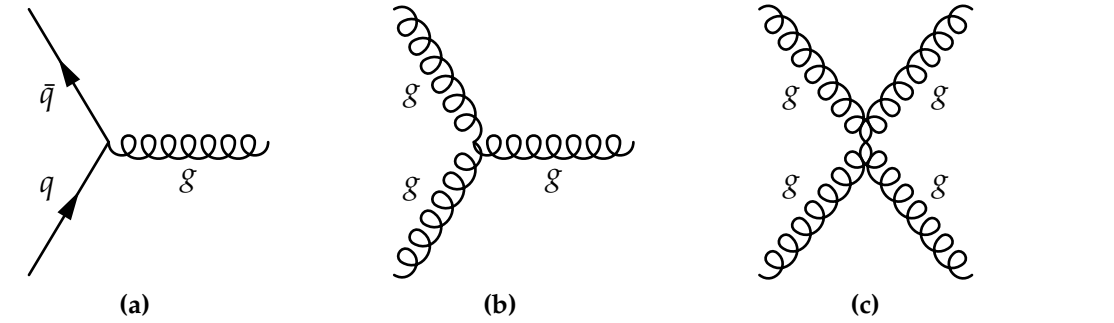

Figure 1.5.: Strong interaction vertices

1.1.3. Electroweak symmetry breaking

Gauge symmetry forbids gauge boson mass terms, yet the $W^{\pm}$ and Z bosons are among the heaviest particles in the SM, with masses at the EW scale $\sim\mathcal{O}(100)$ GeV. The mass terms for these particles are attained via spontaneous breaking of the EW symmetry, introduced by the inclusion of an $\mathrm{SU}(2)_L$ doublet of complex scalar fields

$$\phi = \begin{pmatrix} \phi^+ \\ \phi^0 \end{pmatrix}_L = \frac{1}{\sqrt{2}} \begin{pmatrix} \phi_1 + i\phi_2 \\ \phi_3 + i\phi_4 \end{pmatrix}_L \tag{1.7}$$

where the ϕ^+ field is charged and ϕ^0 is neutral. The doublet invokes a new set of terms in the SM Lagrangian that is invariant under $\mathrm{SU}(2)_L \times \mathrm{U}(1)_\mathrm{Y}$:

$$\mathcal{L}_{Higgs} = (D_\mu\phi)^\dagger(D^\mu\phi) - V(\phi). \tag{1.8}$$

The first term describes the kinematics of the scalar field and the Higgs potential $V(\phi)$ is given by

$$V(\phi^\dagger\phi) = \mu^2\phi^\dagger\phi + \lambda(\phi^\dagger\phi)^2 \tag{1.9}$$

where λ is a positive coefficient and the sign of the μ^2 coefficient determines the shape of the potential. Minimising $V(\phi^\dagger\phi)$ yields

$$\frac{\partial V(\phi^\dagger\phi)}{\partial(\phi^\dagger\phi)} = \mu^2 + 2\lambda\phi^\dagger\phi = 0. \tag{1.10}$$

If $\mu^2 > 0$, the minimum of $V(\phi^\dagger\phi)$ is at $\phi^+ = \phi^0 = 0$ and symmetry is preserved. For $\mu^2 < 0$, there is a local maximum at $\phi^+ = \phi^0 = 0$ and an infinite number of degenerate minima such that

$$\phi^\dagger\phi = (\phi^+_{\text{vacuum}})^2 + (\phi^0_{\text{vacuum}})^2 = \frac{-\mu^2}{2\lambda} \tag{1.11}$$

where $\phi^{+/0}_{\text{vacuum}}$ are the vacuum states of the $\phi^{+/0}$ fields. Without loss of generality, ϕ^+_{vacuum} can be set to 0, resulting in the vacuum expectation value (VEV)

$$\langle 0|\phi|0\rangle = \frac{1}{\sqrt{2}}\begin{pmatrix}0\\ v\end{pmatrix} \tag{1.12}$$

where $v \equiv \sqrt{-\mu^2/\lambda}$ is a free parameter. The choice of VEV breaks the $\mathrm{SU}(2)_L \times \mathrm{U}(1)_\mathrm{Y}$ symmetry but invariance is retained in the residual $\mathrm{U}(1)_{EM}$ symmetry associated with electromagnetism. Expanding the fields about the VEV gives

$$\phi(x) = \frac{1}{\sqrt{2}}\begin{pmatrix}\phi_1(x) + i\phi_2(x)\\ v + \eta(x) + i\phi_4(x)\end{pmatrix}. \tag{1.13}$$

After EWSB, there is one massive scalar boson and a massless Goldstone boson for each of the three spontaneously broken $\mathrm{SU}(2)_L \times \mathrm{U}(1)_\mathrm{Y}$ generators. The Goldstone bosons are absorbed by the $W^\pm$ and Z bosons, imparting longitudinal polarisation states. The resulting scalar field in the unitary gauge is

$$\phi = \frac{1}{\sqrt{2}}\begin{pmatrix}0\\ v + H\end{pmatrix} \tag{1.14}$$

where H is the physical Higgs field. Inputting this ϕ into Equation 1.8 yields a Higgs Lagrangian containing:

- A quadratic Higgs field term with a coefficient of the Higgs boson mass $m_H = -2\mu^2$.
- Terms with interactions between the Higgs and weak gauge fields, shown in Figure 1.6 (b,c), including quadratic gauge field terms with coefficients of the $W^\pm$ and Z masses.
- Cubic and quartic terms of the Higgs field, corresponding to Higgs self-interactions, as shown in Figure 1.6 (d,e).

The physical $W^\pm$ boson fields ($W^\pm_\mu$) following EWSB are combinations of the $W^{1,2}_\mu$ fields

$$W^\pm_\mu = \frac{1}{\sqrt{2}}(W^1_\mu \mp iW^2_\mu) \tag{1.15}$$

and the physical photon (A_μ) and Z boson (Z_μ) fields are combinations of the W^3_μ and B_μ fields

$$\begin{pmatrix} A_\mu \\ Z_\mu \end{pmatrix} = \begin{pmatrix} \cos\theta_W & \sin\theta_W \\ -\sin\theta_W & \cos\theta_W \end{pmatrix} \begin{pmatrix} B_\mu \\ W^3_\mu \end{pmatrix} \tag{1.16}$$

where θ_W is the Weinberg mixing angle and $\sin\theta_W \equiv g'/\sqrt{g_W^2 + g'^2}$ and $\cos\theta_W \equiv g_W/\sqrt{g_W^2 + g'^2}$, while g' and g_W are the $\mathrm{U}(1)_\mathrm{Y}$ and $\mathrm{SU}(2)_L$ couplings, respectively.

Hence, the predicted masses of the $W^\pm$ and Z bosons are

$$m_W = \frac{1}{2} v g_W \tag{1.17}$$

$$m_Z = \frac{1}{2} v \sqrt{g_W^2 + g'^2} \tag{1.18}$$

and are thus related by the mixing angle

$$\frac{m_W}{m_Z} = \cos\theta_W. \tag{1.19}$$

The mixing of left and right-handed chiral states in the mass term of the Dirac Lagrangian $-m\bar{\psi}\psi = -m(\bar{\psi}_R\psi_L + \bar{\psi}_L\psi_R)$ breaks gauge symmetry and thus excludes fermion mass terms. However, the inclusion of the $\mathrm{SU}(2)_L$ doublet of complex scalar fields given in Equation 1.14 results in Yukawa terms that are invariant under $\mathrm{SU}(2)_L \times \mathrm{U}(1)_Y$ gauge transformations.

$$\mathcal{L}_{Yukawa} = g_l \bar{l}_L \phi l_R + g_u \bar{u}_L \phi u_R + g_d \bar{d}_L \phi d_R + h.c. \tag{1.20}$$

where $l = (e, \mu, \tau)$ represents the charged lepton fields, while $u = (u, c, t)$ and $d = (d, s, b)$ represent the up-type and down-type quarks, respectively. Hermitian conjugate terms are denoted by "h.c." and g_f are Yukawa coupling constants directly related to fermion masses

$$g_f = \sqrt{2}\frac{m_f}{v}. \tag{1.21}$$

Since the non-zero component of ϕ consists of a VEV and physical Higgs field, the Yukawa terms each contain a fermion mass term and a term coupling fermions to the Higgs itself, resulting in the Higgs-fermion interaction vertex shown in Figure 1.6 (a).

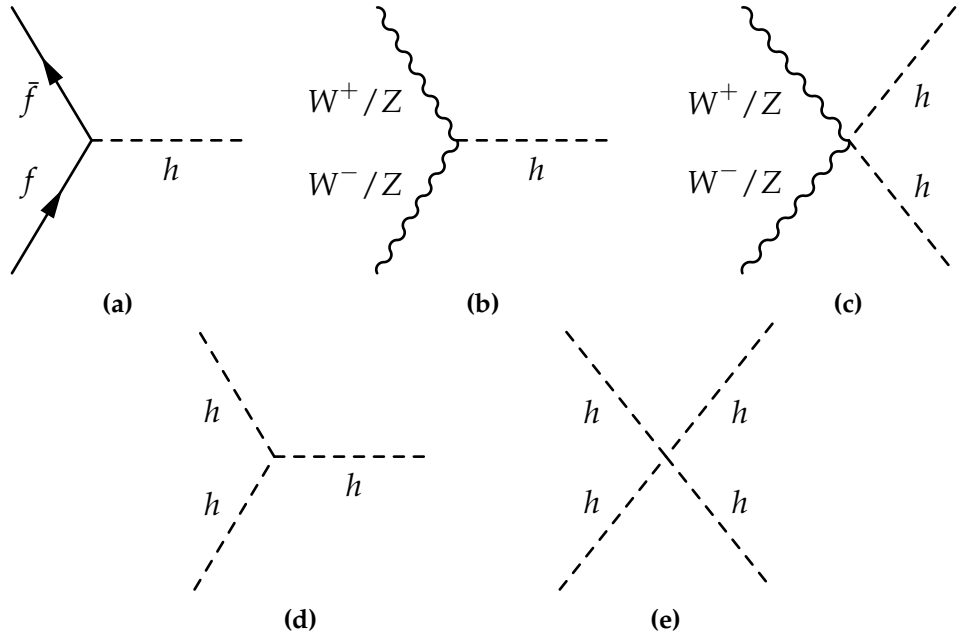

Figure 1.6.: Higgs interaction vertices with (a) fermions, (b,c) the W and Z bosons, and (d,e) Higgs self-interactions.

Following EWSB, the complete SM Lagrangian is

$$\mathcal{L}_{SM} = \mathcal{L}_{Gauge} + \mathcal{L}_{Dirac} + \mathcal{L}_{Higgs} + \mathcal{L}_{Yukawa}, \tag{1.22}$$

where $\mathcal{L}_{Gauge}$ describes the fundamental forces, $\mathcal{L}_{Dirac}$ describes the interactions between matter and the forces, $\mathcal{L}_{Higgs}$ describes the Higgs field and gauge boson masses, and $\mathcal{L}_{Yukawa}$ describes how matter interacts with the Higgs field and gains mass.

1.1.4. Successes of the Standard Model

All particles predicted by the SM have been observed experimentally. The SM interactions have been rigorously tested and its predictions are thus far consistent with the results of all collider experiments.

The Large Electron-Positron collider (LEP) and Stanford Linear Collider (SLC) yielded produced many results validating the SM [3,4], including precision measurements of the masses of the top quark and the W and Z bosons, which were consistent with indirect measurements made using the various relations between the SM particle masses. The Cabibbo-Kobayashi-Maskawa (CKM) matrix unitarity has been verified to high precision [5]. In addition, the polarised electron beams at the SLC allowed the spin structure of the SM was to be validated.

At the LHC, the Higgs boson was observed for the first time at a collider experiment [6,7]. In addition, SM predictions of the known particle interactions have been probed and verified to high precision at energies spanning several orders of magnitude. Figure 1.7 summarises ATLAS measurements of total production cross-sections for several SM processes. The agreement between data and theory is shown to be very good, with the exception of a few rare processes with large uncertainties.

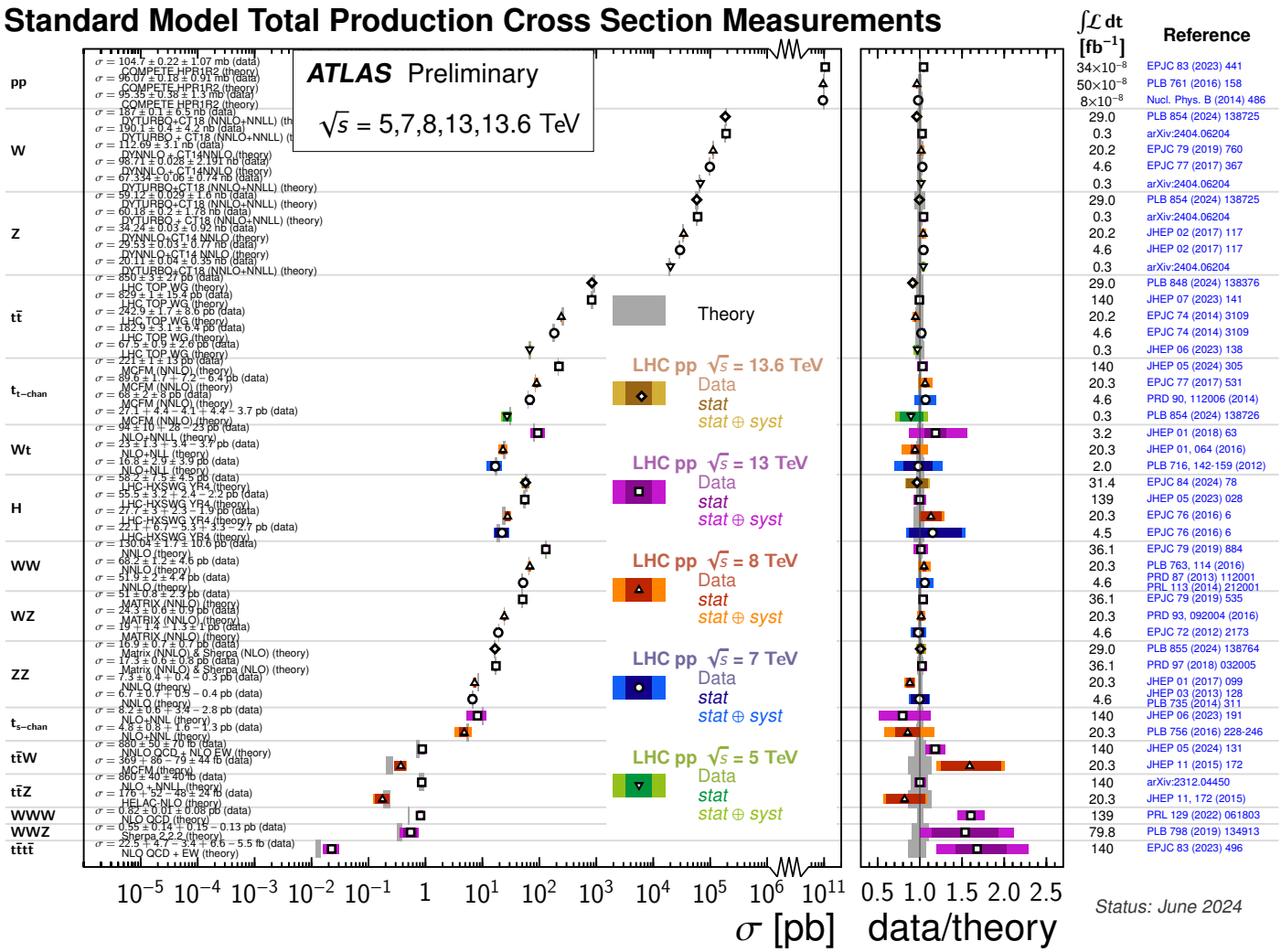

Figure 1.7.: Summary of ATLAS measurements of Standard Model total production cross-sections, compared to the theoretical expectations. Taken from [8].

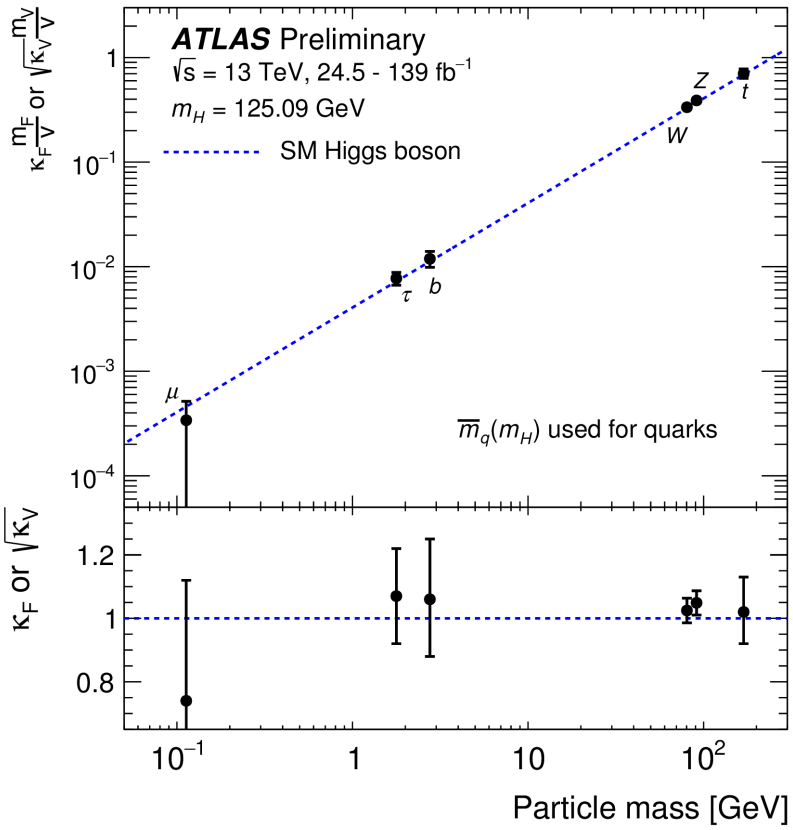

Figure 1.8.: ATLAS measurements of coupling strength modifiers $\kappa_F m_F/v$ for fermions $F = (\mu, \tau, b, t)$ and $\kappa_V m_V/v$ for weak gauge bosons $(V = W, Z)$ as a function of their masses m_F and m_V, respectively, and the Higgs field VEV $v = 246$ GeV. The SM prediction for both cases is indicated by the dashed line. The lower panel shows the ratios of the measured values to their SM predictions. Taken from [9].

1.1.5. Open questions in the Standard Model

There are several limitations of the SM that indicate it is not a complete theory. These include, but are not exclusive to, its lack of explanations for the following:

- Indirect astronomical observations of dark matter (DM), i.e. matter which does not interact with light but constitutes approximately 25% of the mass-energy density of the universe. Discussed in section 1.2.
- The observed acceleration of the expansion of the Universe: this may be due to a new form of matter that maintains a constant energy density in the Universe and therefore creates a repulsive force that drives expansion, known as dark energy. Whatever it truly is, dark energy dominates the mass-energy density in the modern Universe (70% compared to 5% for 'ordinary' matter) and will ultimately determine its fate.
- The matter-antimatter asymmetry, or *baryon* asymmetry, in the universe: If matter and anti-matter were created in equal abundance in the early Universe, then all fermions would have annihilated and the Universe would be empty except for radiation. This is evidently not the case. The observed baryon asymmetry is parameterised by the ratio of the difference in the number of baryons n_B and anti-baryons $n_{\bar{B}}$ to the number of photons n_γ

$$\frac{n_B - n_{\bar{B}}}{n_\gamma} \sim 10^{-9}. \tag{1.23}$$

  With no mechanism for asymmetry, this ratio would be zero. The observed asymmetry of $\mathcal{O}(10^{-9})$ indicates that there was one additional baryon for every 10^9 baryon-antibaryon annihilations in the early Universe.

  The process of creating more baryons than antibaryons is known as baryogenesis, for which there are three requirements, known as the Sakharov conditions [10]:

  - Baryon number (B) violation, resulting in non-constant $n_B - n_{\bar{B}}$.
  - Violation of the charge conjugation symmetry (C) and violation of the combined C and parity (P) symmetry - CP violation - to prevent interactions that produce more baryons than anti-baryons from being counterbalanced by conjugate interactions that produce more anti-baryons than baryons.

In the SM, CP violation can occur in weak charged-current interactions between quarks and has been experimentally studied in depth. However, the amount of CP violation in the SM quark sector is insufficient to account for the observed baryon asymmetry. CP violation between leptons has not yet been observed.

  - Thermal inequilibrium. In thermal equilibrium, interactions are in balance with their inverse process. Thus, baryon-antibaryon production is balanced by annihilation. Departure from equilibrium decreases production rates until they become kinematically unfeasible and annihilations become less frequent as particles are more rarefied.

- Neutrino oscillations and mass: the SM predicts neutrinos to be massless. However, observations of neutrino oscillations - neutrinos changing flavour with a time-dependent probability - indicate that neutrinos must have non-zero masses, with small mass-splittings between the three flavours.

- Grand unification: The SM has 19 free parameters that are not predicted by theory. It is not clear why there are so many free parameters. One way in which the number could be reduced is through grand unification theories which attempt to unify the strong force with the EW force at very high energies.

1.2. Experimental evidence for dark matter

Dark matter has been observed by various methods, including measurements of galactic rotation velocities, gravitational lensing and the anisotropies of the cosmic microwave background (CMB), discussed in Sections 1.2.1, 1.2.2 and 1.2.3, respectively. It is widely believed (or rather, hoped) that DM is particulate in nature as this grants the possibility of observing it directly in dedicated experiments, or even producing it in collider experiments. However, there are no viable candidates for DM in the SM. There are numerous models that attempt to explain the observed DM as BSM particles. Such models generally predict new particles that could be observed in a collider.The work presented in this thesis places constraints on candidate DM models.

1.2.1. Galactic rotation

In the 1970s, Vera Rubin observed [11] that the outer edges of spiral galaxies, such as the Andromeda galaxy, rotate with angular velocities too large to be bound by the gravity of visible matter in the galaxies, despite the galaxies being stable. Rubin calculated that galaxies required 5-10 times more mass to account for the observed rotation. This was the first concrete evidence that galaxies are surrounded by DM. Figure 1.9 shows the observed and expected rotation velocities as functions of distance from the galactic centre for the galaxy NGC 6503. The distribution expected from the visible galactic disc curve falls off with increasing distance, whereas the observed rotation is largely flat. This discrepancy can be accounted for by the presence of a DM halo which permeates the galaxy. The rotation curve for the hypothesised DM halo is also shown.

1.2.2. The bullet cluster

General Relativity describes how spacetime is distorted in the presence of massive objects, giving rise to gravity. Although photons are massless and do not interact via gravity, a massive object such as a galaxy can cause light to follow bent paths through warped space. This gives rise to a phenomena called gravitational lensing, where light from objects that passes through a region containing a large concentration of mass, such as a cluster of galaxies, is distorted and magnified. The presence and effect of DM is inferred from the amount of observed gravitational lensing compared to the amount expected from the visible matter alone. In addition, gravitational lensing can show DM that is separated from visible matter. Figure 1.10 shows the bullet cluster, which is actually two galaxy clusters that have collided head-on. As one subcluster penetrates the other, drag forces decelerate and heat the visible matter, resulting in the observed X-ray emissions (pink) in the centre of the cluster. Gravitational lensing shows there are large concentrations of mass to each side of the cluster, where there is less visible matter, indicating the presence of DM. As DM is not subjected to the same drag forces as visible matter, the DM halos of each subcluster have overtaken the visible matter, resulting in the observed DM concentrations separate from the visible matter.

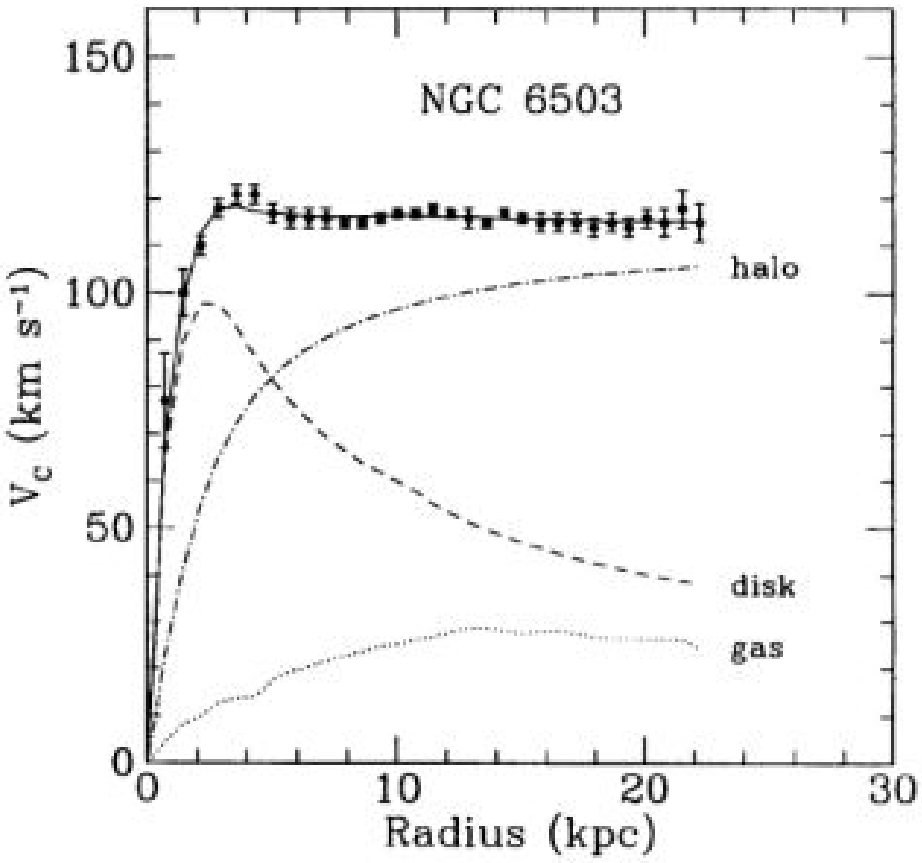

Figure 1.9.: Rotation curve for the galaxy NGC 6503 [12]. The dashed line shows the distribution expected from visible matter in the galactic disk, the dotted line shows the expected modification to the curve from gas and the dot-dashed line shows the distribution of the dark matter halo required to explain the observed rotation curve.

Figure 1.10.: Composite image of the bullet cluster [13]. Galaxies and stars are shown in near-infrared images captured by the James Webb Space Telescope. Hot gas is seen in images from the Chandra X-ray observatory (pink). The DM halo estimated from gravitational lensing is also superimposed (blue).

1.2.3. Cosmic microwave background

In the first 4×10^5 years after the Big Bang, the Universe was a dense plasma too hot for electrons and protons to form atoms. The abundance of free charges resulted in the mean free path of photons being very short; the Universe was essentially opaque until expansion caused it to cool sufficiently for the first atoms to form, allowing photons to propagate uninhibited. This radiation was redshifted by the expansion of the Universe, resulting in the cosmic microwave background (CMB) - the most ancient electromagnetic radiation that will ever be observable.

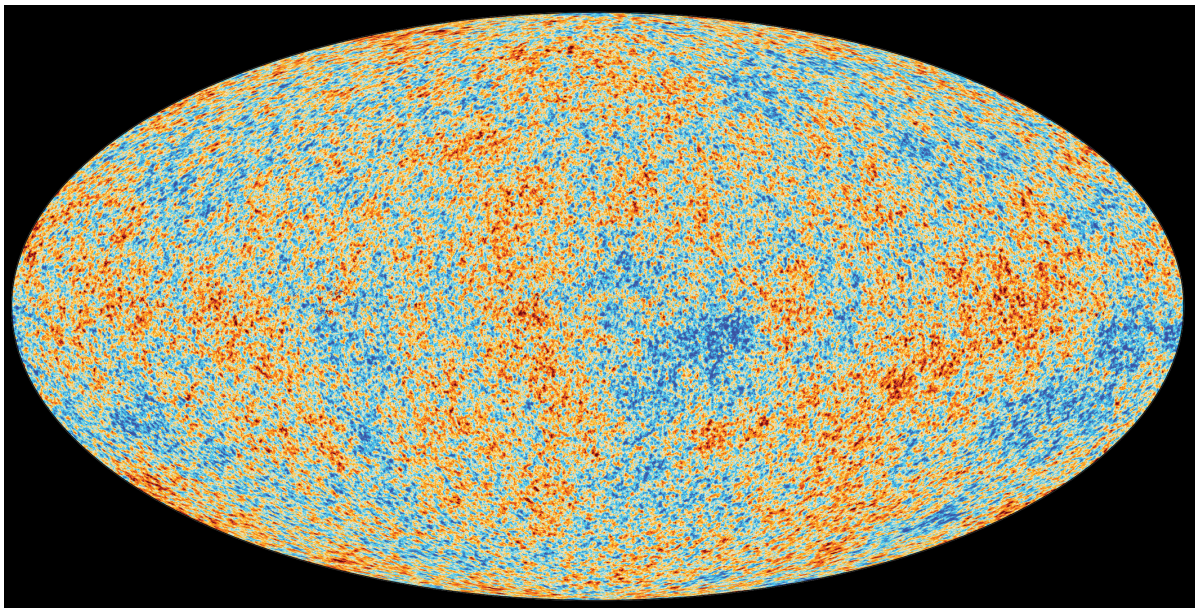

Figure 1.11.: Map of the cosmic microwave background recorded by the Planck satellite [14].

Figure 1.11 shows that the CMB pervades the Universe in all directions and is largely isotropic after subtracting the dipole moment caused by the relative motion of the Earth, with an average temperature $T_{CMB} = 2.7K$ and tiny fluctuations $\delta T_{CMB}/T_{CMB} \sim \mathcal{O}(10^{-5})$. These small anisotropies place constraints on the abundance of DM in the early Universe. The CMB power spectrum, shown in Figure 1.12, is sensitive to several cosmological parameters, including the total energy density of the Universe and relative the abundances of visible matter and DM. The height and angular scale of the peaks in the observed power spectrum are consistent with the Universe consisting of 5% ordinary matter and 26% DM, while the remaining 70% is comprised of dark energy.

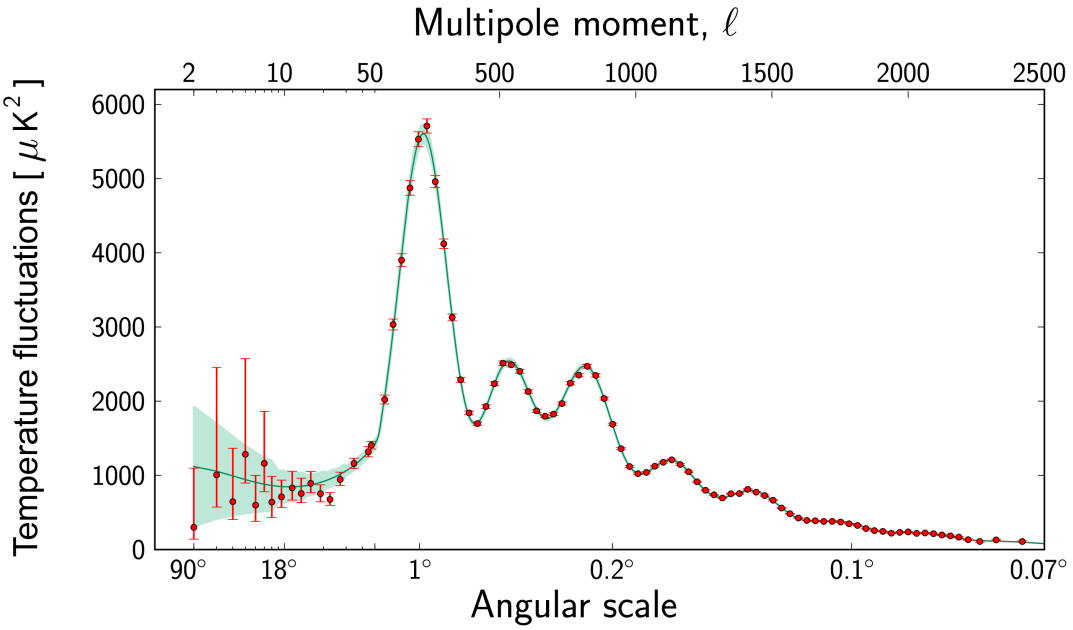

Figure 1.12.: Power spectrum of the cosmic microwave background recorded by the Planck satellite [15].

1.2.4. Hot and cold dark matter

Any candidate DM particle must be stable or be extremely long-lived, must be electrically neutral to avoid interactions with photons, and must be sufficiently massive and abundant to account for the observed evolution of the Universe, particularly in galaxies and clusters. Thus, the only candidates for DM in the SM are neutrinos, which are typically highly relativistic particles due to their very small masses. Relativistic sources of DM such as neutrinos are referred to as *hot* DM (HDM) and are not bound in galaxies. Therefore, HDM cannot account for the DM halos inferred from galaxy rotation velocities and gravitational lensing. Simulations of galactic evolution show that galaxies could not have formed into stable large-scale structures if HDM was the dominant form of DM [16, 17]. Instead, DM must primarily be non-relativistic, i.e. *cold* DM (CDM), ruling out all SM candidates for DM and motivating extensions to the SM that attempt to explain the observed DM.

1.3. Long-lived particles

1.3.1. Motivation for long-lived particle searches

There are numerous BSM models that attempt to overcome the shortcomings of the SM, which typically introduce new particles that could be observed at collider experiments. However, no BSM particles have yet been found. One avenue that still has much to explore is the possibility of long-lived particles (LLPs), which are a common feature of DM models [18–21], as well as BSM models in general and the SM itself. Figure 1.13 shows the decay lengths $c\tau$ of several SM particles, where c is the speed of light and τ is the proper lifetime of the particle – heavy particles like the Higgs boson decay rapidly within a distance that is smaller than the typical resolution of a detector, so the decays are considered to be *prompt*. On the other hand, electrically neutrally BSM LLPs can travel unseen some distance before decaying into SM particles. If the LLPs decay within the detector volume, they can induce detector activity that is displaced significantly from the IP, where the initial pp collision took place. The LLPs in the SM, such as the proton, neutron, and muon, have masses below 5 GeV and have well understood detector signatures, therefore, the highly exotic signatures of BSM LLPs provide a golden opportunity to search for new physics.

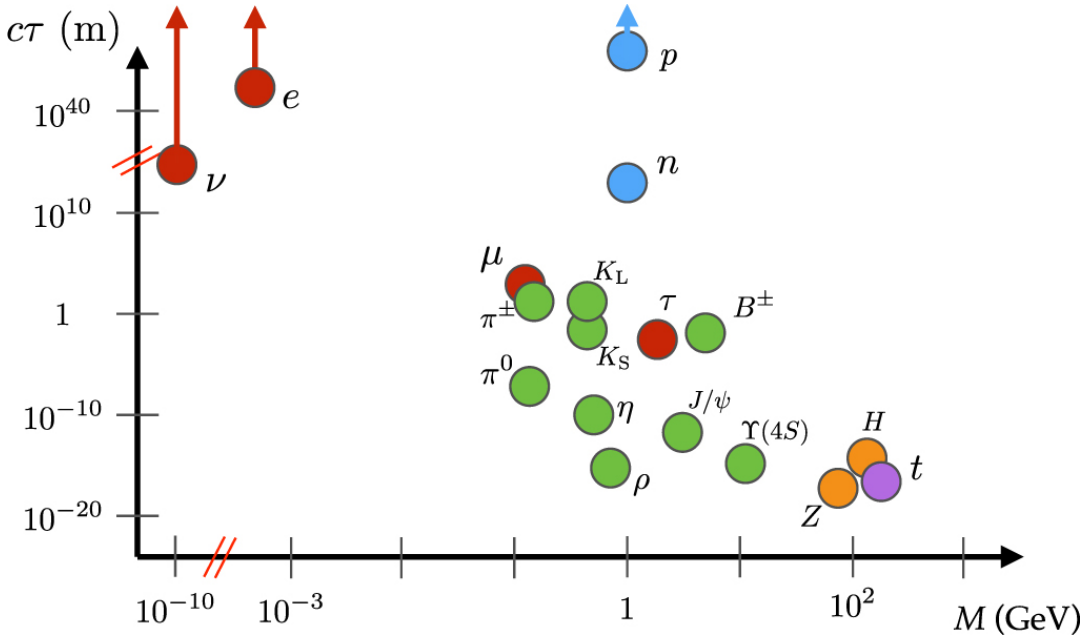

Figure 1.13.: Mean proper decay lengths $c\tau$ of several SM particles as a function of masses [22].

Many extensions to the SM hypothesise the existence of LLPs with a vast range of potential decay lengths, limited by Big Bang Nucleosynthesis to $c\tau \lesssim 10^8$ m [23]. In particular, exotic decays of the Higgs boson are a prime candidate for BSM physics – including LLPs – since numerous BSM models predict Higgs-BSM Yukawa couplings. The observed upper limit on the branching ratio of Higgs decays to invisible particles[5] is $BR(h \to \text{invisibles}) \lesssim 0.12$ at 95% confidence [24], leaving considerable room for these models.

Section 1.3.2 describes mechanisms that affect particle lifetimes. Section 1.3.3 discusses the Higgs/scalar portal model that is typically utilised as the benchmark model in LLP searches at the LHC and Section 1.3.4 presents a brief overview of axion-like particles (ALPs) and describes the ALP model probed in this work.

1.3.2. Mechanisms for long particle lifetimes

The proper lifetime τ of a particle X is given by

$$\tau^{-1} = \Gamma = \frac{1}{2m_X} \int d\Pi_f |\mathcal{M}(X \to \{p_f\})|^2 \tag{1.24}$$

where m_X is the mass of X, $\mathcal{M}$ is the matrix element corresponding to the decay of X into the products $\{p_f\}$, and $d\Pi_f$ is the phase space for the decay [25]. From Equation 1.24, it is clear that X is long-lived when the decay $X \to \{p_f\}$ has little available phase space or a small matrix element, or both.

Phase space for a decay becomes limited if the mass spectrum is nearly degenerate, i.e. if there is a small difference between the mass of X and the combined masses of its decay products. This is shown in the SM in decays of neutral Kaons. The K_S and K_L are different CP eigenstates[6] of the neutral Kaon with very similar masses $m_{K_S} \sim m_{K_L} \sim 498$ MeV and are CP even and odd, respectively. Therefore, in hadronic decays, the K_S typically decays to 2 pions while the K_L mainly decays to 3 pions. The mass differences for these decays are $m_{K_S} - m_{2\pi} \sim 220$ MeV and $m_{K_L} - m_{3\pi} \sim 80$ MeV, resulting in vastly different proper lifetimes of $\tau_{K_S} = 9 \times 10^{-11}$ s and $\tau_{K_L} = 5 \times 10^{-8}$ s.

[5] 'Invisible' particles are electrically neutrally and are thus not directly observable by particle detectors.
[6] If CP was conserved in the weak interaction this would be exactly true. However, there is a small amount of observed CP violation in Kaon decays.

A small matrix element can be caused by small coupling constants or by scale suppression. Small couplings could result from an approximate symmetry[7] being slightly broken. Scale suppression occurs when the decay is mediated by a very off-shell particle and thus can be described by a higher dimension effective operator. Its coupling constant is then suppressed by a factor Λ^{D-4}, where $\Lambda \gg m_X$ is the energy scale at which the decay is mediated and D is the dimension of the operator. In the SM, muons decay via an off-shell W boson, which can be described by a dimension-6 operator. Therefore, muon decay is suppressed by a factor of m_W^2, resulting in a particularly long lifetime of $\tau_\mu = 2.2\ \mu$s.

1.3.3. Scalar portal models

A simple method of introducing new physics to the SM is to postulate the existence of a hidden sector of particles which interacts feebly[8] with the SM via a new field. The interactions between the SM and the hidden sector must respect the Lorentz symmetries of the SM. This constraint gives rise to a number of 'portals' to between the SM and the hidden sector. The simplest case is the scalar portal, where a singlet scalar S with no SM quantum numbers couples to the SM Higgs doublet [26–29]. If S has a non-zero VEV, the physical new scalar particle s can mix with the physical Higgs boson H and therefore decay into pairs of SM fermions via an effective Yukawa coupling, as shown in Figure 1.14. If the mixing is small and decays to other hidden sector particles are sufficiently suppressed, then s can be long-lived. If $m_s \leq \frac{1}{2}m_h$, s can be pair-produced in exotic Higgs decays at collider experiments. Yukawa couplings are stronger for more massive particles, therefore s will decay into the heaviest particles that are kinematically accessible. Thus, the typical decay signature for long-lived scalars is displaced hadronic jets. The scalar portal can also be generalised such that the singlet S couples to a heavy scalar Φ different to the 125 GeV Higgs boson, though the signatures are generally similar.

Previous searches for LLPs [30–35] have typically probed models featuring pair-production of LLPs. Figure 1.15 shows several recent results on the exclusion limits on the branching ratio $BR(H \to ss)$ of Higgs decays to pairs of long-lived scalars [36].

[7] If the symmetry were to be exact, the operator which mediates the decay would be forbidden

[8] The use of 'feeble' rather than 'weak' is to prevent confusion with the weak nuclear interaction.

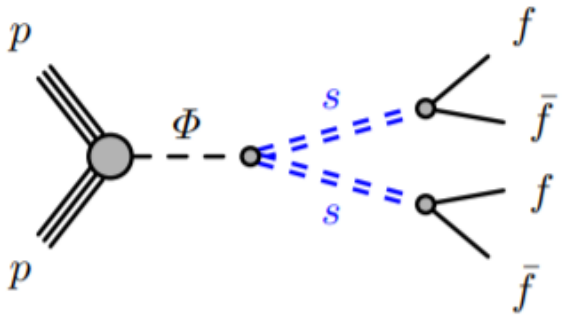

Figure 1.14.: Feynman diagram of a scalar mediator Φ produced in pp collisions decaying to hidden sector scalars s which subsequently decay into SM fermions [30].

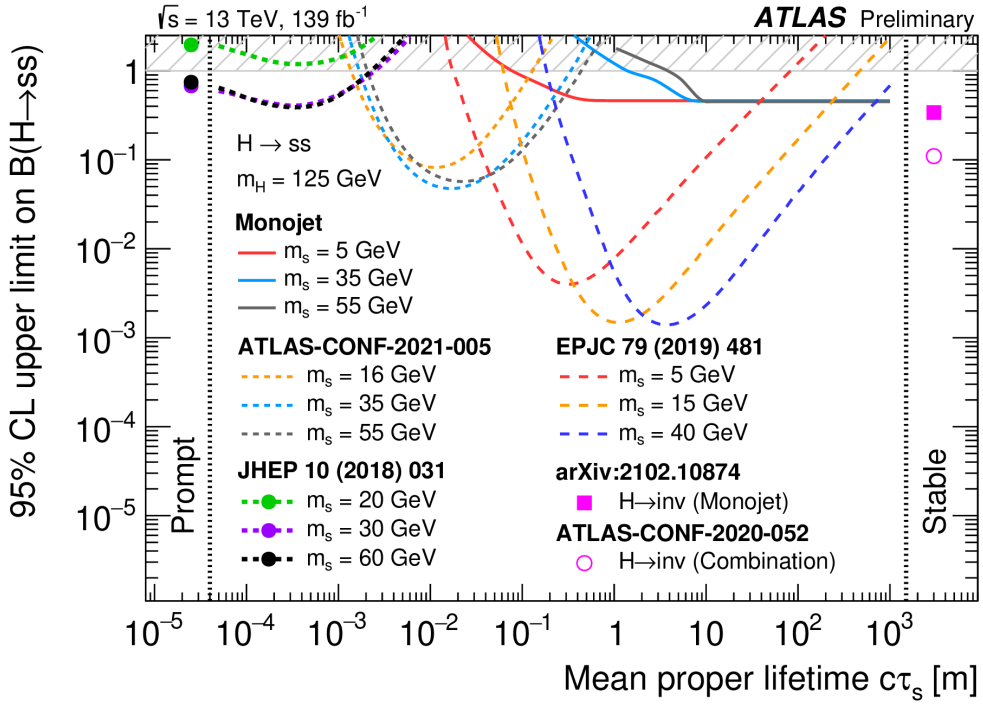

Figure 1.15.: Summary of exclusion limits on $BR(H \to ss)$ as a function of mean proper lifetime $c\tau$ at 95% confidence from several ATLAS Run 2 searches. Taken from [36].

1.3.4. Axions and axion-like particles

1.3.4.1. Axions

Axions are (pseudo-) Nambu-Goldstone (pNG) bosons that arise from the spontaneous breaking of an anomalous global U(1) symmetry [5]. An example is the QCD axion from the Peccei-Quinn solution [37] to the strong CP problem, i.e. the lack of CP violation in QCD despite there being a term in the QCD Lagrangian that in principle allows for CP violation:

$$\mathcal{L}_\Theta = \Theta \frac{g^2}{32\pi} G_a^{\mu\nu} \tilde{G}_{a\mu\nu}, \tag{1.25}$$

where the angle Θ breaks CP symmetry and is closely related to the neutron electric dipole moment d_n such that $d_n \sim \Theta \times 10^{-16}$. There are strong experimental bounds of $d_n \lesssim \mathcal{O}(10^{-26})$ $e$cm, which hence limits the angle to $\Theta \lesssim 10^{-10}$. Given that Θ could take any value between 0 and 2π, this very small value seems unnatural and fine-tuned. The solution, proposed by Peccei and Quinn, is an extension to SM with an additional global U(1) chiral symmetry that is spontaneously broken at a scale f_a. Hence, there is a corresponding pNG boson, named the axion. The Lagrangian for axion couplings to gluons is

$$\mathcal{L}_{ag} = \frac{a}{f_a} \frac{g^2}{32\pi} G_a^{\mu\nu} \tilde{G}_{a,\mu\nu}. \tag{1.26}$$

The combined Lagrangian is hence

$$\mathcal{L}_\Theta + \mathcal{L}_{ag} = \left(\Theta - \frac{a}{f_a}\right) \frac{g^2}{32\pi} G_a^{\mu\nu} \tilde{G}_{a\mu\nu} = 0. \tag{1.27}$$

Allowing the axion field to have an effective potential V_{eff} results in a dynamical coefficient of the CP violating term which vanishes at the minimum of V_{eff}, corresponding to $\langle a \rangle = -\Theta f_a$. thus resolving the strong CP problem.

Axions mix with the neutral pion and gain mass from interactions with gluons, resulting in a strict relation for axion mass:

$$m_a^2 = \frac{m_u m_d}{(m_u + m_d)^2} \left(\frac{f_\pi m_\pi}{f_a}\right)^2 \tag{1.28}$$

where f_π is the pion decay constant, while m_a, m_u, m_d and m_π are the masses of the axion, up and down quarks, and pion, respectively.

1.3.4.2. Axion-like particles

As with axions, axion-like particles (ALPs) are a pseudo-scalars associated with the spontaneous breaking of a new global U(1) symmetry. However, ALPs do not have the axion's stringent mass constraint from Equation 1.28 and do not necessarily solve the strong CP problem.

ALPs can couple to many SM particles, resulting in a variety of production modes and decay channels [38]. There are strong constraints on the couplings of ALPs to photons $g_{a\gamma}$ across a broad range of parameter space, as shown in Figure 1.16. Couplings involving the gauge bosons and the Higgs boson are hypothesised and can only be probed at colliders. The Feynman diagrams for ALPs radiated from a Z or W boson are shown in Figure 1.17. As lifetime is a free parameter of the model, ALPs can be long-lived. Hence, in the work presented in this thesis, a search for long-lived ALPs produced in association with a Z boson is conducted.

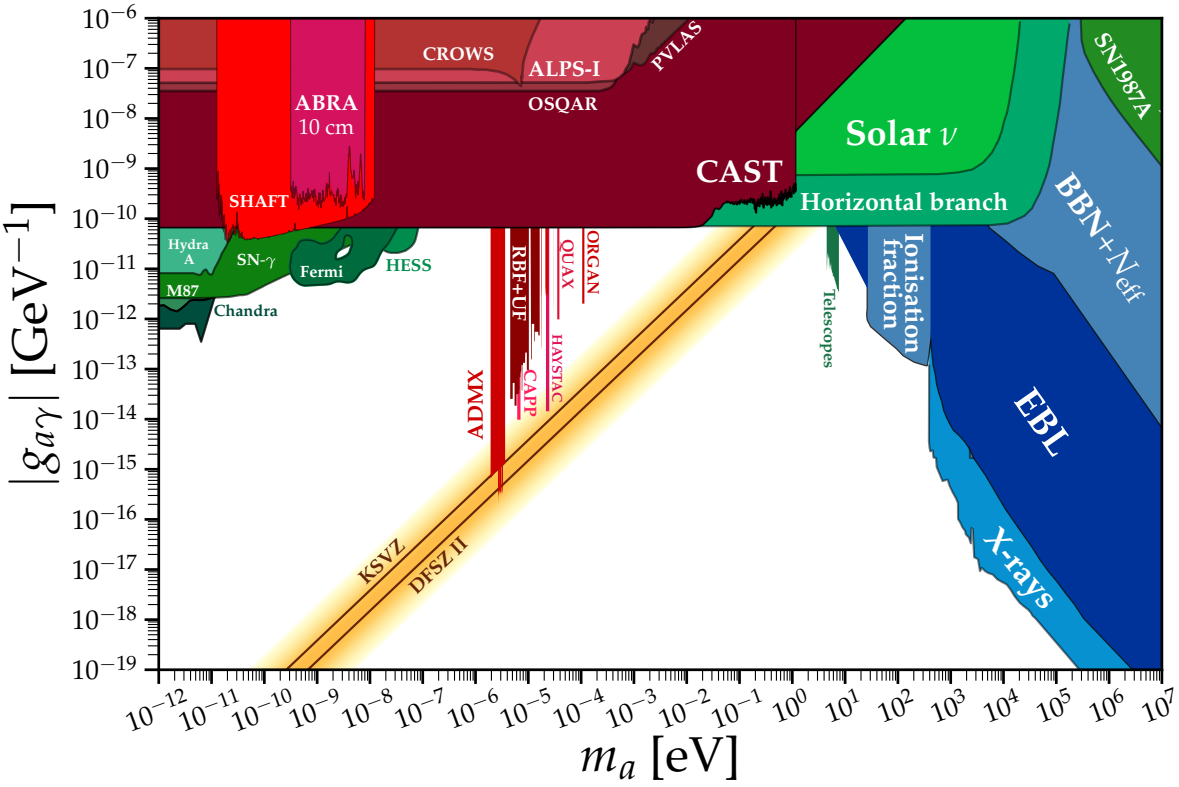

Figure 1.16.: Summary of exclusion limits on the ALP-γ coupling $g_{a\gamma}$. Constraints in red are from terrestrial experiments, those shown in green are astrophysical, and the orange band indicates expectations for the QCD axion. High-mass astrophysical limits are shown in blue. Taken from [5].

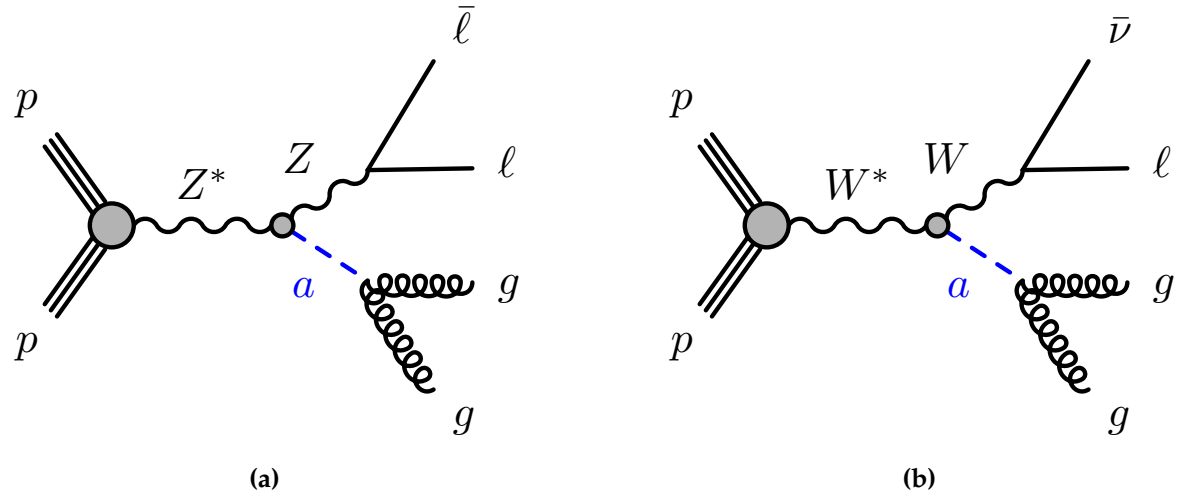

Figure 1.17.: Feynman diagrams of ALP production in association with (a) a Z boson and (b) a W boson.

In this work, MC simulations of Z+ALP events are generated with a variety of m_a and mean proper decay lengths $c\tau$, as discussed in Section 4.1.2. The production and decay mechanism of ALPs are regulated by the mass of the ALP m_a, the couplings to the primary SM gauge fields $C_{\tilde{G}}$, $C_{\tilde{B}}$ and $C_{\tilde{W}}$ and the ALP energy scale f_a. The ALPs considered in this search are assumed to be photophobic, thus the coupling of ALPs to photons $g_{a\gamma}$, derived from the couplings to the primary fields, is set to zero by imposing the condition $C_{\tilde{B}} = -\tan^2(\theta_W)C_{\tilde{W}}$. The ALP production cross-section is determined by the coupling of the ALP with the SM weak-sector. Since $C_{\tilde{B}}$ is a function of $C_{\tilde{W}}$ due to the photophobic condition, the parameters that define the cross-section are $C_{\tilde{W}}$, f_a and m_a. In the model considered, the ALP cross-section is proportional to $C^2_{\tilde{W}}$, therefore $C_{\tilde{W}} = 1$ is fixed to maximise the cross-section. This also allows results to easily be rescaled for lower values of $C_{\tilde{W}}$. In addition, $f_a = 1\,\text{TeV}$ is set. Therefore, the cross-sections of different ALP samples generated for this analysis scale with m_a. The ALPs considered are assumed to have a 100% branching ratio to gluons. Hence, The ALP lifetime scales inversely with $C_{\tilde{G}}$:

$$\tau = \frac{f_a^2 \pi}{2 C_{\tilde{G}} m_a^3}. \tag{1.29}$$

The hadronic shows produced in decays of ALPs into pairs of gluons have a similar topology to decays of hidden-sector scalars discussed in Section 1.3.3. Therefore, an analysis strategy similar to the recent ATLAS search for scalar LLPs that decay in the ATLAS MS [35] is employed to search for ALPs produced in association with a Z boson.

Chapter 2.

Experimental setup

2.1. The Large Hadron Collider

The Large Hadron Collider (LHC) at CERN [39] is the highest energy particle collider in the world. It accelerates two counter-rotating beams of protons around a pair of 27 km circumference superconducting rings and is designed to collide them at centre-of-mass energies up to $\sqrt{s} = 14$ TeV, where s is the Mandelstam variable $s = (p_1^\mu + p_2^\mu)^2$ and p_i^μ are the four-momenta of colliding protons. During Run 2 (2015-2018), the LHC operated at $\sqrt{s} = 13$ TeV and delivered a peak instantaneous luminosity of 1.9×10^{34} cm^{-2}s^{-1} [40]. The concept of luminosity is discussed below. The LHC can also collide heavy ions such as lead nuclei at $\sqrt{s} = 5.5$ TeV and $L = 10^{27}$ cm^{-2}s^{-1}.

There are four main experiments at the LHC: ATLAS [41], CMS [42], LHCb [43], and ALICE [44], all shown in Figure 2.1 and situated at the points where the beams intersect, called interactions points (IPs). ATLAS (A Toroidal LHC ApparatuS) is described in section 2.2. CMS is another general purpose detector similar to ATLAS. If any new physics is observed by either of these detectors, it must also be observed at the other detector for it to be considered a legitimate discovery. LHCb is a specialised forward detector optimised to investigate physics involving bottom and charm quark physics, including CP-violation and baryon asymmetry. ALICE is designed to study the properties of quark-gluon plasma, an extremely hot, dense state of matter that existed within the first 10^{-5} s after the Big Bang, before Big Bang nucleosynthesis occured.

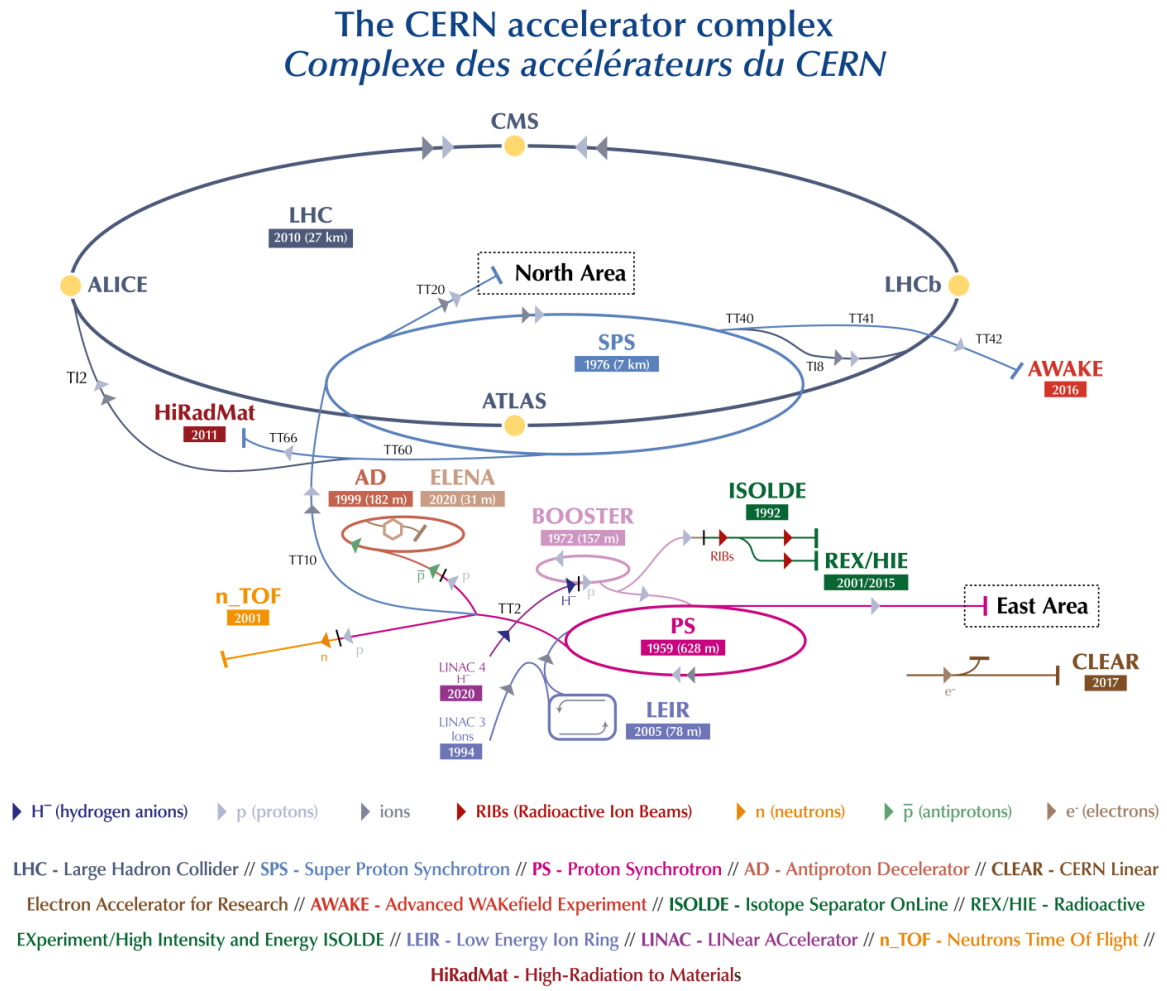

Figure 2.1.: Schematic of the CERN accelerator complex [45], showing the LHC, accelerator chain, and surrounding experiments.

2.1.1. LHC accelerator chain

Protons are injected to the LHC from a chain of pre-accelerators [46], as shown in Figure 2.1. Protons are initially accelerated to 50 MeV with LINAC 2, then up to 1.4 GeV, 25 GeV, and finally to 450 GeV using the Booster, Proton Synchrotron (PS), and Super Proton Synchrotron (SPS), respectively. Bunches of approximately 10^{11} protons are then injected into the LHC. Beams of up to 2556 bunches separated by 25 ns are held in a circular trajectory using superconducting dipole magnets operating at up to 8.2 T, and are accelerated up to 6.5 TeV by superconducting radiofrequency cavities. A narrow beam is desirable as this increases the probability of proton collisions when the beams cross. The beams are focussed in the ring using quadrupole magnets (aided by additional sextupole and octupole magnets) to reduce divergences caused by protons repelling in the bunches, and are 'pinched' down further by inner triplet magnets before they intersect at the IPs.

2.1.2. Luminosity

Instantaneous luminosity L arises from scattering theory and is a measure of the intensity of the proton beams, defined as

$$L = \frac{1}{\sigma}\frac{dN}{dt}, \tag{2.1}$$

where dN/dt is the rate of proton-proton (pp) collisions and σ is the interaction cross-section. Instantaneous luminosity is an important measure of the LHC's performance and can be determined in terms of the beam parameters as such:

$$L = \frac{N_b^2 n_b f \gamma}{4\pi\epsilon_n \beta^*} F, \tag{2.2}$$

where N_b is the number of protons per bunch, n_b is the number of filled bunches, f is the LHC revolution frequency, and γ is the relativistic Lorentz factor. The normalised emittance ϵ_n relates the width of the beam in the transverse plane to the inverse square-root of the beam energy, and the amplitude function β^* describes the focal length of the beam at the bunch crossing. Lastly, F is a geometric factor that accounts for the reduction of luminosity due to the small but non-zero beam crossing angle [39, 47].

The amount of recorded collision data is measured independently by each LHC experiment and is parameterised by the integral of instantaneous luminosity delivered over time, known as integrated luminosity $\mathcal{L}$, given by:

$$\mathcal{L} = \int L\, dt = \frac{N}{\sigma}, \tag{2.3}$$

where N is the total number of pp interactions. The ATLAS experiment recorded 140.1 ± 1.2 fb^{-1} of data usable for physics analysis during Run 2 [40].

As each bunch contains $\mathcal{O}(10^{11})$ protons, there are typically multiple pp interactions occurring within each bunch crossing. This is known as pileup and can both increase the probability of producing exotic particles and cause difficulty in reconstructing particle tracks due to finite detector resolutions, trigger and reconstruction efficiencies, as well as CPU availability. Pileup is quantified by the mean number of pp interactions per bunch crossing $\langle\mu\rangle$. The average pileup recorded by ATLAS during Run 2 is $\langle\mu\rangle = 33.7$ [48].

At the time of writing, the LHC has begun Run 3 (2022-2026) and the ATLAS detector has already recorded more than 240 fb^{-1} of pp collision data at $\sqrt{s} = 13.6$ TeV [49]. Following Run 3, the LHC will be upgraded to increase the delivered instantaneous luminosity to 5×10^{34} cm^{-2}s^{-1} [47]. The *High Luminosity-LHC* (HL-LHC) is expected to deliver around 250 fb^{-1} of data per year during operation, with a baseline target of 3 ab^{-1} within the first 12 years of running.

2.2. The ATLAS experiment

Along with the successful discovery of the Higgs boson in 2012 [6, 7], the primary goals of ATLAS (and CMS) are to probe for signs of new physics at unprecedented energies and perform precision measurements of SM phenomena. ATLAS is the largest particle detector at CERN, with a height of 25 m, a length of 44 m and a mass of 7000 tons. It is composed of several subdetector systems arranged as a series of concentric cylinders and discs, as shown in Figure 2.2, with a total solid angle coverage of nearly 4π steradians. The coordinate system used in ATLAS and important kinematic variables are described below, followed by brief descriptions of the inner detector (ID), calorimeters, and muon spectrometer (MS), then of the

trigger system used to collect interesting events. Finally, the chapter concludes with descriptions of the reconstructed objects used for physics analyses.

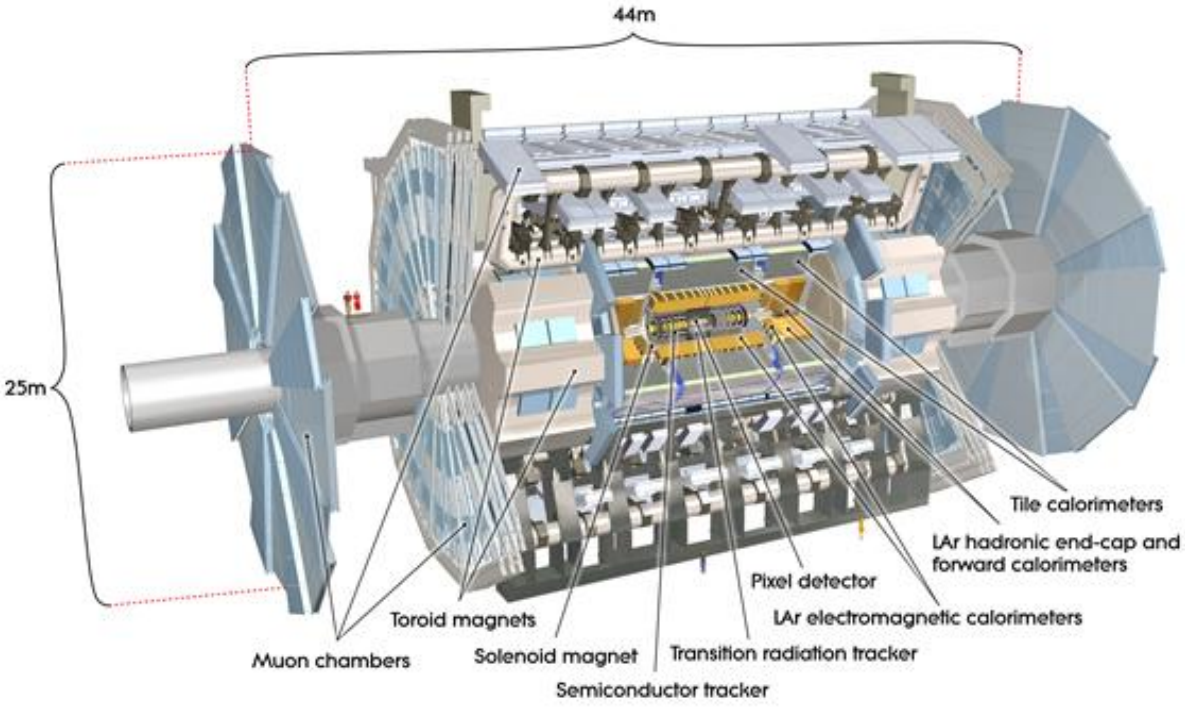

Figure 2.2.: Cut-away diagram of the ATLAS Detector [41].

2.2.1. Coordinate system and kinematic variables

The 4-momentum p^μ of a particle is defined as

$$p^\mu = (E, \vec{p}), \tag{2.4}$$

where E is the particle's energy and $\vec{p} = (p_x, p_y, p_z)$ is the particle's 3-momentum in Cartesian coordinates. ATLAS uses a right-handed coordinate system with the origin at the IP, located in the centre of the detector. The z-axis is aligned along the beam-line in the direction of the solenoid magnetic field, the x-axis points radially inwards towards the centre of the LHC ring, and the y-axis is defined as pointing vertically upwards. The detector geometry allows the transverse (x-y) plane to be described by cylindrical coordinates (r, ϕ), where $r = \sqrt{x^2 + y^2}$ and ϕ is the azimuth angle. In the longitudinal plane, a dimensionless Lorentz invariant quantity called

pseudorapidity η is used to represent particle trajectories, given by

$$\eta = -\ln\left(\tan\left(\frac{\theta}{2}\right)\right). \tag{2.5}$$

where θ is the polar angle from the z-axis and is not invariant under Lorentz boosts. For massless particles, η is identical to rapidity y, given by

$$y = \frac{1}{2}\ln\left(\frac{E + p_z}{E - p_z}\right), \tag{2.6}$$

and for relativistic particles with $|\vec{p}| \gg m$, $\eta \approx y$.

The angular distance ΔR between particles is Lorentz invariant and is defined as

$$\Delta R = \sqrt{\Delta\eta^2 + \Delta\phi^2}. \tag{2.7}$$

The composite nature of protons results in an unknown amount of the beam energy escaping along the beamline. However, as the beams collide head-on to a very good approximation, the net transverse momentum of each collision event is zero. Therefore, if invisible particles are created in a collision, there will be a missing transverse momentum $\mathbf{p}_T^{\text{miss}}$ in the final state, defined as the negative sum of momentum over all particles visible to the detector

$$\mathbf{p}_T^{\text{miss}} = -\sum_{visible} \mathbf{p}_T. \tag{2.8}$$

2.2.2. Inner detector

At the core of ATLAS, the ID [50] is comprised of three individual subdetectors – the pixel detector, the semiconductor Tracker (SCT), and the transition radiation tracker (TRT) – that together provide precision tracking of particles in the region $|\eta| < 2.5$, down to around 100 MeV. The barrel layers and their corresponding radii from the beamline are shown in Figure 2.3. A 2 T solenoid magnetic field is provided by a superconducting magnet, causing electrically charged particles to follow a helical trajectory and allowing the transverse momentum to be measured. The ID also provides measurements of electric charge using the sign of the curvature of the trajectory.

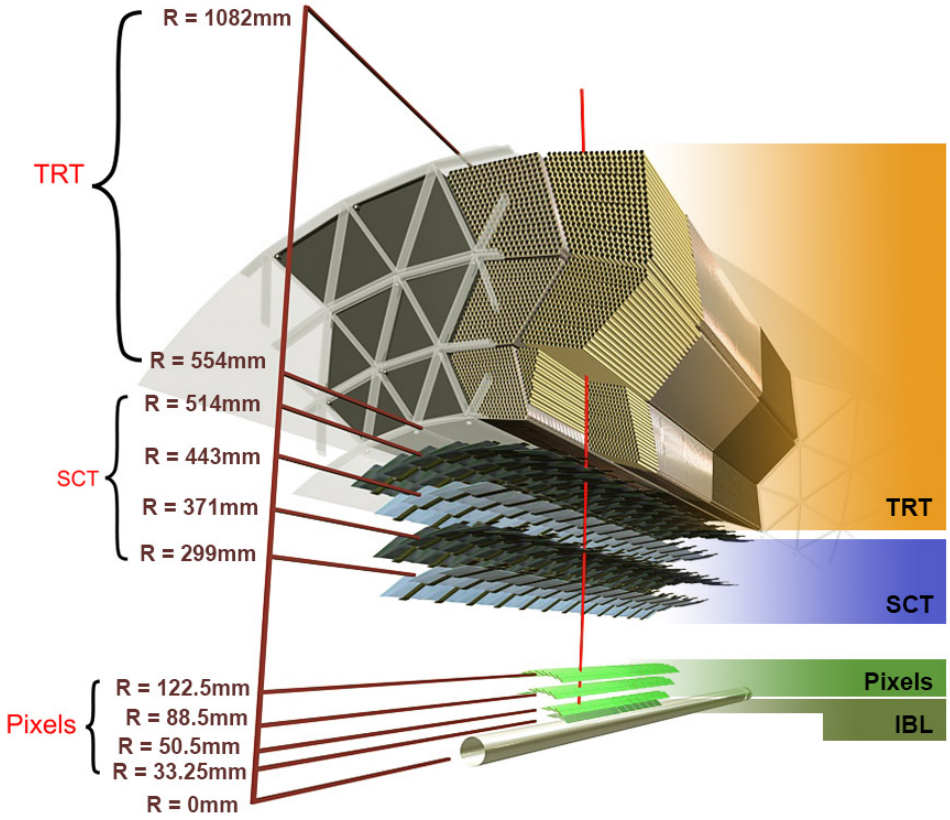

Figure 2.3.: Cutaway of the ATLAS inner detector showing the three tracking subdetectors and their radial distances R from the beamline ($R = 0$ mm) [41].

Pixel detector

Located closest to the IP, the pixel detector is composed of an array of 50×400 μm^2 silicon diodes (pixels) housed in four concentric barrel layers, as well as two endcaps with three pixel discs each, giving a very high resolution. The insertable B-layer (IBL) [51] is an additional layer of 50×250 mm^2 pixel sensors installed for Run 2 between the beam pipe and the previously innermost pixel layer to bolster tracking efficiency and aid in identification of heavy flavour decays.

Semiconductor Tracker

The SCT lies outside of the pixel detector and consists of four barrel layers of tile-shaped modules and nine discs in each endcap. Each module contains two etched silicon microstrips, with one aligned with the beamline and the other offset by a stereo angle of 40 mrad. The barrel sensors are pitched by 80 μm to achieve a high track momentum resolution.

Transition radiation detector

The outermost part of the ID is the TRT: an array of 4 mm diameter polyimide straw tubes that contain an aluminium coating, a tungsten cathode wire, and a gas mixture (primarily Xe, CO2, and O). Charged particles passing through the gas produce ions that induce a signal in the readout electronics. A charged track with $p_T > 0.5$ GeV in the region $|\eta| < 0.2$ will traverse at least 22 straws. Transition radiation resulting from large differences in the refractive indices of materials between the straws allows for discrimination between electrons and hadrons.

2.2.3. Calorimeter

The ATLAS calorimeter system, shown in Figure 2.4, covers the range $|\eta| < 4.9$, and is composed of a high-granularity liquid argon (LAr) electromagnetic calorimeter (ECal) surrounded by a hadronic calorimeter (HCal), with a joint electromagnetic and hadronic LAr calorimeter in the forward region (FCal). These are all sampling calorimeters that utilise dense absorbing materials to induce particle showers and an active material that is ionised when charged particles pass through. The electrical signal in the detector readout electronics is proportional in magnitude to the energy lost by the particle shower as it propagates the calorimeter materials. LAr presamplers provide an estimate for energy lost in the materials preceding the calorimeters.

Electromagnetic calorimeter

The ECal [52] encloses the ID and covers the same pseudorapidity range $|\eta| < 2.5$. It uses a lead absorber and LAr as the active detector material. In the barrel, the ECal consists of three concentric layers, each segmented into modules of lead absorbers arranged in an accordion-like geometry, with LAr and electrodes in-between them. This geometry results in symmetry in ϕ with no azimuthal cracks, maximises the detector volume and optimises signals to the detector electronics. The absorbers in the endcap are arranged in a similar accordion structures housed within three 'wheels'.

Electrons and photons lose energy through two electromagnetic interactions with matter in the detector: pair production $\gamma \to e^+e^-$, and bremsstrahlung $e \to e\gamma$. These both result in narrow electromagnetic showers in the ECal.

Hadronic calorimeter

In the barrel, the HCal [53] consists of three segmented layers of steel absorbers and plastic scintillating tiles connected to photomultiplier tubes by wavelength shifting

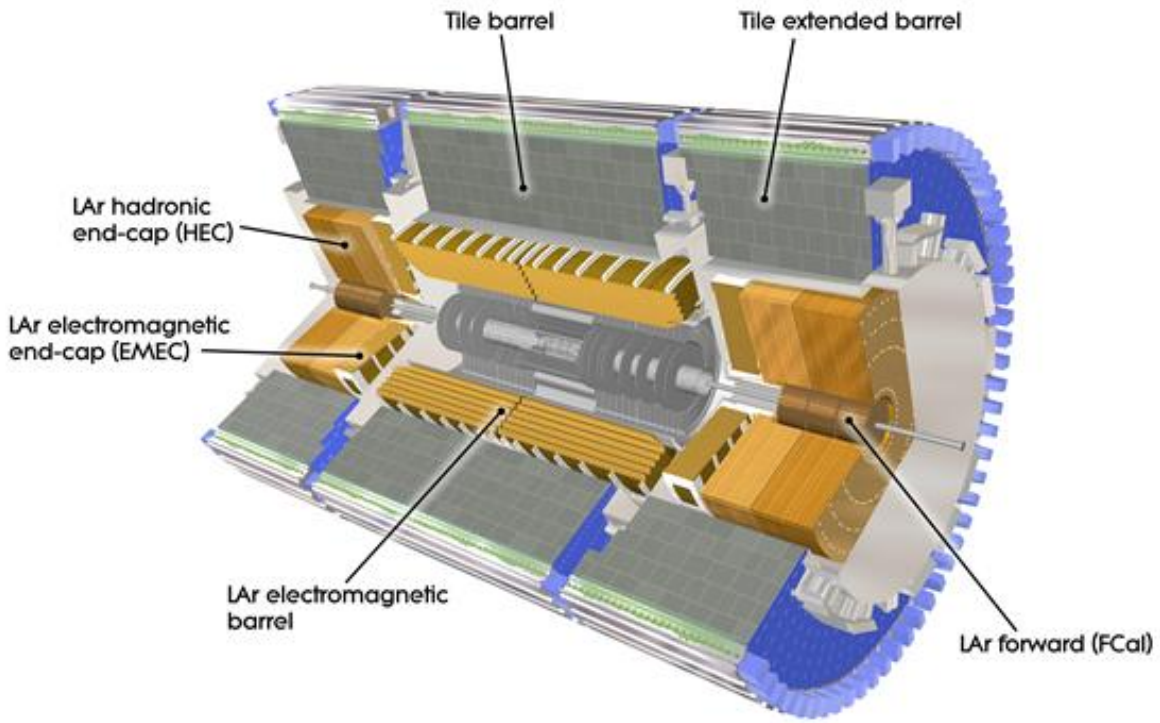

Figure 2.4.: Cut-away of the ATLAS calorimeter subsystems [41].

fibres. The coverage of the HCal is bolstered by an extended barrel. The hadronic endcap calorimeter is a LAr calorimeter consisting of four segments with copper plates as the absorber.

Hadronic jets lose energy through strong interactions with atomic nuclei in the detector materials, typically resulting in more diffuse showers that start later and penetrate further through the detector than electromagnetic showers. Therefore, hadronic calorimeters tend to be considerably larger than electromagnetic calorimeters. The ECal and HCal have a combined depth of 9.7λ at $\eta = 0$, where λ is a nuclear interaction length - the mean free distance between hadronic interactions.

Forward calorimeter

The FCal is comprised of three sections, the first of which is a LAr module with a copper absorber for measurements of electromagnetic showers. The two hadronic portions of the FCal are LAr modules with tungsten absorbers that are intended to be dense enough to limit leakage of showers into the HCal.

2.2.4. Muon spectrometer

The muon spectrometer (MS) [54] is the outermost layer of ATLAS, designed to provide measurements of the position and transverse momenta of muons that penetrate the other detector components due to their relatively high mass and lack of strong interactions. The MS incorporates a large toroid magnet with 8 coils orientated radially about the barrel in the region $|\eta| < 1.4$, as well as smaller toroid magnets in the endcap region $1.6 < |\eta| < 2.7$. The resulting magnetic field is non-uniform, with a strength of 1 T in the centre of the coils, and 0.5 T on average. Muons that enter the MS follow a path that curves in the longitudinal plane with a curvature radius that is inversely proportional to the muon's momentums. The MS utilised four subdetector systems during Run 2, as described below.

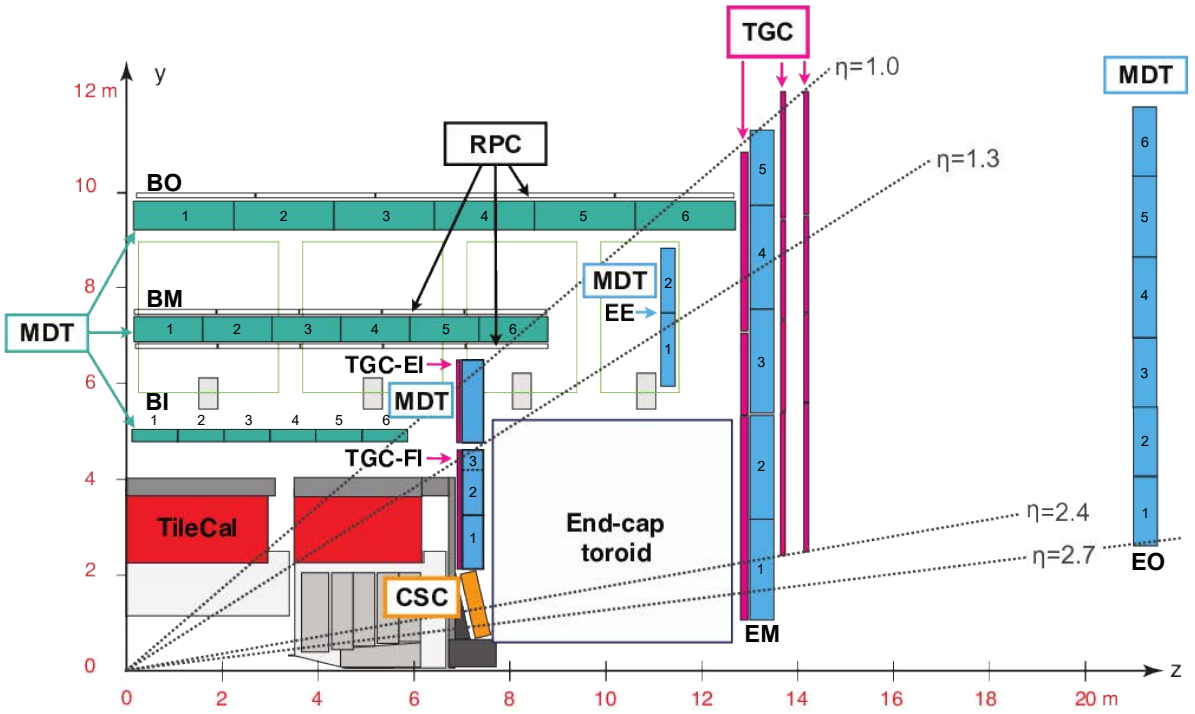

Figure 2.5.: Schematic diagram of the ATLAS muon spectrometer diagram in the η plane, showing the locations of the large subdetector stations. Taken from [55]. The MDTs are indicated by the green (barrel) and blue (endcap) elements.

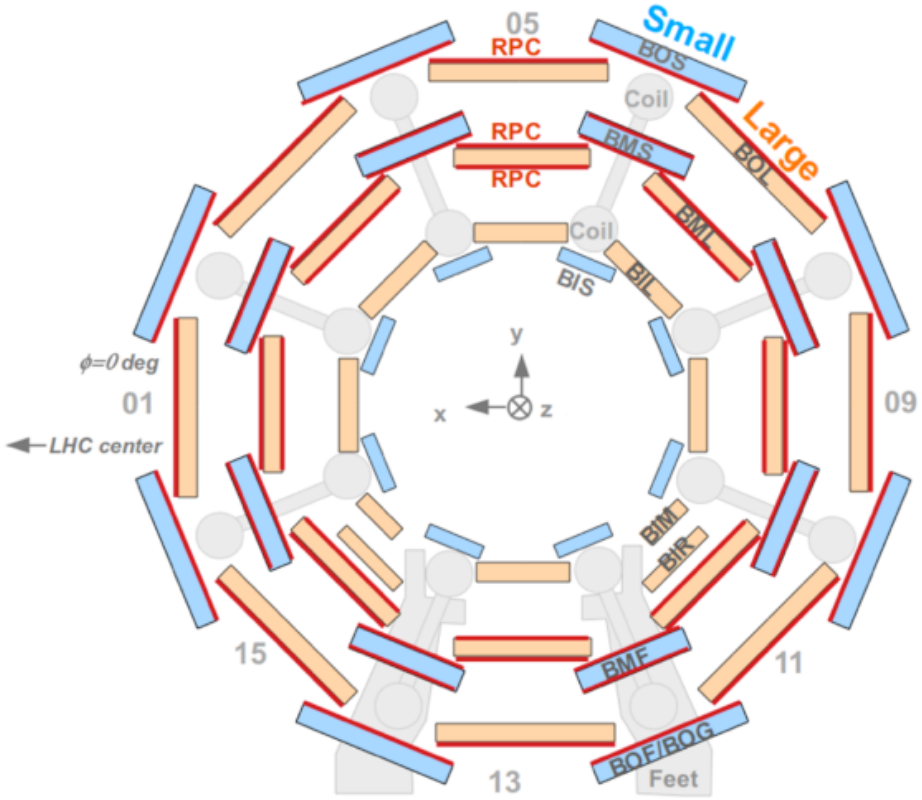

Figure 2.6.: Cross-section of the ATLAS MS barrel in the transverse plane. The blue and pink sections are the small and large MDT stations, respectively, and the red lines in the middle and outer layers are RPC doublets. Taken from [56].

2.2.4.1. Tracking chambers

In the barrel region $|\eta| < 1.0$, the MS utilises monitored drift tubes (MDTs) in three concentric layers each comprised of 8 small stations and 8 large stations to perform precise measurements of muon tracks in the central pseudorapidity region $|\eta| < 2.7$. The station naming convention is summarised in Table 2.1. As shown in Figures 2.5 and 2.6, the small MDT stations are housed radially internal to, within, and outside of the large magnet coils, respectively. The large stations are housed in the spaces between the coils, overlapping with the adjacent small stations to provide almost complete coverage, with some gaps in ϕ around the ATLAS support structures – additional stations in the ribs (BIR) and feet (BMF, BOF) provide some coverage in these regions. There is also a small gap at $|\eta| \sim 0$ for service access.

Region	Layer	Size	Other
Barrel	**I**nner	**S**mall	**R**ib
Endcap	**M**iddle	**L**arge	**F**oot
	Outer		

Table 2.1.: The station naming convention used in the MS. The location of a station is typically denoted in part by the acronym corresponding to its region in the detector, the layer it is part of, and its size. Some stations are specially designed to fit into areas such as the ribs and around the feet of ATLAS.

MDTs are aluminium tubes approximately 30 mm in diameter and varying between 1-6 m in length. They contain a 50 μm diameter tungsten wire that acts as an anode, as well as a gas mixture of Ar and CO_2. When charged particles enter the tubes, gas molecules become ionised and the liberated electrons drift radially inward in the electric field to the anode, where the collection of the charge creates an electric signal in the readout electronics. The time taken for the electrons to reach the anode from the closest distance R_{min} (drift time) allows the position of the incident charged particle to be measured precisely. The maximum drift time is 700 ns. The MDTs in ATLAS are housed in modules containing two multilayers each comprised of 3-4 layers of tubes. A single MDT has an average resolution of 80 μm, while the two-multilayer modules used in ATLAS provide an average resolution of 35 μm in the bending plane. MDTs are very coarse in ϕ due to their length, therefore RPCs are used in combination with MDTs to provide measurements in ϕ. The MDTs provide a precision of $\sigma(p_T)/p_T \approx 10\%$ for muons with a transverse momentum of $p_T = 1$ TeV. The precision depends inversely on p_T because the muon bending radius is inversely proportional to its p_T, so the finite per-hit resolution results in a larger uncertainty in track p_T.

The forward region $2.0 < |\eta| < 2.7$ is expected to have the highest particle flux in the MS due to a large amount of the pp collision energy being collimated along the beam. This impairs pattern recognition and reconstruction efficiency. Hence, cathode strip chambers (CSCs) with a time resolution of 7 ns are utilised in the inner layer of the endcap. CSCs contain wires housed radially, with cathode strips arranged orthogonally to the wires to provide measurements in both η and ϕ simultaneously to improve pattern recognition in the high-flux region. Particle positions are measured by analysing the signal induced in the cathode strips by the wires when charged particles pass through the chambers. The CSCs in ATLAS provide a resolution of 40 μm in η and 5 mm in ϕ.

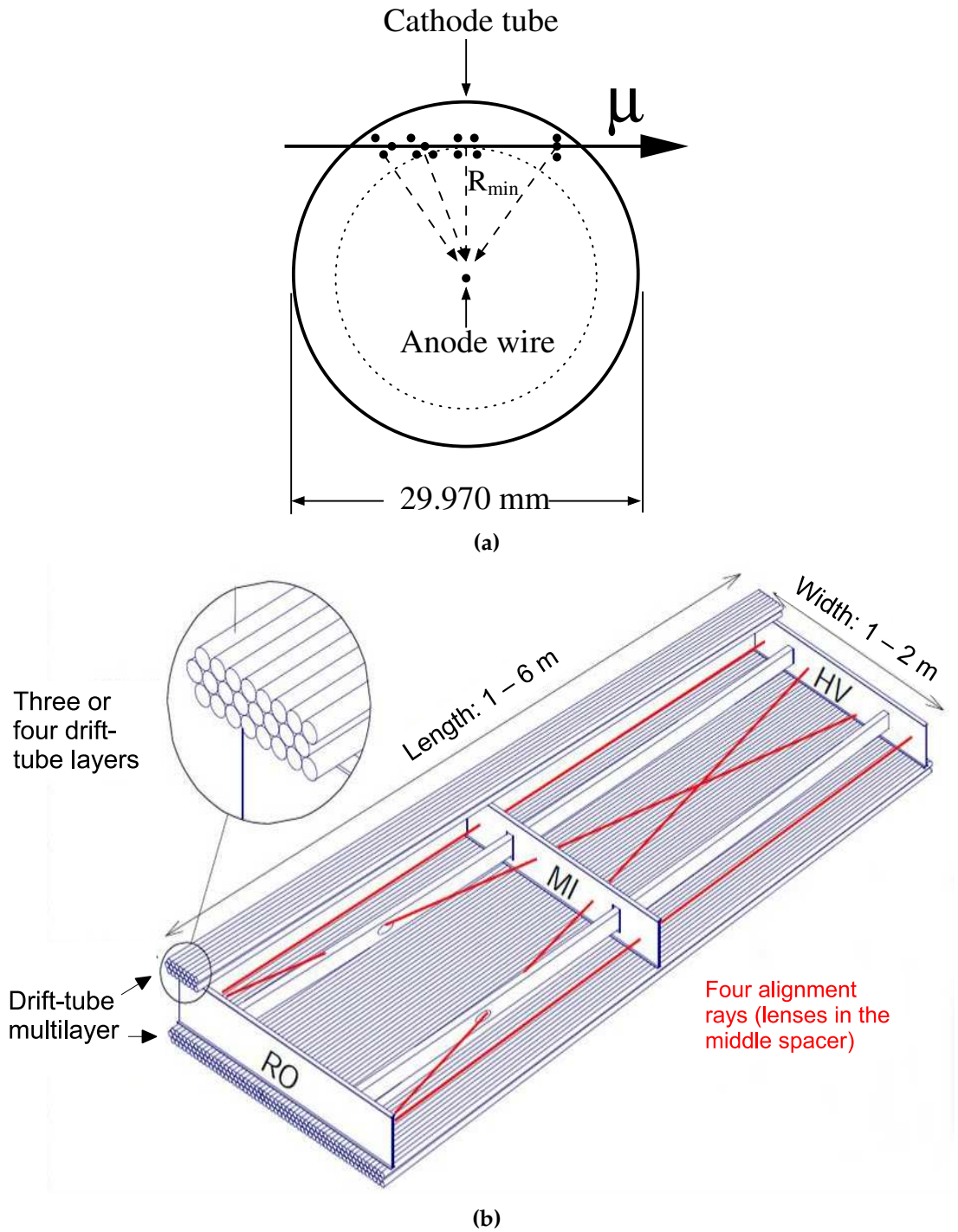

Figure 2.7.: Diagram of an MDT cross-section showing the effect of a muon passing through (a) and a schematic diagram of an ATLAS MDT chamber (b) [41].

2.2.4.2. Trigger chambers

During operation, triggering of muons in the barrel is achieved using resistive plate chambers (RPCs) with a rapid response time of 1.5 ns, arranged primarily in three concentric layers, with large RPCs situated between the magnet coils and small RPCs within and around the magnet coils, as shown in Figures 2.5 and 2.6. RPCs are also used in offline reconstruction to provide additional measurements of particle positions within 10 mm in both η and ϕ, to complement MDT position measurements. If the MDT and RPCs hits in the bending plane match, then the coordinate measured by the RPC in the non-bending plane is used along with the MDT measurement in the bending plane to reconstruct the track. The first two RPC stations sandwich the BM MDT stations and are used for triggering on low-p_T muons, while the third set of stations are housed on the outer surface of the BOL MDTs and the inner surface of the BOS MDTs, and are used for high-p_T triggering. No RPCs were present in the BI stations during Run 2.

The RPC modules used in ATLAS during Run 2 are doublets – pairs of RPC singlets. Figure 2.8 is a schematic of an RPC singlet, which consists of a pair of parallel resistive plates 2 mm thick with a 2 mm gas-gap containing a mixture of $C_2H_2F_4$ (94.7%), C_4H_{10}(5%), and SF_6(0.3%) gas. A potential difference of 9.8 kV is applied across the plates. The ATLAS RPCs operate in avalanche mode: when ionising particles traverse the gas-gap, ions and free electrons are produced, which in turn ionise more gas particles as they drift towards the plates in the applied electric field. An electronic signal is produced when the ions hit copper readout strips housed on the outer surfaces of the resistive plates. The strips adjacent to the negative electrode measure the ϕ coordinate and register a positive signal, while the strips on the positive electrode measure the η coordinate and register a negative signal.

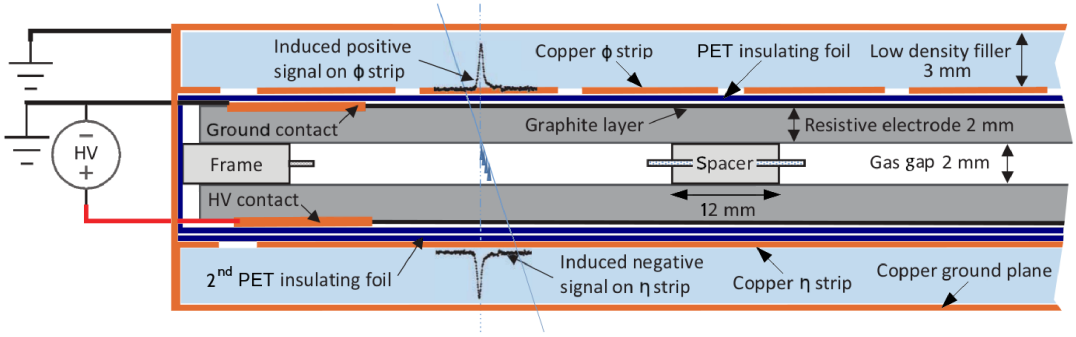

Figure 2.8.: Schematic diagram of an RPC singlet [41].

In the endcap region $|\eta| > 1.0$, thin-gap chambers (TGCs) are used instead of RPCs to provide allow forward muon triggering and secondary position measurements with a 60 μm resolution. The inner layer of TGCs is comprised of two sections: the endcap and a forward layer known as the small wheel. The middle TGC station (EML) is situated in the endcap and consists of seven layers of TGCs. The outer layer of MDTs (EOL) is situated several metres from the bulk of ATLAS (7.5 m from the EML) and does not feature any trigger chambers. Instead, the ϕ coordinate measured by the EML is extrapolated, which is possible since the EOL lies outside of the magentic field. TGCs have a response time of 4 ns, which is slower than RPCs, but have a better resolution of 2-6 mm in η and 3-7 mm in ϕ.

2.2.5. Trigger and data acquisition

In ATLAS, pp collisions occur at a rate of approximately 40 MHz, but not all events are considered useful for physics analyses. Therefore, a trigger is used to extract only the most interesting events and to reduce the immense computing power that would be required to capture every single event. The ATLAS trigger is a multi-stage system designed to reduce the event rate down to an average of 1 kHz [57]. The first stage of the trigger, known as Level 1 (L1), is a hardware-based trigger that uses low-granularity information from the calorimeter (L1Calo) and MS (L1Muon)[1] to decide whether to keep an event within a latency of 2.5 μs and reduce the rate to 100 kHz. A topological trigger system (L1Topo) takes kinematic information from L1Calo and L1Muon to suppress backgrounds. Each event triggered by L1 contains Regions of Interest (RoIs) defined in η and ϕ that provide information about areas of the detector that may contain physics objects such as leptons, photons, or jets.

The second stage of the trigger is the High-Level Trigger (HLT), which is a software-based trigger that reduces the rate to approximately 1 KHz. The HLT uses the RoI information from the L1 trigger to reconstruct events in greater detail than L1 using the same reconstruction algorithms used in offline reconstruction, or in some cases dedicated algorithms for complex physics objects and computationally intense processes.

[1] L1Muon also uses information from the hadronic tile calorimeter.

2.2.6. ATLAS object reconstruction

Particles are identified by the unique signatures they produce in ATLAS, such as those shown in Figure 2.9. Information from all the subdetectors is combined to reconstruct "physics objects" that are candidates for real particles. The objects utilised in this thesis are tracks, jets, photons, electrons, muons, and missing transverse energy. In addition, a non-standard ATLAS object called a displaced vertex (DV) is utilised to target LLP decays in the MS. The DV reconstruction algorithm utilised is described in Section 2.2.6.6.

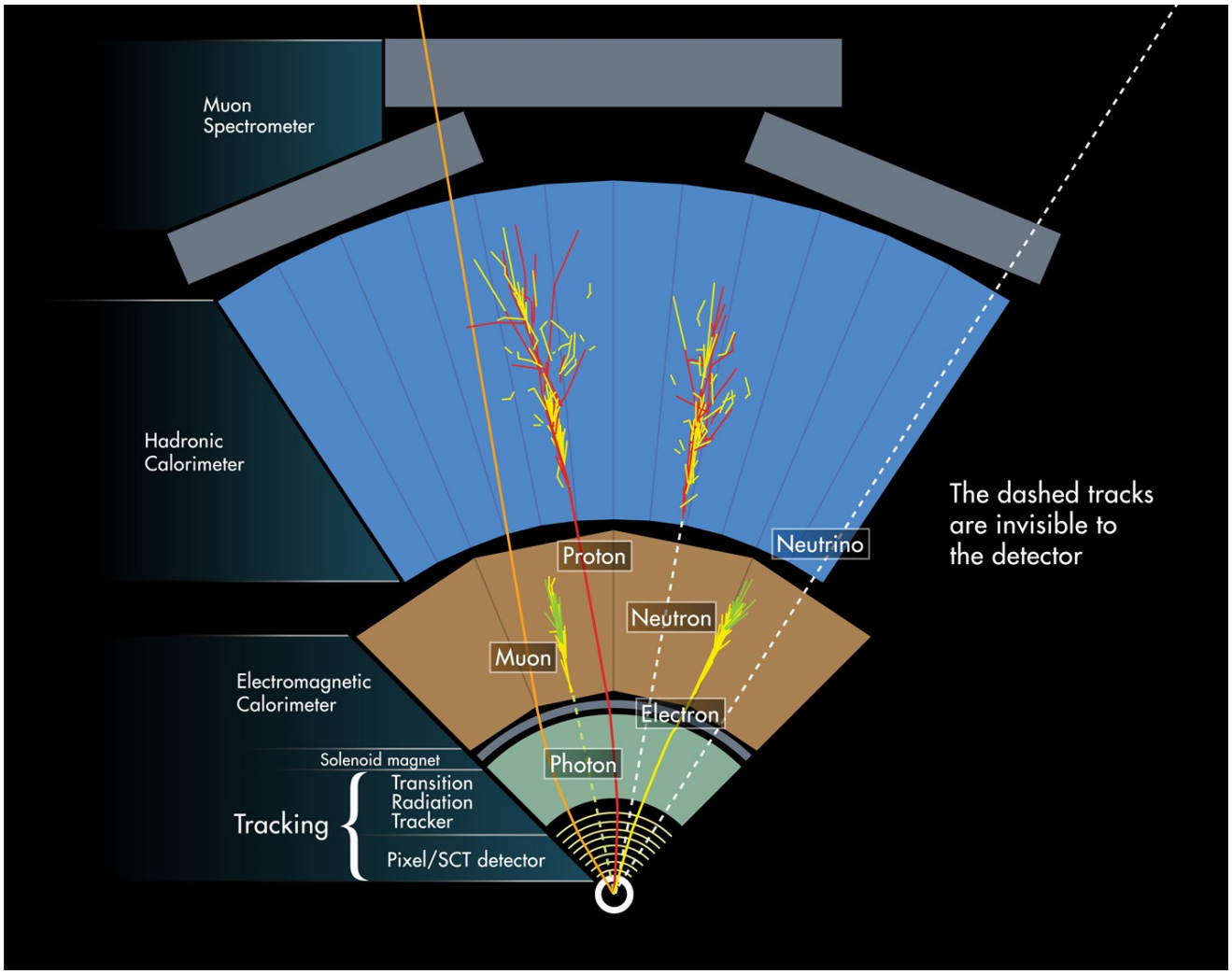

Figure 2.9.: Diagram of particle signatures in the transverse plane of the ATLAS detector [58].

2.2.6.1. Tracks and primary vertices

Reconstruction of tracks in the ID is the first stage of event reconstruction at ATLAS and is essential for identification of particles as well as primary vertices (PVs), which indicate the occurrence and positions of hard proton-proton scatters. PV candidates are comprised of at least two tracks, each with $p_T^{\text{track}} > 500$ MeV. Pileup typically results in several PV candidates in an event. Therefore, the vertex that possesses the highest associated $\sum_{\text{track}} p_T^2$ is considered the PV.

Tracks encode the momenta and trajectories of particle candidates with five parameters that are measured with respect to the PV:

- q/p: the ratio of charge to the magnitude of momentum defines the curvature of tracks in a magnetic field.
- d_0: the impact parameter in the transverse plane.
- z_0: the impact parameter in the longitudinal plane.
- ϕ_0: the azimuth angle of the track direction at d_0.
- θ_0: the polar angle of the track direction at z_0.

These parameters are illustrated in Figure 2.10. The solenoid magnetic field that permeates the ID is homogenous and results in helical track trajectories.

For particles originating from the PV, an inside-out approach is utilised to reconstruct the track. Measurements of hits in the pixel detector and SCT are combined to form clusters that are used to create 3D position measurements called space points. A track is seeded by three space points from either the pixel detector, SCT, or both. The seeds are extrapolated outwards, iteratively combining space points that are consistent with the seeded track trajectory to form track candidates. This can result in a very large number of track candidates that may share clusters. Therefore, ambiguity resolution algorithms are utilised to assign any shared cluster to the single track it matches best. A global χ^2 fit is performed to select final high-precision track candidates and to reject poorly fitted track candidates that are likely the result of random combinations of hits and not representative of real particles – such tracks are thus known as fakes. The reconstruction algorithm will then attempt to extrapolate the track candidate to matching TRT hits and refitting the entire track including the TRT information. If the inclusion of TRT hits improves the track fit, the track candidate is saved and the addi-

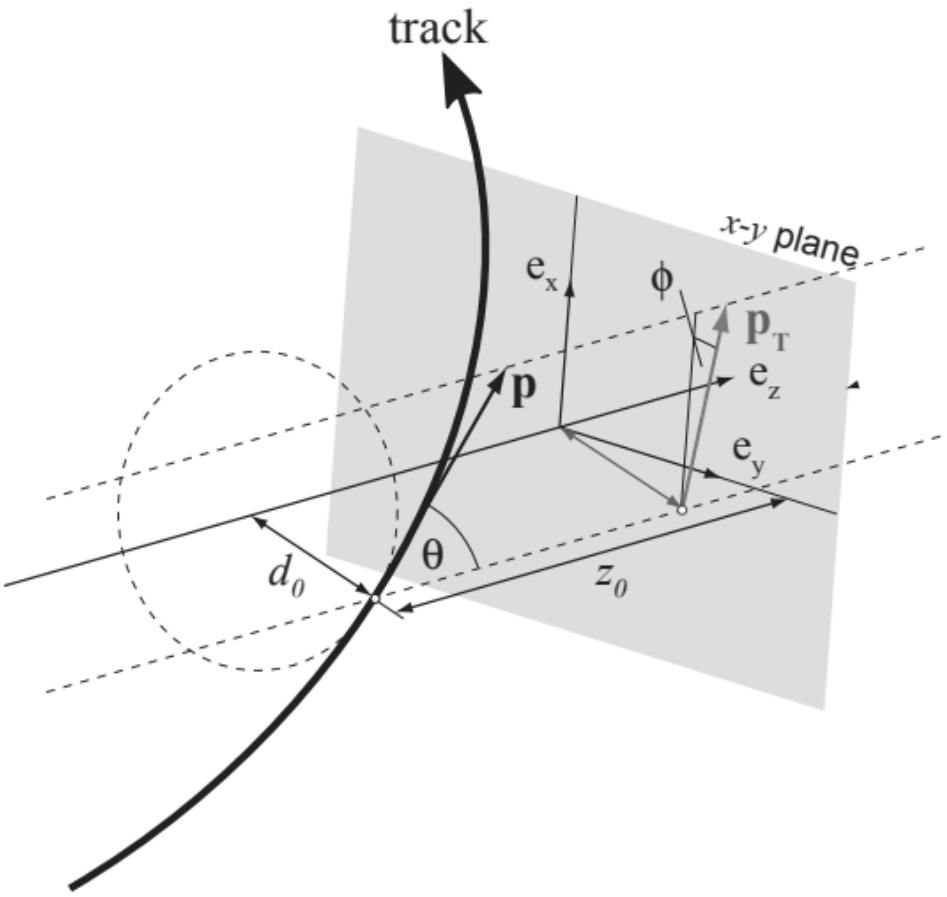

Figure 2.10.: Diagram showing a track in the ID and its associated parameters [59].

tional measurements from the TRT improve the momentum resolution. Otherwise, the silicon-only track is kept.

For particles that are created away from the PV, such as electrons from converted photons or the decay products of LLPs, an outside-in approach is taken where ID tracks are seeded by TRT hits and extrapolated inwards. However, only ID tracks originating from the PV are considered in this thesis.

2.2.6.2. Jets

Numerous interactions produce highly energetic quarks and gluons at the LHC. Colour confinement prevents the existence of non-singlet colour states. Therefore, quarks and gluons hadronise, resulting in collimated streams of particles that penetrate deep into the calorimeters, known as hadronic jets.

Jets are reconstructed from 3D topological clusters of calorimeter cells. Cluster formation is dictated by cell signal significance ζ_{cell}, defined as the ratio of the energy deposited in a cell E_{cell} to the average expected noise σ_{cell}, as such

$$\zeta_{cell} = \frac{E_{cell}}{\sigma_{cell}}. \tag{2.9}$$

Clusters are seeded by cells where $\zeta_{cell} > 4$. The anti-k_t algorithm [60] is then used to reconstruct a jet. Adjacent cells with $\zeta_{cell} > 2$ are added to in the cluster, then the surrounding cells with $\zeta_{cell} > 0$ are included to capture the tails of the showers. If neighbouring cells are seeds, the two clusters are merged. After reconstruction, jets are calibrated [61, 62].

2.2.6.3. Electrons and photons

Electrons and photons both produce EM showers in the ECal via cascades of bremsstrahlung radiation and photon conversion. The distance a shower traverses in the ECal is characteristic of its energy. As before with in the case of hadronic jets, ECal clusters are seeded if the energy deposits in the ECal cells are greater than 4 times the expectation from pileup i.e. $\zeta_{cell} > 4$. ID tracks matched to ECal clusters are utilised to distinguish photons and electrons. An electron object is defined as a cluster of energy deposits in the ECal that is matched to an ID track. A photon that has converted to an electron-positron pair in the ID is identified by a vertex in the ID that matches ECal clusters, and an unconverted photon is identified by ECal clusters with no matching ID tracks. In some cases, electrons can be misidentified as photons if their tracks are not reconstructed.

2.2.6.4. Muons

As shown in Figure 2.9, a muon will penetrate the calorimeters without inducing an electromagnetic shower, unlike its leptonic relative, the electron. This is because the rate of bremmstrahlung radiation for a charged particle is inversely proportional to the particle's mass squared. Therefore, muon-emitted bremmstrahlung radiation is suppressed by a factor of approximately $1/40000$ compared to that of electrons. Information from all three subdetector systems is utilised to reconstruct several types of muon objects. Tracks are reconstructed independently in the ID as described in Section 2.2.6.1 and in the MS, then combined if possible, as discussed below.

The first step of muon track reconstruction is a straight-line fit of hits in adjacent MDT tubes to create muon segments. A preliminary 2D track candidate is formed by combining segments from multiple MS layers. A candidate muon track is seeded by segments in the middle MS layer and a combinatorial search is conducted for segments that approximately fit the expected trajectory of a muon in the toroidal magnetic field. Due to the coarse resolution of MDTs in the non-bending plane, the ϕ-coordinate is measured using hits in the trigger chambers and combined with the 2D track to form a 3D muon track candidate. Following this, an overlap removal procedure then resolves ambiguities in the case that multiple track candidates are formed from a single segment. A global χ^2 fit of the hits associated with the track candidate is then conducted, accounting for material interactions, energy losses in the calorimeter, and any muon chamber misalignment. Hits that negatively affect the fit are removed and hits that subsequently become consistent are added. The fit is repeated iteratively until the best fitting combination is found. Track candidates are then rejected if the χ^2 fit does not meet the selection criteria.

The four types of muon object are described below and their corresponding detector signatures are shown in Figure 2.11. In the work presented in this thesis, pure, high-p_T muons in the region $|\eta| < 2.5$ are required. Therefore, only combined muons are utilised.

- **Combined muons:** The highest purity muon object with the largest acceptance range is obtained by extrapolating a muon track inwards and matching it to an ID track that shares the same trajectory to form a *combined muon*. A global refit of the hits associated with the individual tracks in both systems is performed. As with the fitting of muon track candidates, hits in the MS can be added or removed to improve the track fitting.

- **Standalone muons:** In the case that a matching ID track cannot be found, an MS track will be extrapolated to the beamline. These *standalone muons* help recover acceptance in the region $2.5 < |\eta| < 2.7$ where there is a gap in the ID.
- **Segment-tagged muons:** If a muon does not pass through multiple MS layers, either because its p_T is too low or its trajectory is largely outside the MS acceptance, a *segment-tagged muon* object can be reconstructed by combining an ID track with a least one MS segment.
- **Calo-tagged muons:** If no muon track or segment is found, an ID track can be matched to calorimeter energy deposits that are characteristic of a minimally ionising particle to reconstruct a *calo-tagged muon*. This is the lowest purity muon object, however, it recovers acceptance in regions where there are gaps in the MS coverage, particularly in the MS service gap at $|\eta| < 0.1$.

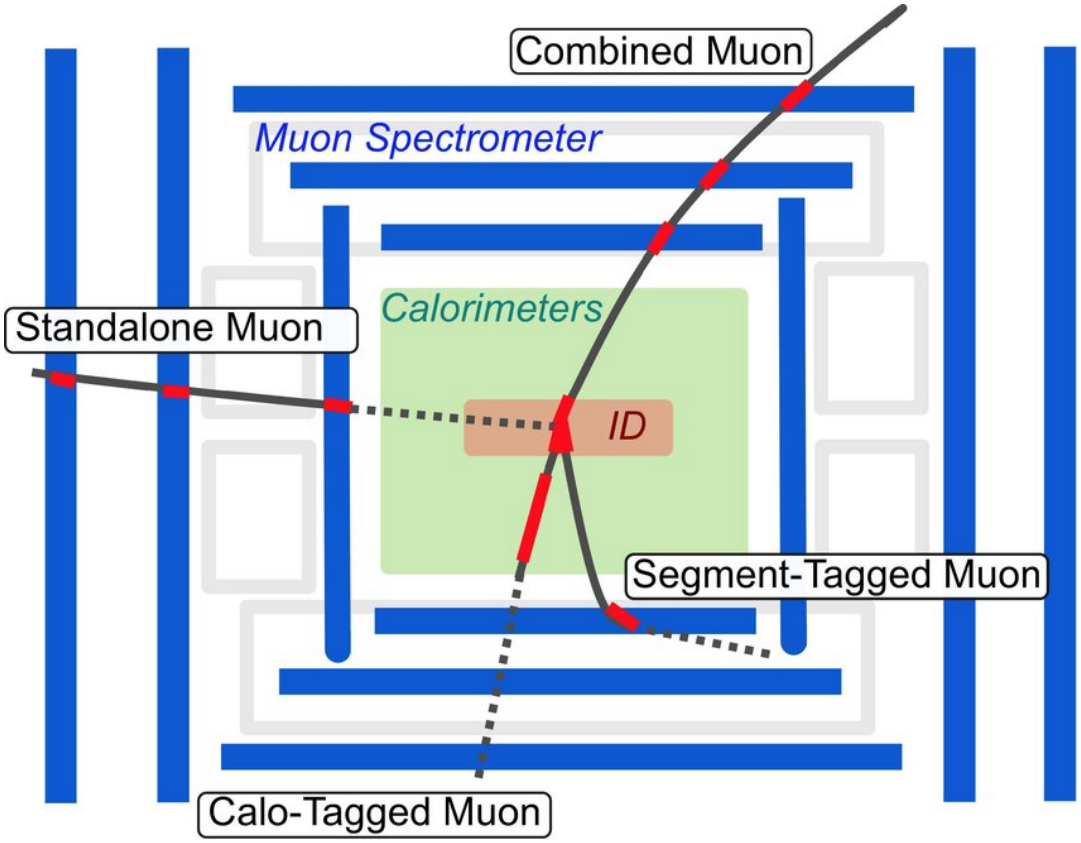

Figure 2.11.: Diagram showing the signatures of each muon type [63]. The red and green regions respectively indicate the ID and calorimeter, while the MS tracking stations are represented by the blue bars. Hits in active detector materials are shown in bright red. The solid and dotted black lines represent reconstructed and extrapolated sections of tracks, respectively.

2.2.6.5. Missing transverse energy

As mentioned in Section 2.2.1, the presence of invisible particles can be inferred from the amount of missing transverse energy E_T^{miss} in an event, where

$$E_T^{\text{miss}} = |\boldsymbol{E}_T^{\text{miss}}| = \sqrt{(E_x^{\text{miss}})^2 + (E_y^{\text{miss}})^2}. \tag{2.10}$$

The azimuth angle ϕ^{miss} corresponding to the E_T^{miss} can indicate the trajectory of an invisible particle and is given by

$$\phi^{\text{miss}} = \tan^{-1}\left(\frac{E_y^{\text{miss}}}{E_x^{\text{miss}}}\right). \tag{2.11}$$

The $\boldsymbol{E}_T^{\text{miss}}$ vector is obtained by calculating the negative vector sum of the transverse momenta of all physics objects that pass the selection criteria defined by an analysis, denoted here by $\sum_{\substack{\text{selected}\\ \text{object}}} \boldsymbol{p}_T^{\text{object}}$. Therefore,

$$\boldsymbol{E}_T^{\text{miss}} = -\sum_{\substack{\text{selected}\\ \text{electrons}}} \boldsymbol{p}_T^{e} - \sum_{\substack{\text{selected}\\ \text{muons}}} \boldsymbol{p}_T^{\mu} - \sum_{\substack{\text{selected}\\ \text{taus}}} \boldsymbol{p}_T^{\tau} - \sum_{\substack{\text{selected}\\ \text{photons}}} \boldsymbol{p}_T^{\gamma} - \sum_{\substack{\text{selected}\\ \text{jets}}} \boldsymbol{p}_T^{\text{jet}} - \sum_{\substack{\text{unused}\\ \text{tracks}}} \boldsymbol{p}_T^{\text{track}}, \tag{2.12}$$

where $\sum_{\substack{\text{unused}\\ \text{tracks}}} \boldsymbol{p}_T^{\text{track}}$ is a soft term that accounts for tracks not utilised to construct other physics objects, but still pass quality selection. $\boldsymbol{p}_T^{\tau}$ denotes the tranverse momenta of τ lepton objects, which are not utilised in this thesis.

2.2.6.6. Displaced vertices in the muon spectrometer

Hadronic decays of LLPs in the MS typically produce hadronic showers that produce significant amount of activity in the MS. The amount of MS activity depends on the shower multiplicity and width, which is dictated by the LLP mass and boost. The general signature is a collection of MS tracks that originate from a single point within the MS. By identifying and matching the appropriate tracks, a displaced vertex (DV) can be reconstructed. However, the standard muon segment-finding algorithm is designed to work in a relatively clean environment and is suboptimal for segment-finding when there is a large concentration of hits due to a displaced hadronic shower.

Therefore, a dedicated algorithm capable of reconstructing low-momentum tracks in a busy environment was developed to reconstruct DVs in the MS [56] and to date has been employed in all searches for DVs in the ATLAS MS [30, 35, 64–66], including the work presented in this thesis. The DV-finding algorithm is briefly described below.

The MS DV-finding algorithm exploits the spatial separation between the two multilayers (MLs) inside a single MDT chamber. First, straight-line segments are reconstructed in each ML from hits in at least three tube layers that satisfy a minimum χ^2 fit requirement. The segments from ML1 are matched with those from ML2 to form a combined set of single-ML segments and corresponding track parameters called a *tracklet*, as shown in Figure 2.12. The tracklets are then grouped into clusters within a cone of dimensions $|\Delta\eta| < 0.7$ and $|\Delta\phi| < \pi/3$ that originates at the IP. A cluster is required to contain at least three (four) tracklets in the barrel (endcap) region.

As MDTs do not provide precise ϕ information for the tracklets, the ϕ coordinates of matching RPC (TGC) hits in the barrel (endcap) are used to measure the straight-line trajectory of the LLP in η and ϕ. For the same reason, it is necessary to map the tracklets onto the $R - z$ plane to calculate the DV position. In the $R - z$ plane, the tracklets are extrapolated back to the IP and the DV position is calculated using an iterative fit. In the barrel, the tracklets are extrapolated back using the full magnetic field map and a χ^2 fit is performed to determine the DV position. If the χ^2 probability is below 5%, the worst fitting tracklet is removed and the cluster is refit until either the χ^2 probability is above 5% or there are too few tracklets in the cluster. In the endcap region, the magnetic field is negligible. Therefore, the DV position is calculated by performing a simple linear extrapolation and a least-squares regression fit where tracklets that are more 30 cm from the DV are iteratively removed.

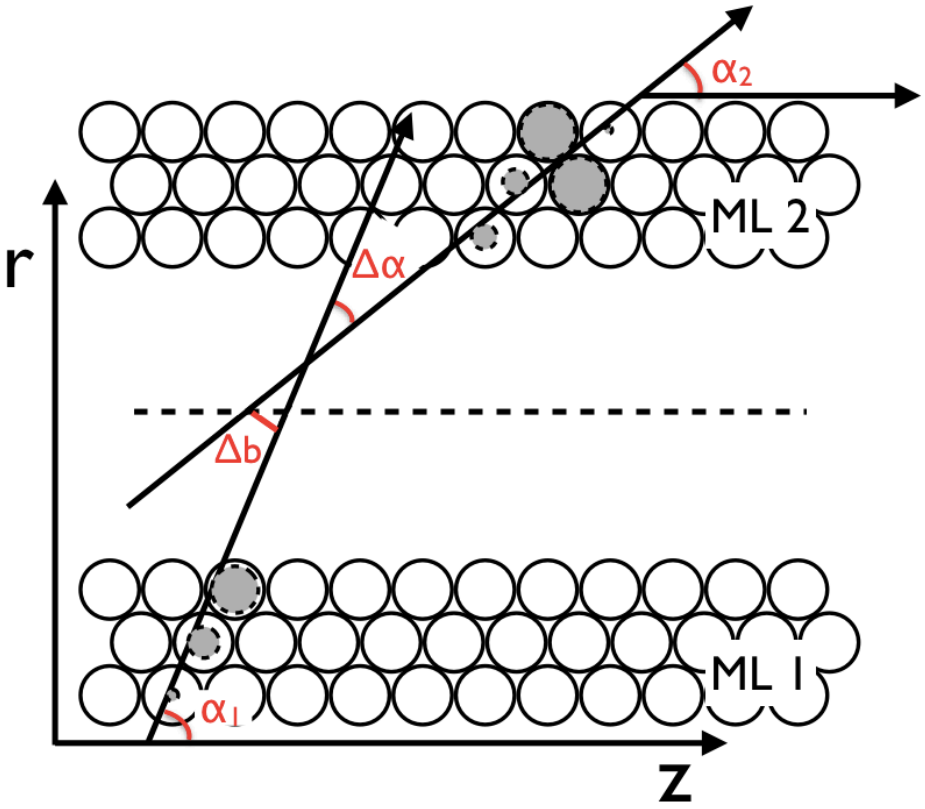

Figure 2.12.: Sketch of a barrel MDT chamber with a segment in each multilayer (ML) [56]. The variable $\alpha_{1(2)}$ is the angle with respect to the z-axis of the segment in ML1(2) and $\Delta\alpha = \alpha_1 - \alpha_2$. Δb is the distance of closest approach between the two segments at the middle plane of the MDT chamber, represented by the dashed line.

Part II.

Searching for long-lived particles with the ATLAS muon spectrometer

Chapter 3.

Previous searches for long-lived particles

This chapter summarises the previous searches for LLP decay signatures in the MS that were conducted using ATLAS Run 2 data and provide the basis for the search presented in Chapter 4. Section 3.3 describes the search for LLPs conducted using data collected during 2015 and 2016 [30], which is then reinterpreted by the author to study the sensitivity of ATLAS to ALPs that decay into hadronic jets in the MS. Section 3.4 describes the search for LLPs that utilises the full Run 2 dataset, which was developed in parallel and published with the author's work [35].

3.1. Muon RoI cluster trigger

Previous searches for LLPs that decay into hadronic jets in the ATLAS MS, such as those discussed in Sections 3.3 and 3.4, have employed the muon RoI cluster trigger [67] to identify candidate events. The muon RoI cluster trigger is a signature-driven trigger that selects events based on the detector signature of an LLP that decays into hadronic jets in the MS, without requiring additional prompt objects. In such decays, the hadronic showers tend to be reconstructed by the L1 muon trigger system as a cluster of L1 muon RoIs centred on the LLP trajectory.

The L1Muon trigger uses hit information from the MS trigger chambers to determine the deviation of the distribution of hits from that of a muon with infinite momentum, i.e. a straight-line track in the MS that points towards the IP. L1 muon RoIs are constructed in a $\Delta\eta \times \Delta\phi = 0.1 \times 0.1$ (0.03×0.03) region in the barrel (end-

cap) from combinations of hits in the RPC (TGC) chambers. A coincidence of hits is required in at least three of the RPC singlets that sandwich the BM MDT layer in the barrel, or in the two outer TGC planes in the endcap. For high-p_T muon RoIs, additional hits are required in at least one of the outer two RPC singlets in the barrel or in two of the innermost TGC layer in the endcaps. Only the two highest-p_T RoIs in each MS sector are utilised by the HLT. To pass the muon RoI cluster trigger, an event must first pass the L1 dimuon trigger, requiring at least two L1 RoIs with $p_T > 10$ GeV. At the HLT, a cluster of three (four) RoIs contained within $\Delta R = 0.4$ of the L1 object is required in the barrel (endcaps) region.

The muon RoI cluster trigger described in [67] was developed for searches using ATLAS Run 1 data and includes isolation criteria for jets and tracks. A version of the trigger without the isolation requirements was introduced for Run 2 and is employed in the searches described in Chapter 3. Hence, all further references to the muon RoI cluster trigger in this thesis are to the non-isolated version. Data collected with the non-isolated Run 2 muon RoI cluster trigger comprises of both isolated signal-like events and non-isolated background-like events that are utilised to conduct data-driven background estimates.

Figure 3.1 shows the efficiency of the muon RoI trigger for long-lived scalars that are pair-produced via a Higgs portal interaction and decay into hadronic jets in the MS [35], calculated for the search for LLPs in the MS that is described in Section 3.4. For low-mass, boosted LLPs that decay into highly collimated jets, the muon RoI cluster trigger is most efficient when the LLP decays near the outer layer of the HCal since low multiplicity jets with a small opening angle need sufficient distance to create enough RoIs to fire the trigger. For heavier LLPs with low boost, the trigger efficiency peaks closer to the first layer of trigger chambers since the opening angle of the LLP decay products can be too wide in decays close to the HCal. The efficiency of the muon RoI cluster trigger for long-lived ALPs is studied in Section 3.3.2.

3.2. The ABCD method for background estimation

Backgrounds in searches for LLPs in the MS are difficult to model with precision, particularly jets that punch-through the HCal into the MS since this involves modelling many potential material interactions. Therefore, data-driven approaches to background estimation are often taken.

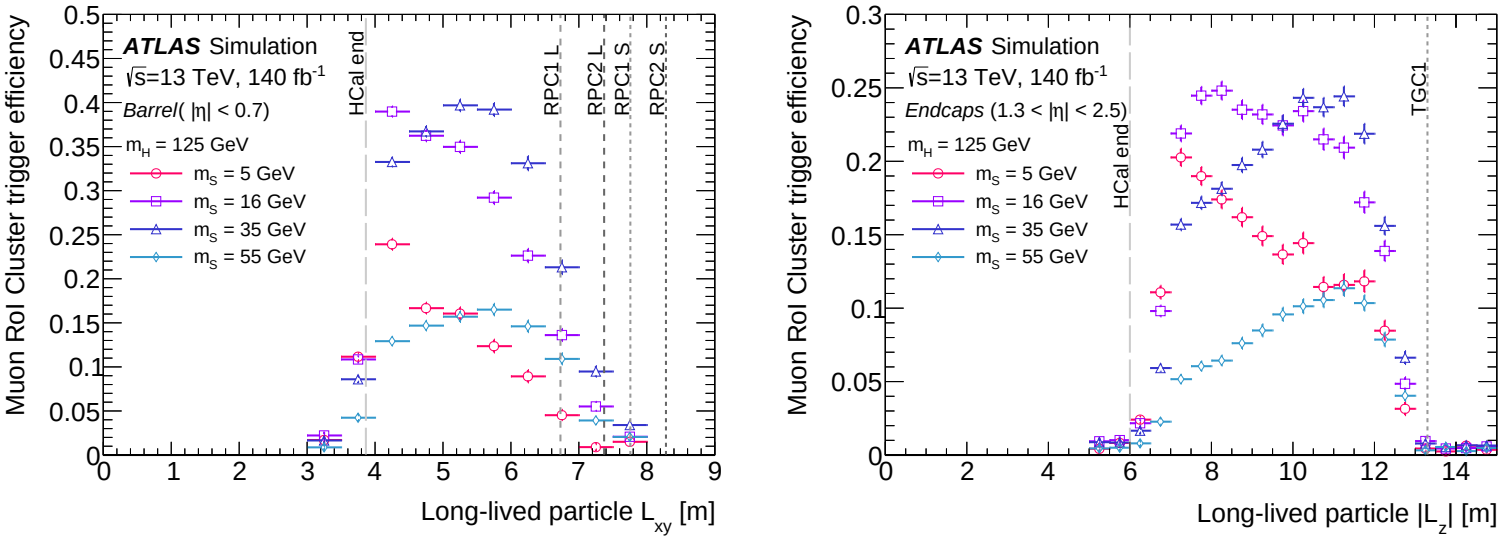

(a) **(b)**

Figure 3.1.: Efficiency for the Muon RoI Cluster trigger against the LLP decay position for scalar portal samples in the (a) barrel and (b) endcap regions [35]. The efficiencies are derived exclusively from MC simulation and do not undergo any corrections for mis-modeling. The vertical lines in the plots denote subdetector boundaries. "HCal end" signifies the outer boundary of the hadronic calorimeter, while "RPC 1/2" indicates the first/second stations of RPC chambers. "TGC 1" represents the first stations of TGC chambers. "S/L" denotes the small/large sectors.

The ABCD method utilises two uncorrelated variables X and Y that distinguish signal-like events from background events. The two variables are plotted against each other and the resulting 2D distribution is divided into four regions using values of X and Y that distinguish signal-like events from background events, such that the majority of signal events reside in region A and the remaining regions, labelled B, C, and D, are dominated by background. Figure 3.2 shows the ABCD plane used to estimate the background in the barrel region of the 36 fb^{-1} 1DV+E_T^{miss} search. As X and Y are uncorrelated, the fractional distribution of events along X should not change as a function of Y, and vice-versa. Thus, for any given point $X = X_0$, the ratio $N_{X>X_0}/N_{X<X_0}$ is constant as a function of Y. The number of events in each region $N_{\text{A/B/C/D}}$ are therefore related by

$$\frac{N_{\text{A}}}{N_{\text{B}}} = \frac{N_{\text{C}}}{N_{\text{D}}}. \tag{3.1}$$

Hence, the expected number of events in region A $N_{\mathrm{A}}^{\mathrm{Expected}}$ is given by

$$N_{\mathrm{A}}^{\mathrm{Expected}} = N_{\mathrm{B}} \times \frac{N_{\mathrm{C}}}{N_{\mathrm{D}}}. \tag{3.2}$$

3.3. Search for displaced vertices with the partial Run 2 dataset

A search for LLPs that decay into hadronic jets in the ATLAS MS was conducted using 36 fb^{-1} of pp collison data at centre-of-mass energy $\sqrt{s} = 13$ TeV recorded by ATLAS in 2015 and 2016 [30]. This partial-Run 2 search targeted three signal models that featured pair-production of neutral LLPs, including the scalar portal and baryogenesis models described in Section 1.3.3, as well as a SUSY scenario [68]. Three distinct channels were utilised to probe the different decay topologies. A two DV (2DV) channel was employed to probe events where both LLPs decay within the MS fiducial volume. The other channels targeted events that contain only one DV (1DV) and some additional detector activity to probe the case where only one LLP decays within ATLAS. One of these channels targeted events with prompt jets while the other targeted events with a significant amount of E_T^{miss}. To gain a first estimate of the sensitivity of ATLAS to the ALP model considered in this thesis, the results of the 1DV+E_T^{miss} channel were reinterpreted. A brief summary of this search is given below and the reinterpretation is discussed in Section 3.3.1. The other channels of this analysis are omitted from the description below.

The 36 fb^{-1} search utilised the muon RoI cluster trigger and vertex reconstruction algorithm that are described in Sections 3.1 and 2.2.6.6, respectively. The full selection criteria for the 1DV+E_T^{miss} channel is listed in Table 3.1. The main source of background was considered to be jets that punch-through to the MS from the HCal. Due to mismodelling of punch-through jets in MC, a data-driven background estimation method was implemented. As described in Section 3.2, an ABCD plane – shown in Figure **??** – was constructed using the azimuth angle $|\Delta\phi(\mathrm{DV}, E_T^{\mathrm{miss}})|$ between the DV and the E_T^{miss} and the angular separation ΔR_{min} between the DV and closest jet or high-p_T track. The estimated background counts were 244 ± 38 (stat.) ± 29 (syst.) in the barrel and 497 ± 51 (stat.) ± 30 (syst.) in the endcap, which are both consistent with the observed number of events.

Event passes muon RoI cluster trigger	
Event has a PV with at least two tracks with $p_{\mathrm{T}} > 400$ MeV	
Event has one MS DV	
DV matched to triggering muon RoI cluster (ΔR(DV, cluster) < 0.4)	
$E_T^{\mathrm{miss}} > 30$ GeV	
$300 \leq n_{\mathrm{MDT}} < 3000$	
$\lvert\Delta\phi(\mathrm{DV}, E_T^{\mathrm{miss}})\rvert < 1.2$	
ΔR_{min}(DV, jet/high-p_T track) > 0.8	
Barrel	Endcap
$\lvert\eta_{\mathrm{DV}}\rvert < 0.7$	$1.3 < \lvert\eta_{\mathrm{DV}}\rvert < 2.5$
$n_{\mathrm{RPC}} \geq 250$	$n_{\mathrm{TGC}} \geq 250$
$n_{\mathrm{MDT}} + n_{\mathrm{RPC}} \geq 1200$	$n_{\mathrm{MDT}} + n_{\mathrm{TGC}} \geq 1500$
	$n_{\mathrm{tracklets}} \geq 5$

Table 3.1.: Summary of the selection criteria applied in the 36 fb^{-1} 1DV+E_T^{miss} search [30]. The variables $n_{\mathrm{MDT}}/n_{\mathrm{RPC}}/n_{\mathrm{TGC}}$ indicate the counts of MDT/RPC/TGC hits within the DV cone. Additionally, η_{DV} represents the pseudorapidity of the DV relative to the IP. $n_{\mathrm{tracklets}}$ denotes the number of tracklets associated with the DV.

3.3.1. Axion-like particle reinterpretation of partial Run 2 search

The 36 fb^{-1} 1DV+E_T^{miss} search was reinterpreted as a first probe of the sensitivity of the ATLAS MS to ALPs. The selection criteria listed in Table 3.1 – with the exceptions of the cut on the number of tracklets in the endcap and the ΔR matching between the DV and triggering RoI cluster – were applied to the ALP signal MC samples with $m_a = \{0.1, 1, 10, 40\}$ GeV that are discussed in Section 4.1.2. Figure 3.3 shows the number of ALP MC events that pass each successive selection, scaled by a factor of 36 fb$^{-1} \times \sigma_{\mathrm{Gen}}/N_{\mathrm{Gen}}$ to estimate the number of ALP signal events expected in the 2015-2016 ATLAS dataset, where σ_{Gen} and N_{Gen} are respectively the generated ALP cross-section and number of events listed for each ALP sample in Table 4.3.

The number of ALP signal events expected to pass the are $\mathcal{O}(0.1)$ in the barrel and $\mathcal{O}(1)$ in the endcap, which are dwarfed by several orders of magnitude compared to the $\mathcal{O}(100)$ background counts for the 1DV+E_T^{miss} search. If the selections on $n_{\mathrm{tracklets}}$ and ΔR(DV, triggering cluster) were included, the ALP efficiency would have been even lower.

The least efficient selections are the requirement of one MS DV, the RoI cluster trigger, and the detector region and ΔR_{min} selections. The efficiency of selecting events containing one DV that is displayed in the "has 1 MSVtx" bin in Figure 3.3 includes the approximately 10% probability of an ALP decaying in the MS fiducial volume in addition to the pure efficiency of the vertex reconstruction algorithm. The vertex reconstruction efficiency and detector region selections are not optimisable without significant developments to the vertex reconstruction algorithm, which has not been done in this work. The $\Delta R_{min} > 0.8$ selection is suboptimal as it is designed primarily for models that do not produce prompt jets or tracks, whereas the ALPs considered are associated with prompt leptons that could take a similar trajectory to the ALP. The low efficiency of the muon RoI cluster trigger is investigated in Section 3.3.2, then an alternative trigger strategy targeting the leptonic decays of the associated Z boson is studied.

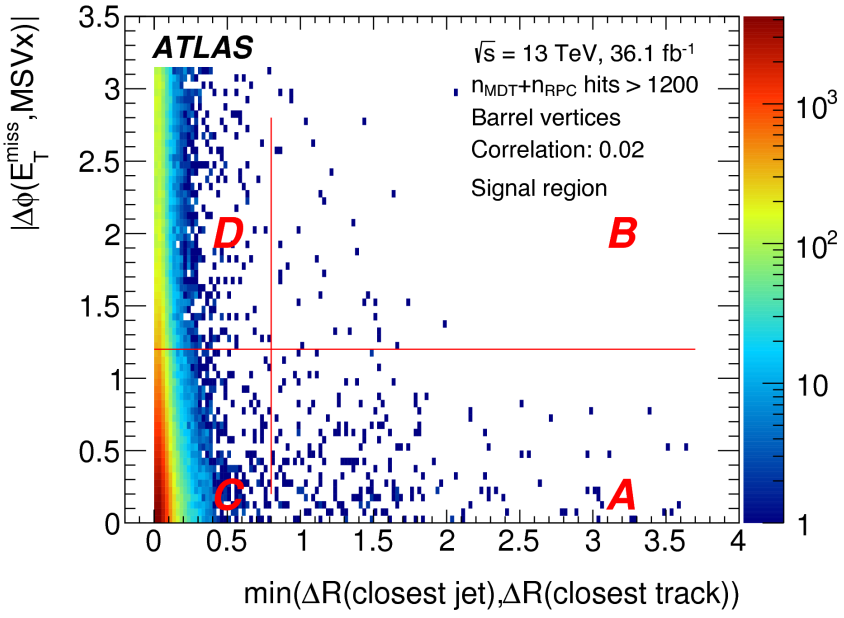

Figure 3.2.: The barrel region ABCD plane for the 36 fb^{-1} 1DV+E_T^{miss} search [30].

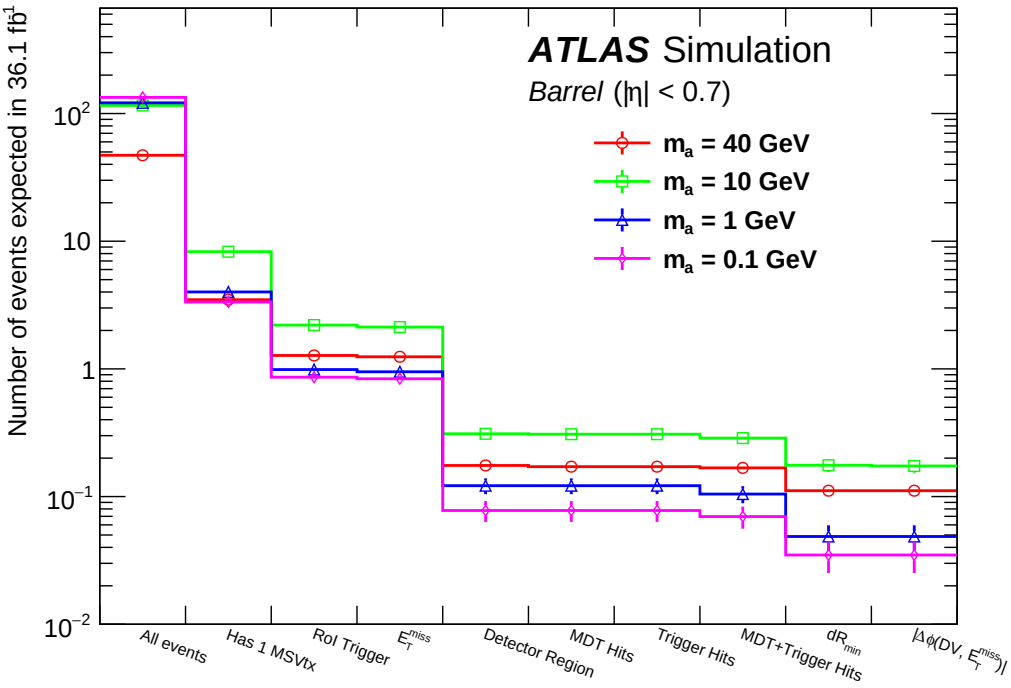

(a)

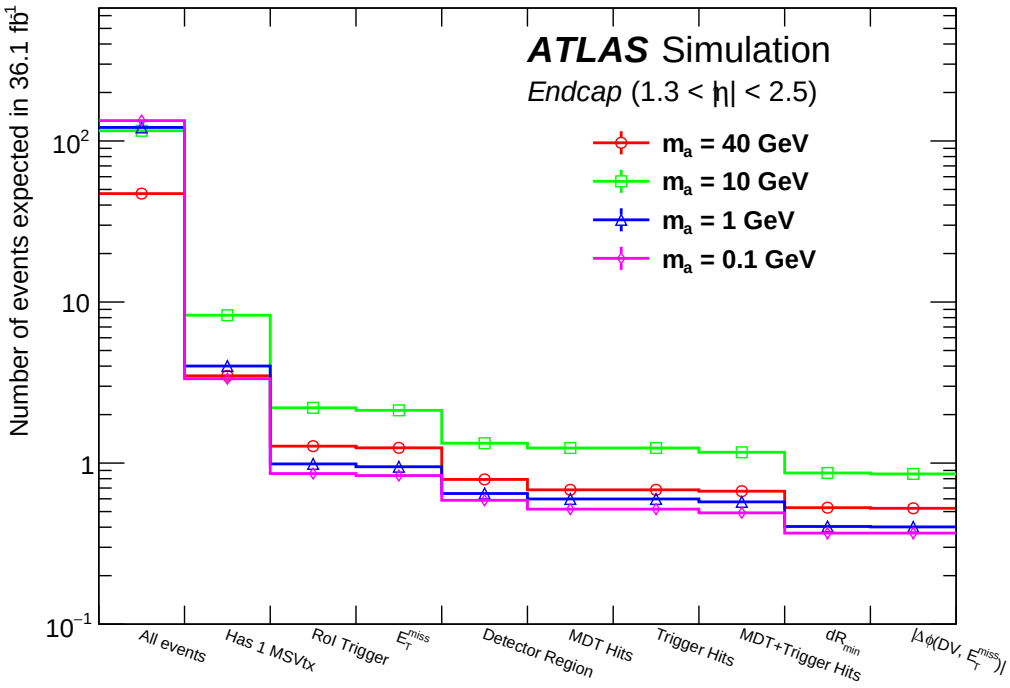

(b)

Figure 3.3.: The number of ALP signal events expected to pass each successive selection from the 36 fb^{-1} 1DV+E_T^{miss} search in (a) the barrel and (b) endcap regions.

3.3.2. Trigger efficiency studies

The number of muon RoIs was studied to investigate the low efficiency of the muon RoI cluster trigger. Figure 3.4 (3.5) shows the number of muon RoIs within $\Delta R = 0.4$ of an ALP decay in the MS barrel (endcap) volume thgat does not fire the muon RoI cluster trigger. For the majority of events, the requirement of three (four) RoIs to form RoI clusters in the barrel (endcap) is not met, resulting in the trigger not firing. The lowest efficiency comes from ALP decays in the region 3 m $< L_{xy} <$ 4 m (5 m $< L_z <$ 6 m) in the barrel (endcap), which corresponds with the material in the outer layer of the calorimeter, where ALP decay products may be absorbed or scattered, thus producing few or no RoIs within the ΔR cone.

In addition, the opening angle ΔR_{gg} between the particle-level gluons that ALPs decay into was studied to investigate the low number of RoIs. Figure 3.6 shows ΔR_{gg} approximately scales as an inverse function of the ALP decay length. Figure 3.7 (3.7) shows ΔR_{gg} as a function of L_{xy} (L_z) in the barrel (endcap) for ALPs that decay in the MS in events where the muon RoI cluster trigger is not fired. Corresponding plots without the fail-trigger requirement are shown in Appendix C. The opening angle of a particle decay is approximately $\Delta R_{gg} \approx 2m_a/p_{T,a}$ [69]. Figures 4.3-4.5 show that ALPs that decay in the MS generally have high p_T, though some low-p_T ALPs do reach the MS. The p_T distributions for $m_a \leq 10$ GeV are approximately the same and the 40 GeV ALP generally has slightly higher p_T. Therefore, it is expected that relative differences in ΔR_{gg} will scale approximately with the ALP mass, which is indeed shown in Figures 3.7 and 3.8 – ALPs with $m_a \leq 10$ GeV and high p_T decay into very narrow jets that will also have lower multiplicity than the heavier ALPs and thus produce few RoIs. Additionally, ALPs with low mass and high p_T are very boosted, resulting in further collimation of the decay products. For the 40 GeV ALP and low-p_T 10 GeV ALP, the ALP decay products can be too widely spread to create a sufficient number of RoIs within a $\Delta R = 0.4$ cone to form a cluster.

An alternative triggering strategy is devised by taking advantage of the leptonic decays of the ALP-associated Z boson. This strategy utilises the highly efficient ATLAS lepton triggers and selects events that contain a pair of same flavour, opposite charge leptons with a combined invariant mass close to the Z boson mass. This lepton trigger strategy was implemented with a preliminary dilepton selection that yieleded promising results. The results shown below utilise the finalised dilepton selection, summarised in Table 4.9, that was developed for the search that is presented

in Section 4. Figures 3.9 and 3.9 compare the efficiencies of the muon RoI cluster trigger and the lepton trigger strategy for each ALP sample in the barrel and endcap, respectively. Events are required to contain an ALP decay in the MS fiducial volume, the respective trigger must fire and a DV must be reconstructed. No selection criteria is applied to the DV. The lepton trigger strategy generally outperforms the muon RoI cluster trigger, particularly at larger decay lengths.

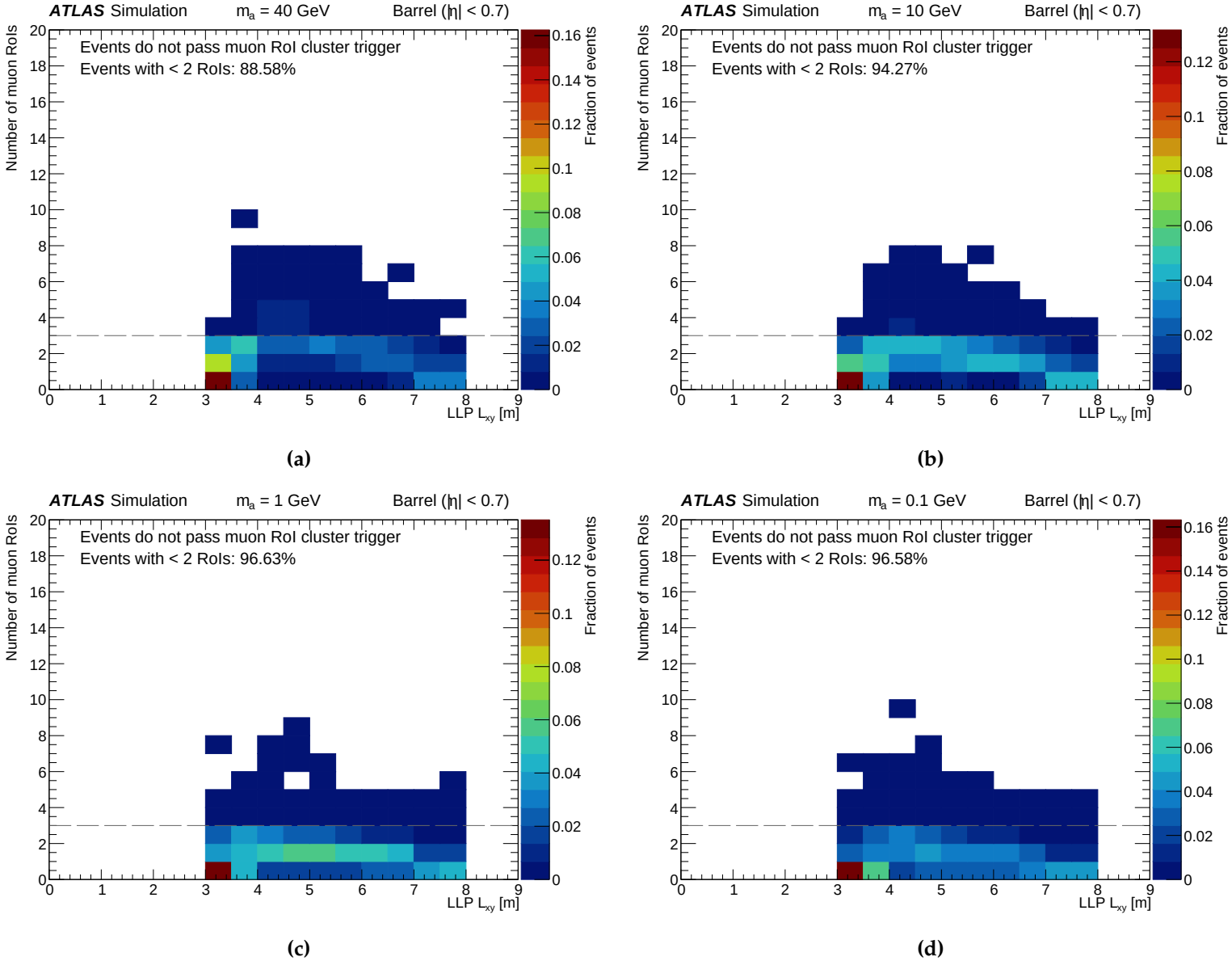

Figure 3.4.: Number of muon RoIs produced by ALPs with masses m_a = (a) 40 GeV, (b) 10 GeV, (c) 1 GeV, and (d) 0.1 GeV that decay in the MS barrel volume, presented as a function of L_{xy}. The events shown do not pass the muon RoI cluster trigger.

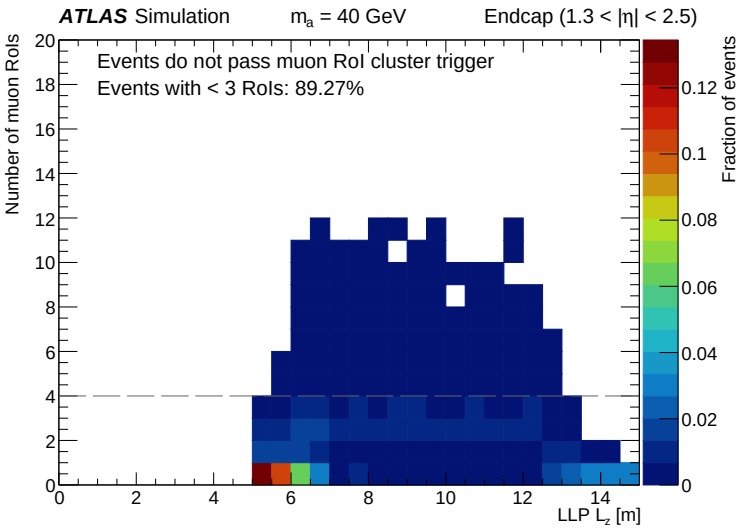

(a)

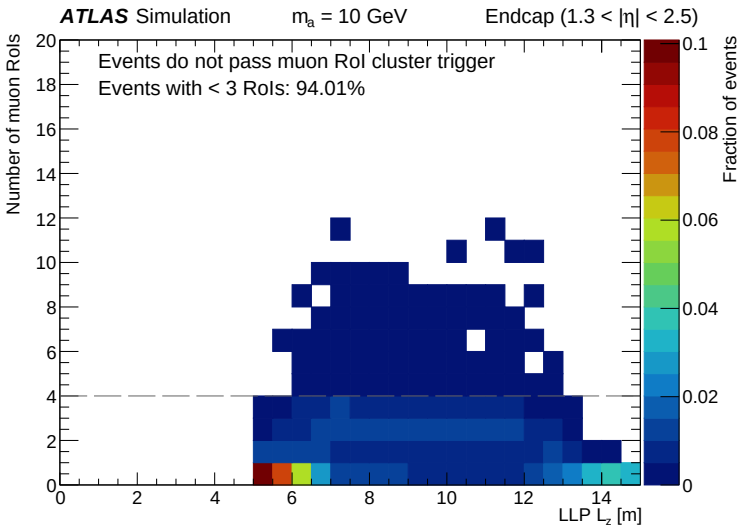

(b)

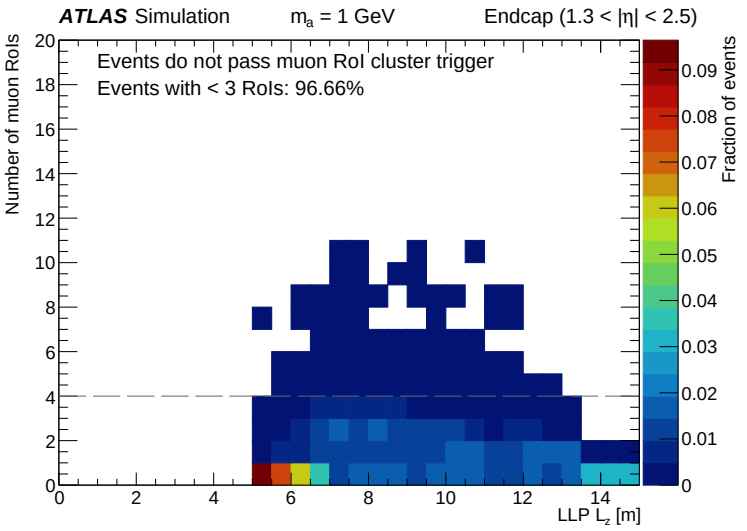

(c)

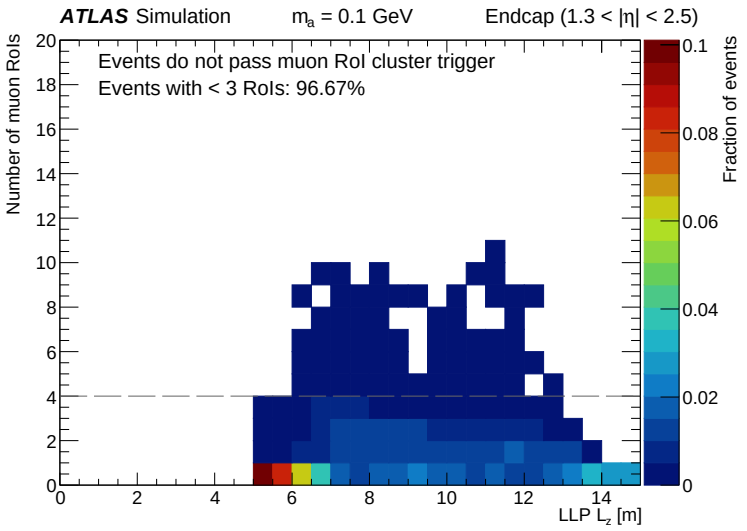

(d)

Figure 3.5.: Number of muon RoIs produced by ALPs with masses m_a = (a) 40 GeV, (b) 10 GeV, (c) 1 GeV, and (d) 0.1 GeV that decay in the MS endcap volume, presented as a function of L_z. The events shown do not pass the muon RoI cluster trigger.

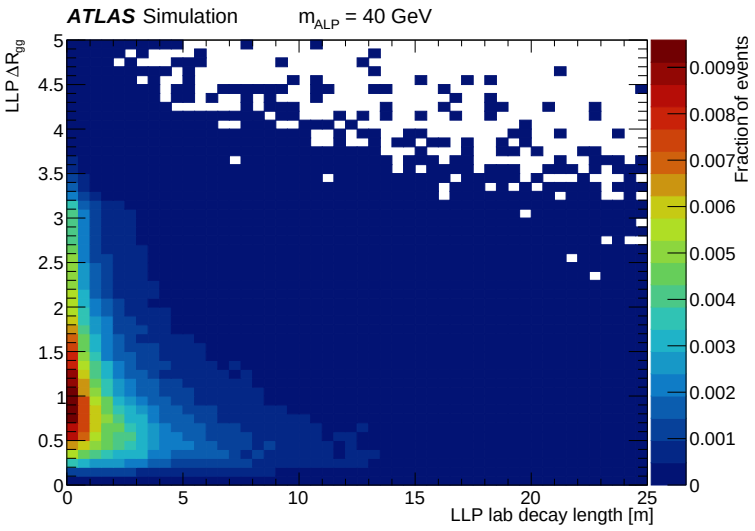

(a)

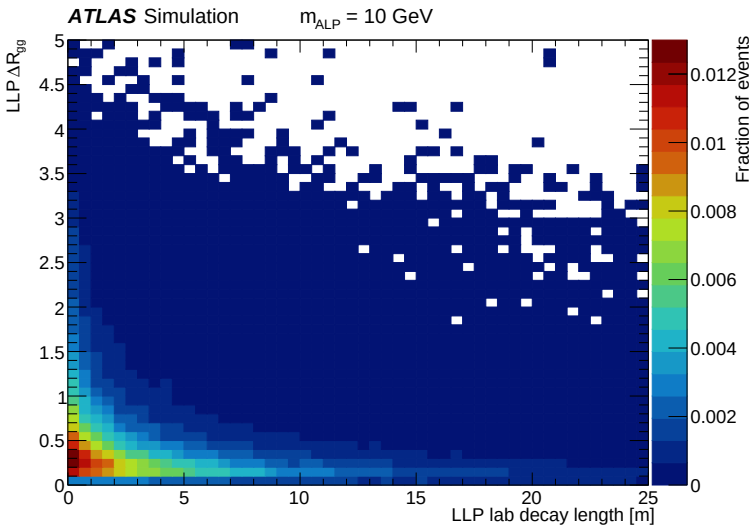

(b)

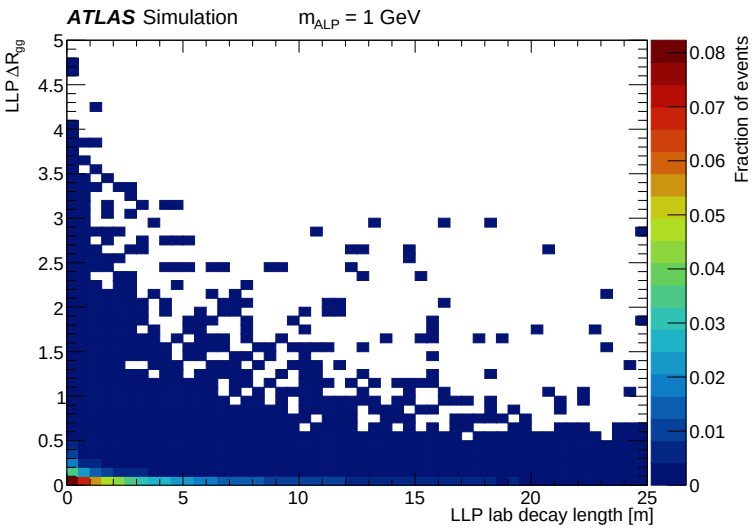

(c)

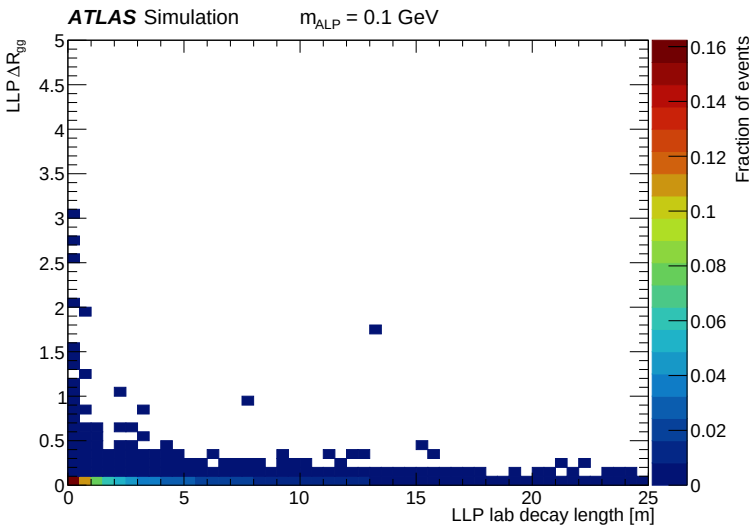

(d)

Figure 3.6.: Opening angle of the ALP decay products as a function of decay length for all events in the generated ALP samples.

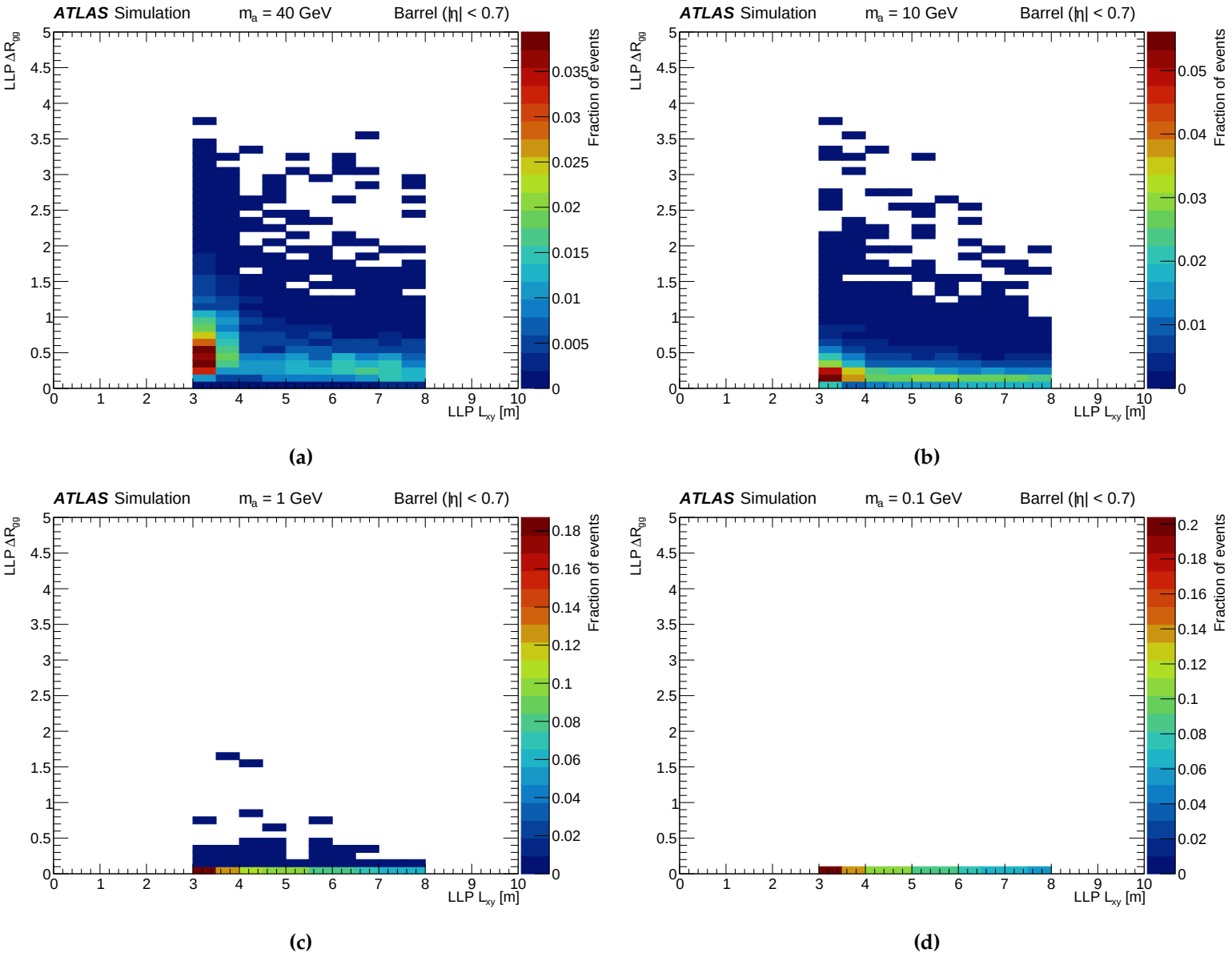

Figure 3.7.: Opening angle of the ALP decay products as a function of L_{xy} for ALPs with masses m_a = (a) 40 GeV, (b) 10 GeV, (c) 1 GeV, and (d) 0.1 GeV that decay in the MS barrel volume. The events shown do not pass the muon RoI cluster trigger.

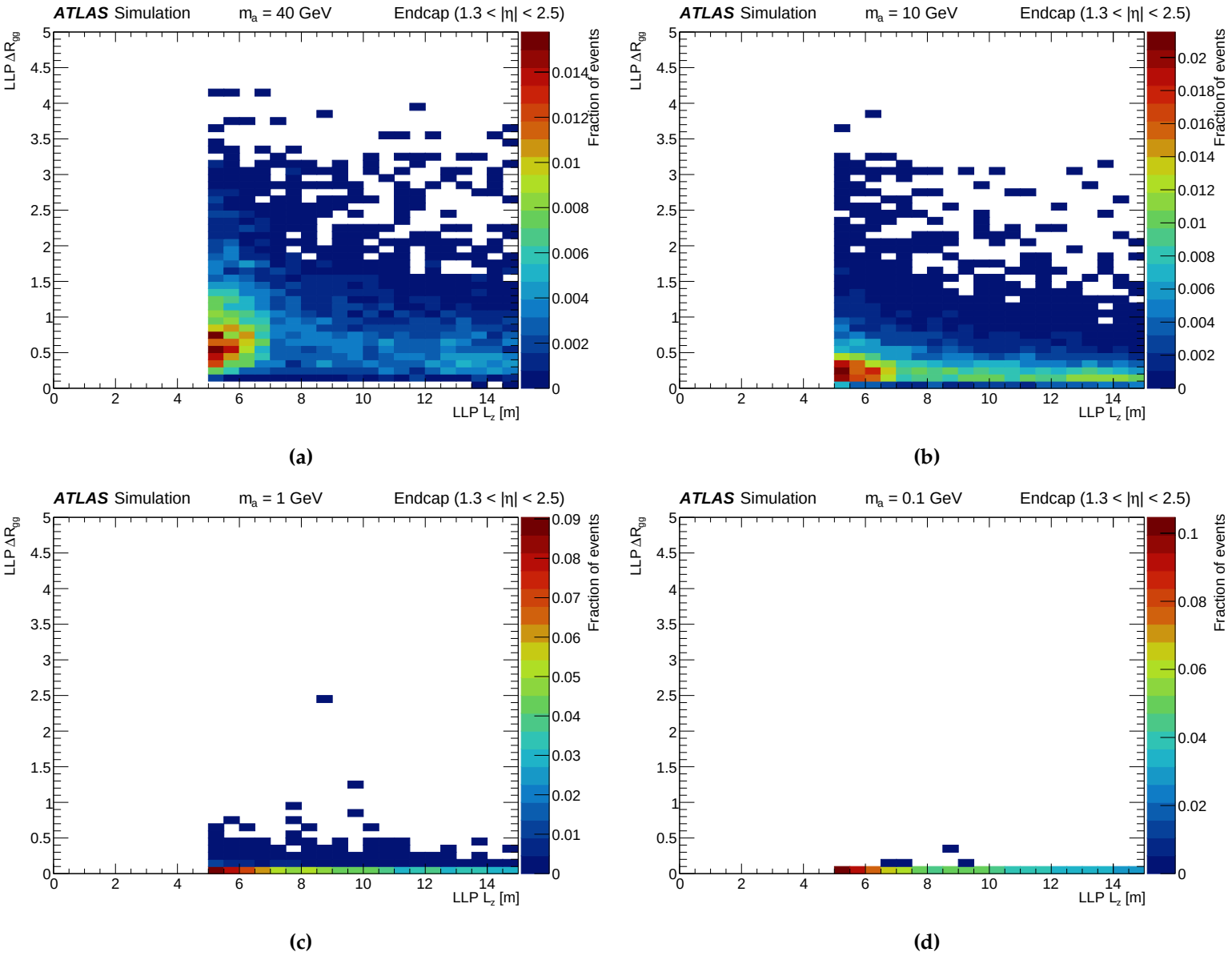

Figure 3.8.: Opening angle of the ALP decay products as a function of L_z for ALPs with masses m_a = (a) 40 GeV, (b) 10 GeV, (c) 1 GeV, and (d) 0.1 GeV that decay in the MS endcap volume. The events shown do not pass the muon RoI cluster trigger.

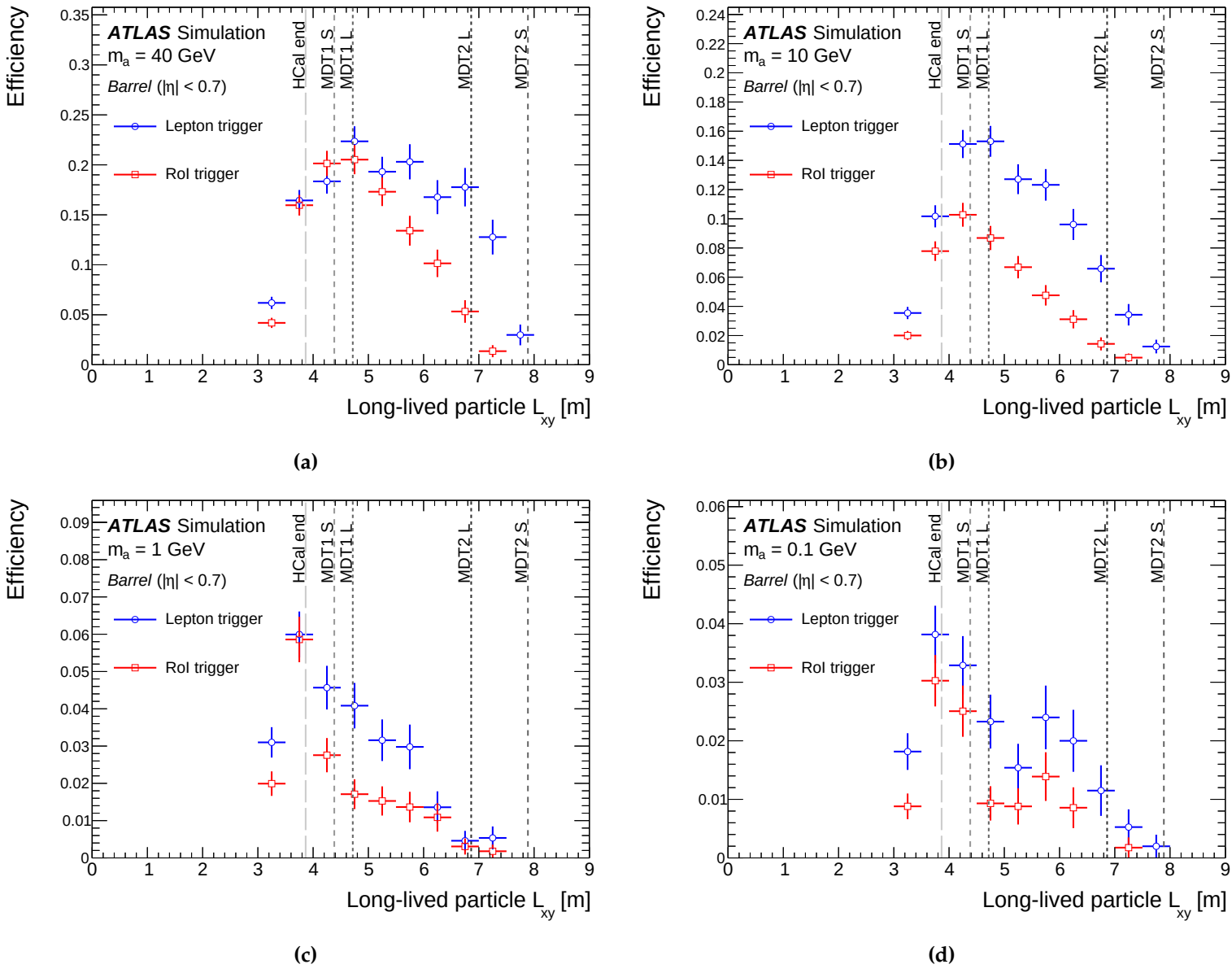

Figure 3.9.: Efficiencies of the muon RoI cluster trigger (red) and the lepton trigger strategy (blue) as a function of L_{xy} for ALPs with masses $m_a =$ (a) 40 GeV, (b) 10 GeV, (c) 1 GeV, and (d) 0.1 GeV that decay in the MS barrel volume. Events are required to contain an ALP decay in the MS barrel fiducial volume, the trigger must fire and a DV must be reconstructed. No futher selection is applied to the DV. The lepton trigger strategy generally outperforms the RoI trigger, particularly at larger L_{xy}.

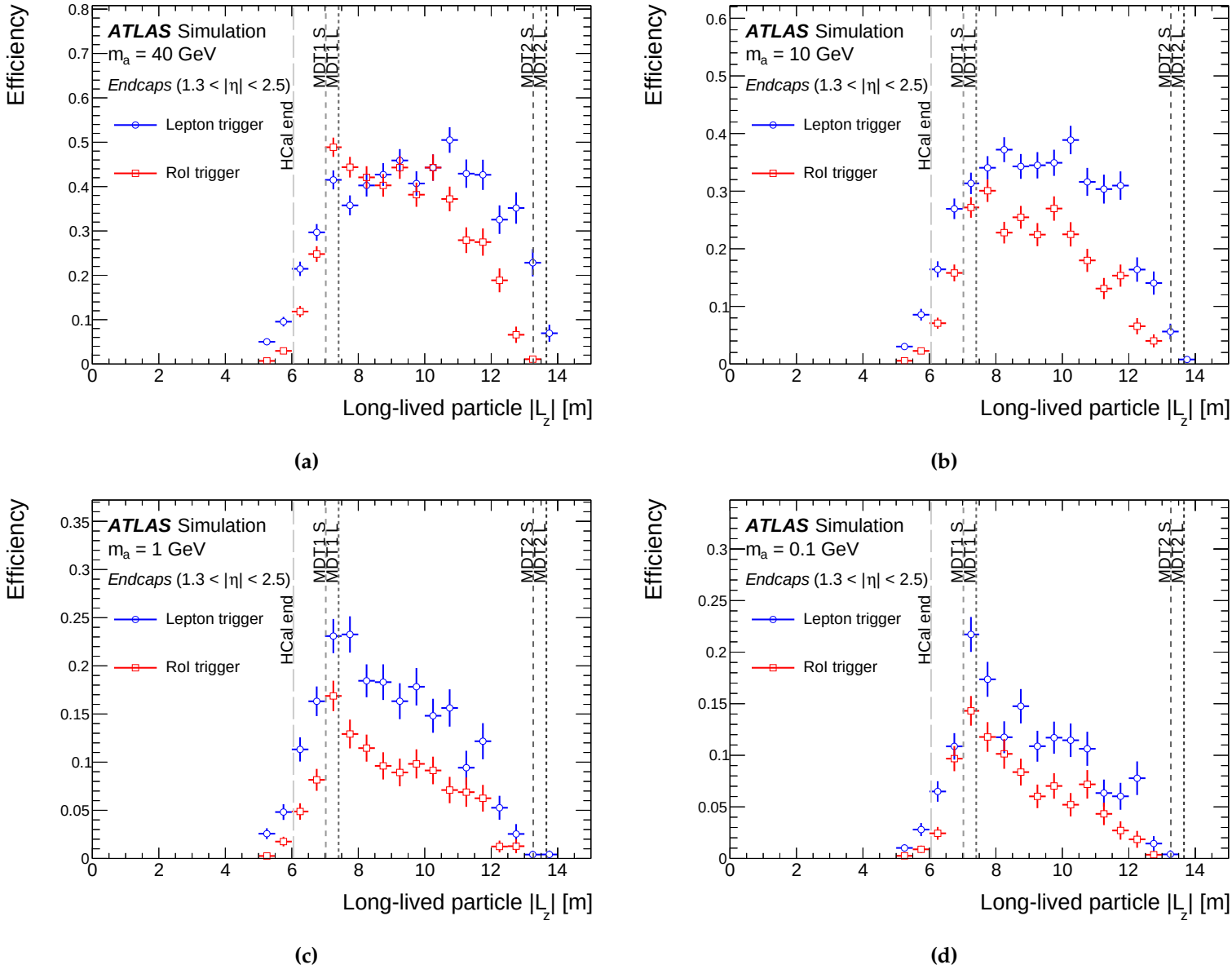

Figure 3.10.: Efficiencies of the muon RoI cluster trigger (red) and the lepton trigger strategy (blue) as a function of L_z for ALPs with masses m_a = (a) 40 GeV, (b) 10 GeV, (c) 1 GeV, and (d) 0.1 GeV that decay in the MS endcap volume. Events are required to contain an ALP decay in the MS endcap fiducial volume, the trigger must fire and a DV must be reconstructed. No futher selection is applied to the DV. The lepton trigger strategy generally outperforms the RoI trigger, particularly at larger L_z.

3.4. Search for displaced vertices with the full Run 2 dataset

A search for events that contain two MS DVs was conducted using the complete 140 fb^{-1} of pp collison data recorded at centre-of-mass energy $\sqrt{s} = 13$ TeV by ATLAS during Run 2 [66]. In addition, a search for events with a single MS DV was carried out using the full Run 2 dataset was carried out [35] as described in Section 3.4. Both searches probed the scalar portal and baryogenesis models described in Section 4.1.2, which involve pair-production of LLPs. The 2DV and 1DV searches were designed to be orthogonal and complimentary. The 2DV search has better sensitivity in the range 1 m $\lesssim c\tau \lesssim$ 10 m as it has a lower background. However, the requirement that both LLPs decay within the ATLAS volume limits the sensitivity at longer lifetimes, which scales as $1/(c\tau)^2$. For the 1DV search, the sensitivity is greater at longer lifetimes and scales as $1/c\tau$. Therefore, the results of the two searches were combined to produce the limits shown in Figure 3.13.

The 140 fb^{-1} search for events with a single MS DV provided the basis for the search presented in Section 4. The two searches were developed in parallel and published together as different channels of the same analysis, with the primary difference being the triggering strategies. As this search utilises the muon RoI cluster trigger described in Section 3.1, it will henceforth be refered to as the *RoI-triggered channel*.

The RoI-triggered channel employs the vertex reconstruction algorithm described in Section 2.2.6.6. The selection criteria – listed in Table 3.2 – has been developed significantly compared to that of the 36 fb^{-1} 1DV+E_T^{miss} search. The hadronic missing transverse energy $H_T^{\text{miss}} > 40$ GeV is constructed in a similar manner as E_T^{miss} but only considering jets with $p_T > 20$ GeV. A low background validation region (VR) in data is defined by data with $H_T^{\text{miss}} < 40$ GeV that passes all other selections. To reject background from non-collision sources such as cosmic muons and beam-induced backgrounds, there is a selection on the number of muon segments n_{Seg} in the outer MS layer and a tighter selection on the number of hits $n_{\text{RPC/TGC}}$ in the RPC/TGC chambers. Two distinct isolation criteria are employed to reject backgrounds from jets. To reject jets composed of many low-p_T tracks, an upper limit on the vector sum of the p_T of (low-p_T) tracks with $p_T < 5$ GeV within a $\Delta R = 0.2$ cone of the DV is set at 5 GeV. To reject jets that mainly consist of high energy hadrons, the minimum angular separation between the DV and the closest jet or (high-p_T) track with $p_T > 5$ GeV is required to be $\Delta R_{\text{min}} > 0.8$.

Event passes the muon RoI cluster trigger	
Event has a PV with at least two tracks with $p_{\mathrm{T}} > 500$ MeV	
Event has exactly one DV in the MS	
$\Delta R(\text{DV, triggering cluster}) < 0.4$	
$H_T^{\text{miss}} > 40$ GeV	
$E_T^{\text{miss}} > 20$ GeV	
$300 \leq n_{\text{MDT}} < 3000$	
$\Sigma p_T(\Delta R < 0.2) < 5$ GeV	
$\Delta R_{min}(\text{DV, jet/high-}p_T\text{ track}) > 0.8$	
Barrel	Endcaps
$\lvert\eta_{\text{DV}}\rvert < 0.7$ $3\text{ m} < L_{xy} < 8\text{ m}$	$1.3 < \lvert\eta_{\text{DV}}\rvert < 2.5$ $L_{xy} < 10\text{ m}$
$n_{\text{RPC}} > 800$	$n_{\text{TGC}} > 900$
$n_{\text{Seg}} > 15$	$n_{\text{Seg}} > 30$
NN1 > 0.5 NN2 > 0.5	NN1 > 0.8 NN2 > 0.8

Table 3.2.: Summary of the selection criteria applied to both data and simulated events in the RoI-triggered channel. H_T^{miss} is the hadronic component of the E_T^{miss}. The variables $n_{\text{MDT}}/n_{\text{RPC}}/n_{\text{TGC}}$ indicate the counts of MDT/RPC/TGC hits within the vertex cone and n_{Seg} is the number of segments in the outer MDT layer. L_{xy} and L_z denote the transverse and longitudinal distance from the IP, respectively.

The final signal-background discrimination is performed by a pair of neural nets (NNs) – described in detail in Section 4.2.2 – that are input features related to DV topology and isolation. The NNs are trained on scalar portal signal MC samples and background-dominated data with $H_T^{\text{miss}} < 40$ GeV. A data-driven background estimate is conducted by constructing ABCD planes from the two NNs. Figures 3.11 and 3.12 show the SR ABCD planes for a scalar portal sample and Run 2 data, respectively. These planes and the results shown in Table 3.3 (excluding the systematic uncertainties) were produced by the author of this thesis. The observed number of events in region A are consistent with the predictions in both the barrel and endcap. Therefore, the results were extrapolated using the method described in Section 4.4 to set limits on the production cross-section times branching ratios for the various mass points of the scalar portal and baryogenesis models considered. The combined 1DV and 2DV search limits on the scalar portal model are shown in Figure 3.13.

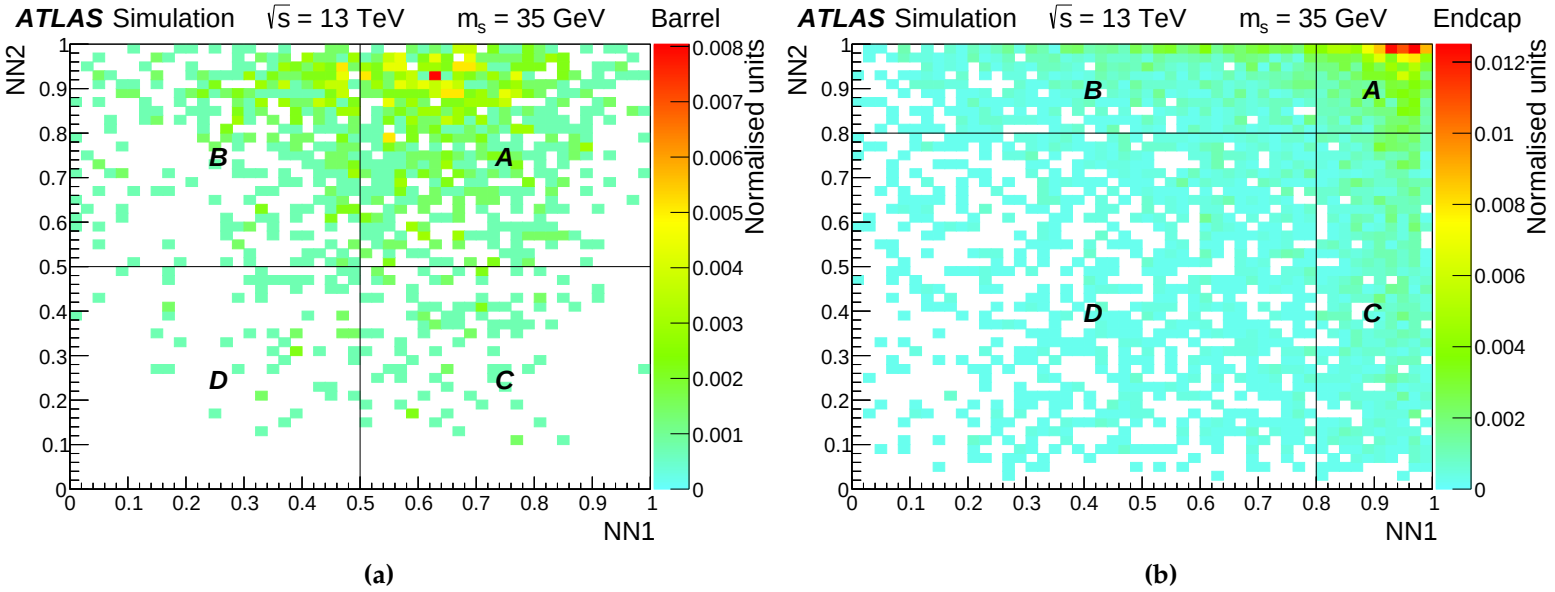

Figure 3.11.: ABCD planes for the Higgs boson portal model with $m_s = 35$ GeV and $c\tau = 1.310$ m in the (a) barrel and (b) endcap regions of the RoI-triggered channel.

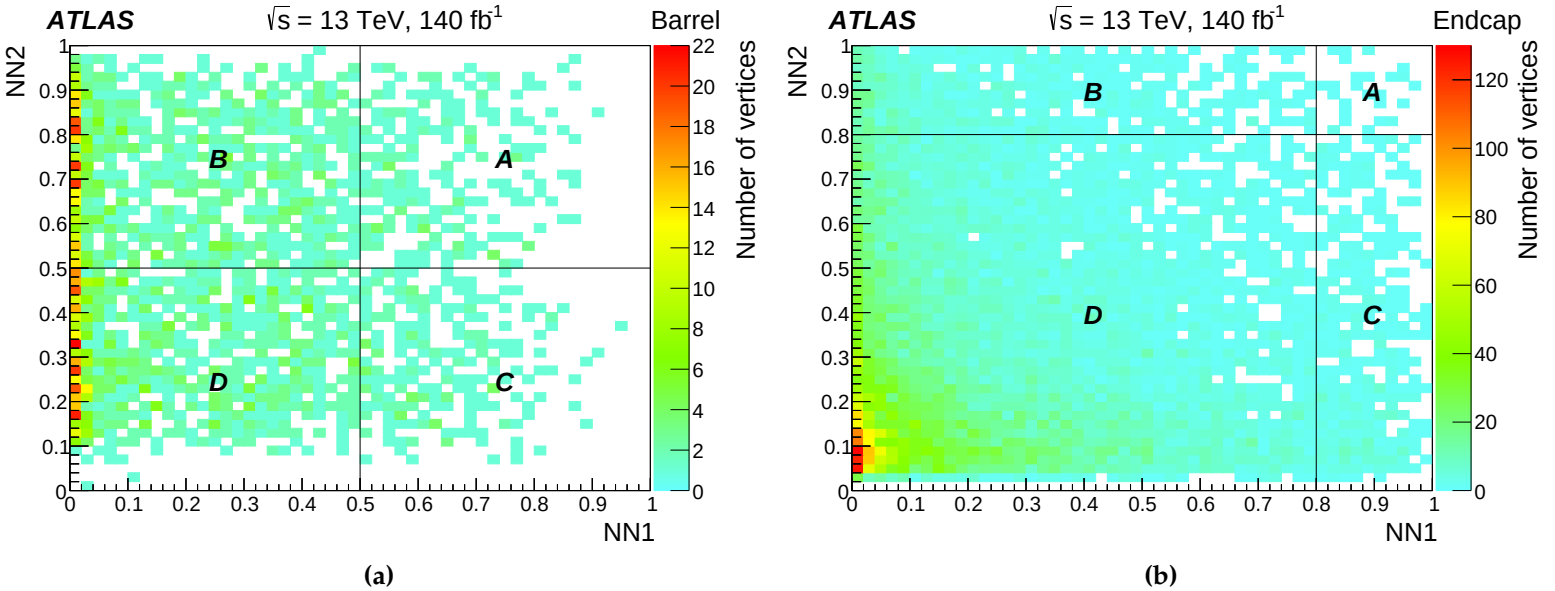

Figure 3.12.: ABCD planes for Run-2 data in the (a) barrel and (b) endcap regions of the muon-RoI triggered channel. The correlation between NN1 and NN2 is negligible.

Region	$N_A^{Observed}$	$N_A^{Expected}$	N_B	N_C	N_D
Barrel	245	241 ± 18 (stat.) ± 6 (syst.)	1136	249	1176
Endcaps	31	46 ± 2 (stat.) ± 9 (syst.)	1072	570	13190

Table 3.3.: Event counts $N_{A,B,C,D}$ in each of the four regions of the ABCD plane and the expected number of events $N_A^{Expected}$ in region A for the muon-RoI triggered signal region.

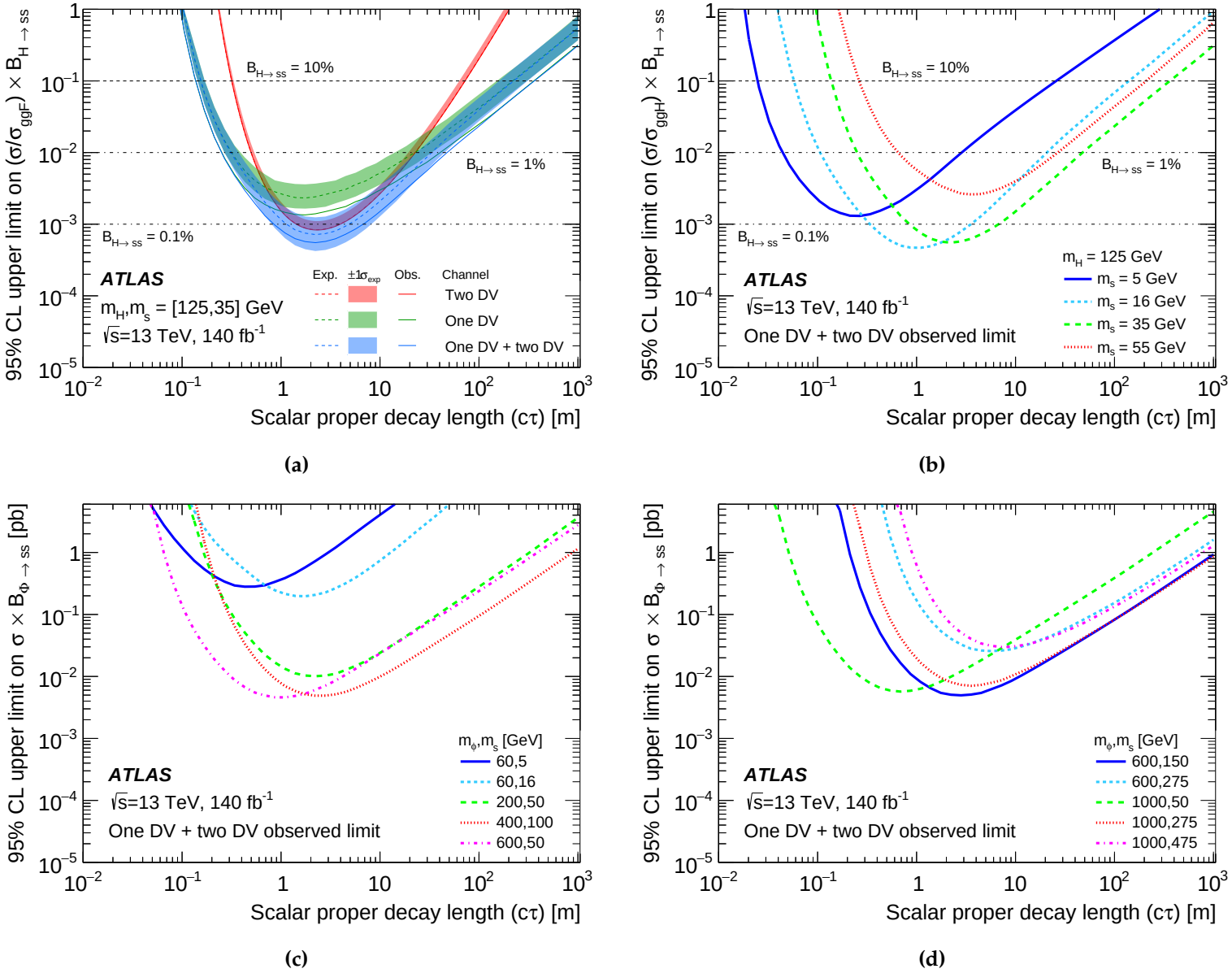

Figure 3.13.: Summary of the one-DV and two-DV limit combinations for the $H/\Phi \to ss$ model [35]. (a) Comparison between the one- and two-DV results, and their combined 95% CL limits on $\left(\sigma/\sigma_{\mathrm{ggH}}\right) \times B$ for the Higgs boson portal mediator and $m_s = 35$ GeV. (b) Observed 95% CL limits on $\left(\sigma/\sigma_{\mathrm{ggH}}\right) \times B$ for all Higgs boson portal mediator samples where the cross-section is normalized to the SM Higgs boson gluon–gluon fusion production cross-section, $\sigma_{\mathrm{ggH}} = 48.61$ pb [70]. (c)–(d) Observed 95% CL limits on $\sigma \times B$ for $m_\Phi \neq 125$ GeV benchmark samples. The observed limits are consistent with the expected ones within the uncertainties.

Chapter 4.

Search for long-lived particles with an associated Z boson

This chapter presents a search for LLPs that are produced in association with a Z boson and decay into hadronic jets in the ATLAS MS. 140 fb^{-1} of pp collision data recorded at $\sqrt{s} = 13$ TeV by the ATLAS detector during Run 2 of the LHC is utilised. The search uses the lepton trigger strategy studied in Section 3.3.2, the DV reconstruction algorithm described in Section 2.2.6.6 and a similar selection criteria as the RoI-triggered channel summarised in Section 3.4, including the same NNs and ABCD plane to estimate the expected number of background events. The search strategy was developed by the author to probe the Z+ALP model discussed in Section 1.3.4.2. After the search was unblinded, it was reinterpreted by Julian Wack to set limits on models where a scalar portal or dark photon is produced in association with a Z boson [35].

This chapter is structured as follows. The details of the data samples and generated MC signal samples, including particle-level kinematic distributions, are given in Section 4.1. Section 4.2 describes in depth the signal selection criteria utilised, including the Z boson reconstruction and optimisation studies. In Section 4.3, the ABCD method is validated and utilised to estimate the expected number of events in the signal region (SR). The observed SR ABCD planes and corresponding event displays are also shown. Sections 4.4, 4.5 and 4.6 respectively describe the lifetime extrapolation procedure, systematic uncertainties and the statistical framework used to set limits on the model considered. Finally, the results are shown in Section 4.7.

4.1. Data and Monte Carlo samples

This search utilises 140 fb^{-1}of pp collision data recorded at $\sqrt{s} = 13$ TeV by the ATLAS detector during the LHC Run 2 (2015 - 2018) data-taking period. The luminosity is measured using the LUCID-2 detector [71]. Events are selected exclusively from data-taking periods in which the LHC beams were stable and the ATLAS detector was fully operational. The datasets used are listed in Appendix A. Events are pre-selected if they pass the lepton triggers discussed in Section 4.1.1 and contain a PV, a DV in the MS, and at least two same-flavour electrons or muons that match the lepton definitions in Table 4.4.

Several Monte Carlo (MC) signal samples were generated using the Z+ALP model described in Section 1.3.4.2 for a range of ALP masses and proper lifetimes. The details of the generated ALP samples are discussed in Section 4.1.2 and the ALP phenomenology is detailed in Section 4.1.3.

4.1.1. Triggers

The data utilised in this search was collected using a logical OR of several electron and muon triggers that were active at different times during Run 2 [**?**], as indicated in Tables 4.1 and 4.2. The name of each trigger indicates the selection applied to the corresponding object at trigger-level. For example, `HLT_mu_40` indicates a single-muon trigger with a p_T threshold of 40 GeV, while `HLT_2e24_lhvloose_nod0` is a dilepton trigger with a p_T of 24 GeV, loose identification criteria, and no d_0 impact parameter requirement.

Data is also collected using the muon RoI cluster trigger described in Section 3.1. In particular, the muon RoI cluster trigger is used to collect data in unpaired and empty bunch-crossings, known as latestream data, for background studies.

Electron trigger	2015	2016	2017	2018
HLT_e24_lhmedium_L1EM20VH	✓			
HLT_e24_lhmedium_nod0_L1EM20VH		✓		
HLT_e24_lhtight_nod0_ivarloose		✓		
HLT_e26_lhtight_nod0_ivarloose		✓	✓	✓
HLT_e60_lhmedium	✓			
HLT_e60_lhmedium_nod0		✓	✓	✓
HLT_e120_lhloose	✓			
HLT_e140_lhloose_nod0	✓			
HLT_e300_etcut		✓	✓	✓
HLT_2e12_lhvloose_L12EM10VH	✓			
HLT_2e17_lhvloose_nod0		✓	✓	✓
HLT_2e17_lhvloose_nod0_L12EM15VHI		✓	✓	✓
HLT_2e24_lhvloose_nod0			✓	✓

Table 4.1.: The single and di-electron triggers employed in each data-taking year of Run 2.

Muon trigger	2015	2016	2017	2018
HLT_mu20_iloose_L1MU15	✓			
HLT_mu24_ivarmedium		✓		
HLT_mu26_ivarmedium		✓	✓	✓
HLT_mu40	✓	✓		
HLT_mu50	✓	✓	✓	✓
HLT_mu60_0eta105_msonly		✓	✓	✓
HLT_2mu10	✓			
HLT_2mu14		✓	✓	✓

Table 4.2.: The single and di-muon triggers employed in each data-taking year of Run 2.

4.1.2. Monte Carlo generation

ALP MC events were generated at leading-order using MADGRAPH5_AMC@NLO [72] following the `ALP_linear_UFO_WIDTH` [38] model that is described in Section 1.3.4.2. The generation was interfaced to the PYTHIA 8.2 [73] parton shower model with the A14 parameter tune [74] and the NNPDF2.3LO parton distribution function (PDF) set [75] was used in all models featuring production of LLPs in association with a Z-boson. The EVTGEN 1.2.0 program [76] was used to model b- and c-hadron decays. To ensure comprehensive coverage of the accessible parameter space a range of masses was selected, as outlined in Table 4.3. The mean proper decay length in each sample was tuned to maximise the occurrence of decays in the HCal and MS as the samples used in this search were shared with the corresponding search for long-lived ALPs in the HCal [34].

The generated events were processed through a full GEANT4 [77] simulation of the ATLAS detector geometry and response [78]. The simulation includes pileup and accounts for the effect on the detector response due to interactions from bunch crossings before or after the hard interaction. Pileup was simulated with PYTHIA 8.1 [79] using the A3 tune [80] and the NNPDF2.3LO [75] PDF set. Per-event weights were applied to the simulated events to match the distribution of the average pileup measured in data.

m_{ALP} [GeV]	$C_{\tilde{G}}$	$c\tau_{\text{Gen}}$ [m]	N_{Gen}	σ_{Gen} [fb]
0.1	10^{-2}	0.003	200000	3.1
	5×10^{-3}	0.012	200000	
1	10^{-4}	0.031	200000	3.1
10	3.2×10^{-6}	0.030	200000	2.9
	10^{-6}	0.310	200000	
	7.5×10^{-7}	0.551	200000	
40	10^{-7}	0.481	200000	2.0

Table 4.3.: Parameters used for simulations of ALP produced in association with a Z boson, where m_{ALP} is the ALP mass, $C_{\tilde{G}}$ is the coupling to the gluon field that dictates the generated mean proper lifetime $c\tau_{\text{Gen}}$. For m_{ALP} = 0.1 or 10 GeV, additional samples with different lifetimes were generated to validate the lifetime extrapolation procedure. The number of generated events is denoted by N_{Gen} and σ_{Gen} is the ALP production cross-section calculated by MADGRAPH5_AMC@NLO.

4.1.3. Axion-like particle phenomenology

The particle-level p_T, η, and m_Z distributions for the associated Z boson are shown in Figure 4.1. Heavier ALPs generally result in larger Z boson p_T due to the larger recoil mass. For all m_a, the expected narrow truth mass peak is observed. The particle-level p_T and η distributions of the Z boson daughter muons and electrons are shown in Figure 4.2.

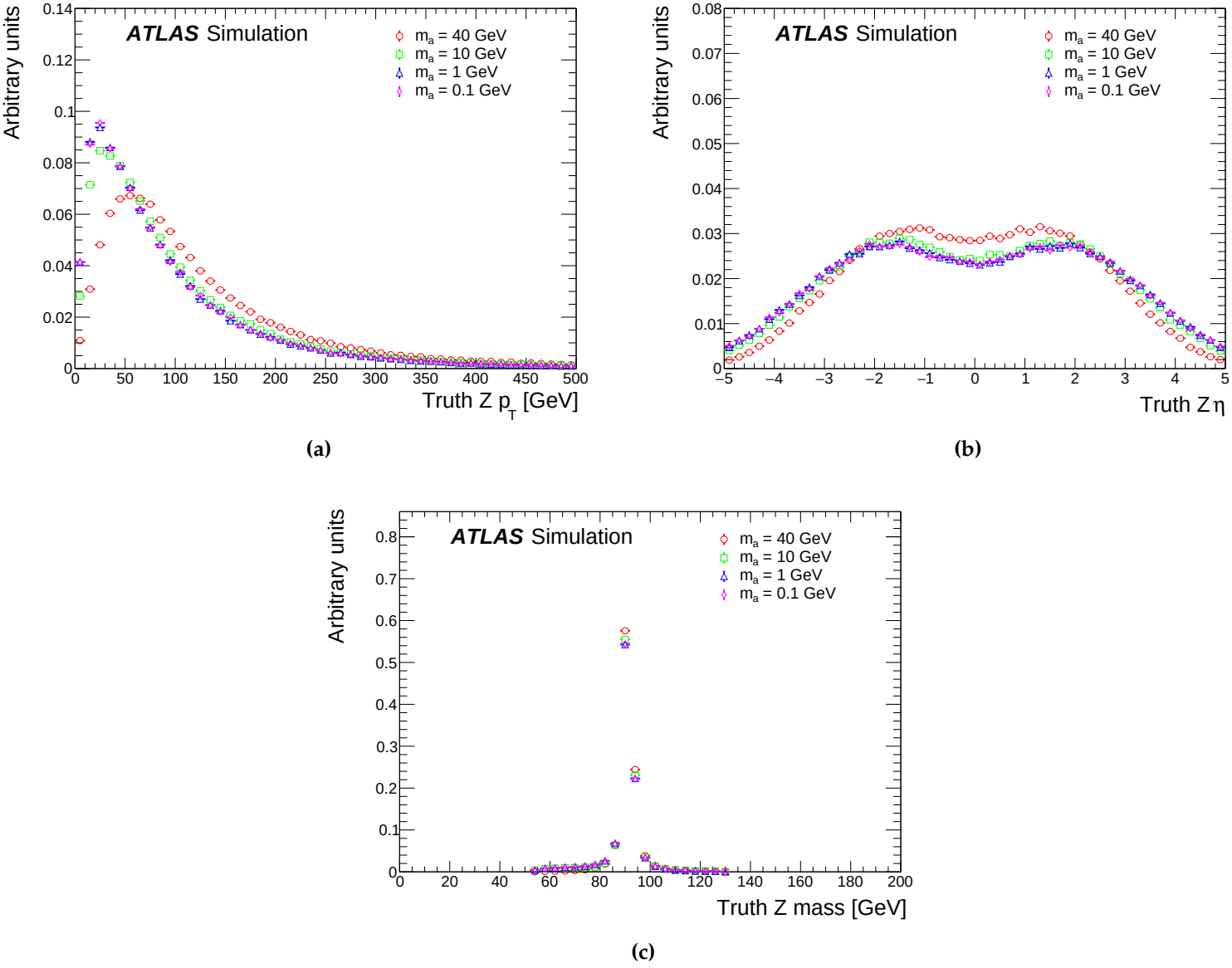

(a) **(b)** **(c)**

Figure 4.1.: Particle-level p_T, η, and m_Z distributions for Z bosons produced in association with an ALP.

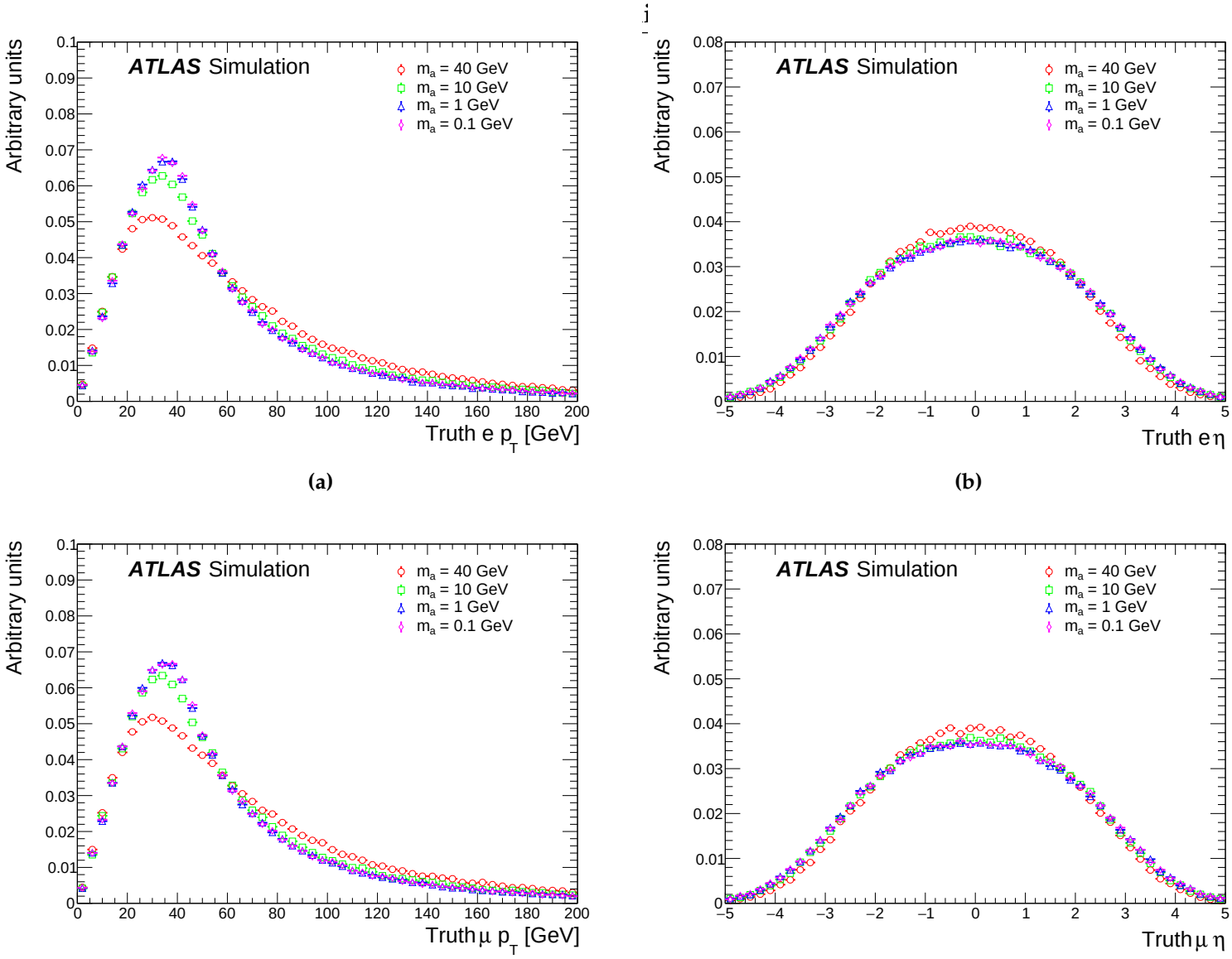

Figure 4.2.: Particle-level p_T (left) and η (right) distributions for Z boson daughter (a,b) electrons and (c,d) muons.

Figure 4.3 shows the particle-level distributions of the ALP p_T, β, γ, η, as well as the decay lengths in the transverse (L_{xy}) and longitudinal (L_z) planes for all events in the generated Z+ALP samples. Figures 4.4 and 4.5 show the distributions of the same variables in events where the ALP decays within the MS barrel or endcap, respectively. The barrel fiducial volume is defined by $|\eta| < 0.7$ and 3 m $< L_{xy} <$ 10 m, while the endcap is defined by $1.3 < |\eta| < 2.5$, 5 m $< L_z <$ 15 m, and $L_{xy} <$ 10 m. ALPs that decay in the MS are typically highly boosted, resulting in collimated hadronic jets in the MS, particularly for $m_a \leq 1$ GeV. ALPs that decay in the endcap are generally even more boosted.

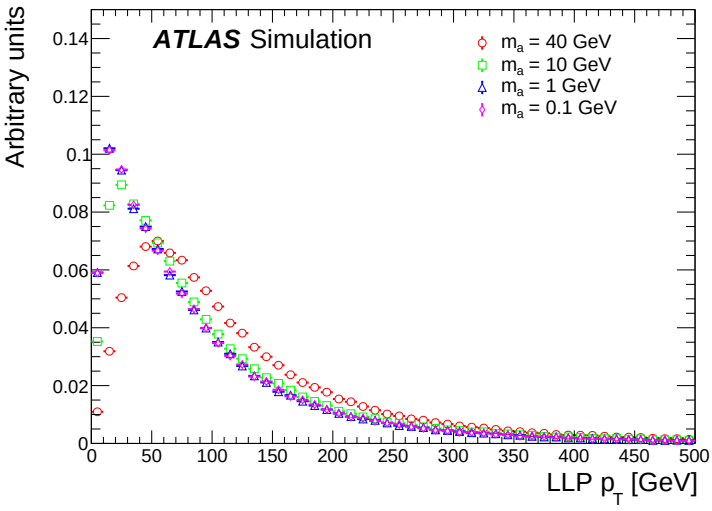

(a)

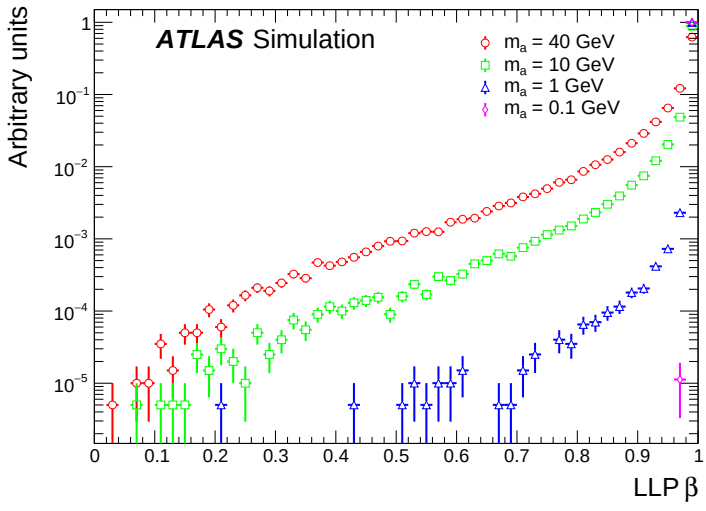

(b)

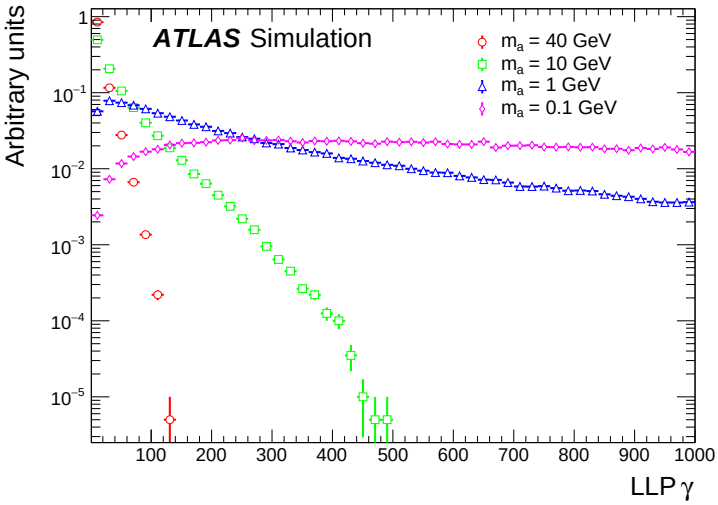

(c)

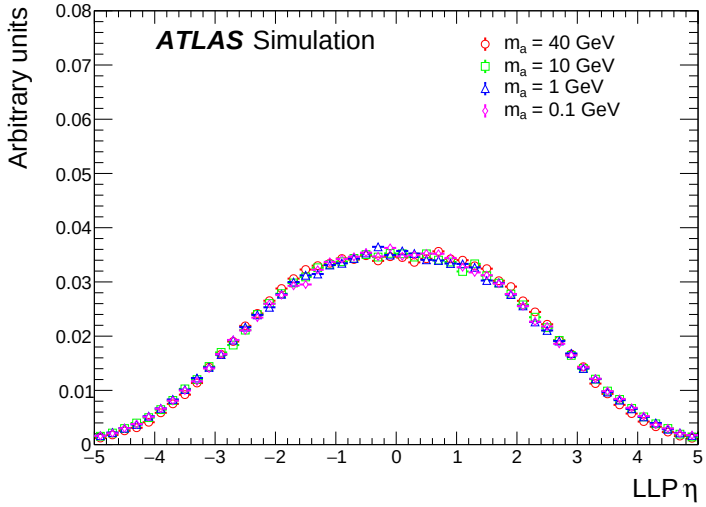

(d)

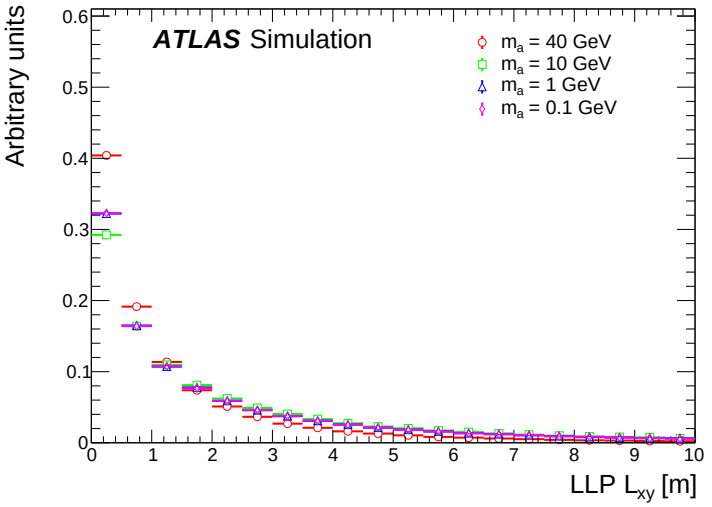

(e)

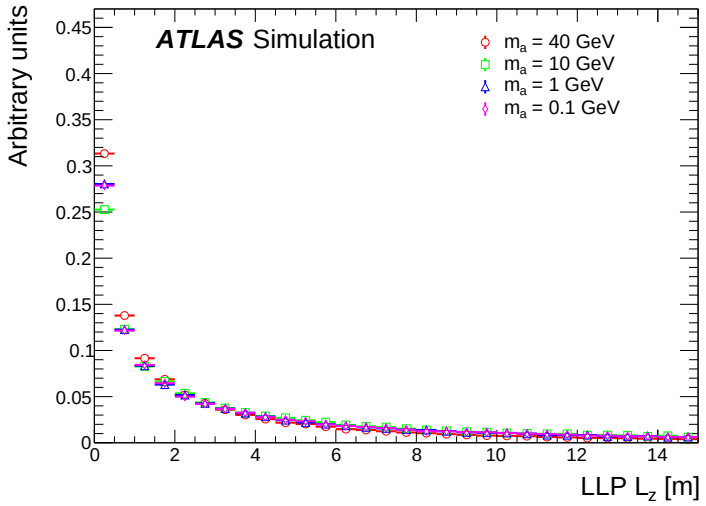

(f)

Figure 4.3.: Particle-level distributions of LLP kinematic variables obtained from all events in the generated Z+ALP MC samples.

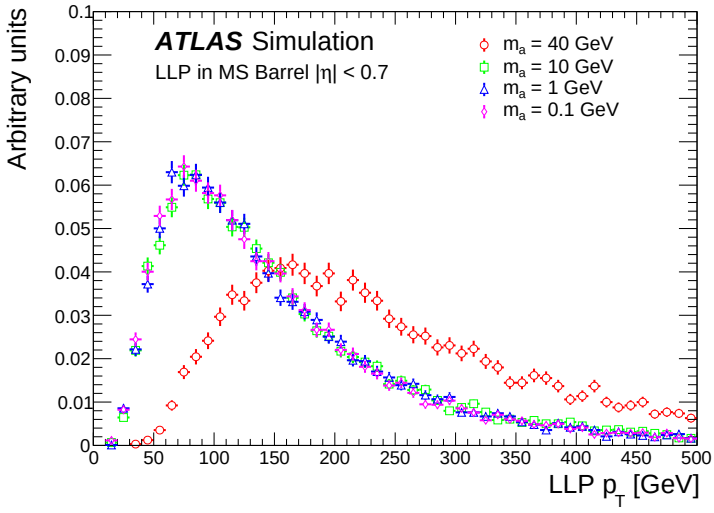

(a)

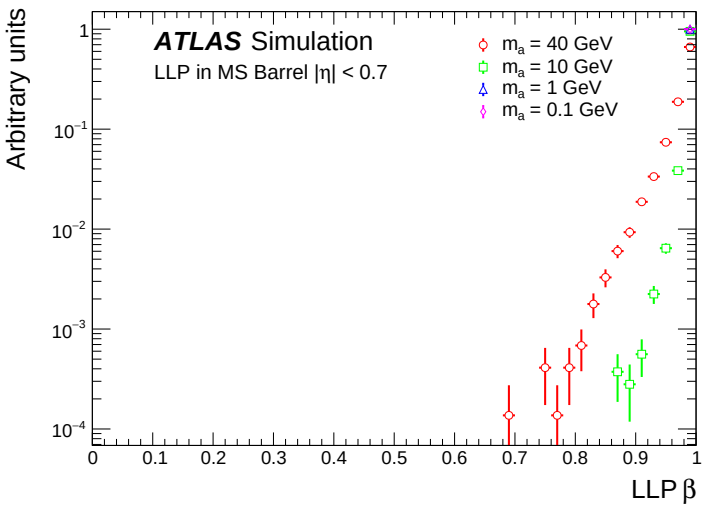

(b)

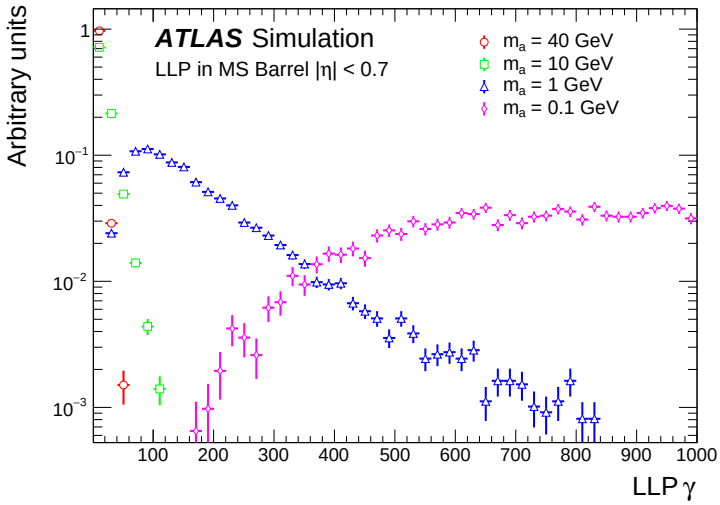

(c)

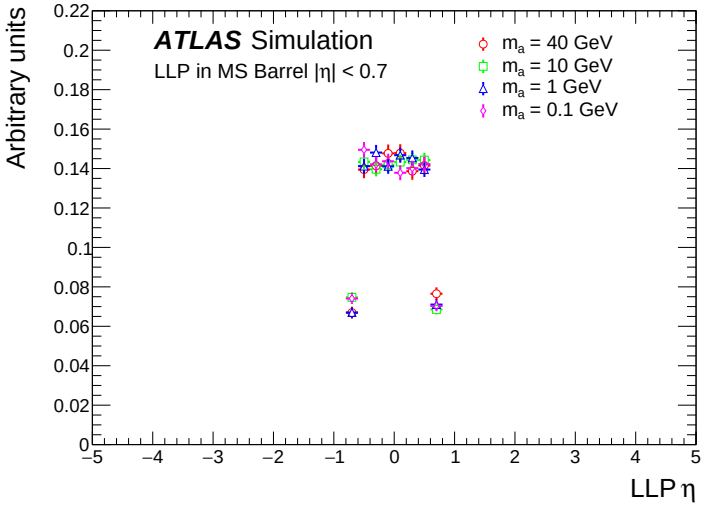

(d)

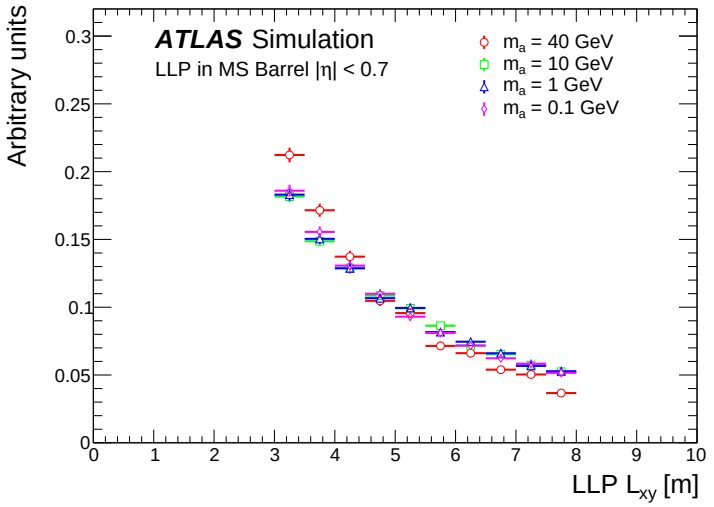

(e)

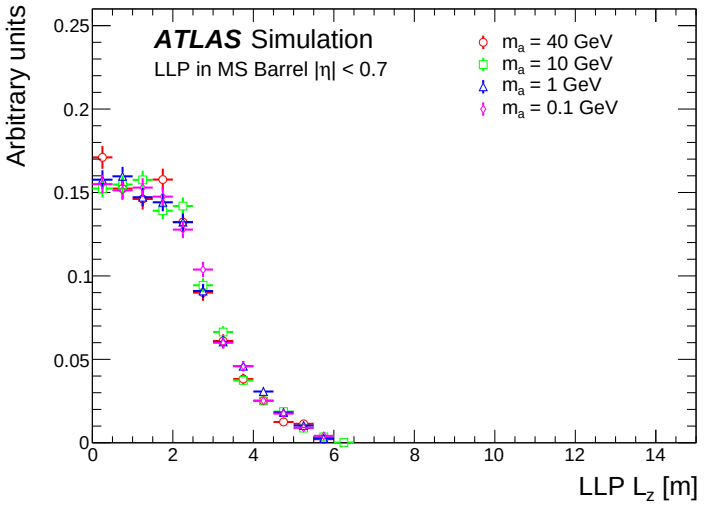

(f)

Figure 4.4.: Particle-level distributions of LLP kinematic variables obtained from events in the generated Z+ALP MC samples where the ALP decays in the MS barrel fiducial volume.

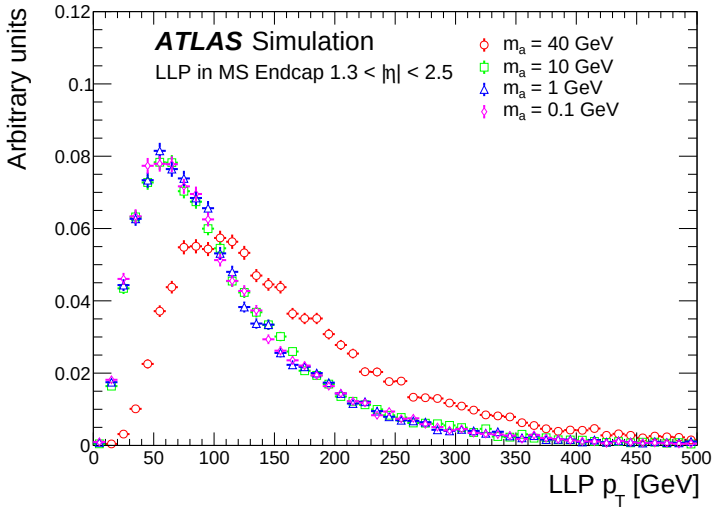

(a)

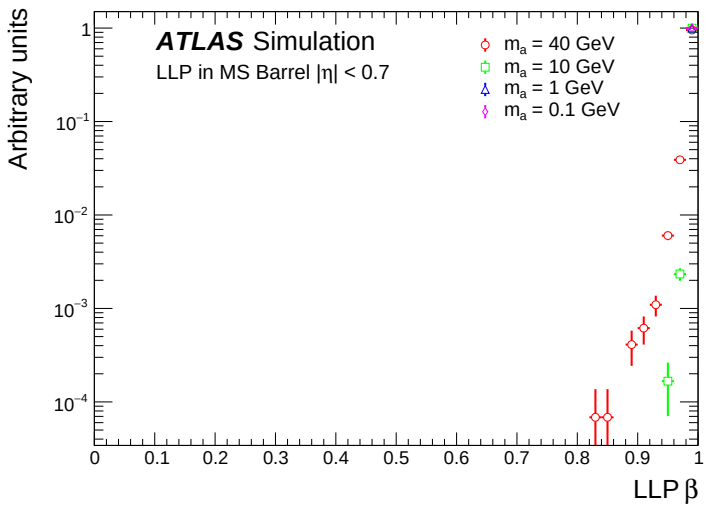

(b)

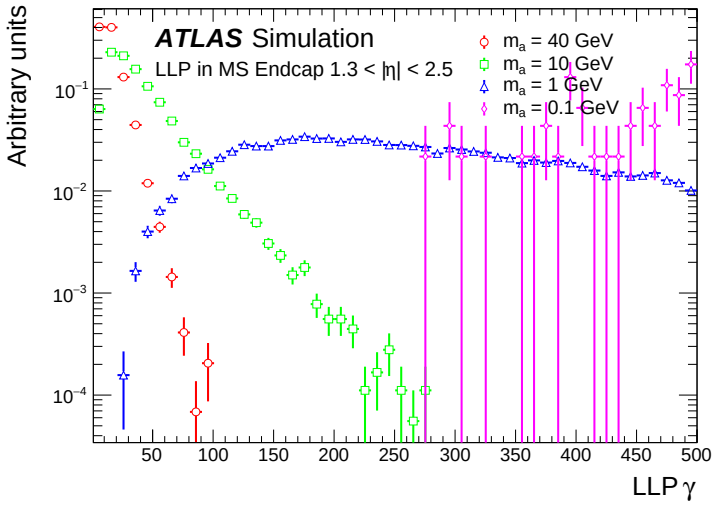

(c)

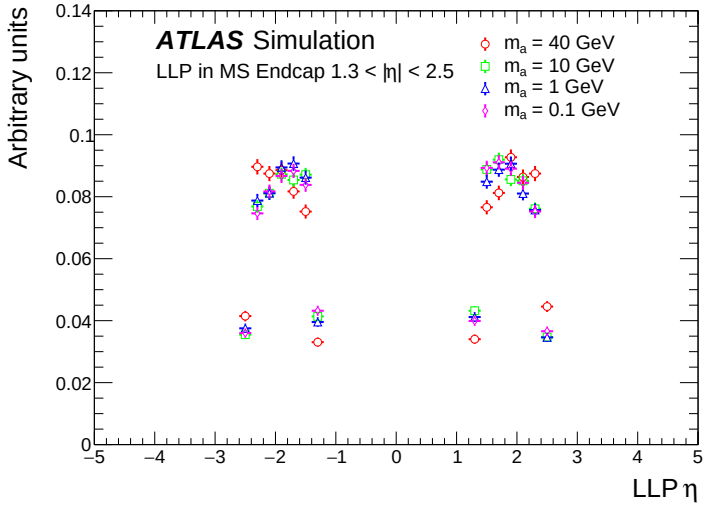

(d)

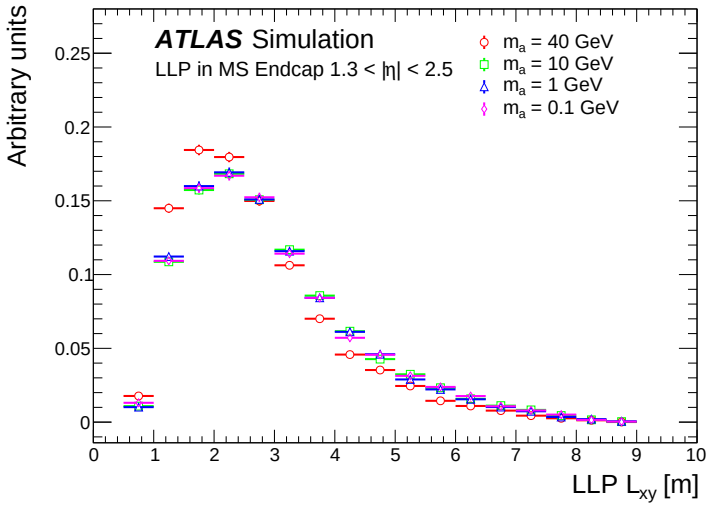

(e)

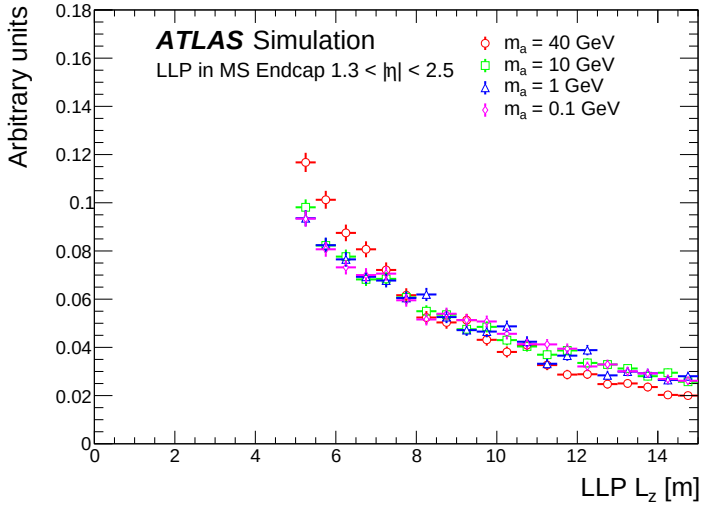

(f)

Figure 4.5.: Particle-level distributions of LLP kinematic variables obtained from events in the generated Z+ALP MC samples where the ALP decays in the MS endcap fiducial volume.

4.2. Event selection

4.2.1. Z boson reconstruction

The electron and muon baseline selections are reported in Table 4.4, following the standard ATLAS recommendations for selecting Z boson candidates with the exception of employing a looser isolation working point. An overlap removal procedure is applied to remove any identification ambiguities caused by the independent reconstruction of physics objects. Candidate Z bosons are selected if an event contains exactly one pair of same-flavour opposite-charge (SFOC) leptons passing the requirements listed in Table 4.4, referred to as the 2 lepton selection. At least one of the leptons is required to be matched to a fired lepton trigger and leading lepton must have $p_T > 27$ GeV. If the subleading lepton is trigger-matched, it too must have $p_T > 27$ GeV. Finally, the mass m_Z of the Z boson candidate must be close to the known Z boson mass 91.2 GeV.

Selections	Electron	Muon
Trigger	Table 4.1	Table 4.2
p_T	$> 10\,\text{GeV}$	
$\lvert\eta\rvert$	< 2.47	< 2.5
$\lvert d_0/\sigma_{d_0}\rvert$	< 5	< 3
$\lvert z_0 \sin\theta\rvert$	$< 0.5\text{mm}$	
Identification WP	MediumLH	Medium
Isolation WP	FCLoose	
Overlap removal	Pass	
Multiplicity	Exactly one SFOC pair	
Trigger-matched lepton	At least one within SFOC pair	
Leading/Trigger-matched lepton p_T	$> 27\,\text{GeV}$	
Dilepton mass	$60\,\text{GeV} < m_{ll} < 120\,\text{GeV}$	

Table 4.4.: The lepton baseline selections. The elesctron and muon working points (WPs) are defined in [81] and [82], respectively.

Figure 4.6 shows the p_T, η and m_Z distributions of reconstructed Z bosons in the Z+ALP MC samples. The reconstructed distributions generally match the particle-level distributions in Figure 4.1 with some slight smearing.

The p_T and η distributions of the leptons used in the reconstruction are presented in Figure 4.7, respectively. The distributions are broadly similar to the particle-level distributions in Figure 4.2 within the detector acceptance regions of $|\eta| < 2.47$ for electrons and $|\eta| < 0.5$ for muons. The dips in the electron η distributions are due to the transition region $1.37 < |\eta| < 1.52$ between the barrel and endcap calorimeters, which is typically excluded due to mismodelling of material interactions in the region. The dip in the muon η distribution is caused by the MS service gap at $|\eta| \sim 0$.

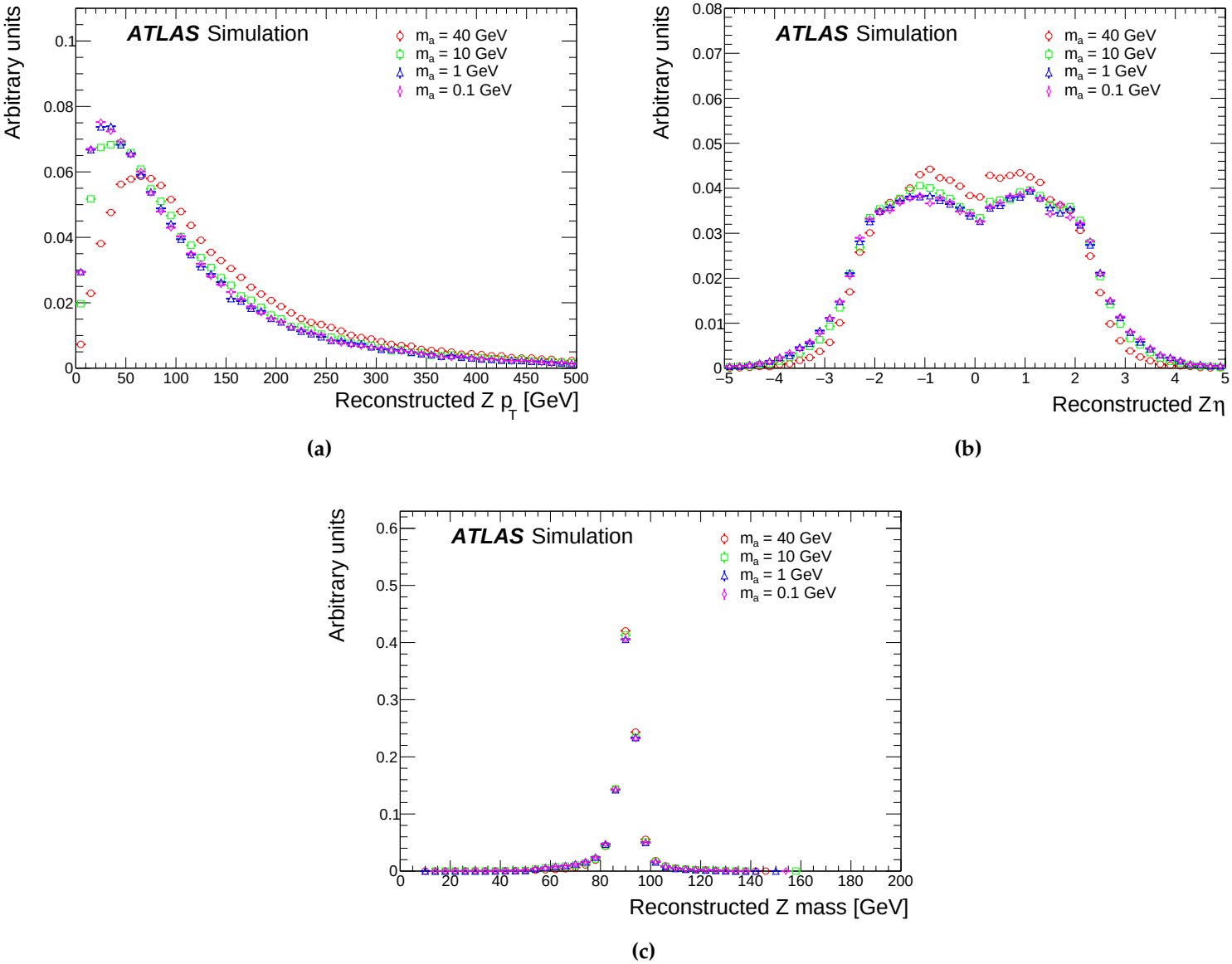

Figure 4.6.: Reconstructed (a) p_T, (b) η, and (c) m_Z distributions of reconstructed Z bosons in the generated Z+ALP MC samples.

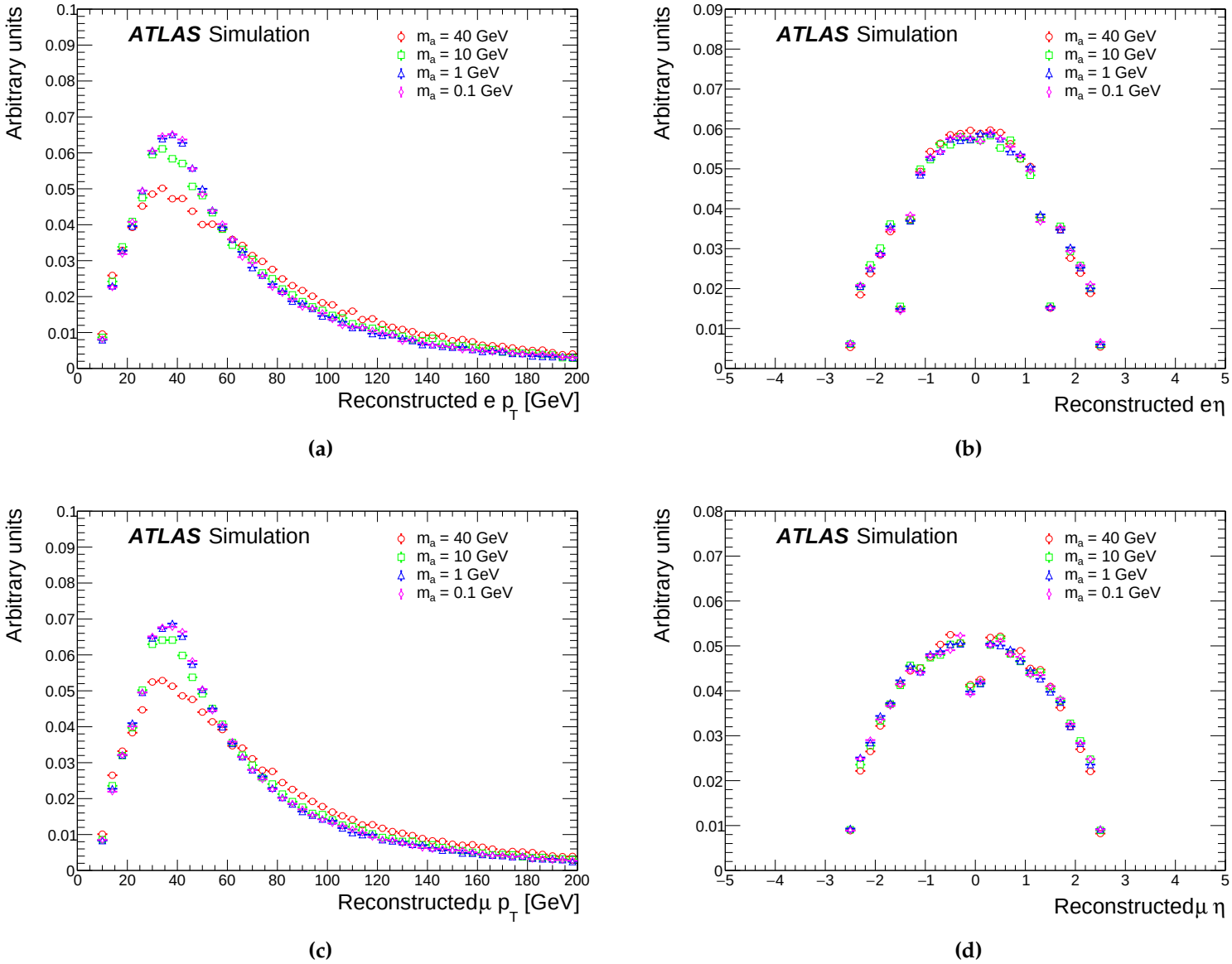

(a) **(b)**

(c) **(d)**

Figure 4.7.: Reconstructed p_T (left) and η (right) distributions of (a,b) electrons and (c,d) muons used to reconstruct a Z boson in the generated Z+ALP MC samples.

4.2.2. Neural nets

A pair of uncorrelated neural nets (NNs) were developed to perform the final signal-background discrimination and to construct the ABCD plane for the background estimation. The NNs used were originally designed for the RoI-triggered channel and are briefly described below.

A multilayer perceptron (MLP) is a NN consisting of an input layer, multiple hidden layers and an output layer that are fully connected such that every input influences all of the neurons in the hidden layers, which then all affect the output layer, as shown in Figure 4.8. The input layer takes all the features from the input dataset and passes them to all the neurons in the hidden layer. In each neuron, every input from the previous layer is multiplied with a weight and then added with a bias. The sum of these linearly transformed inputs is passed to an activation function which gives an output that is passed to the next layer.

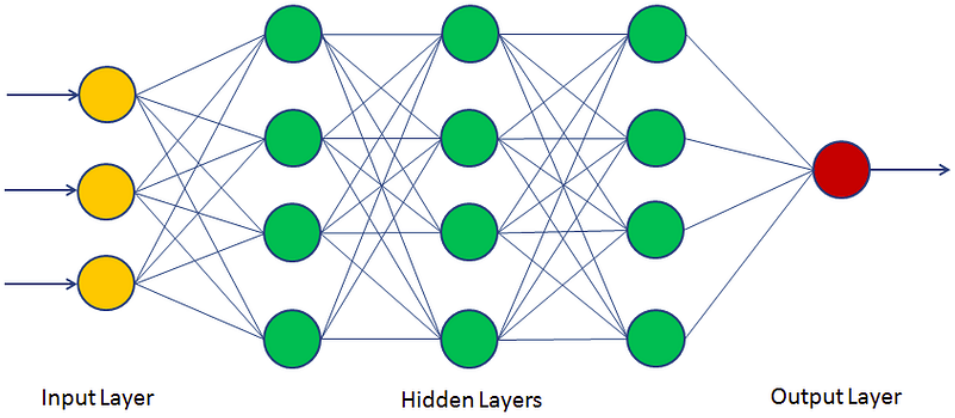

Figure 4.8.: Sketch of a multilayer perceptron consisting of three hidden layers [83].

To construct the ABCD plane used to estimate the background, two MLPs are utilised with two different sets of input features in order to get two NN scores, which are referred to as NN1 and NN2. The input variables corresponding to NN1 have little correlation with the input variables corresponding to NN2 so that the two NN scores are not correlated with each other. Both sets of input features are listed in Table 4.5. The MLPs are constructed with the sequential model provided by Keras and TensorFlow [84, 85] and both consist of two hidden layers. Each hidden layer has 128 neurons and uses the Rectified Linear Unit function as the activation function. The output layer has one node and uses the Sigmoid function as its activation function to yield a final NN score output between 0 and 1.

Neural net	Input features
NN1	Ratio of the number of segments in the inner and middle MDT stations. Sum of $\lvert p_T \rvert$ of high-p_T tracks within $\Delta R = 0.4$ of the DV. Total, average, RMS and maximum energy of calorimeter clusters. Calorimeter cluster energy at each ECal and HCal sampling layer. ΔR between the DV and closest jet or high-p_T track. Vector sum of p_T of low-p_T tracks within $\Delta R = 0.2$ of the DV.
NN2	Average and RMS ΔR between the DV and tracklets. Average and RMS ΔR between the DV and segments. Sum of MDT hits and trigger chamber hits. $\Delta\phi$ between the DV and E_T^{miss}. Average, RMS and maximum time of calorimeter clusters. Number of tracklets.

Table 4.5.: Input features corresponding to NN1 and NN2. Jets considered are required to have $p_T > 20$ GeV. The terms "low-p_T" and "high-p_T" tracks refer to tracks with $p_T < 5$ GeV and $p_T > 5$ GeV, respectively. Segments, tracklets, calorimeter clusters and MDT/trigger chamber hits are required to be within $\Delta R = 0.4$ of the DV.

As the NNs were originally designed for the RoI-triggered channel, the selections defined in Table 3.2 were used for the NN training, with the exception of the $E_T^{\text{miss}} > 20$ GeV selection in order to increase the number of events for the training. Since DVs from background sources are not well-modelled in MC simulations, the NNs were trained on background-dominated data with $H_T^{\text{miss}} < 40$ GeV, as well as on scalar portal MC signal samples with mediator ϕ masses of $m_\phi = \{60, 125, 1000\}$ GeV and a wide variety of LLP masses ranging from 5 GeV to 475 GeV. The scalar portal signal model is described in Section 1.3.3 and the parameters used in the scalar portal MC generation are listed in Table B.1.

Figure 4.9 shows the NN scores in the barrel and endcap regions for the Z+ALP samples. The finalised lepton-triggered channel selections defined in Table 4.9 are applied, except for the requirements on NN1 and NN2. Although the NNs were trained using a different signal model, they perform well for the Z+ALP signal samples due to the similar decay topologies. Therefore, the NNs were not retrained for the Z+ALP model. However, to improve the signal efficiency, the requirements of NN1 > 0.5 (0.8) and NN2 > 0.5 (0.8) in the barrel (endcap) that were defined for the RoI-

triggered channel were optimised to NN1 > 0.2 and NN2 > 0.1 in both detector regions, as discussed in Section 4.2.3.5.

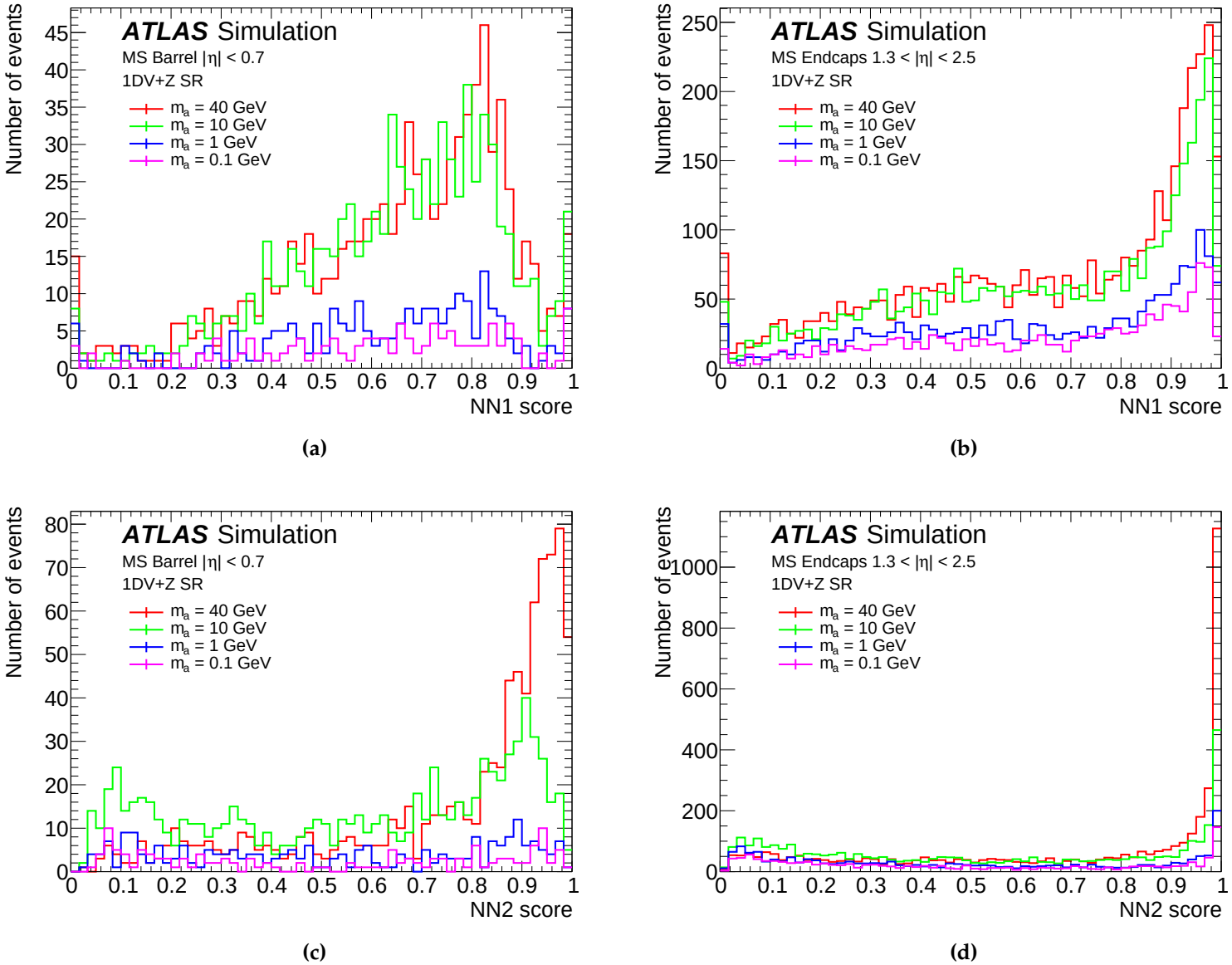

Figure 4.9.: The distributions of NN1 (top) and NN2 (bottom) in the barrel (left) and endcaps (right) regions for the generated Z+ALP samples. The events shown have passed the lepton-triggered channel selection defined in Table 4.9, with the exception of the requirements on NN1 and NN2.

4.2.3. Optimisation

Although the original aim of this search was to remain as close as possible to the selection defined for the RoI-triggered channel, preliminary studies showed the selection criteria defined in Table 3.2 were suboptimal for the Z+ALP model. In particular, the reinterpretation studies in Section 3.3.1 showed that the muon RoI cluster trigger is suboptimal for ALPs, whereas a lepton trigger strategy is much more efficient and is therefore utilised in this search. The overall efficiencies of the RoI-triggered channel selection ϵ_a^{RoI} and finalised lepton-triggered channel selection ϵ_a^{lep} are listed in Table 4.10. The ratio of the efficiencies $\epsilon_a^{\text{lep}}/\epsilon_a^{\text{RoI}}$ is more approximately 4 for $m_a = 40$ GeV and ranges between 6.8 and 7.9 for $m_a = \{0.1, 1, 10\}$ GeV.

Additionally, since the ALP model produces only one LLP, unlike the scalar portal scenarios considered in the RoI-triggered channel that pair-produce LLPs, it is not necessary to retain orthogonality with the 2DV search. Hence, rather than pre-selecting events with exactly one MS vertex, the 1DV+Z search pre-selects events with at least one MS vertex, then requires exactly one MS vertex to have passed all vertex selection criteria before inputting this single "good vertex" into the NNs. This reduces rejection of events where signal and background activity are concurrent. Further optimisations to the selections in Table 3.2 are discussed below.

4.2.3.1. Missing transverse energy selection

The $H_T^{\text{miss}} > 40$ GeV requirement in the RoI-triggered channel is suboptimal for ALPs as H_T^{miss} does not account for the associated leptons. Figure 4.10 shows that Z+ALP events can have a low H_T^{miss} despite having a large E_T^{miss}. Applying $H_T^{\text{miss}} > 40$ GeV removes a large amount of the Z+ALP signal. Therefore, the H_T^{miss} selection is omitted in the lepton-triggered channel.

Since H_T^{miss} is used to define the SR and a background-rich VR in the RoI-triggered channel, it is necessary to assign this role to another variable. Figure 4.11 shows the E_T^{miss} distributions for the generated ALP samples as well as Z+jet MC events and data recorded in 2015 and 2016, which was already unblinded by a previous search. Events shown in these distributions have passed the lepton trigger and Z boson selections and contain a DV. No further selection applied to the DV. It is clear there is a background-dominated region where $E_T^{\text{miss}} < 40$ GeV and good signal/background discriminating power where $E_T^{\text{miss}} > 40$ GeV. Therefore, the lepton-triggered channel

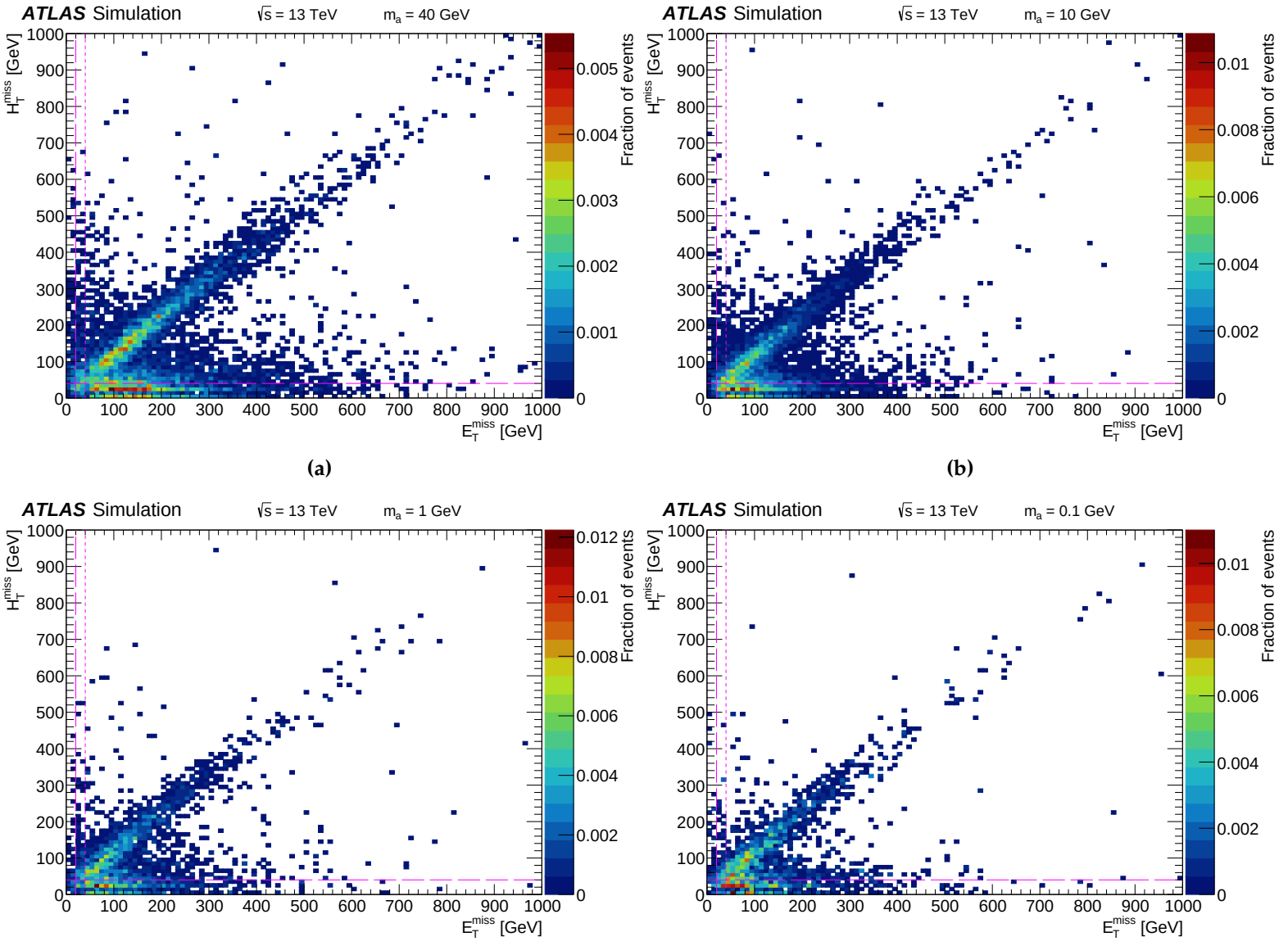

Figure 4.10.: Two-dimensional distributions of the H_T^{miss} and E_T^{miss} for Z+ALP samples with $m_a =$ (a) 40 GeV, (b) 10 GeV, (c) 1 GeV, (d) 0.1 GeV. Events are required to pass the lepton triggers and Z boson selection and contain a DV. No selection is applied to the DV. The dashed lines indicate the H_T^{miss} and E_T^{miss} selections applied in the RoI-triggered channel, while the dotted line indicates the finalised E_T^{miss} selection.

SR is defined by $E_T^{\text{miss}} > 40$ GeV and a E_T^{miss} VR – discussed in Section 4.3.1 – is defined by $E_T^{\text{miss}} < 40$ GeV. Table 4.6 shows the ALP signal efficiency ϵ_E of the lepton-triggered channel $E_T^{\text{miss}} > 40$ GeV selection is approximately 90% for all m_a, whereas the efficiency ϵ_H of the $H_T^{\text{miss}} > 40$ GeV and $E_T^{\text{miss}} > 20$ GeV selections utilised in the RoI-triggered channel is approximately 70% for all m_a.

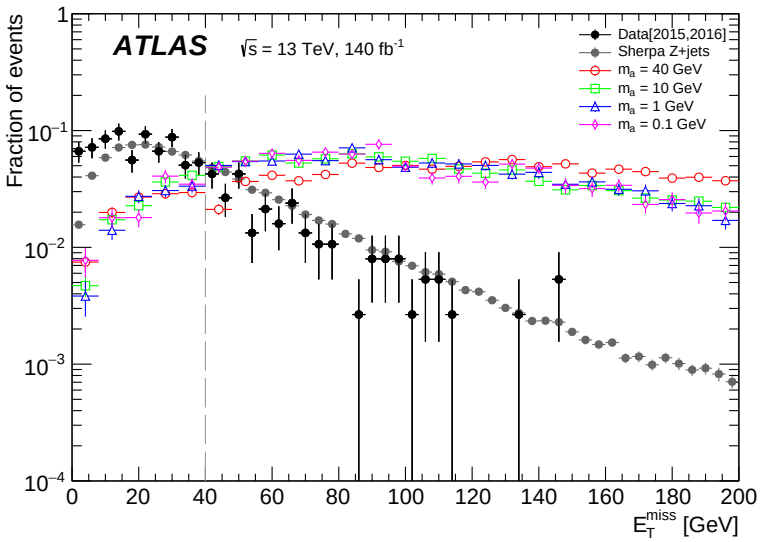

Figure 4.11.: The distributions of E_T^{miss}. The black filled points show data recored in 2015 and 2016, the grey filled points show Z+jets MC events and the other points show the ALP MC. The events shown have passed the lepton trigger and Z boson selections and contain a DV, with no selection applied to the DV. The grey dashed line indicates the lepton-triggered channel selection.

m_a [GeV]	ϵ_H	ϵ_E	ϵ_E/ϵ_H
40	0.71	0.93	1.3
10	0.67	0.90	1.3
1	0.68	0.92	1.4
0.1	0.68	0.91	1.3

Table 4.6.: The efficiency ϵ_H of the RoI-triggered channel H_T^{miss} and E_T^{miss} selections compared to the efficiency ϵ_E of the lepton-triggered channel E_T^{miss} selection for the generated ALP samples. Events considered have fired a lepton trigger, passed the Z boson selection and contain a DV in the MS. No further selection is applied to the DV.

4.2.3.2. Displaced vertex isolation

As discussed in Section 3.4, the vector sum of the p_T of low-p_T (< 5 GeV) tracks located within $\Delta R < 0.2$ of the MS DV ($\sum_{\text{low-}p_T \text{ tracks}} \vec{p}_T(\Delta R < 0.2)$) was identified as a powerful selection criteria to reject punch-through jets in the RoI-triggered channel. Figure 4.12 shows the distributions of the sum of low-p_T tracks for the generated ALPs. All selections that precede this variable in Table 4.9 have been applied. A negligible fraction of events lie outside of the $\sum_{\text{low-}p_T \text{ tracks}} \vec{p}_T(\Delta R < 0.2) < 5$ GeV threshold.

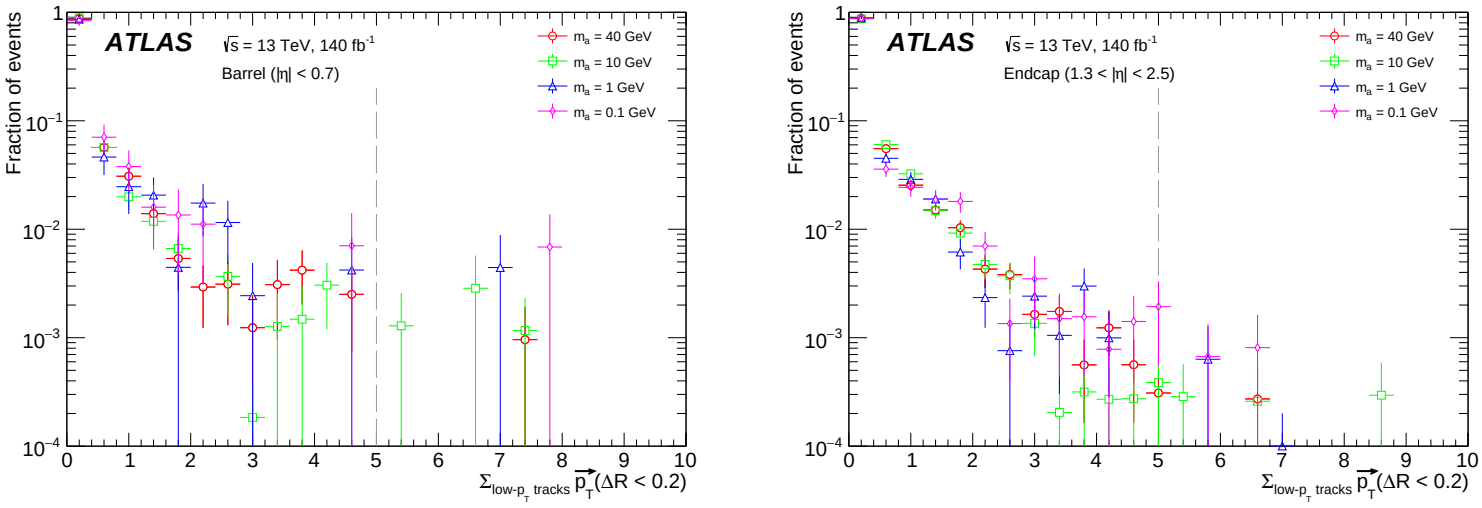

(a) **(b)**

Figure 4.12.: The distributions of the vector sum of p_T for low-p_T tracks within $\Delta R < 0.2$ of the MS DV ($\sum_{\text{low-}p_T \text{ tracks}} \vec{p}_T(\Delta R < 0.2)$) for the generated ALPs in (a) the barrel and (b) the endcap volumes. The grey dashed line indicates the selection applied in the search. All selections that precede this variable in Table 4.9 have been applied.

Figure 4.13 shows the distributions of ΔR_{min}(DV, jet/high-p_T track)) for ALPs. In the RoI-triggered channel, DVs are required to be highly isolated from jets and high-p_T tracks ($\Delta R_{min} > 0.8$) since there is no prompt activity expected in the models considered. For Z+ALP, the ΔR_{min} requirement can in principle be looser because several sources of background are suppressed by the presence of the Z boson. In addition, one of the associated leptons can share a similar trajectory to the ALP, resulting in a high-p_T track near to the DV. Therefore, a looser ΔR_{min} selection is desirable. Figure 4.13 shows good signal/background discrimination at $\Delta R_{min} > 0.4$. However, the studies in the E_T^{miss} VR presented in Section 4.3.1 revealed there are insufficient events in data to validate the ABCD plane when $\Delta R_{min} > 0.2$. The selection is hence loosened to $\Delta R_{min} > 0.1$.

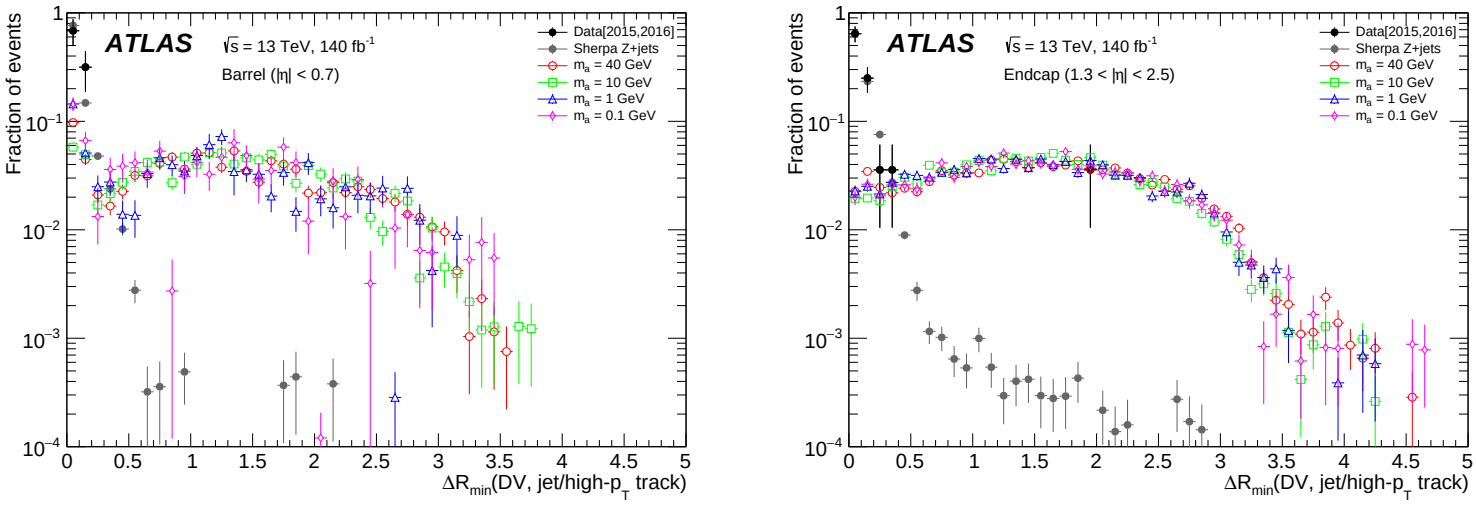

(a) **(b)**

Figure 4.13.: The distributions of the angular separation between the MS DV and closest jet or high-p_T track (ΔR_{min}(DV, jet/high-p_T track)) in (a) the barrel and (b) the endcap volumes. The black filled points show data recored in 2015 and 2016, the grey filled points show Z+jets MC events and the other points show the ALP MC. All selections listed in Table 4.9 are applied except for the requirements on ΔR_{min} and the neural nets scores.

4.2.3.3. Non-collison background rejection

Figures 4.14 and 4.15 show the number of segments in the outer MDT layer as a function of the number of trigger chamber hits in the barrel and endcap, respectively. The events shown have passed all the selections that preceded the NNs in Table 4.9. The dashed lines indicate the requirements of $n_{\text{RPC}} > 800$ and $n_{\text{Seg}} > 15$ ($n_{\text{RPC}} > 900$ and $n_{\text{Seg}} > 30$) that are applied in the barrel (endcap) region of the RoI-triggered channel and illustrate that these selections, which are intended to suppress the NCB, reject much of the ALP signal. These selections can be removed if the requirement of a Z boson suppresses NCB to a sufficiently low rate. However, this rate cannot be measured directly. NCB is stochastic and difficult to model so it must be studied in dedicated non-collision data, referred to as *latestream* data, that is collected in unpaired and empty bunch crossings using the muon RoI cluster trigger. Since the bunch crossings are not paired, no Z bosons are produced. However, the degree of NCB suppression provided by the Z boson can be roughly estimated by calculating the probability of a random bunch crossing in Run 2 containing both a Z boson and NCB.

Table 4.7 shows the luminosities $\mathcal{L}_{\text{year}}$ for each year of data taking in Run 2 [40], as well as the number of paired bunch crossings $N_{\text{BC}}^{\text{Paired}}$ and the number of Z bosons

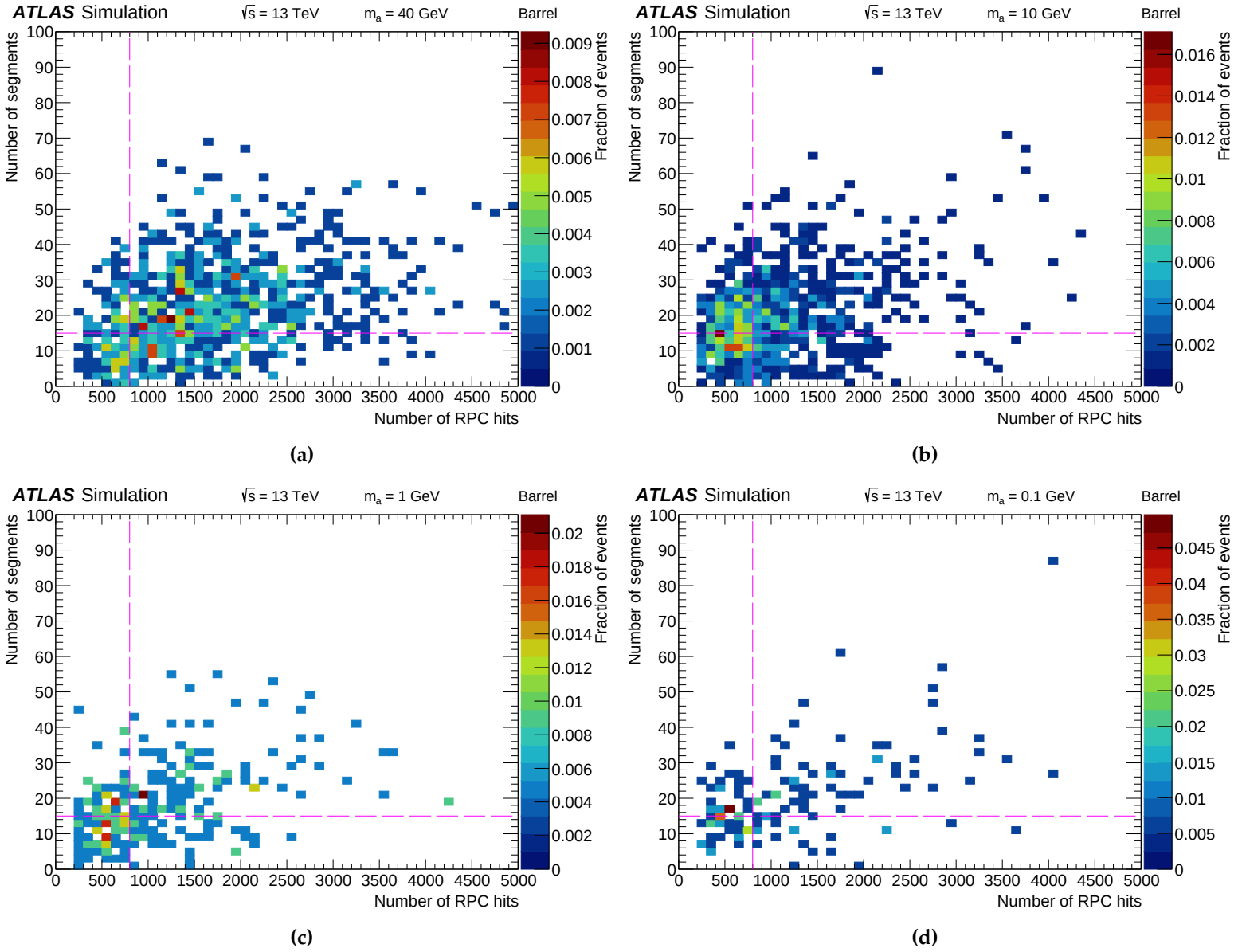

Figure 4.14.: Distributions of the number of muon segments in the outer MDT layer as a function of RPC hits in the barrel region for the Z+ALP samples with m_a = (a) 40 GeV, (b) 10 GeV, (c) 1 GeV, (d) 0.1 GeV. All selections listed in Table 4.9 are applied except for the neural nets. The dashed lines indicate the selections applied in the RoI-triggered channel.

N_Z in the dataset that decay into electrons or muons, estimated as $N_Z = \sigma_Z \times B(Z \to ee/\mu\mu) \times \mathcal{L}_{\text{year}}$, where $\sigma_Z = 60$ nb is the inclusive Z production cross-section [8] and $B(Z \to ee/\mu\mu) = 6.6\%$ [86] is the combined branching ratio into electron or muon pairs. The probability $P(Z \to ee/\mu\mu) = N_Z / N_{\text{BC}}^{\text{Paired}}$ of a random bunch crossing containing a leptonically decaying Z boson is reported for each year. Events that contain NCB have a $\mathcal{O}(10^{-6})$ probability of also featuring a leptonically decaying Z boson. Thus, the requirement of a Z boson will greatly suppress NCB.

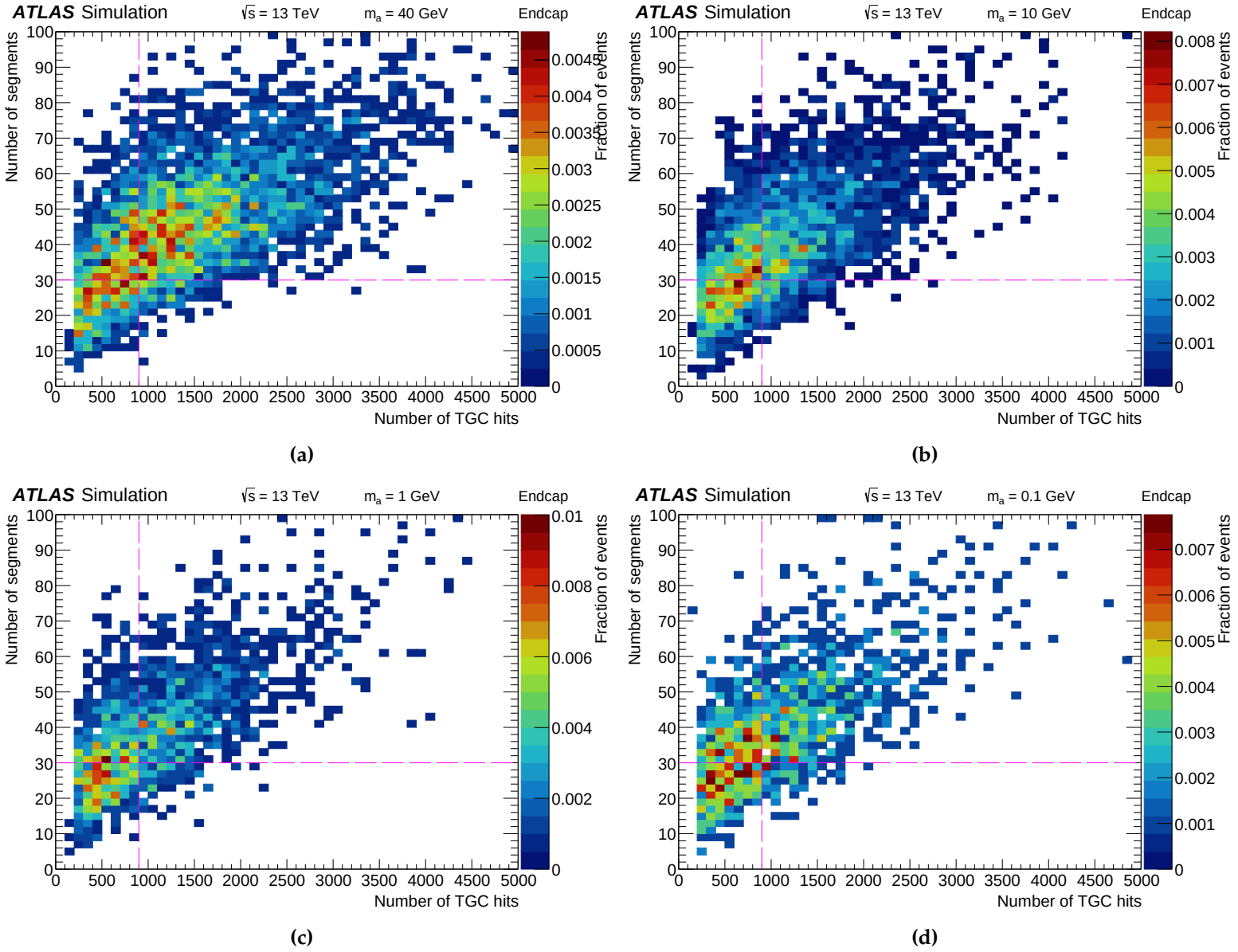

Figure 4.15.: Distributions of the number of muon segments in the outer MDT layer as a function of TGC hits in the endcap region for the Z+ALP samples with m_a = (a) 40 GeV, (b) 10 GeV, (c) 1 GeV, (d) 0.1 GeV. All selections listed in Table 4.9 are applied except for the neural nets. The dashed lines indicate the selections applied in the RoI-triggered channel.

Since the requirement of a Z boson would automatically reject all latestream data events, a loosened selection was employed to estimate the amount of NCB that enters the lepton-triggered channel ABCD planes. All prompt lepton selection was omitted and the isolation from tracks was turned off since there are often no tracks in latestream data. The number of latestream events that pass the muon RoI cluster trigger and the loosened selection is denoted as $N_{\text{Late}}^{\text{Loose}}$.

Year	2015	2016	2017	2018
$\mathcal{L}_{int}$ [fb^{-1}]	3.24	33.4	44.63	58.79
$N_{\text{BC}}^{\text{Paired}}$	1.20×10^{13}	1.24×10^{14}	1.10×10^{14}	1.47×10^{14}
N_{Z}	1.28×10^{7}	1.32×10^{8}	1.77×10^{8}	2.33×10^{8}
$P(Z \to ee/\mu\mu)$	1.07×10^{-6}	1.07×10^{-6}	1.61×10^{-6}	1.58×10^{-6}

Table 4.7.: The integrated luminosities and number of paired bunch-crossings for each year in Run 2 [40] and the corresponding estimates of the probability for an event to feature a $Z \to ee/\mu\mu$ decay.

To properly estimate the number of NCB events in mainstream Run 2 data, the difference in the efficiencies of the muon RoI trigger used to collect the latestream data and the lepton triggers used in the lepton-triggered channel must also be considered. It is also necessary to factor in the difference in the amount of data recorded by the mainstream and latestream triggers, quantified as the ratio of the number of paired and unpaired bunch crossings $R_{\text{BC}} = N_{\text{BC}}^{\text{Paired}}/N_{\text{BC}}^{\text{Unpaired}} \sim 4$ [87]. The effect of the loosened selection is estimated for the RoI-triggered channel as $R_{\text{Loose}} = N_{\text{Main}}^{\text{Full}}/N_{\text{Main}}^{\text{Loose}} \sim 0.3$ [87], where $N_{\text{Main}}^{\text{Full}}$ and $N_{\text{Main}}^{\text{Loose}}$ are the number of mainstream data events that pass the full and loosened selections, respectively. The same value is used in this estimate. Hence, the expected number $N_{\text{Z+NCB}}$ of Z+NCB background events is

$$N_{\text{Z+NCB}} = \frac{\epsilon_{\text{Z}}^{\text{Reco}}}{\epsilon_{\text{NCB}}^{\text{RoI}}} \times P(Z \to ee/\mu\mu) \times R_{\text{BC}} \times R_{\text{Loose}} \times N_{\text{Late}}^{\text{Loose}}, \tag{4.1}$$

where $\epsilon_{\text{Z}}^{\text{reco}} \sim 0.5$ is the combined lepton trigger and Z boson reconstruction efficiency estimated from the values in Table 4.9, $\epsilon_{\text{NCB}}^{\text{RoI}}$ is the efficiency of the muon RoI trigger to fire on NCB, and $N_{\text{Late}}^{\text{Loose}} = 253$. Any NCB that enters the ABCD plane has passed the DV selection and is somewhat signal-like. The efficiency of the muon RoI cluster trigger is $\mathcal{O}(10\%)$ for signal, thus $\epsilon_{\text{NCB}}^{\text{RoI}}$ is conservatively set to 0.1 for this estimation. With these values, Equation 4.1 yields $N_{\text{Z+NCB}} \sim \mathcal{O}(10^{-3})$. Therefore, the selections on $n_{\text{RPC/TGC}}$ and n_{Seg} were removed without introducing significant NCB.

4.2.3.4. Muon spectrometer fiducial volume

The requirements on the transverse (L_{xy}) and longitinal (L_z) components of the DV position in the barrel (3 m $< L_{xy} <$ 8 m) and endcap ($L_{xy} <$ 10 m, 5 m $< L_z <$ 15 m) regions are dictated by the necessity of at least two tracking layers to reconstruct a DV and therefore cannot be optimised. The same is true of the DV pseudorapidity requirements of $|\eta_{\text{DV}}| < 0.7$ in the barrel and $1.3 < |\eta_{\text{DV}}| < 2.5$ in the endcap. Figure 4.16 shows the η distributions of DVs in ALP MC samples. Events have passed the lepton trigger, the Z boson requirement and have $E_T^{\text{miss}} > 40$ GeV. No selection is applied on the DVs. There are dips in the distribution in the transition region $0.7 < |\eta| < 1.3$ and around $|\eta| \sim 0$, where there is a gap in the MS coverage for service access. Figure 4.3 (e) shows there is a significant fraction of generated signal in these regions. Further, 4.4 (e) shows that ALPs decays in the MS barrel region are distributed uniformly in η. Therefore, the DV reconstruction efficiency around $|\eta| \sim 0$ is very poor. Future improvements to the MS DV reconstruction algorithm could combine hits in the barrel and endcap to recover signal lost in the transition region. However, this is beyond the scope of this work and the η selection is thus not optimised.

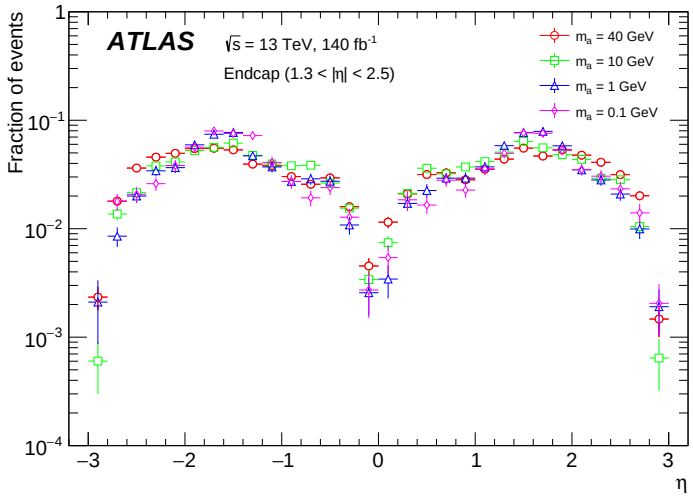

Figure 4.16.: The DV η distributions for the generated ALP samples. The events shown have passed the lepton trigger and Z boson selections, contain a DV and have $E_T^{\text{miss}} > 40$ GeV. No selection is applied to the DV.

4.2.3.5. Neural net score selection

Figure 4.9 shows the NN score distributions for the ALP samples with the finalised lepton-triggered channel selection defined in Table 4.9, while Figures 4.17 and 4.18 respectively show the barrel and endcap ABCD planes constructed from the NN score distributions. In the RoI-triggered channel, region A is defined by NN1 $>$ 0.5 (0.8) and NN2 $>$ 0.5 (0.8) in the barrel (endcap). This selection would exclude much of the ALP signal from region A, particularly for ALPs with $m_a \leq 1$ GeV which are likely to be considered background-like to the NNs because they are lighter and decay into more collimated, lower-multiplicity jets than the scalar LLPs with masses $m_s \geq 5$ GeV that the NNs were trained with. The lepton-triggered channel is expected to have a much lower background count than the RoI-triggered channel. In the absence of correlations, the ABCD method should work regardless of how the ABCD regions are defined, provided there are events in region D to allow the method to be predictive. Therefore, to maximise signal efficiency in region A and minimise signal contamination in regions B, C and D, the region A definition was loosened to NN1 $>$ 0.2 and NN2 $>$ 0.1 in both the barrel and endcap regions.

Table 4.8 compares the signal efficiency $\epsilon_{\text{NN}}^{\text{lep}}$ of the lepton-triggered channel NN selection to the efficiency $\epsilon_{\text{NN}}^{\text{RoI}}$ of the RoI-triggered channel selection. The finalised lepton-triggered channel selection listed in Table 4.9 is applied in addition to the corresponding NN score selections. The ratio $\epsilon_{\text{NN}}^{\text{lep}}/\epsilon_{\text{NN}}^{\text{RoI}}$ is 2.5-4.7 depending on m_a. The efficiency is improved most for light ALPs with $m_a \leq 1$ GeV.

m_a [GeV]	$\epsilon_{\text{NN}}^{\text{RoI}}$	$\epsilon_{\text{NN}}^{\text{lep}}$	$\epsilon_{\text{NN}}^{\text{lep}}/\epsilon_{\text{NN}}^{\text{RoI}}$
40	0.34	0.86	2.5
10	0.23	0.81	3.5
1	0.16	0.76	4.7
0.1	0.17	0.75	4.5

Table 4.8.: The Z+ALP signal efficiency $\epsilon_{\text{NN}}^{\text{lep}}$ for the lepton-triggered channel NN score selections of NN1 > 0.2 and NN2 > 0.1, compared to the efficiency $\epsilon_{\text{NN}}^{\text{RoI}}$ of the RoI-triggered channel NN score selections of NN1 > 0.5 (0.8) and NN2 > 0.5 (0.8) in the barrel (endcap). The denominator in both efficiencies is the number of Z+ALP MC events that pass all non-NN selections listed in Table 4.9 and the numerator is the number of events that subsequently pass the corresponding NN score selection.

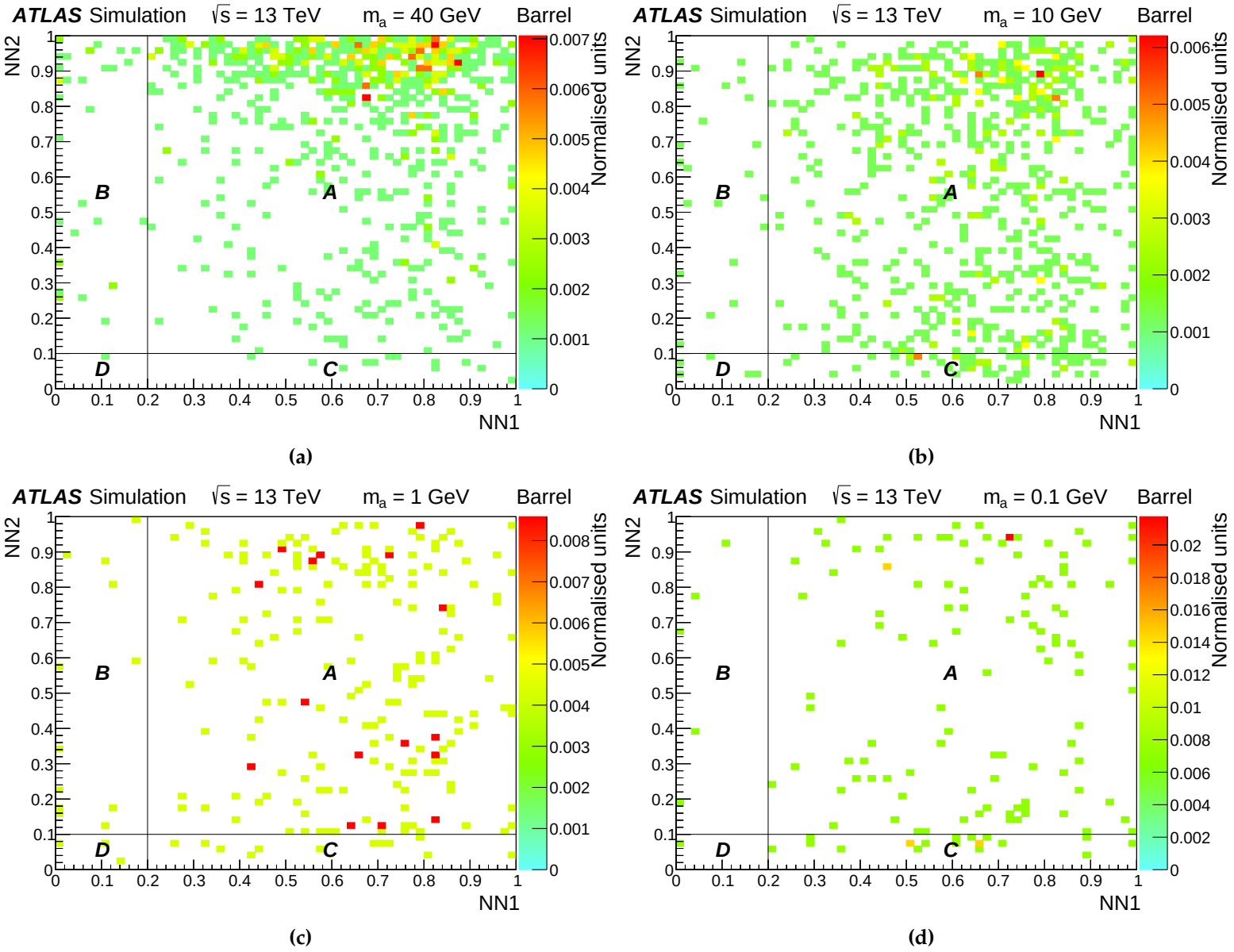

Figure 4.17.: ABCD planes for the simulated Z+ALP samples in the barrel signal region. Events shown have passed all non-NN selections defined in Table 4.9.

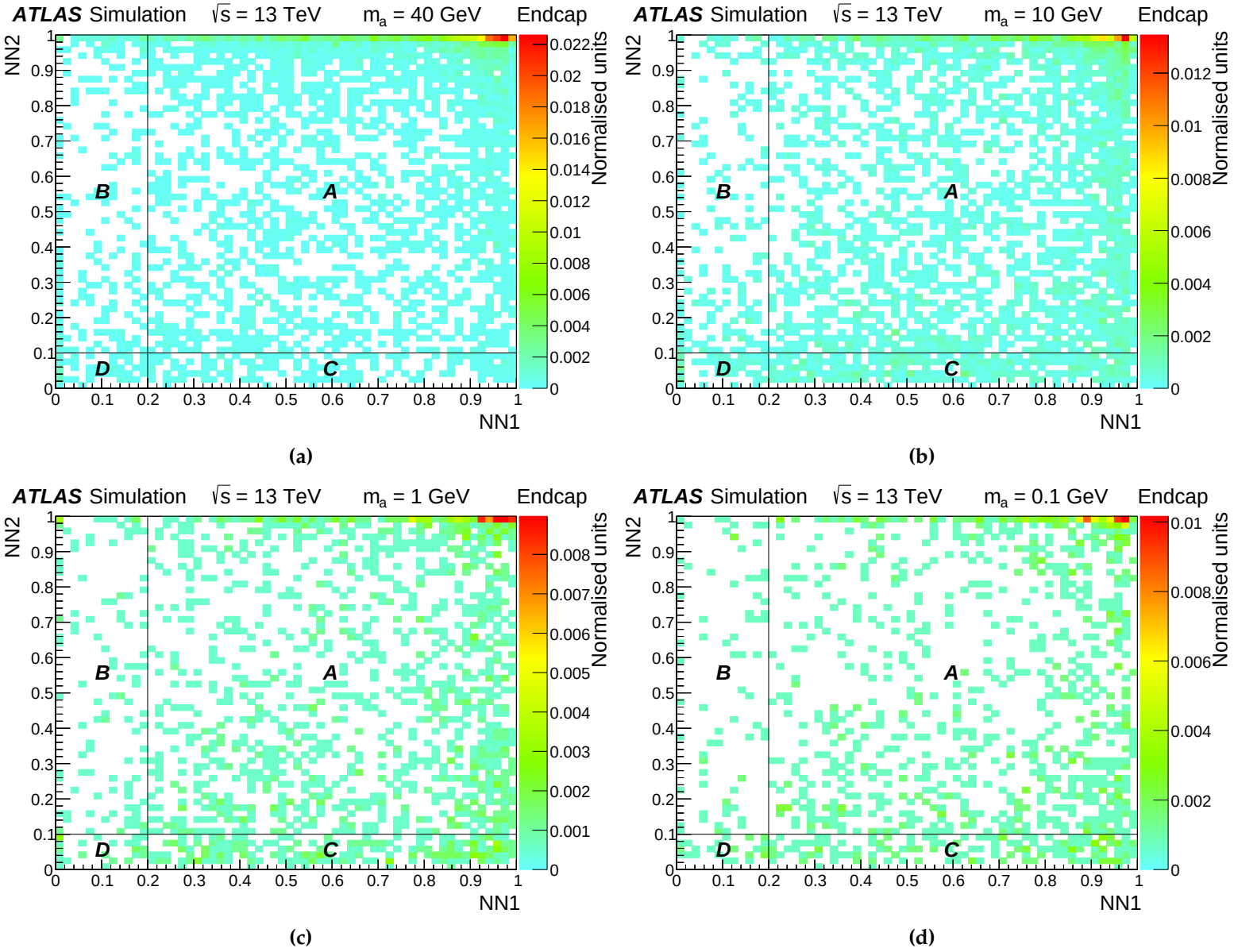

Figure 4.18.: ABCD planes for the simulated Z+ALP samples in the endcap signal region. Events shown have passed all non-NN selections defined in Table 4.9.

4.2.4. Signal selection

The finalised lepton-triggered channel selection and the ALP signal yield following each successive selection are reported in Table 4.9. In all events considered, event cleaning criteria are applied: the ATLAS detector must be fully operational, the event must be fully reconstructed, and there must be a PV. Events must pass an electron or muon trigger and contain a pair of SFOC leptons that satisfy the criteria listed in Table 4.4. A requirement of $E_T^{\text{miss}} > 40$ GeV is applied and at least one DV must be reconstructed in the MS barrel region defined by $|\eta| < 0.7$ and 3 m $< L_{xy} <$ 8 m, or the endcap region defined by $1.3 < |\eta| < 2.5$, 5 m $< L_z <$ 15 m, and $L_{xy} <$ 10 m. The number of MDT hits n_{MDT} associated with a DV is required to be > 300 to reject backgrounds from SM hadrons that generally produce fewer MDT hits than hadronic decays of long-lived ALPs, while a maximum threshold of $n_{\text{MDT}} < 3000$ is applied to reject background from coherent noise bursts in the MDT chambers [35]. DVs are required to be isolated from jets and high-p_T (> 5 GeV) tracks by a minimum angular separation $\Delta R_{min} > 0.1$. In addition, the vector p_T sum of low-p_T (< 5 GeV) tracks within $\Delta R < 0.2$ of the DV must be below 5 GeV. In the case that multiple DVs are reconstructed in the MS fiducial volume, the above selections are applied to all DVs in the event and events are chosen if exactly one DV passes. This is done to reduce loss of signal events that contain concurrent background activity. The final signal/background discrimination of the single DV that passes all previous selections is performed by the two NNs described in Section 4.2.2. The SR is defined by NN1 > 0.2 and NN2 > 0.1 in both the barrel and endcap regions.

The cumulative efficiency of the selection criteria is displayed graphically for each m_a in Figure 4.19, while Figure 4.20 shows the lepton-triggered channel signal efficiency as a function of L_{xy} (L_z) in the barrel (endcap). In general, the signal selection efficiency increases with m_a. The efficiency is much lower for lighter ALPs, especially at larger decay lengths. This is primarily due to the dependence of the DV reconstruction efficiency on m_a. Light ALPs that decay in the MS are very boosted – as shown in Figures 4.3-4.5 – and generally decay into highly collimated, low multiplicity hadronic showers, typically producing hits in a very narrow region of the MS that may not produce enough tracklets to reconstruct a DV. On the other hand, the heavier ALPs are generally less boosted and decay into higher multiplicity, broader showers that create more activity in the MS and are therefore more easily reconstructed as DVs.

Selection	m_a [GeV]			
	0.1	1	10	40
All Events	198999	199998	200000	200000
Event passes event cleaning criteria	198999	199998	200000	200000
Event passes lepton trigger	152388	153504	155155	161472
Event has 1 Z boson candidate	91221	91891	94109	99701
Lepton trigger matching	87643	88279	90519	96146
60 GeV $< m_Z <$ 120 GeV	86220	86829	89107	95118
$E_T^{\text{miss}} >$ 40 GeV	44684	45529	48381	46930
Event has at least 1 DV in MS	2138	2943	6394	7283
$300 < n_{\text{MDT}} < 3000$	2138	2943	6394	7283
DV is in barrel/endcap fiducial volume	1591	2254	4680	5408
ΔR_{min}(DV, jet/high-p_T track) > 0.1	1468	2071	4411	5028
$\sum_{\text{low-}p_T \text{ tracks}} \vec{p}_T <$ 5 GeV	1463	2065	4404	5024
Exactly 1 DV passes above selection	1463	2064	4402	5018
NN1 > 0.2	1310	1851	4019	4556
NN2 > 0.1	1104	1570	3557	4333

Table 4.9.: The selection criteria for the lepton-triggered channel and the cumulative number of generated Z+ALP MC events that pass each successive selection.

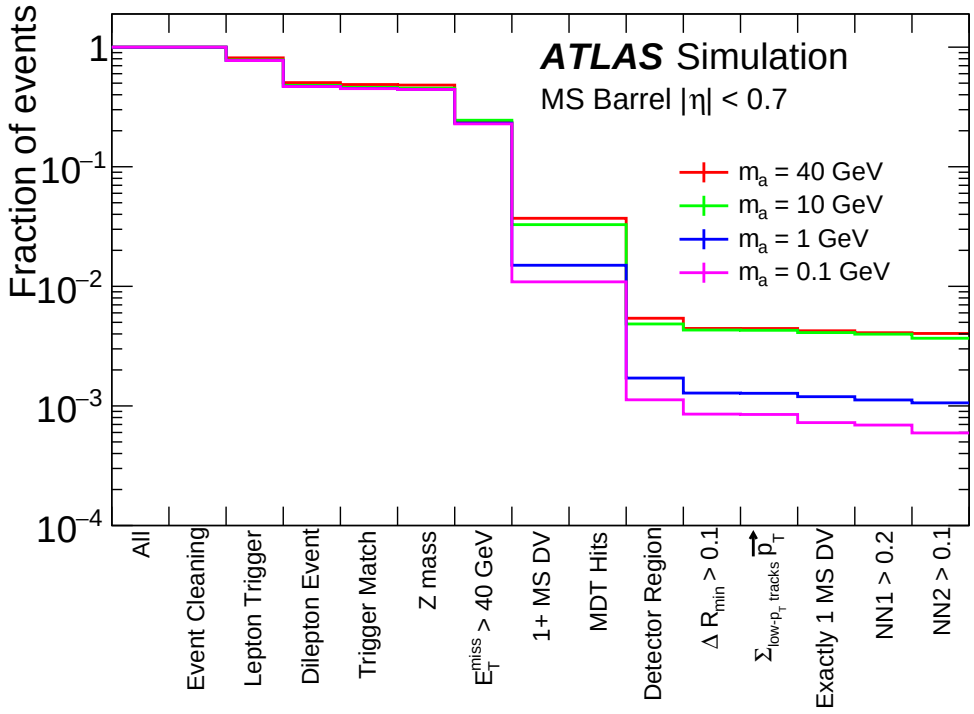

(a)

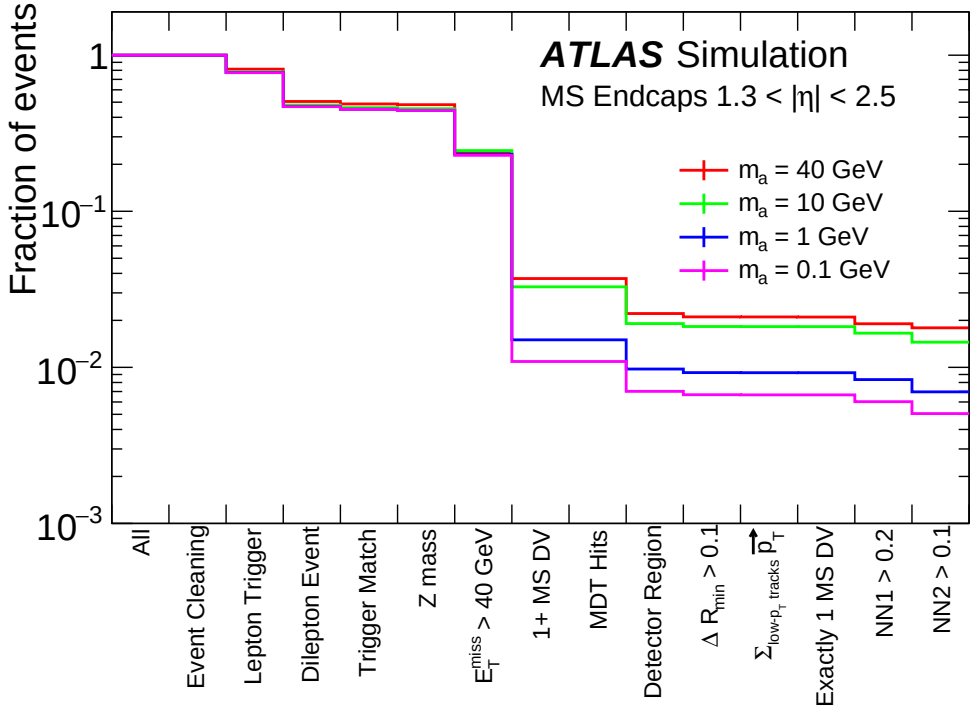

(b)

Figure 4.19.: The fraction of generated Z+ALP samples that pass each successive selection in the (a) barrel and (b) endcap regions of the lepton-triggered channel.

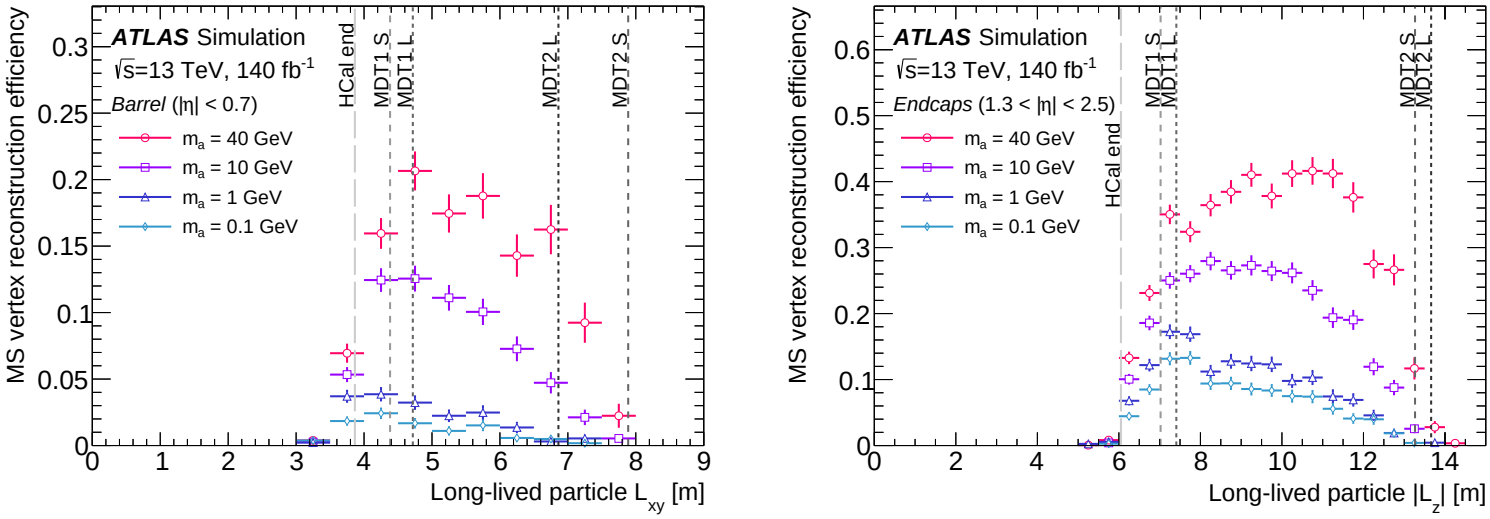

(a) **(b)**

Figure 4.20.: Efficiency to reconstruct an MS DV for ALP samples with vertices that satisfy the full event selection defined in Table 4.9. (a): efficiency to reconstruct a barrel MS DV as a function of the transverse decay position of the LLP. (b): efficiency to reconstruct an endcap MS DV as a function of the longitudinal decay position of the LLP relative to the center of the detector.

Table 4.10 compares the overall efficiency ϵ_a^{lep} of the finalised lepton-triggered channel selection to the efficiency ϵ_a^{RoI} of the RoI-triggered channel selection for each m_a. The lepton-triggered channel is significantly more efficient, with ϵ_a^{lep} being 4-8 times higher than ϵ_a^{RoI} depending on m_a.

m_a [GeV]	ϵ_a^{RoI}	ϵ_a^{lep}	$\epsilon_a^{\text{lep}}/\epsilon_a^{\text{RoI}}$
40	0.0053	0.0217	4.1
10	0.0026	0.0178	6.8
1	0.0010	0.0079	7.9
0.1	0.0008	0.0056	7.0

Table 4.10.: The efficiency of the lepton-triggered channel selection for each of the generated ALP samples, denoted by ϵ_a^{lep}. The ratio of ϵ_a^{lep} to the RoI-triggered channel efficiency ϵ_a^{RoI} is also shown.

To study the precision of the MS DV reconstruction algorithm, residuals $\sigma_x = x_{\text{reco}} - x_{\text{truth}}$ are calculated for the variables $x = \{\eta, \phi, L_{xy}, L_z\}$, where x_{reco} and x_{truth} are respectively the positions of the reconstructed DV and the truth LLP decay in the variable x. L_{xy} and L_z are the transverse and longitudunal components of the truth LLP decay length and are compared to the reconstructed DV R- and z-coordinates. Simulated ALPs are required to decay in the MS barrel or endcap volume within $\Delta R = 0.4$ of a reconstructed DV and pass all non-NN selections listed in Table 4.9. Different distributions are observed in the barrel and endcap residuals shown in Figures 4.21 and 4.22, respectively. This is expected as different DV reconstruction algorithms are employed in the barrel and endcap. The largest difference is the endcap σ_{L_z} distribution, which features a double-peak structure around 0 m that is not present in any barrel residuals and is more pronounced for lighter m_a. This feature is expected in the DV reconstruction [56]: after an LLP decays into numerous charged tracks, the magnetic field in the endcap toroid bends the charged tracks. As endcap tracklets are measured after the magnetic field and extrapolated back through the magnetic field to the IP as straight lines, the DV position in z is systematically shifted with respect to the truth decay position. In addition, Figures 4.4 and 4.5 show that ALPs that decay in the endcap region tend to be more boosted than ALPs that decay in the barrel. The highly collimated decays of boosted ALPs produce few tracklets in a narrow region of the MS, making DV-finding less precise and resulting in further systematic shift in the DV z-coordinate. Table 4.11 lists the DV reconstruction resolutions for each m_a, calculated as the root-mean-square of the normalised residual distributions $\sigma_x / x_{\text{truth}}$.

Region	m_a [GeV]	η	ϕ	L_{xy}	L_z
Barrel	40	0.09	0.093	0.28	0.45
	10	0.07	0.094	0.27	0.39
	1	0.062	0.1	0.33	0.56
	0.1	0.071	0.088	0.31	0.41
Endcap	40	0.041	0.09	0.33	0.28
	10	0.035	0.08	0.29	0.26
	1	0.034	0.086	0.3	0.27
	0.1	0.034	0.082	0.28	0.26

Table 4.11.: Summary of MS DV reconstruction resolutions in η, ϕ, L_{xy}, and L_z for ALPs with masses $m_a = \{0.1, 1, 10, 40\}$ GeV that decay in the MS barrel and endcap regions.

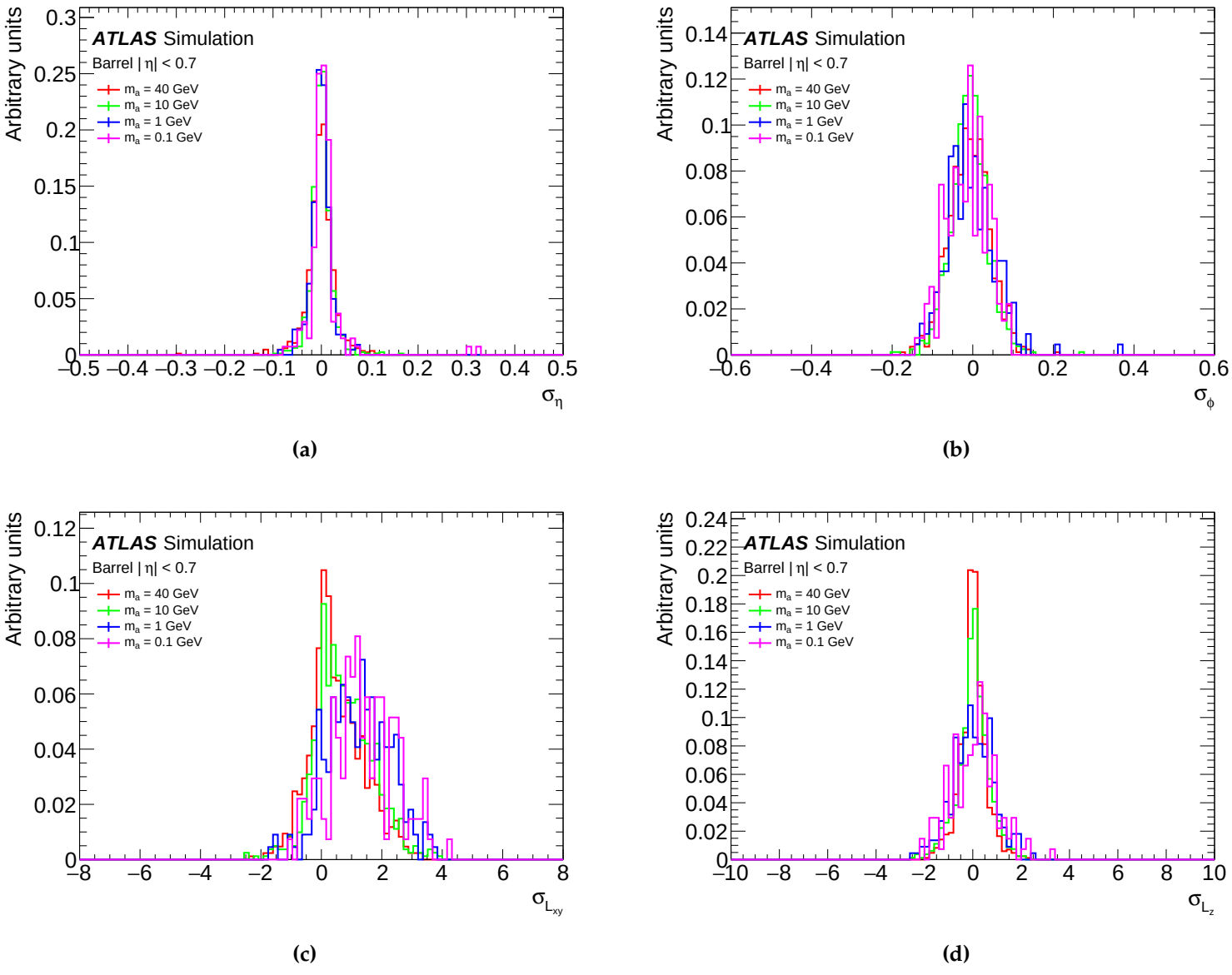

Figure 4.21.: Residuals σ in the (a) η, (b) ϕ, (c) L_{xy}, and (d) L_z coordinates for decays of ALPs with masses $m_a = \{0.1, 1, 10, 40\}$ GeV in the MS barrel region.

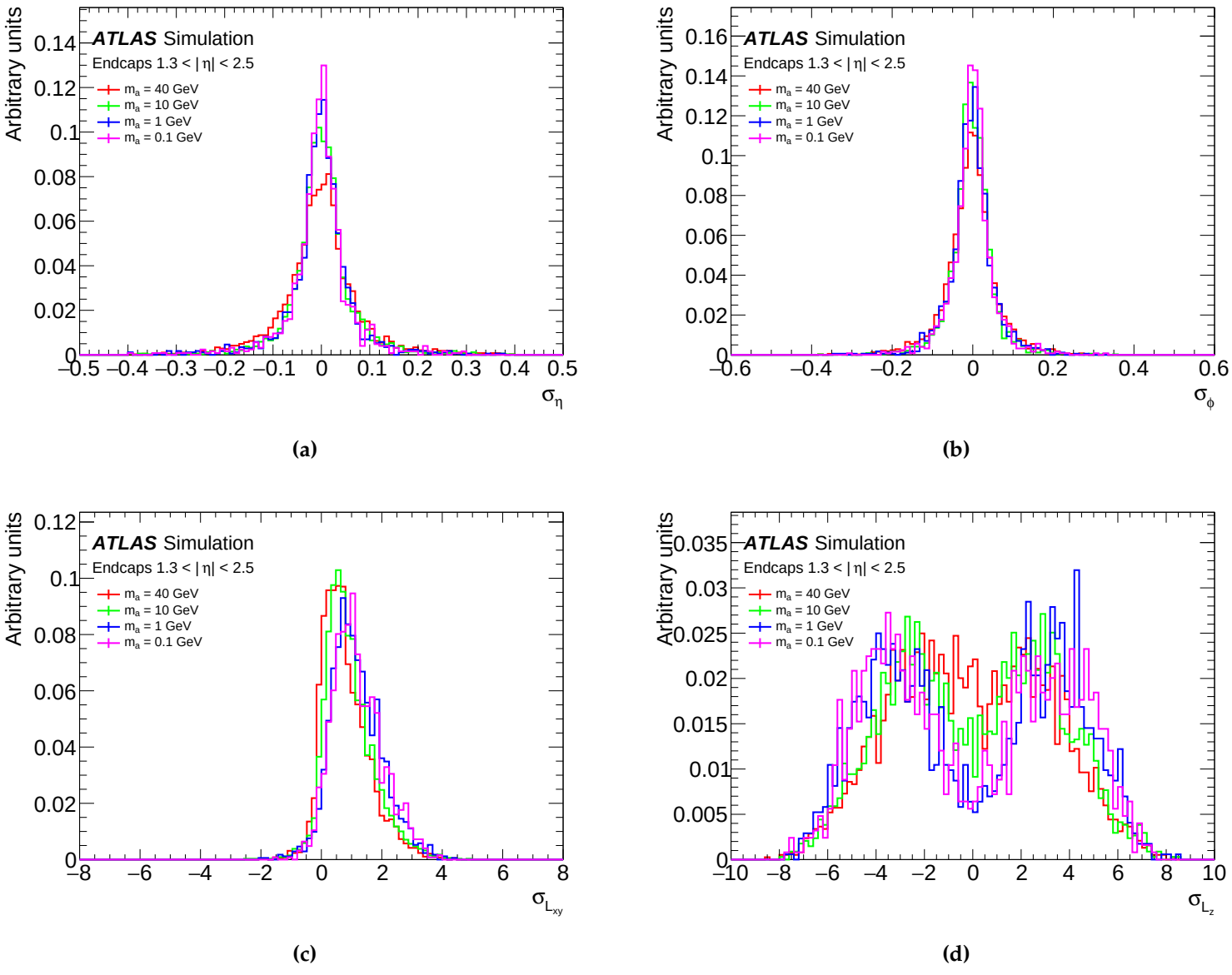

Figure 4.22.: Residuals σ in the (a) η, (b) ϕ, (c) L_{xy}, and (d) L_z coordinates for decays of ALPs with masses $m_a = \{0.1, 1, 10, 40\}$ GeV in the MS endcap region.

4.3. Background estimation

Sources of background that affect searches for DVs in the MS include jets that penetrate the calorimeter material into the MS, as well as non-collision backgrounds such as beam-induced sources (e.g. beam halo muons) and cosmic rays. The requirement of a Z boson in addition to a DV suppresses all backgrounds. In particular, the studies in Section 4.2.3.3 showed that the requirement of a Z boson renders non-collision backgrounds neglible. The primary residual background comes from jets produced in association with a Z boson that punch through the calorimeter into the MS and create a reconstructed DV. MS DVs produced by punch-through jets are not well modelled in simulations. Therefore, a fully data-driven background estimation method is utilised.

An ABCD plane is constructed using the two NNs described in Section 4.2.2. Events entering the plane are required to pass all other selections defined in Table 4.9. In order to validate that an ABCD method will correctly predict the background, it is necessary to identify a *validation region* (VR) to verify that the expected number of events $N_{\mathrm{A}}^{\mathrm{Expected}}$ in the SR is consistent with the observed number of events $N_{\mathrm{A}}^{\mathrm{Observed}}$ before the SR is unblinded. A VR is developed by identifying event-level criteria that select a subset of events close to the signal region in characteristics, but not overlapping or containing a potentially significant fraction of signal. The methodology of the ABCD method is already validated for the RoI-triggered channel described in Section 3.4 and the conclusions of that validation are expected to also apply to this search. However, the method may have some residual dependencies on the muon RoI cluster trigger, hence its validity in the lepton-triggered channel is tested explicitly in dedicated VRs.

4.3.1. $E_{\mathrm{T}}^{\mathrm{miss}}$ validation region

To validate the ABCD method, a VR is created by inverting the $E_{\mathrm{T}}^{\mathrm{miss}}$ selection to < 40 GeV. Additionally, since one of the NN inputs is $\Delta\phi(\mathrm{DV}, E_{\mathrm{T}}^{\mathrm{miss}})$, it is necessary to set a minimum requirement of $E_{\mathrm{T}}^{\mathrm{miss}} > 10$ GeV to ensure the NN functions correctly. This VR is hence referred to as the $E_{\mathrm{T}}^{\mathrm{miss}}$ VR. All other selections defined in Table 4.9 are applied to events in the $E_{\mathrm{T}}^{\mathrm{miss}}$ VR.

In initial studies, the minimum ΔR_{min} requirement was set to 0.4 as Figure 4.13 showed this value is a powerful discriminant between signal and background. However, the ABCD method was found to be non-predictive in the barrel region of the $E_{\mathrm{T}}^{\mathrm{miss}}$

VR when $\Delta R_{min} > 0.4$. This was due to a lack of events in region D. Therefore, the ΔR_{min} threshold is lowered to populate the ABCD plane with additional background from punch-through jets, thus allowing $N_{\mathrm{A}}^{\mathrm{Expected}}$ to be calculated. Several ΔR_{min} thresholds are studied, ranging from 0 to 0.4 in intervals of 0.05. The finalised ΔR_{min} selection used in the SR is required to yield a value of $N_{\mathrm{A}}^{\mathrm{Expected}}$ that is consistent with $N_{\mathrm{A}}^{\mathrm{Observed}}$ in the $E_{\mathrm{T}}^{\mathrm{miss}}$ VR. Figure 4.23 illustrates the closure between $N_{\mathrm{A}}^{\mathrm{Expected}}$ and $N_{\mathrm{A}}^{\mathrm{Observed}}$ for each ΔR_{min} threshold. In the barrel $E_{\mathrm{T}}^{\mathrm{miss}}$ VR, there are no events in region D that satisfy the requirement of $\Delta R_{min} > 0.2$. Thus, the ABCD plane is non-predictive and cannot be validated above $\Delta R_{min} > 0.15$. There is closure for all other values of ΔR_{min} in the barrel region and closure in the endcap VR for $\Delta R_{min} > 0.05$ and above. The final selection of $\Delta R_{min} > 0.1$ is hence applied in both the barrel and endcap regions to ensure the ABCD planes are sufficiently populated to be predictive.

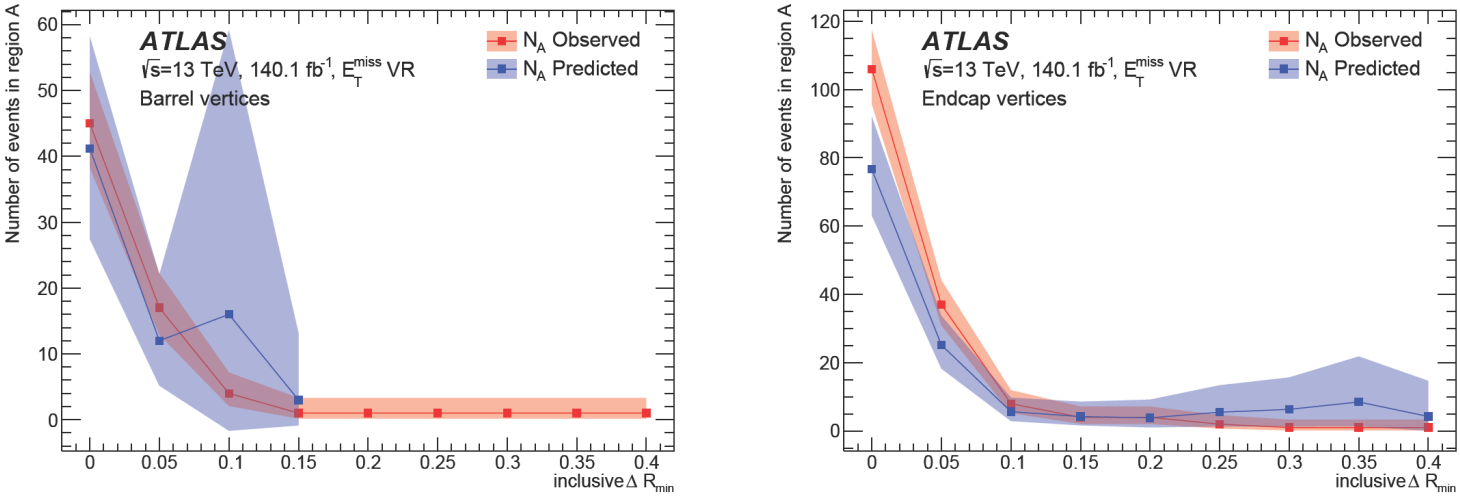

(a) **(b)**

Figure 4.23.: The inclusive observed (red) and predicted (blue) number of events in region A of the $E_{\mathrm{T}}^{\mathrm{miss}}$ validation region in the (a) barrel and (b) endcap, as a function of ΔR_{min}. The 68.3% Poisson confidence intervals are shown as shaded bands.

Figure 4.24 shows the ABCD planes for the $E_{\mathrm{T}}^{\mathrm{miss}}$ VR with the finalised requirement of $\Delta R_{min} > 0.1$, while Table 4.12 summarises the number of events in each region and the predicted number of events in region A, as well as their statistical uncertainties. In both the barrel and endcap regions, $N_{\mathrm{A}}^{\mathrm{Observed}}$ is consistent with $N_{\mathrm{A}}^{\mathrm{Expected}}$ within the statistical uncertainties, which are relatively large due to the low number of events, particularly in the barrel region.

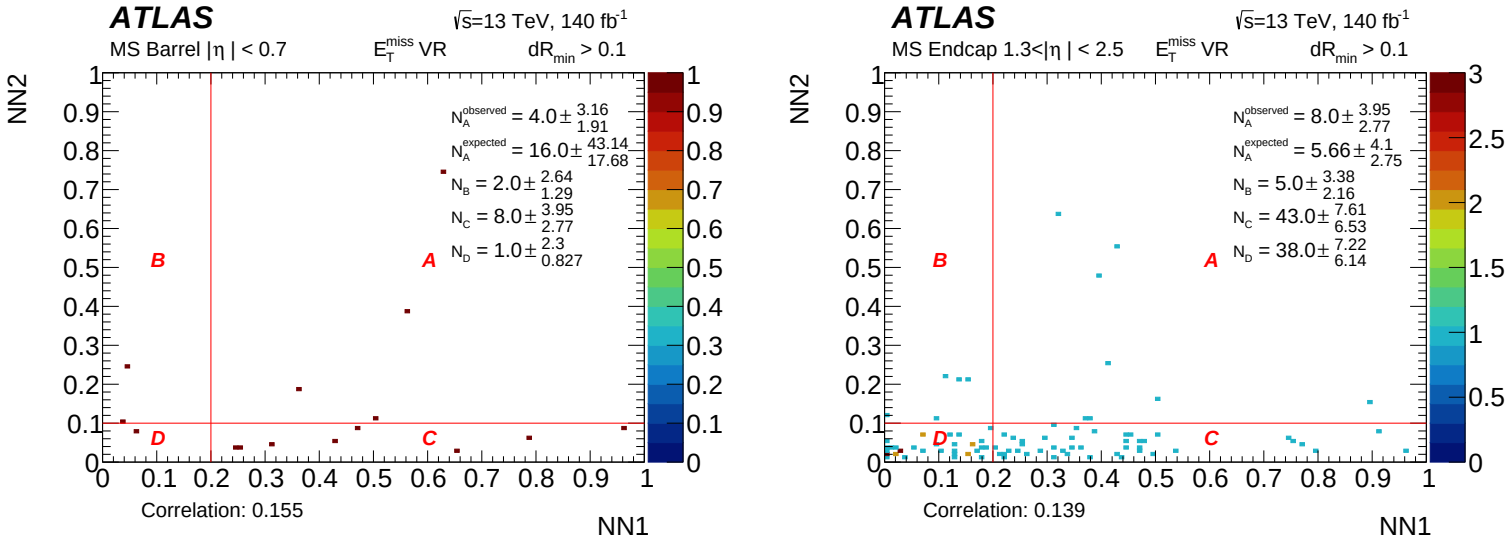

(a) (b)

Figure 4.24.: The (a) barrel and (b) endcap ABCD planes for the $E_{\mathrm{T}}^{\mathrm{miss}}$ validation region. The observed (red) number of events in each region and the predicted (blue) number in region A are shown with their 68.3% Poisson confidence intervals.

Region	$N_{\mathrm{A}}^{\mathrm{Observed}}$	$N_{\mathrm{A}}^{\mathrm{Expected}}$	N_{B}	N_{C}	N_{D}
Barrel	4	$16 \pm \frac{43}{18}$ (stat.)	2	8	1
Endcap	8	$6 \pm \frac{4}{3}$ (stat.)	5	43	38

Table 4.12.: Event counts in each of the four regions of the $E_{\mathrm{T}}^{\mathrm{miss}}$ VR ABCD plane. The predicted number of events in region A is within one standard deviation of the observed number of events in both the barrel and endcap regions.

The presence of signal in a VR can result in non-closure between $N_{\mathrm{A}}^{\mathrm{Expected}}$ and $N_{\mathrm{A}}^{\mathrm{Observed}}$. Table 4.13 shows the number of ALP signal events N^S expected to enter the $E_{\mathrm{T}}^{\mathrm{miss}}$ VR ABCD plane, estimated as $N^S = 140\ \mathrm{fb}^{-1} \times \sigma_{\mathrm{Gen}} \times N_{\mathrm{ABCD}}/N_{\mathrm{Gen}}$, where σ_{Gen} and N_{Gen} are respectively the generated ALP cross-section and number of events given in Table 4.3 for the corresponding m_a. N_{ABCD} is the number of ALP MC events that enter the $E_{\mathrm{T}}^{\mathrm{miss}}$ VR ABCD plane. Also shown are the number of observed data events N^B in the ABCD plane and the ratio N^S/N^B. Several ΔR_{min} thresholds ranging from 0 to 0.4 in intervals of 0.05 are studied. For all values of ΔR_{min}, the expected Z+ALP signal contamination is negligible.

		Barrel			Endcap		
ΔR_{min}	m_a [GeV]	N^S	N^B	N^S/N^B	N^S	N^B	N^S/N^B
0.0	0.1	0.036	151	0.000238	0.275	649	0.000424
	1	0.0443		0.000293	0.328		0.000505
	10	0.132		0.000874	0.828		0.00128
	40	0.0907		0.000601	0.41		0.000632
0.05	0.1	0.0311	56	0.000555	0.262	247	0.00106
	1	0.0344		0.000614	0.288		0.00117
	10	0.0984		0.00176	0.74		0.003
	40	0.0533		0.000952	0.34		0.00138
0.1	0.1	0.013	15	0.000867	0.238	94	0.00253
	1	0.00592		0.000395	0.248		0.00264
	10	0.0604		0.00403	0.634		0.00674
	40	0.0198		0.00132	0.239		0.00254
0.15	0.1	0.0107	6	0.00178	0.221	60	0.00368
	1	0.00314		0.000523	0.224		0.00373
	10	0.0439		0.00732	0.573		0.00955
	40	0.00968		0.00161	0.153		0.00255
0.2	0.1	0.00926	2	0.00463	0.215	44	0.00489
	1	0.00314		0.00157	0.209		0.00475
	10	0.0419		0.0209	0.544		0.0124
	40	0.00304		0.00152	0.117		0.00266
0.25	0.1	0.00926	2	0.00463	0.209	34	0.00615
	1	0.00314		0.00157	0.205		0.00603
	10	0.0419		0.0209	0.532		0.0156
	40	0.0		0.0	0.0949		0.00279
0.3	0.1	0.00926	2	0.00463	0.204	28	0.00729
	1	0.00314		0.00157	0.203		0.00725
	10	0.0419		0.0209	0.525		0.0187
	40	0.0		0.0	0.0866		0.00309
0.35	0.1	0.00687	2	0.00344	0.204	24	0.0085
	1	0.00314		0.00157	0.199		0.00829
	10	0.0419		0.0209	0.509		0.0212
	40	0.0		0.0	0.0782		0.00326
0.4	0.1	0.00459	2	0.0023	0.198	23	0.00861
	1	0.00314		0.00157	0.194		0.00843
	10	0.0419		0.0209	0.509		0.0221
	40	0.0		0.0	0.0737		0.0032

Table 4.13.: Z+ALP signal contamination in the $E_{\mathrm{T}}^{\mathrm{miss}}$ VR ABCD plane as a function of ΔR_{min}.

To check for systematic trends in the ABCD method, $N_{\mathrm{A}}^{\mathrm{Expected}}$ and $N_{\mathrm{A}}^{\mathrm{Observed}}$ are determined in exclusive bins of ΔR_{min}, as shown in Figure 4.25. The binning is such that the first bin is defined by $0 < \Delta R_{min} < 0.05$, the second bin is defined by $0.05 < \Delta R_{min} < 0.1$, and so on. The final bin is inclusive of DVs with $\Delta R_{min} > 0.4$. Some bins do not have values of $N_{\mathrm{A}}^{\mathrm{Expected}}$ plotted because there are no events that meet the ΔR_{min} requirements in region D, thus the ABCD method is not predictive. For all intervals ΔR_{min} that are predictive, $N_{\mathrm{A}}^{\mathrm{Observed}}$ is consistent with $N_{\mathrm{A}}^{\mathrm{Expected}}$ within the uncertainties and no systematic under- or overestimation is observed. Therefore, since the statistical uncertainties are so large, the systematic uncertainty related to the ABCD method is considered to be negligible.

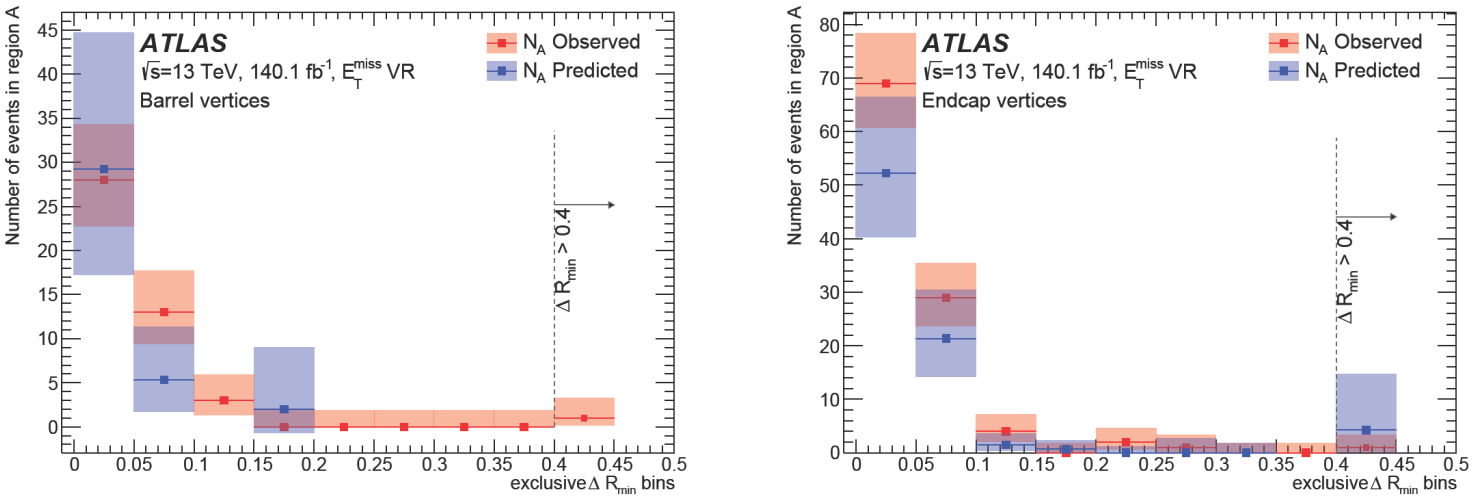

(a) **(b)**

Figure 4.25.: The predicted and observed number of events in region A of the $E_{\mathrm{T}}^{\mathrm{miss}}$ validation region in the (a) barrel and (b) endcap, binned in ΔR_{min}. The 68.3% Poisson confidence intervals are shown as shaded bands.

4.3.2. Photon validation region

A second VR is utilised to cross-check the $E_{\mathrm{T}}^{\mathrm{miss}}$ VR. Since the ALPs in the model considered do not couple to photons, the second VR targets events containing a DV and a photon with the aim of producing a VR devoid of any signal contamination. The DVs in this VR are created by jets produced in association with a photon via SM processes. Hence, this VR is referred to as the γ+jets VR. The γ+jets VR studies were conducted by Julian Wack and are summarised below. Additional details are given in Appendix D.

Photons used in the γ+jets VR are defined by criteria detailed in Table D.2 and are required to fire at least one of the photon triggers listed in Table D.1. Additionally, since γ+jets processes do not generally produce a large $E_{\mathrm{T}}^{\mathrm{miss}}$, the minimum $E_{\mathrm{T}}^{\mathrm{miss}}$ requirement is loosened to 10 GeV to increase the number of events entering the ABCD plane. All remaining SR selections are applied, as listed in Table 4.14.

Selection
Event passes event cleaning criteria
Event passes photon trigger
Event containts at least one photon
Photon trigger matching
$E_{\mathrm{T}}^{\mathrm{miss}} > 10$ GeV
Event has at least 1 DV in MS
$300 < n_{\mathrm{MDT}} < 3000$
DV is in barrel/endcap fiducial volume
ΔR_{min}(DV, jet/high-p_T track) > 0.1
$\sum_{\text{low-}p_T \text{ tracks}} \vec{p}_T < 5$ GeV
Exactly 1 DV passes above selection
NN1 > 0.2
NN2 > 0.1

Table 4.14.: The selection criteria for the γ+jets validation region.

Z+ALP signal events may enter the γ+jets VR if an electron produced in the decay of the associated Z boson is misreconstructed as a photon. The γ+jets VR is also susceptible to contamination from W+ALP signal [38], which is predicted by the same

ALP effective field theory as Z+ALP. Following the same method as the $E_{\mathrm{T}}^{\mathrm{miss}}$ VR, the Z/W+ALP signal contamination in the γ+jets VR is found to be negligible.

Table 4.15 lists the number of events in each region of the ABCD plane $N_{\mathrm{A/B/C/D}}$ and the expected number of events $N_{\mathrm{A}}^{\mathrm{Expected}}$ in region A. In both the barrel and endcap regions, $N_{\mathrm{A}}^{\mathrm{Observed}}$ is consistent with $N_{\mathrm{A}}^{\mathrm{Expected}}$ within the statisitical uncertainties.

Region	$N_{\mathrm{A}}^{\mathrm{Observed}}$	$N_{\mathrm{A}}^{\mathrm{Expected}}$	N_{B}	N_{C}	N_{D}
Barrel	1	$3 \pm \frac{7}{3}$ (stat.)	18	1	6
Endcap	57	$44 \pm \frac{13}{11}$ (stat.)	30	82	56

Table 4.15.: Event counts in each region of the γ+jets VR ABCD plane. The predicted number of events in region A is consistent with the observed number of events in the both the barrel and endcap regions.

The ABCD method was again tested for systematic trends using the same method as the $E_{\mathrm{T}}^{\mathrm{miss}}$ VR. Figure 4.26 shows $N_{\mathrm{A}}^{\mathrm{Expected}}$ and $N_{\mathrm{A}}^{\mathrm{Observed}}$ binned exclusively in ΔR_{min}. There is closure for all points where the ABCD method is predictive and no systematic trends are observed.

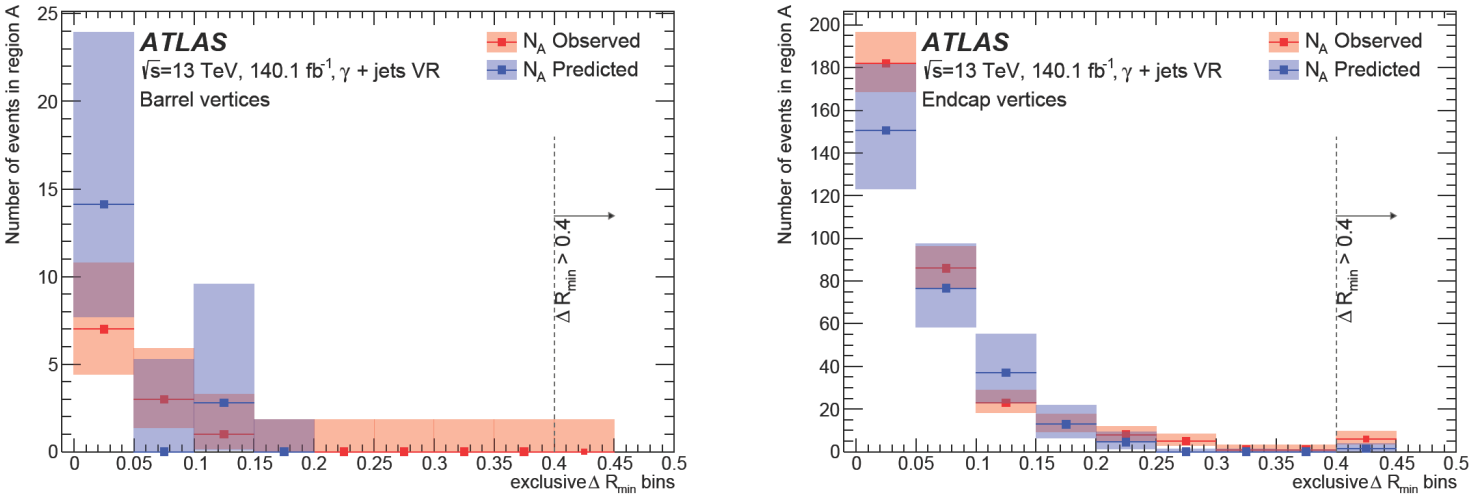

(a) **(b)**

Figure 4.26.: The observed (red) and predicted (blue) number of events in region A of the γ+jets validation region in the (a) barrel and (b) endcap, binned in ΔR_{min}. 68.3% Poisson confidence intervals are shown as shaded bands. Produced by Julian Wack.

4.3.3. Background estimation in the signal region

Figure 4.27 shows the SR ABCD planes and Table 4.16 summarises the number of events in each region and the predicted number of events in region A with its statistical uncertainty.

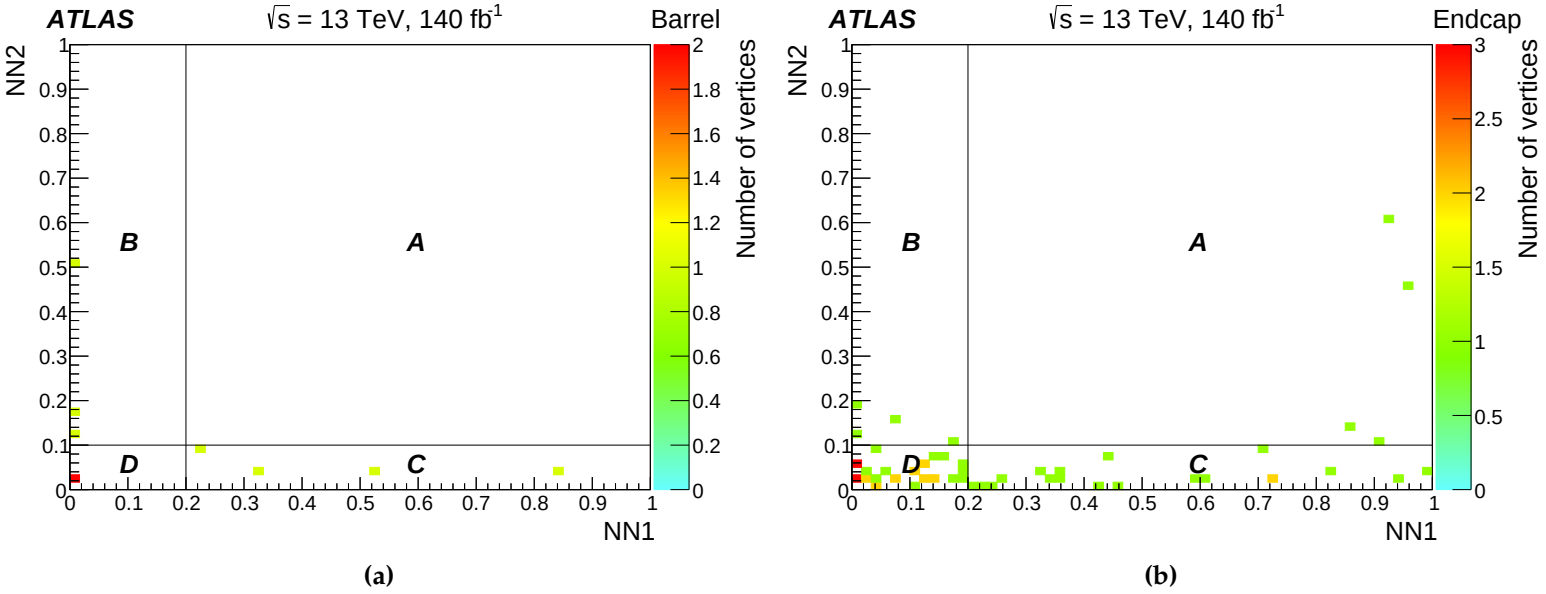

Figure 4.27.: ABCD planes for Run 2 data in (a) the barrel and (b) the endcap regions of the lepton-triggered channel.

Region	N_A^{Observed}	N_A^{Expected}	N_B	N_C	N_D
Barrel	0	$6 \pm {}^{11}_{6}$ (stat.)	3	4	2
Endcaps	4	$2 \pm {}^{2}_{1}$ (stat.)	4	19	31

Table 4.16.: Event counts in each of the four regions of the SR ABCD plane and the expected number in region A.

A 3-dimensional event display for one of the events observed in the SR is shown in Figure 4.28. 2-dimensional event displays are shown for all four events observed in the SR in Figures 4.29, 4.30, 4.31 and 4.32. The η, ϕ, R and z positions of the DV in each of the events are summarised in Table 4.17.

Figure	Run number	Event number	η_{DV}	ϕ_{DV}	R_{DV} [m]	z_{DV} [m]
4.28 & 4.29	302391	511952098	1.80	-2.95	3.42	10.0
4.30	304128	2157677754	1.87	0.383	3.16	10.0
4.31	327764	2556563021	1.48	0.855	5.55	11.5
4.32	337833	3021225742	-2.16	-0.409	3.24	-14.0

Table 4.17.: List of the run and event numbers of events in the 1DV+Z SR and the corresponding positions of the DVs in η, ϕ, R, z. The event displays for each event are also indicated.

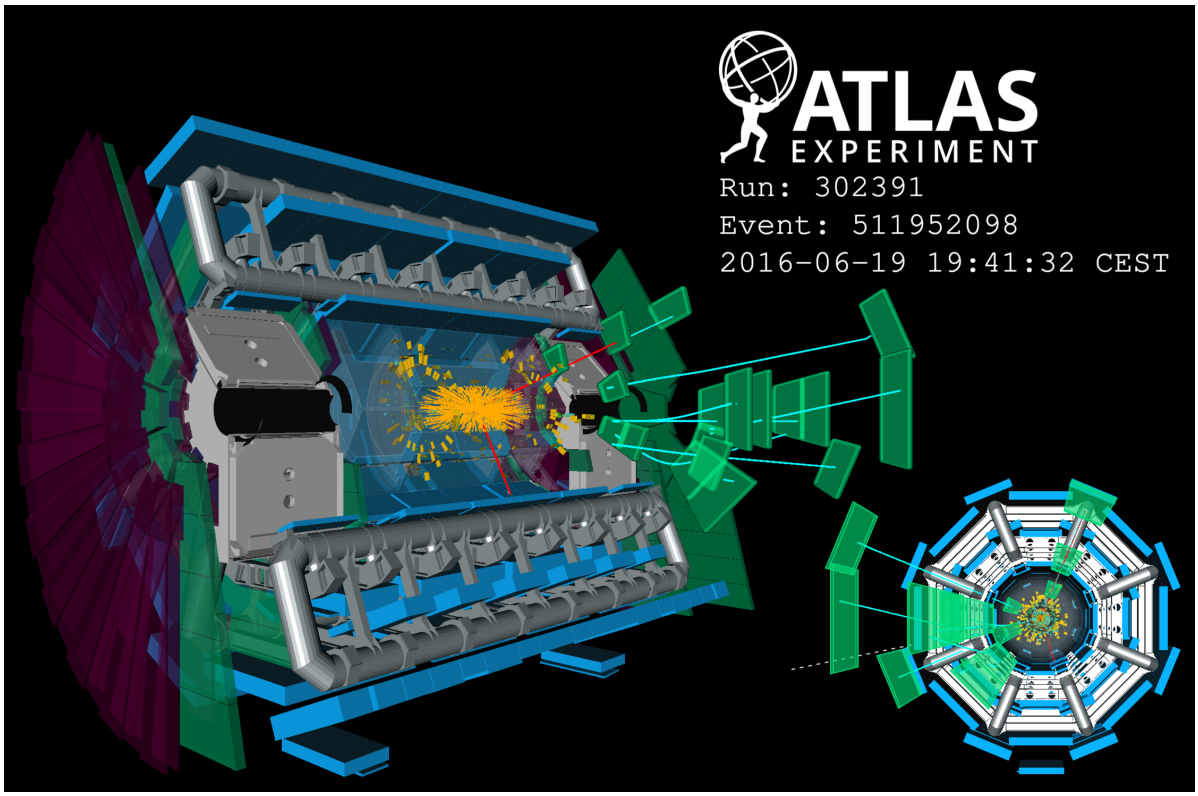

Figure 4.28.: Event display for an event in the signal region, recorded on 19th June, 2016. The red lines indicate combined MS tracks corresponding to prompt muons that are required to have $p_T > 10$ GeV. The blue lines are standalone tracks associated with the MS DV. The orange lines are ID tracks and the yellow blocks are energy deposits in calorimeter cells. The grey line in the cross-section view indicates the ϕ direction of the E_T^{miss}. The blue panels are MDT chambers in the barrel while the green and purple panels are the endcap MDT and TGC chambers, respectively.

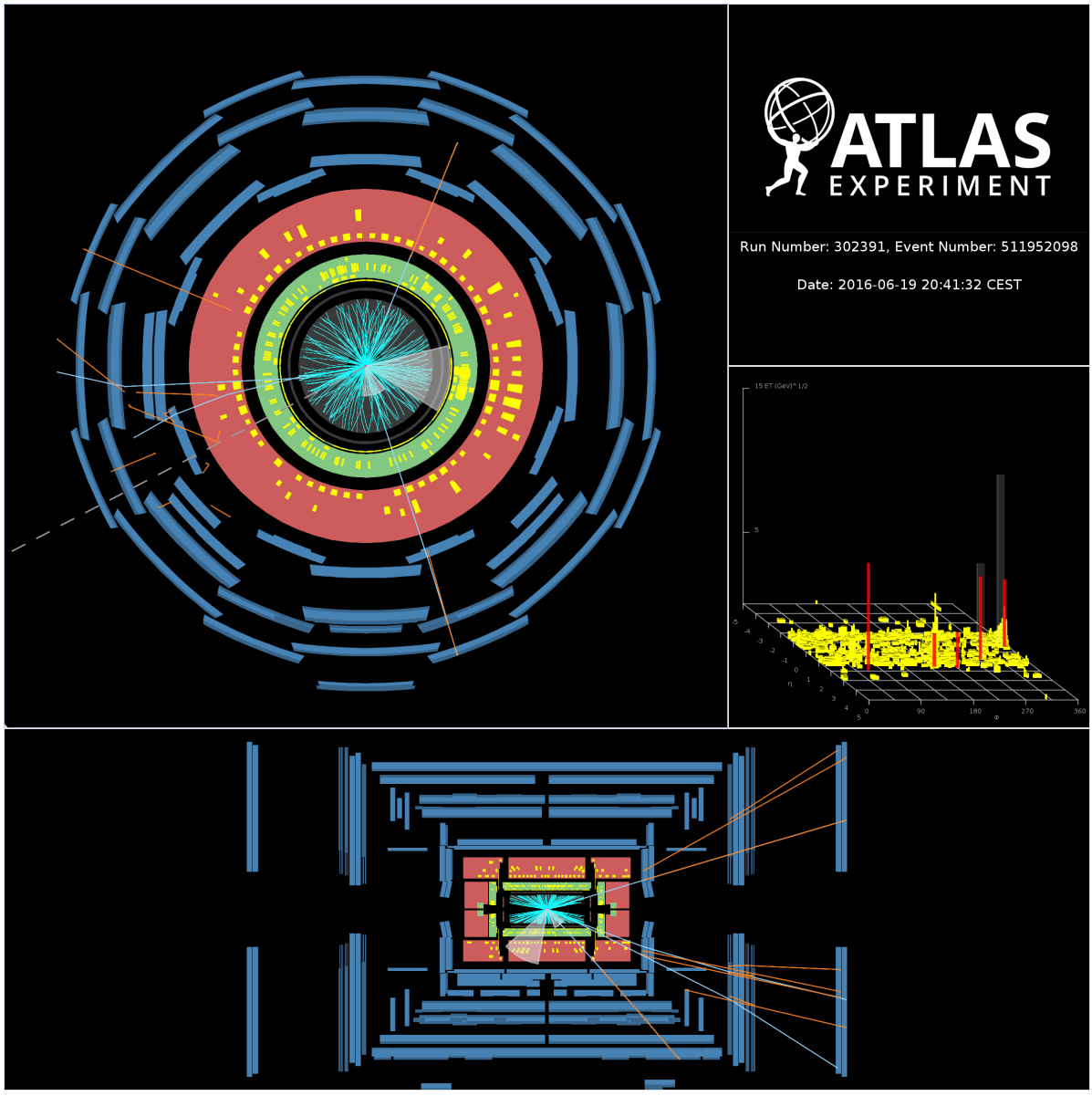

Figure 4.29.: Event display for an event in the signal region, recorded on 19th June, 2016. The blue lines indicate combined MS tracks corresponding to prompt muons. No p_T requirement is applied. The orange lines are standalone MS tracks. The cyan lines are ID tracks and the yellow blocks are energy deposits in calorimeter cells. The grey dashed line indicates the ϕ direction of the E_T^{miss}. Jets are indicated by shaded cones. The blue panels are MDT chambers while the green and red rings indicate the ECal and HCal, respectively.

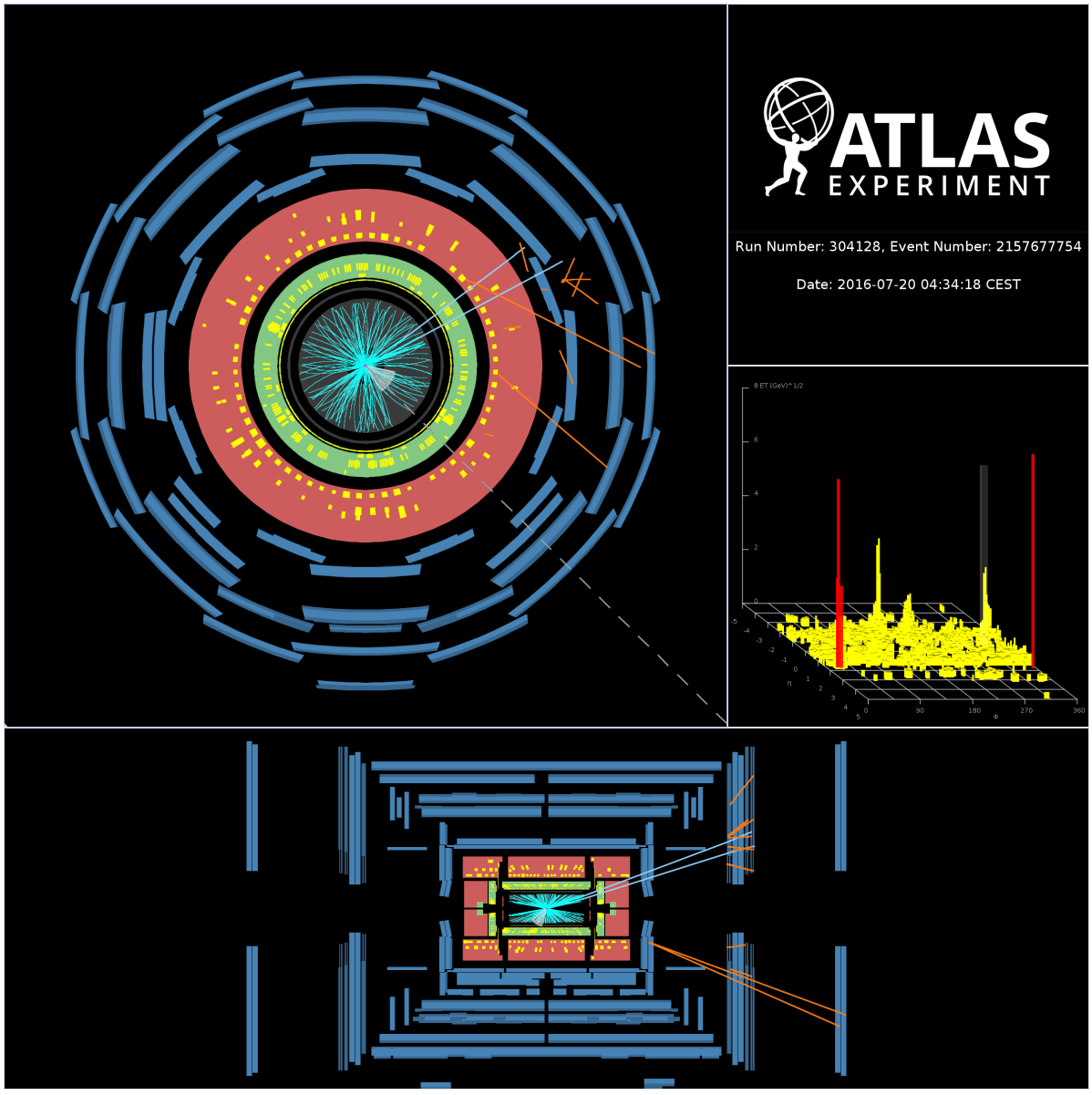

Figure 4.30.: Event display for an event in the signal region, recorded on 10th July, 2016. The blue lines indicate combined MS tracks corresponding to prompt muons. No p_T requirement is applied. The orange lines are standalone MS tracks. The cyan lines are ID tracks and the yellow blocks are energy deposits in calorimeter cells. The grey dashed line indicates the ϕ direction of the E_T^{miss}. Jets are indicated by shaded cones. The blue panels are MDT chambers while the green and red rings indicate the ECal and HCal, respectively.

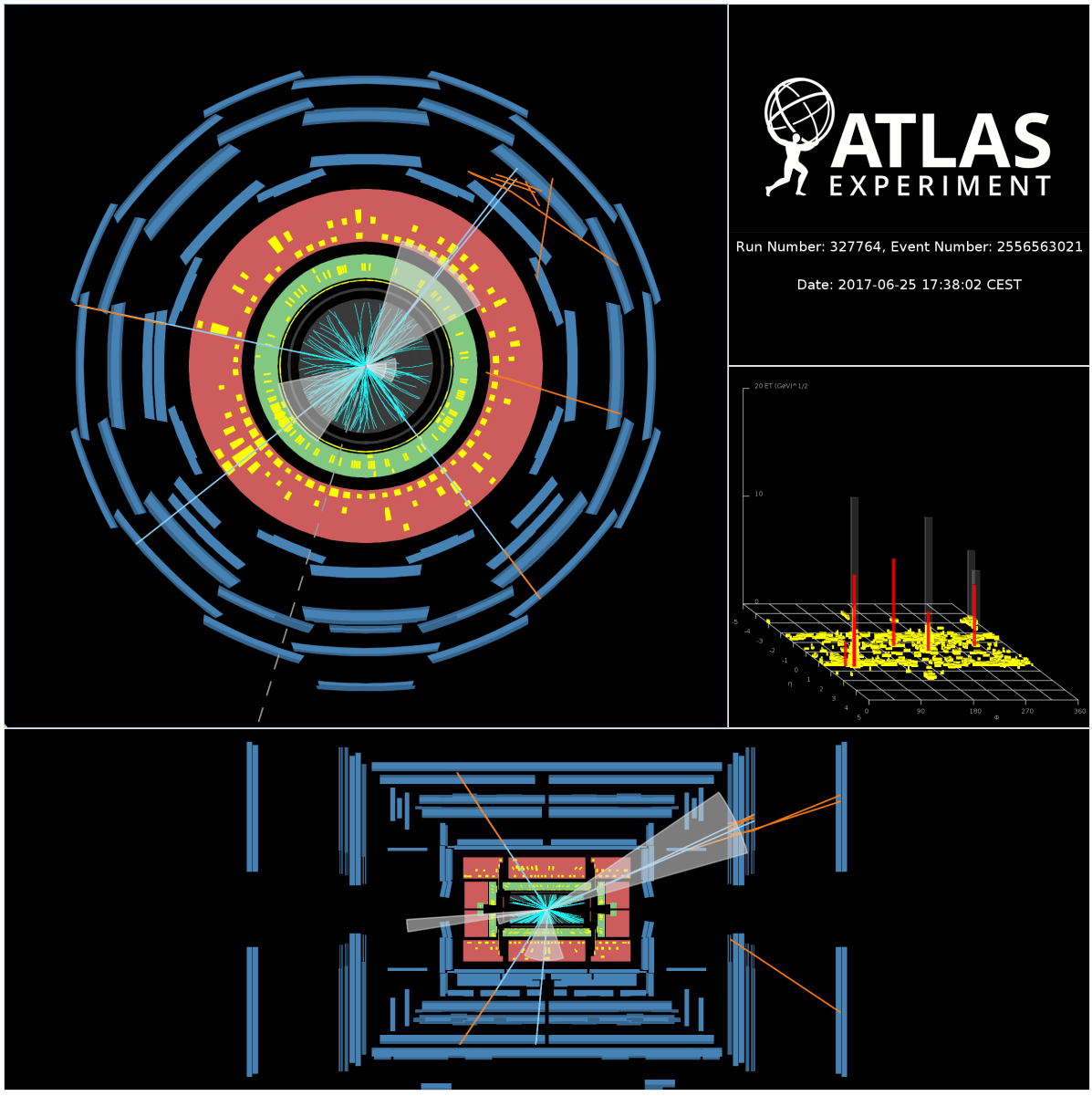

Figure 4.31.: Event display for an event in the signal region, recorded on 25th June, 2017. The blue lines indicate combined MS tracks corresponding to prompt muons. No p_T requirement is applied. The orange lines are standalone MS tracks. The cyan lines are ID tracks and the yellow blocks are energy deposits in calorimeter cells. The grey dashed line indicates the ϕ direction of the E_T^{miss}. Jets are indicated by shaded cones. The blue panels are MDT chambers while the green and red rings indicate the ECal and HCal, respectively.

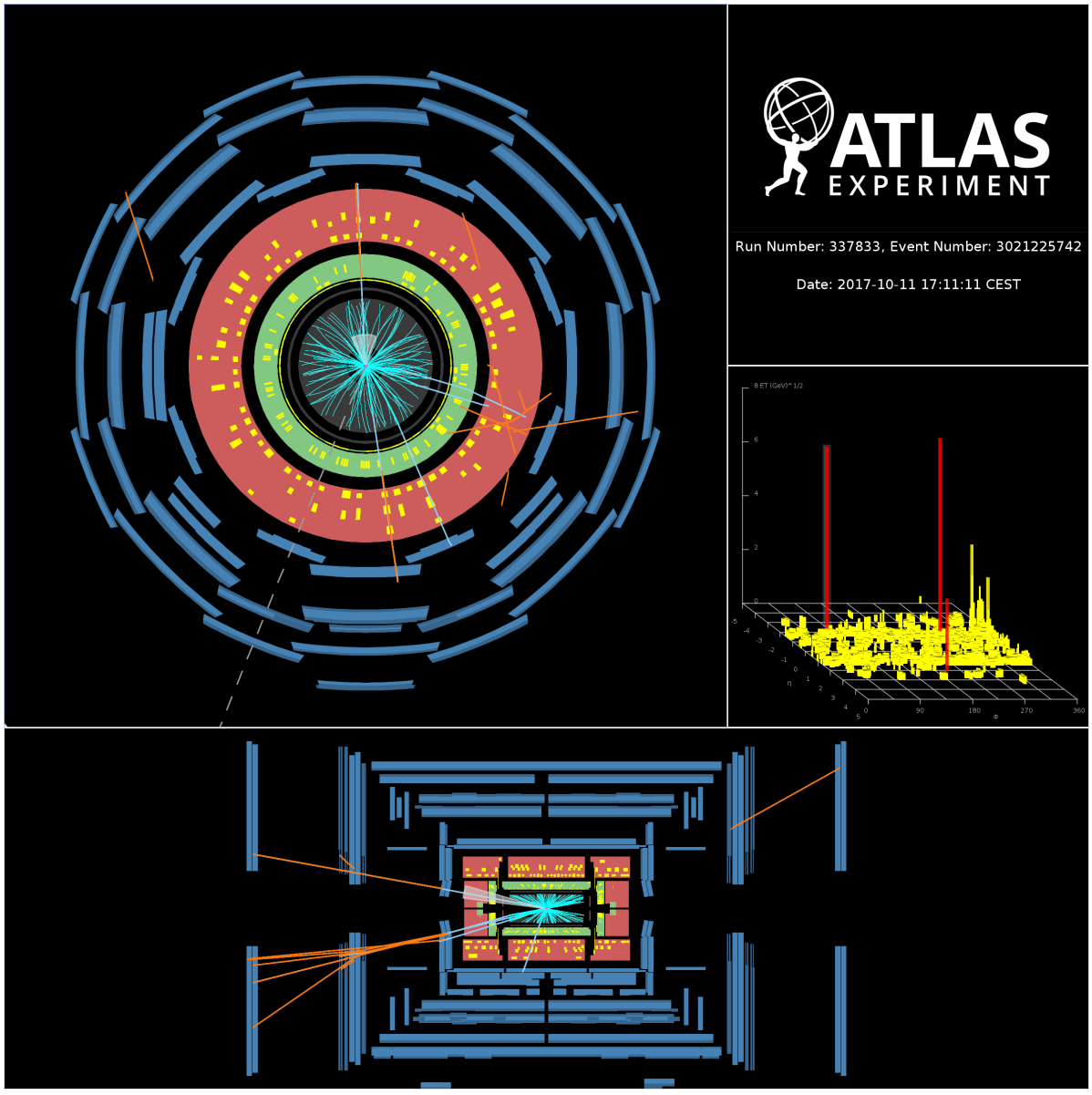

Figure 4.32.: Event display for an event in the signal region, recorded on 11th October, 2017. The blue lines indicate combined MS tracks corresponding to prompt muons. No p_T requirement is applied. The orange lines are standalone MS tracks. The cyan lines are ID tracks and the yellow blocks are energy deposits in calorimeter cells. The grey dashed line indicates the ϕ direction of the E_T^{miss}. Jets are indicated by shaded cones. The blue panels are MDT chambers while the green and red rings indicate the ECal and HCal, respectively.

4.4. Lifetime extrapolation

As this search is sensitive to a broad range of LLP proper decay lengths, generating a sufficient number of fully simulated MC samples with different mean LLP proper decay lengths to cover the entire sensitivity range would be computationally expensive. Therefore, the expected signal yields are extrapolated for mean proper decay lengths across the range 10^{-4} m $\leq c\tau \leq 10^{3}$ m using pseudo-experiments. This lifetime extrapolation procedure was carried out by Michael Revering and is summarised below.

The Z boson and DV reconstruction efficiencies are calculated separately for each of the fully-simulated MC samples and are used to determine if an LLP with an extrapolated lifetime would pass the analysis selections. In general, the DV reconstruction efficiency at a given detector location will differ between MC samples generated with different LLP mean proper lifetimes and mass as the different LLP kinematics will affect the reconstruction efficiency. Therefore, it is necessary to ensure the efficiencies are lifetime-independent by parameterising them as not only as functions of the lab-frame decay length L_{xy} (L_z) in the barrel (endcap) but also of the LLP β.

The Z boson selection includes the lepton trigger requirements. Hence, the combined trigger+Z efficiency $\epsilon_{\text{Trig+Z}}$ is defined as the fraction of MC events that pass a lepton trigger and contain a reconstructed Z boson at a given LLP decay length and β. This efficiency is expected to be approximately independent of the LLP decay position but is still paramerised by the lab-frame decay length and boost to account for the effect of the LLP kinematics on the Z boson p_T, which can affect $\epsilon_{\text{Trig+Z}}$. The DV reconstruction efficiency ϵ_{DV} is defined as the fraction of MC events passing the trigger+Z selection that also pass the full analysis selection at a given LLP decay length and β. Examples of distributions of $\epsilon_{\text{Trig+Z}}(L_{xy/z}, \beta)$ and $\epsilon_{\text{DV}}(L_{xy/z}, \beta)$ are shown in Figures 4.33 and 4.34.

The lifetime extrapolation procedure is outlined below. Events are rejected if they fail any requirements.

1. For each event in the pseudo-data, a new lab-frame decay length L is randomly generated for the LLP by sampling an exponential distribution $f(L) = \exp(-L/\beta\gamma c\tau)$, where $c\tau$ is the intended extrapolated mean proper decay length.

2. Next, the LLP decay is required to be within the MS barrel or endcap fiducial volume.

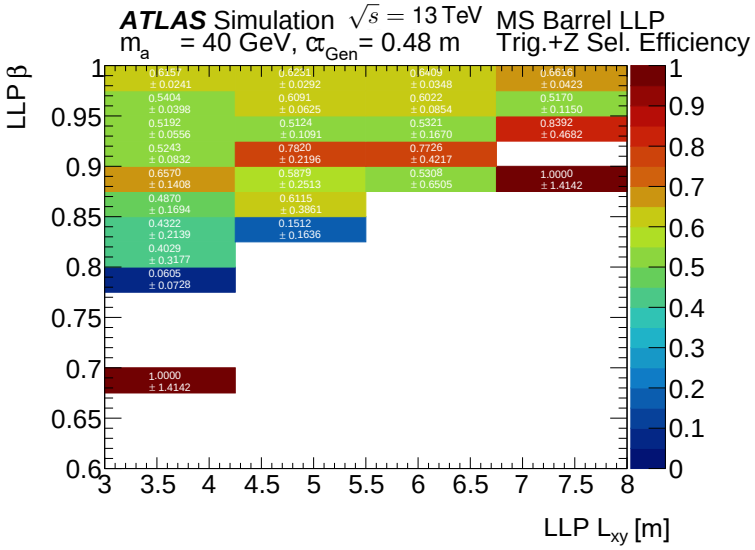

(a)

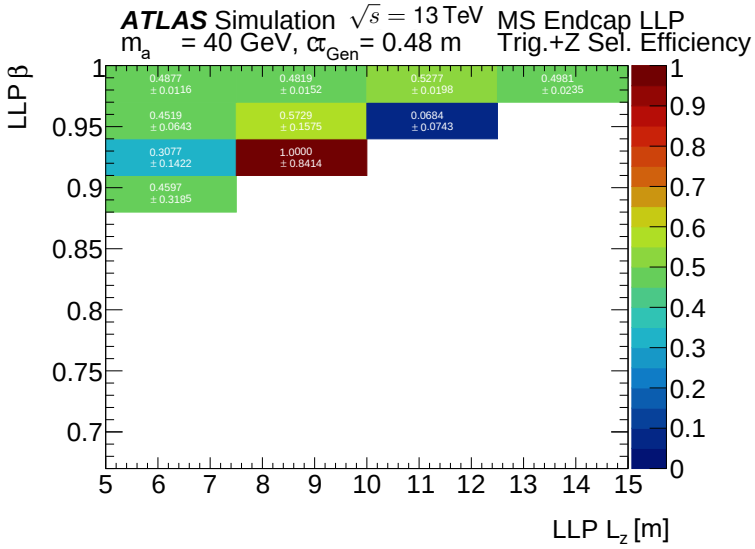

(b)

Figure 4.33.: MS barrel (a) and endcap (b) combined trigger and Z selection efficiency in the Z+ALP region for $m_a = 40$ GeV sample. Bins with no events are treated as having zero efficiency. Produced by Micheal Revering.

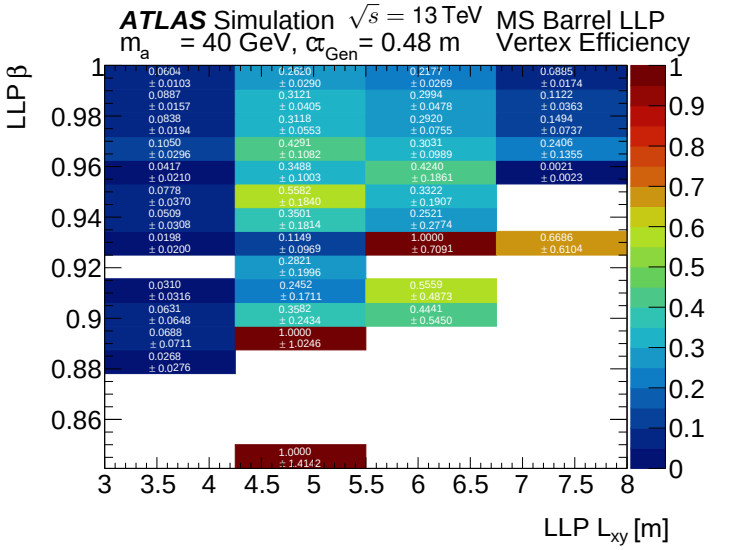

(a)

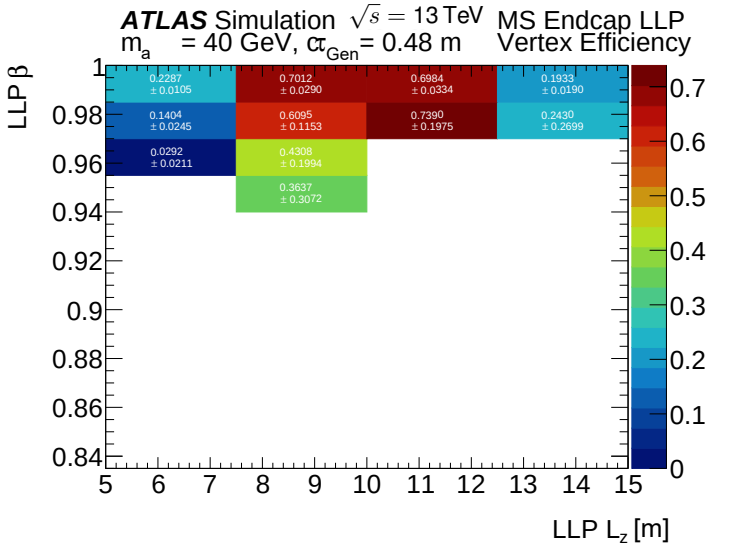

(b)

Figure 4.34.: MS barrel (a) and endcap (b) LLP vertex reconstruction efficiency in the Z+ALP region for $m_a = 40$ GeV sample. Bins with no events are treated as having zero efficiency. Produced by Micheal Revering.

3. The LLP decay is then required to be in-time (within 25 ns) with the bunch-crossing in which the hard scatter took place.

4. A random number between 0 and 1 is generated and if it is less than $\epsilon_{\text{Trig+Z}}$ at the same LLP decay length and β, the event "passes" the trigger.

5. Another random number between 0 and 1 is generated and if it is less than ϵ_{DV} at the same LLP decay length and β, the event "passes" the full selection.

6. The above steps are repeated for 100 exponentially spaced values of $c\tau$.

7. The final result is the number of signal events as a function of LLP proper lifetime for each m_a, which are then rescaled by 140.1 fb^{-1} $\times$ $\sigma_{\text{Gen}}/N_{\text{Pseudo}}$ to obtain the expected signal yield in the Run 2 dataset at each given proper lifetime, where σ_{Gen} are the generated ALP cross-sections listed in Table 4.3 and N_{Pseudo} are the number of generated pseudo-data events.

To validate the lifetime extrapolation procedure, additional fully-simulated samples were generated for $m_a = 0.1$ and 10 GeV, as listed in Table 4.3. For both of these mass points, there is a nomimal sample with the optimal mean $c\tau$ to maximise the rate of ALP decays in the HCal and MS, as well as a sample generated with a larger mean $c\tau$. There is also a sample with a lower $c\tau$ for $m_a = 10$ GeV. These low and high lifetime samples were used to validate the lifetime extrapolation procedure by comparing their signal yields to the extrapolated signal yields at the same $c\tau$. Figure 4.35 compares the extrapolated signal yields as a function of $c\tau$ for the $m_a = 10$ GeV samples.

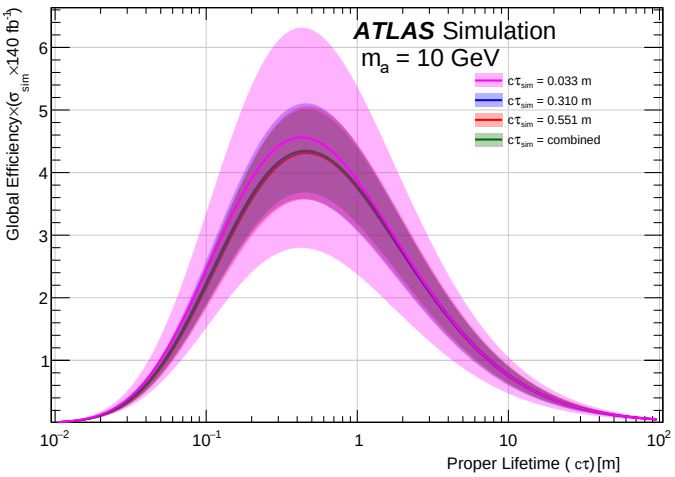

Figure 4.35.: Extrapolated global signal strengths for $m_a = 10$ GeV MC samples with different generated lifetimes. Good agreement is seen between the different samples. The uncertainties presented are a combination of the systematic uncertainties associated with data-MC correction scale factors and statistical uncertainties from the efficiencies calculated for each MC sample. Produced by Micheal Revering.

4.5. Systematic uncertainties

Studies of the systematic uncertainties in this analysis were conducted by Michael Revering and are briefly summarised below.

Using the luminosity measured by the LUCID-2 detector [71], the uncertainty in the integrated luminosity of the Run 2 dataset is 0.83% [88].

As discussed in Section 4.3.1, the systematic uncertainty associated with the ABCD background estimation is negligible compared to the statistical uncertainty.

There are systematic uncertainties in the signal efficiency related to the modelling of the signal physics processes, pileup and detector response, as well as the lifetime extrapolation procedure. Additional uncertainties can arise from mismodelling of lepton trigger efficiency, identification, and isolation. However, the combined lepton systematic uncertainty was found to be negligible. The systematic uncertainties due to pileup and PDF contributions to the MS DV reconstruction efficiency were calculated by varying the pileup and PDF weights according to their respective $\pm 1\sigma$ systematic uncertainties and evaluating the resulting differences in the DV reconstruction efficiency. For the PDF-related uncertainty, the nominal PDF set was evaluated using 100 replica variations. In both cases, the systematic uncertainty was found to be negligible.

The systematic uncertainty associated with the lifetime extrapolation procedure was estimated as the difference in the signal efficiencies yielded from the fully-simulated MC samples and pseudo-data at the same proper decay length. The uncertainty varies from 5% to 30% depending on m_a.

There is a systematic uncertainty due to the mismodelling of DV reconstruction in MC. Two different methods are utilised to estimate the degree of mismodelling and the difference in the two estimates is taken as the systematic uncertainty. In the first method, the distributions of the number of tracklets contained within $\Delta R < 0.4$ of a punch-through jet in data and MC are compared. Tracklets used to reconstruct a DV are discarded according to the difference in the data and MC, then the resulting difference in the DV reconstruction efficiency is evaluated. In the second method, MC events are weighted such that the distribution of tracklets matches that of data, then the resulting variation in the DV reconstruction efficiency was calculated. The difference in the efficiency variations of these two methods was taken as the systematic uncertainty and found to be 11% and 13% in the barrel and endcap regions, respectively.

4.6. Limit setting

The signal yields that were calculated for a wide range of LLP proper lifetimes using the lifetime extrapolation method described in Section 4.4 were used to calculate the expected and observed upper limits on the Z+ALP production cross-section σ times the branching ratio into gluons $B_{a\to gg}$ as a function of proper decay length. The limits on $\sigma \times B_{a\to gg}$ were derived with the CL_S method [89] using a profile likelihood function [90] in the `pyhf` [91] package.

Figures 4.17 and 4.18 show that the leakage of ALP signal into regions B, C and D is generally not negligible, especially in the endcap region. Therefore, the limits cannot be evaluated by only considering the expected and observed number of signal events in region A; the likelihood function input to the CL_S method must be modified to account for the signal contamination in regions B, C and D. Hence, a Poisson likelihood function is constructed for each region in the ABCD plane and the product of these four functions is used to derived the limits:

$$\mathcal{L}(n_A, n_B, n_C, n_D|\mu, \theta_\mu) = \prod_{i=A,B,C,D} \frac{e^{-N_i} N_i^{n_i}}{n_i!} \tag{4.2}$$

where i denotes the region in the ABCD plane, n_i denotes the number of events observed in the i^{th} ABCD region in data. The signal strength μ is defined as the ratio of the observed and expected number of events and θ_μ is a set of nuisance parameters that describe the systematic uncertainties. N_i are linear combinations of the expected number of signal (N_i^S) and background (N_i^B) events in each region:

$$N_A = \mu N_A^S + N_A^B \tag{4.3}$$
$$N_B = \mu \epsilon_B N_A^S + N_A^B \tau_B \tag{4.4}$$
$$N_C = \mu \epsilon_C N_A^S + N_A^B \tau_C \tag{4.5}$$
$$N_D = \mu \epsilon_D N_A^S + N_A^B \tau_B \tau_C \tag{4.6}$$

where $\epsilon_i = N_i^S / N_A^S$ are signal scaling factors derived from MC and τ_B and τ_C are nuisance parameters that relate the number of background events in the signal region to the other regions. The μ, N_A^B and τ_i values are allowed to float in the simultaneous likelihood fit to the four data regions.

4.7. Results

The number of events observed in the lepton-triggered channel SR is consistent with the expected SM background. The MC signal yields are extrapolated to a broad range of LLP proper decay lengths using pseudo-experiments, following the procedure described in Section 4.4. Upper limits on the cross-section σ times branching ratio $B_{a\to gg}$ for long-lived ALPs that are produced in association with a Z boson and decay into gluons are calculated with the CL_S method [89] using a profile likelihood function [90] in the `pyhf` [91] package, as described in Section 4.6. The limits assume the branching fraction of Z decays into e^+e^- and $\mu^+\mu^-$, $B_{Z\to e^-e^+/\mu^-\mu^+} = 6.6\%$ [86].

Figure 4.36 shows the expected and observed 95% confidence level (CL) upper limits on $\sigma \times B_{a\to gg}$ as a function of the ALP proper decay length for $m_a = \{0.1, 1, 10, 40\}$ GeV. For all m_a, the observed and expected limits are consistent within the uncertainties. The limits are more stringent for larger m_a as the reduced boost, wider decay opening angles and higher jet multiplicity increase the DV reconstruction efficiency.

Figure 4.37 compares the expected and observed limits reported in this work to those of a previous ATLAS search for a displaced jet in the HCal [34] and a search for a DV in the ID [33] that both probe the same Z+ALP model. The ID search probed ALPs with masses $m_a = \{40, 55\}$ GeV while the HCal search probed the same m_a as this work. Hence, Figure 4.37(a) compares the limits for $m_a = 40$ GeV and Figure 4.37(b) compares the limits for $m_a = \{0.1, 1, 10\}$ GeV. These combined ATLAS results are the first and currently only constraints on long-lived ALPs with masses $m_a = \{0.1, 1, 10, 40\}$ GeV that are produced in association with a Z boson. The results of this work are currently the most stringent limits for $m_a = \{0.1, 1\}$ GeV at $c\tau \gtrsim \mathcal{O}(0.01)$ m, as well as for $m_a = \{10, 40\}$ GeV at $c\tau \gtrsim \mathcal{O}(0.1)$ m.

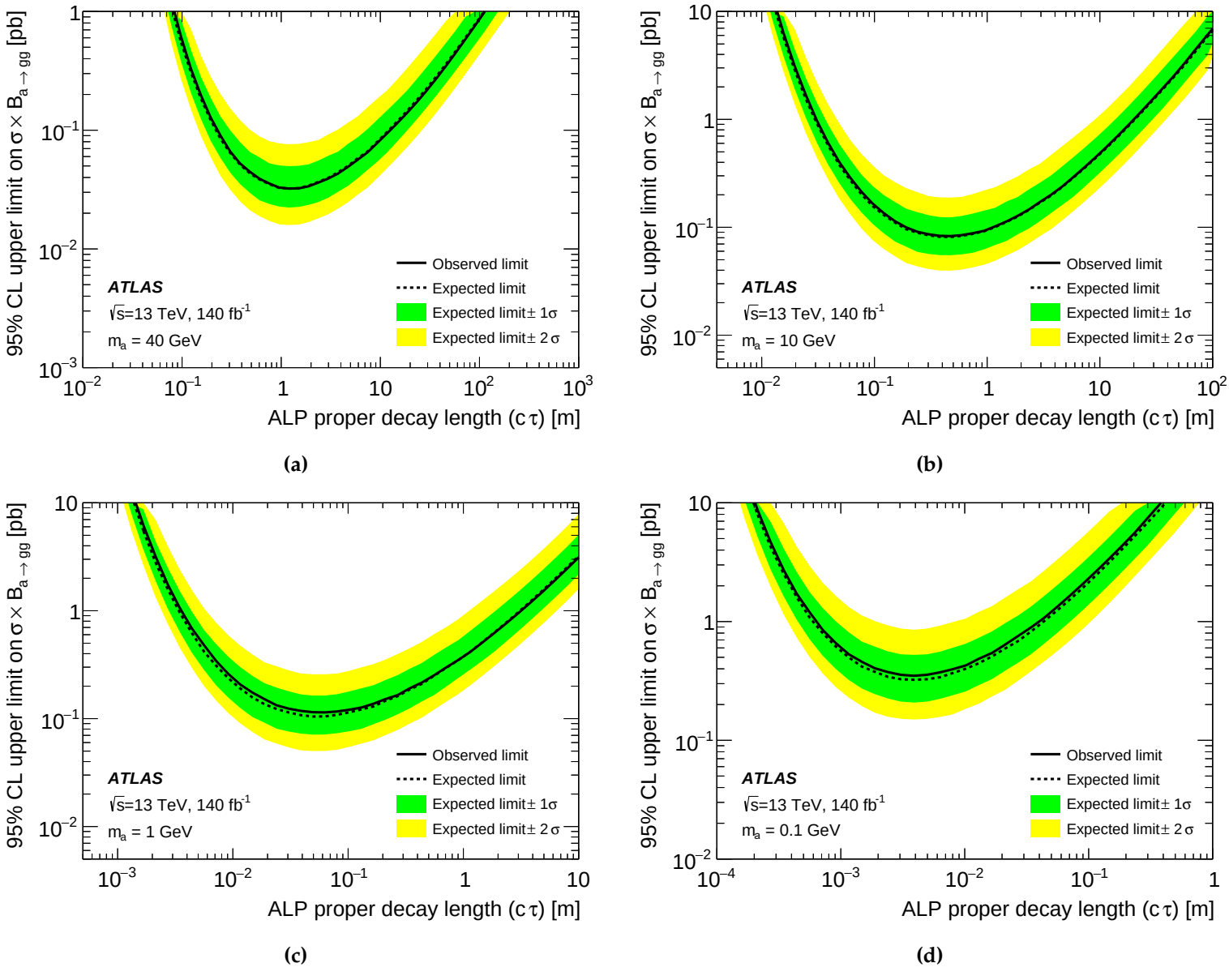

Figure 4.36.: Observed and expected 95% CL upper limits on the Z+ALP production cross-section time branching ratio $\sigma \times B_{a\to gg}$ presented as a function of ALP proper decay length for m_a = (a) 40 GeV, (b) 10 GeV, (c) 1 GeV and (d) 0.1 GeV.

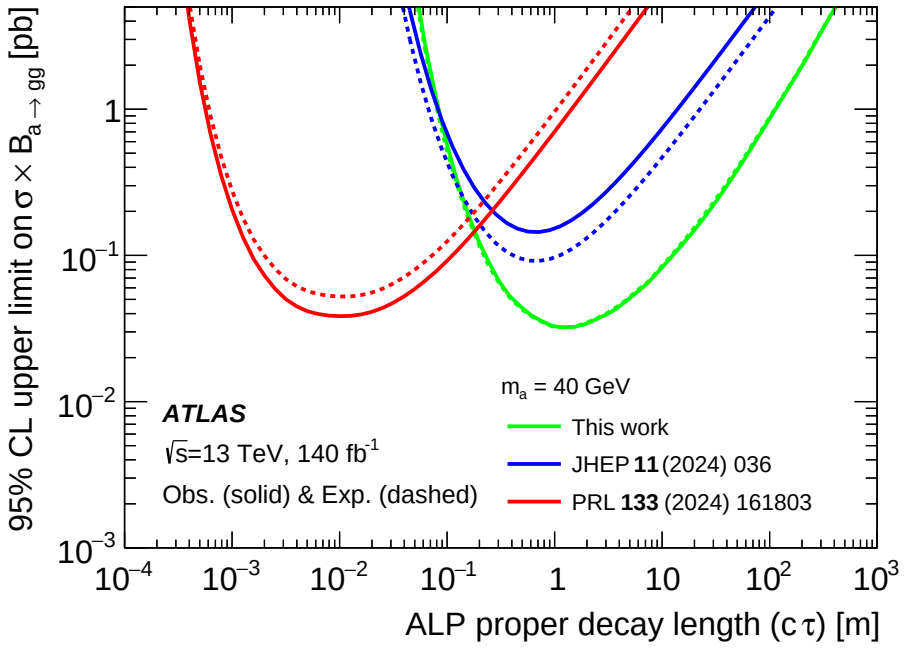

(a)

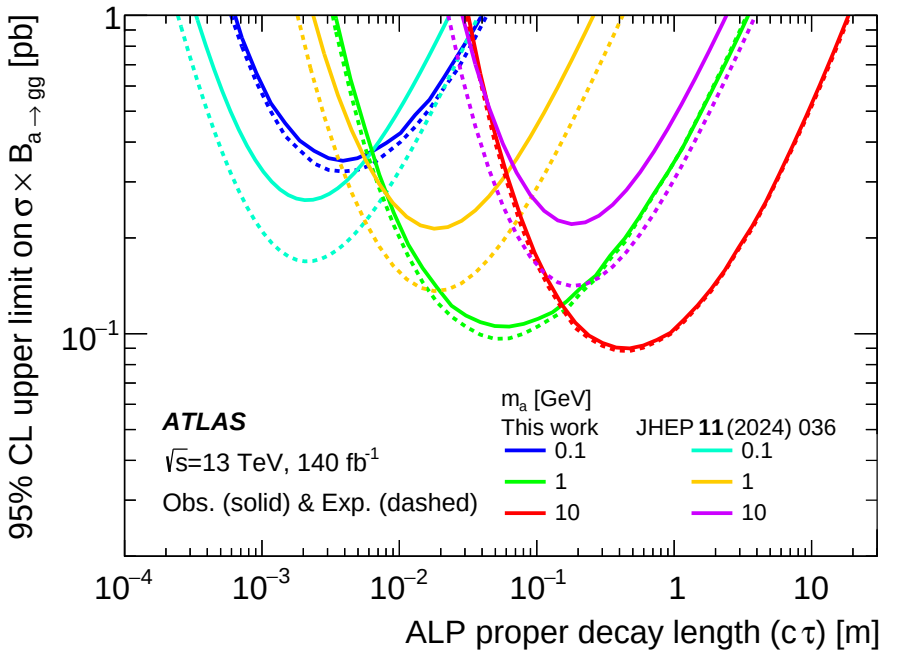

(b)

Figure 4.37.: Comparisons between the expected and observed 95% CL limits on the Z+ALP cross-section times branching ratio this result and the corresponding result from previous ATLAS searches using the ID [34] and HCal [33]. The only mass point shared with the ID search is $m_a = 40$ GeV. Therefore, the limits for $m_a = 40$ GeV are compared for all three searches in (a) and the limits for $m_a = \{0.1, 1, 10\}$ GeV are displayed in (b) for this search and the HCal search.

Chapter 5.

Conclusion and outlook

Conclusion

A search for events that contain a prompt Z boson and a single displaced vertex (DV) reconstructed in the muon spectrometer (MS) produced by hadronic decays of long-lived particles (LLPs) is presented. The search utilises 140 fb^{-1} of proton-proton collisions at $\sqrt{s} = 13$ TeV recorded by the ATLAS detector during Run 2 of the LHC (2015-2018). Candidate events are triggered by single and di-lepton triggers, then are required to contain a Z boson candidate that decays into a pair of electrons or muons, must pass a minimum E_T^{miss} threshold and contain a DV reconstructed in the MS fiducial volume. The DV is required to pass selection criteria related to the amount of detector activity associated with the DV, as well as isolation from tracks and jets. The final signal/background discrimination is conducted using neural networks and a data-driven method is employed to estimate the expected background count in the signal region. A model featuring production of long-lived axion-like particles (ALPs) in association with a Z boson and decays of ALPs into hadronic jets is considered. No excess above the expected background is observed, therefore upper exclusion limits on the ALP production cross-section times branching ratio are computed as a function of LLP proper decay length $c\tau$. The combined ATLAS results presented in Figure 4.37 are the first constraints on long-lived ALPs with masses $m_a = \{0.1, 1, 10, 40\}$ GeV that are produced in association with a Z boson. The results of the work presented in this thesis are currently the world-leading limits for $m_a = \{0.1, 1\}$ GeV at $c\tau \gtrsim \mathcal{O}(0.01)$ m, as well as for $m_a = \{10, 40\}$ GeV at $c\tau \gtrsim \mathcal{O}(0.1)$ m.

Outlook

The results of the search presented in this thesis constitute the current most stringent upper limits on the production cross-section times branching ratio for ALPs with a wide range of masses and proper decay lengths that decay to gluons, with the exclusion limit being as low as 30 fb for $m_a = 40$ GeV at $c\tau \sim 1$ m, as well as approximately 100 fb for $m_a = 1$ GeV at $c\tau \sim 0.05$ m. The results of this search can also be used to set limits on other LLP models. The search has already been reinterpreted to set stringent limits on the cross-section times branching ratio of long-lived hidden-sector scalars and dark photons [35]. Further, the trigger and DV reconstruction efficiency maps produced for the lifetime reweighting procedure, such as Figures 4.33 and 4.34, have been published to allow theorists to easily reinterpret the search.

The lifetime of BSM particles is typically a free parameter. Therefore, new physics may be hidden in the form of LLPs that have extremely long proper lifetimes constrained only by Big Bang Nucleosynthesis to $c\tau \lesssim 10^8$ m [23]. Additionally, numerous models and decay topologies remain to be probed, while existing probes can be refined with more data and improvements to the experiments. Given the vast breadth of the parameter space still yet to be covered, the field of LLPs shall itself be long-lived. Several prospects for future LLP searches are discussed below. First, the major ongoing and upcoming developments at ATLAS and the LHC that will benefit LLP searches are described. Then, dedicated detectors that are being developed as auxiliary to the main LHC experiments and will bolster sensitivity to LLPs with very long lifetimes are discussed. Finally, the great promise of the next generation of particle colliders is explored.

A striking result of this search is the very small number of events in the ABCD planes despite the relaxed MS DV selection compared to the RoI-triggered channel. The Z boson production cross-section suppresses the number of DVs significantly and results in large statistical uncertainties in the predicted number of background events. At the time of writing, the LHC is in Run 3 (2022 - 2026) and ATLAS has recorded more than 240 fb^{-1} of proton-proton collisions at $\sqrt{s} = 13.6$ TeV [49]. It is expected that the final ATLAS Run 3 dataset reach at least 300 fb^{-1} – more than double the size of the Run 2 dataset, allowing rarer interactions to be probed and increasing the likelihood of observing new physics. In addition, refinements to the vertexing algorithms utilised in the MS are currently in development.

Run 4 of the LHC, known as the High Luminosity-LHC (HL-LHC), will aim to achieve an integrated luminosity of at least 3 ab^{-1} at 14 TeV, which is an order of magnitude larger than the original LHC designs. To achieve this integrated luminosity, the mean number of pp collisions per paired bunch-crossing (pileup) will be increased to $\langle\mu\rangle \sim 200$. Therefore, in preparation for the HL-LHC, upgrades will be made to the ATLAS detector systems, the trigger and data aquisition system, as well as its readout electronics, to allow ATLAS to better cope with the demands of tracking in a very busy environment as well as the increase in radiation damage due to the large pileup. Notably, upgrades to the MS [92] will include new thin-gap RPC triplets and small-diameter MDT chambers in the inner barrel layer, in addition to the new small wheel in the endcap. These upgrades will provide better coverage, particularly in the barrel-endcap transition region $0.7 < |\eta| < 1.3$ that is excluded from the MS fiducial volume in searches for DVs in the MS due to the poor vertex reconstruction efficiency in this region. In addition, the upgrades will allow more precise and thus more selective triggering, as well as better resolution in the MS than the Run 2 ATLAS configuration. The new MS subdetector systems are expected to help to improve the MS vertex reconstruction efficiency, as well as potentially allow more of the detector to be included in the MS fiducial volume in searches for DVs. In addition, the ATLAS inner detector will be replaced with a new all-silicon tracker, known as the ITk [93]. The ITk will comprise of less material than the Run 2 ID while achieving a similar or better performance. The reduction in material will aid LLP searches as there will be less displaced activity due to material interactions. Furthermore, a high granularity timing detector [94] will be installed in the endcap to assist the ITk in the forward region $2.4 < |\eta| < 4.0$, allowing charged particles to be tracked in time as well as in space, with a track timing resolution of 30 ps. This will help mitigate pileup in the busy forward region. The track timing capabilities could be employed to search for LLPs that decay in the forward region of the ID.

Although the main LHC experiments are powerful tools for searching for LLPs at colliders, they are affected by large backgrounds from hadronic interactions and pileup, while their sensitivity to particles with very long lifetimes is fundamentally limited by the size of the detectors. Hence, there are several particle detectors designed specifically to search for LLPs currently in development. These detectors are typically based substantially far from an LHC experiment and often have thick shielding, resulting in lower backgrounds than main LHC experiments that are easy to veto with angular requirements. There are two main categories of auxilliary LLP detectors: forward and transverse, which respectively provide complimentary coverage in the

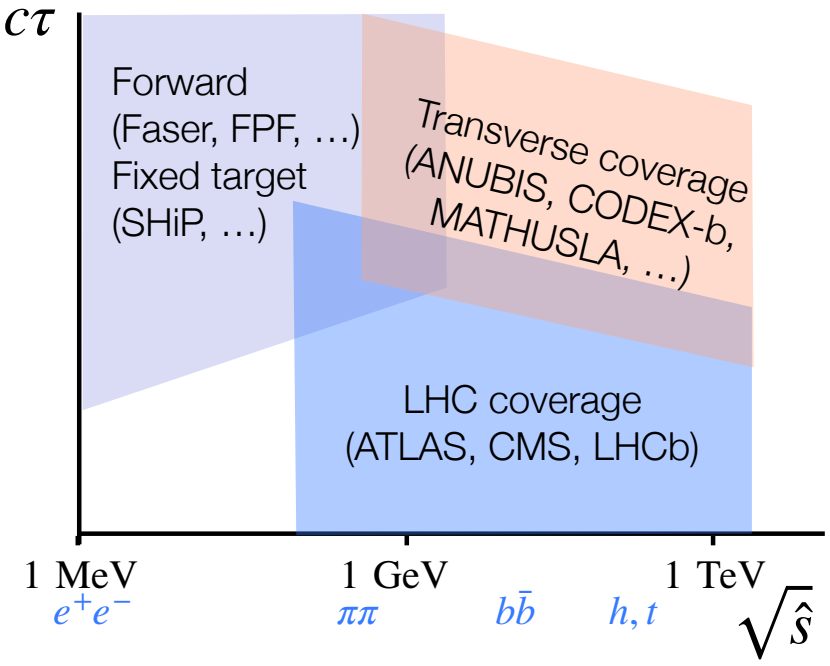

Figure 5.1.: Representation of the complimentarity coverage of different types of long-lived particle experiments presented as a function of partonic centre-of-mass energy $\sqrt{\hat{s}}$ [95].

forward and transverse regions of a main LHC experiment. The complimentarity of these experiments to the main LHC detectors is illustrated in Figure 5.1.

Forward detectors provide coverage at longer lifetimes than the main LHC experiments and are sensitive to light LLPs with mass $m_{\text{LLP}} < \mathcal{O}(10)$ GeV. However, due to kinematics, forward detectors are unable to probe LLPs with $m_{\text{LLP}} > \mathcal{O}(10)$ GeV or LLPs that are produced in decays of heavy mediators with masses at the electroweak scale and above The first auxilliary LLP detector to be fully realised at the LHC is the FASER detector [96], which is situated in an access tunnel approximately 400 m from the ATLAS interaction point, close to the beam axis. Much of the distance between ATLAS and FASER consists of rock that shields from backgrounds. FASER is sensitive to very light LLPs that are produced in the forward direction at ATLAS and has already set world-leading constraints on photophilic ALPs with masses up to 300 MeV [97].

Complimentary to forward detectors, transverse detectors are sensitive to LLPs with masses $m_{\text{LLP}} > \mathcal{O}(10)$ GeV and LLPs that are produced in decays of heavy mediators such as the Higgs boson. For example, the ANUBIS detector [98, 99] is planned to instrument the ATLAS cavern ceiling with the same RPC triplet technology that will upgrade the MS for the HL-LHC. A prototype module called proANUBIS is currently taking data in the ATLAS cavern [100].

One of the primary motivations for BSM models that include interactions with the Higgs boson is the branching ratio of invisible Higgs decays, which is currently indirectly constrained by ATLAS to $B_{H\to\text{invisible}} < 12\%$ [24]. It is possible to directly probe $B_{H\to\text{invisible}}$ by measuring the recoil mass in events with a leptonically decaying Z boson and requiring that it matches the Higgs mass. The mass m_{recoil} of a particle recoiling from a Z boson can be written as

$$m^2_{\text{recoil}} = \hat{s} + m^2_Z - 2\sqrt{\hat{s}}E_Z, \tag{5.1}$$

where $\sqrt{\hat{s}}$ is the partonic centre of mass energy, i.e. the energy exchanged in the hard scatter, while m_Z and E_Z are the Z boson mass and energy, respectively. However, m_{recoil} cannot be measured at a hadron collider since $\sqrt{\hat{s}}$ is an unknown fraction of the centre of mass energy $\sqrt{s}$ due to the composite nature of the colliding protons. The next generation of particle colliders is expected to include e^+e^- colliders capable of reaching centre-of-mass energies of at least several hundred GeV to provide the highest precision measurements of SM processes, particularly Higgs interactions. Examples of such colliders in development are the FCC-ee [101, 102], CLIC [103], and ILC [104]. Since electrons are elementary, $\sqrt{\hat{s}} = \sqrt{s}$ in e^+e^- collisions and will therefore be known for all events recorded at future e^+e^- colliders, allowing $B_{H\to\text{invisible}}$ to be measured directly for the first time. This will tighten constraints on Higgs-BSM interactions, including any that produce LLPs. Furthermore, Equation 5.1 can be utilised to probe models where LLPs are produced in association with a Z boson, such as the models considered in this work, by conducting a resonance search in the recoil mass distribution of events containing a prompt Z boson and displaced detector activity.

It may be the case that BSM physics, including LLPs, lies at energy scales beyond the reach of the LHC. Therefore, plans for the next generation of hadron colliders capable of achieving $\sqrt{s} \sim \mathcal{O}(100)$ TeV are in development, such as the FCC-hh [101, 105]. To maximise the physics discovery potential of future colliders experiments, it is important that LLP signatures are considered in the design of future detectors. The general purpose particle detectors that succeed ATLAS and CMS must be better designed from the ground up to search for LLPs and include large-scale forward and transverse LLP detectors, which will likely be based on the research and development of auxilliary LHC detectors like FASER and ANUBIS. The lessons learned at the LHC will be instrumental in guiding future searches for LLPs and mapping out the landscape of physics Beyond the Standard Model.

Appendix A.

Data sample names

Tables A.1, A.2, A.3, A.4 report all the pp collision datasets in the ATLAS Run 2 good run list that are used in this analysis.

2015 $\sqrt{s} = 13$ TeV pp collisions
data15_13TeV.periodF.physics_Main.PhysCont.DAOD_EXOT15.grp15_v01_p4309
data15_13TeV.periodG.physics_Main.PhysCont.DAOD_EXOT15.grp15_v01_p4309
data15_13TeV.periodJ.physics_Main.PhysCont.DAOD_EXOT15.grp15_v01_p4309
data15_13TeV.periodA.physics_Main.PhysCont.DAOD_EXOT15.grp15_v01_p4309
data15_13TeV.periodH.physics_Main.PhysCont.DAOD_EXOT15.grp15_v01_p4309
data15_13TeV.periodE.physics_Main.PhysCont.DAOD_EXOT15.grp15_v01_p4309
data15_13TeV.periodD.physics_Main.PhysCont.DAOD_EXOT15.grp15_v01_p4309
data15_13TeV.periodC.physics_Main.PhysCont.DAOD_EXOT15.grp15_v01_p4309

Table A.1.: List of the pp collision datasets used for 2015 data taking period.

2016 $\sqrt{s} = 13$ TeV pp collisions
data16_13TeV.periodA.physics_Main.PhysCont.DAOD_EXOT15.grp16_v01_p4309
data16_13TeV.periodL.physics_Main.PhysCont.DAOD_EXOT15.grp16_v01_p4309
data16_13TeV.periodD.physics_Main.PhysCont.DAOD_EXOT15.grp16_v01_p4309
data16_13TeV.periodI.physics_Main.PhysCont.DAOD_EXOT15.grp16_v01_p4309
data16_13TeV.periodK.physics_Main.PhysCont.DAOD_EXOT15.grp16_v01_p4309
data16_13TeV.periodE.physics_Main.PhysCont.DAOD_EXOT15.grp16_v01_p4309
data16_13TeV.periodB.physics_Main.PhysCont.DAOD_EXOT15.grp16_v01_p4309
data16_13TeV.periodF.physics_Main.PhysCont.DAOD_EXOT15.grp16_v01_p4309
data16_13TeV.periodG.physics_Main.PhysCont.DAOD_EXOT15.grp16_v01_p4309
data16_13TeV.periodC.physics_Main.PhysCont.DAOD_EXOT15.grp16_v01_p4309

Table A.2.: List of the pp collision datasets used for 2016 data taking period.

2017 $\sqrt{s} = 13$ TeV pp collisions
data17_13TeV.periodC.physics_Main.PhysCont.DAOD_EXOT15.grp17_v01_p4309
data17_13TeV.periodE.physics_Main.PhysCont.DAOD_EXOT15.grp17_v01_p4309
data17_13TeV.periodB.physics_Main.PhysCont.DAOD_EXOT15.grp17_v01_p4309
data17_13TeV.periodD.physics_Main.PhysCont.DAOD_EXOT15.grp17_v01_p4309
data17_13TeV.periodH.physics_Main.PhysCont.DAOD_EXOT15.grp17_v01_p4309
data17_13TeV.periodN.physics_Main.PhysCont.DAOD_EXOT15.grp17_v01_p4309
data17_13TeV.periodK.physics_Main.PhysCont.DAOD_EXOT15.grp17_v01_p4309
data17_13TeV.periodI.physics_Main.PhysCont.DAOD_EXOT15.grp17_v01_p4309
data17_13TeV.periodF.physics_Main.PhysCont.DAOD_EXOT15.grp17_v01_p4309

Table A.3.: List of the pp collision datasets used for 2017 data taking period.

2018 $\sqrt{s} = 13$ TeV pp collisions
data18_13TeV.periodI.physics_Main.PhysCont.DAOD_EXOT15.grp18_v01_p4309
data18_13TeV.periodE.physics_Main.PhysCont.DAOD_EXOT15.grp18_v01_p4309
data18_13TeV.periodC.physics_Main.PhysCont.DAOD_EXOT15.grp18_v01_p4309
data18_13TeV.periodO.physics_Main.PhysCont.DAOD_EXOT15.grp18_v01_p4309
data18_13TeV.periodL.physics_Main.PhysCont.DAOD_EXOT15.grp18_v01_p4309
data18_13TeV.periodD.physics_Main.PhysCont.DAOD_EXOT15.grp18_v01_p4309
data18_13TeV.periodB.physics_Main.PhysCont.DAOD_EXOT15.grp18_v01_p4309
data18_13TeV.periodM.physics_Main.PhysCont.DAOD_EXOT15.grp18_v01_p4309
data18_13TeV.periodF.physics_Main.PhysCont.DAOD_EXOT15.grp18_v01_p4309
data18_13TeV.periodQ.physics_Main.PhysCont.DAOD_EXOT15.grp18_v01_p4309
data18_13TeV.periodK.physics_Main.PhysCont.DAOD_EXOT15.grp18_v01_p4309

Table A.4.: List of the pp collision datasets used for 2018 data taking period.

Appendix B.

Additional Monte Carlo samples

B.1. Monte Carlo samples employed in the RoI-triggered channel

Model	Parameters		
	$m_{H/\Phi}$ [GeV]	m_s [GeV]	$c\tau$ [m]
Scalar portal	125	5	0.127, 0.411
		16	0.580
		35	1.310, 2.630
		55	1.050, 5.320
	60	5	0.217
		16	0.661
	200	50	1.255
	400	100	1.608
	600	50	0.590
		150	1.840, 3.309
		275	4.288
	1000	50	0.406
		275	2.399, 4.328
		475	6.039
	m_χ [GeV]	χ decay channel	$c\tau$ [m]
Baryogenesis	10	$\tau^+ \tau^- \nu_\ell$, $c\,b\,s$, $\nu\,b\,\bar{b}$	0.920
	55		5.550
	100		3.500

Table B.1.: Parameters used in the RoI-triggered channel [35] for the simulated scalar portal based on the Hidden Abelian Higgs Model [106] and the baryogenesis model [107].

B.2. Axion-like particles produced in associaton with a $W^{\pm}$ boson

MC W+ALP events were generated using the same as the Z+ALP samples, as described in Section 4.1.2. Although no search for ALPs produced in association was conducted in this work, the W+ALP MC samples were used to check for signal contamination in the γ+jets VR.

m_{ALP} [GeV]	$C_{\tilde{G}}$	$c\tau_{\text{Gen}}$ [m]	N_{Gen}	σ_{Gen} [fb]
0.1	10^{-2}	0.003	400000	36.3
	5×10^{-3}	0.012	200000	
1	10^{-4}	0.031	400000	36.2
10	10^{-6}	0.310	398000	31.7
	7.5×10^{-7}	0.551	200000	
40	10^{-7}	0.481	398000	19.9

Table B.2.: Parameters used for simulations of ALP produced in association with a $W^{\pm}$ boson, where m_{ALP} is the ALP mass, $C_{\tilde{G}}$ is the coupling to the gluon field that dictates the generated mean proper lifetime $c\tau_{\text{Gen}}$. For m_{ALP} = 0.1 and 10 GeV, additional samples with different lifetimes were generated to validate the lifetime extrapolation procedure. The number of generated events is denoted by N_{Gen} and σ_{Gen} is the ALP production cross-section calculated by MADGRAPH5_AMC@NLO.

B.3. Prompt jets produced in association with a Z boson

Z+jets MC tables

Appendix C.

ALP decay opening angles

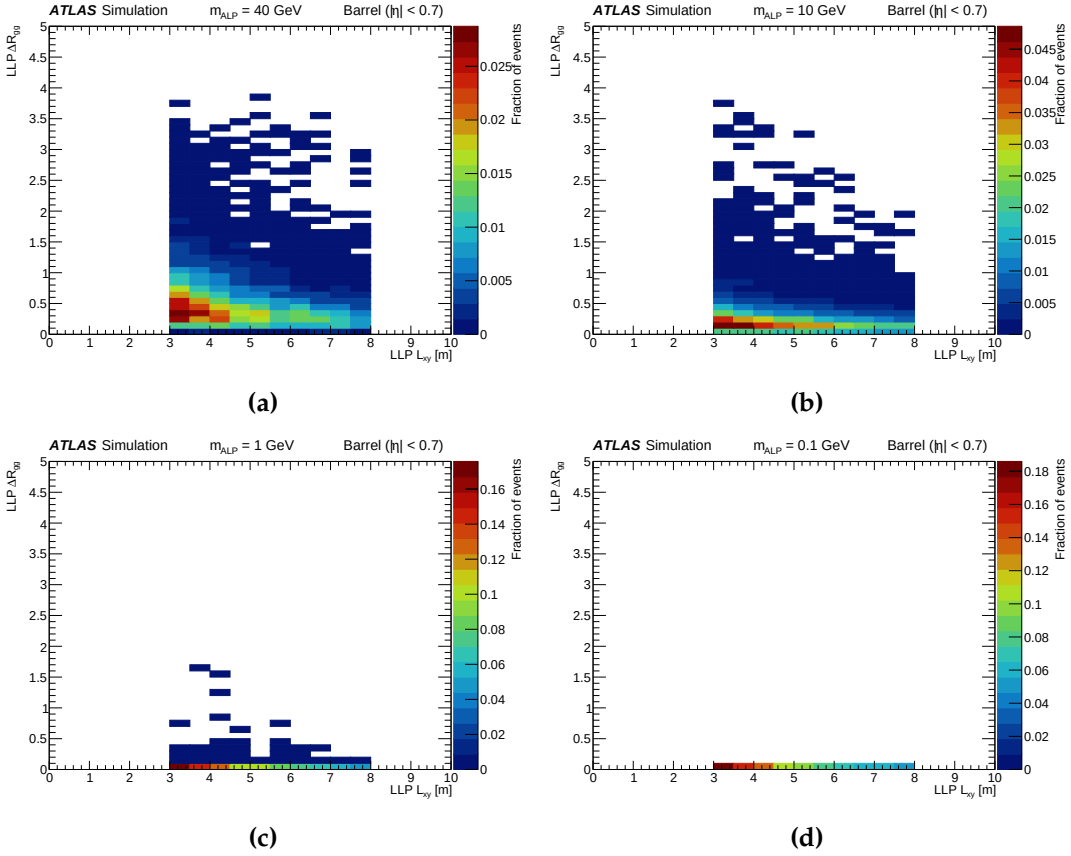

Figure C.1.: Opening angle of the ALP decay products as a function of L_{xy} for ALPs that decay in the MS barrel.

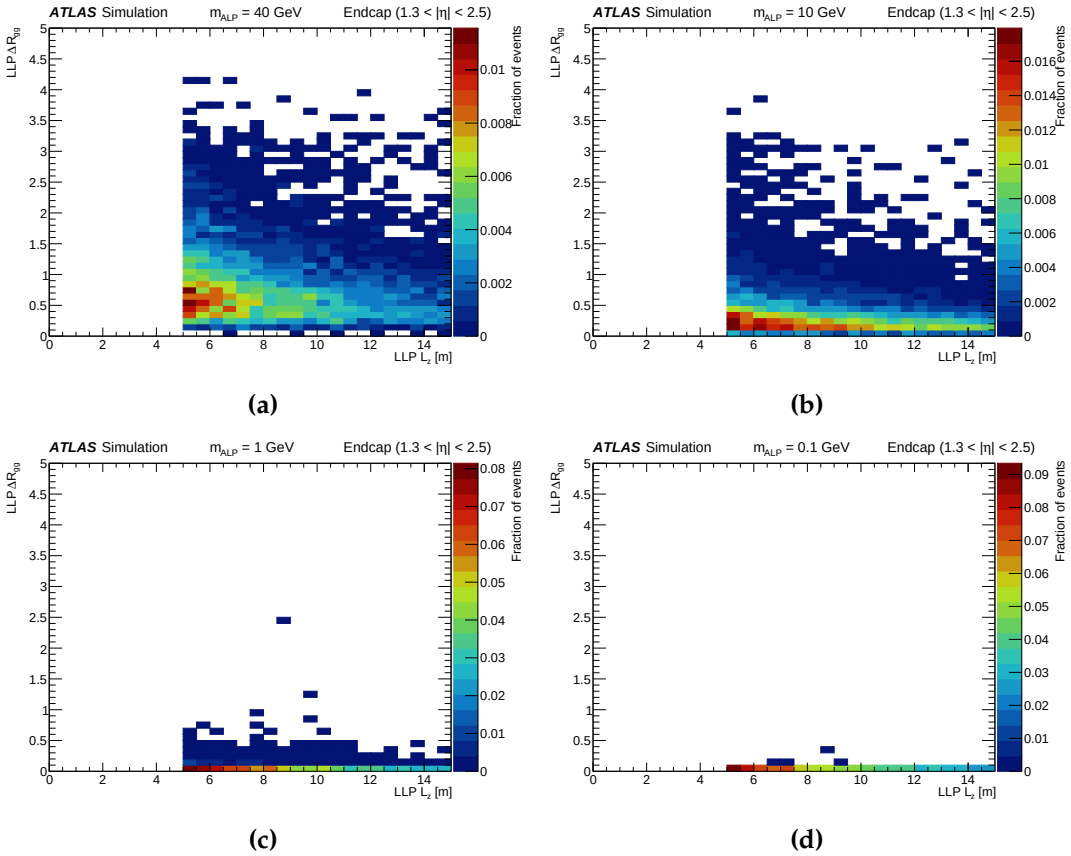

Figure C.2.: Opening angle of the ALP decay products as a function of L_z for ALPs that decay in the MS endcap.

Appendix D.

Additional information on the photon validation region

Photons for the background validation of the one vertex + Z search are selected by the triggers listed in Table D.1 for the different data-taking years.

The photon reconstruction and calibration follow similar steps to those for electrons with additional complexity from photon conversions occurring before the electromagnetic calorimeter is reached [108, 109]. The photon baseline selections are reported in Table D.2. Due to the acceptance overlap between the electromagnetic calorimeter barrel and endcap components, photons whose pseudorapidity falls into the transition region between 1.37 and 1.52 are rejected. To avoid photon p_T mismeasurements significantly influencing the $E_{\mathrm{T}}^{\mathrm{miss}}$ calculation, a minimum photon p_T of 20 GeV is required. Again, the standard overlap removal ordering is applied.

Triggers	2015	2016	2017	2018
Single photon triggers				
HLT_g120_loose	✓			
HLT_g140_loose		✓	✓	✓
HLT_g200_etcut	✓			
HLT_g300_etcut		✓	✓	✓
Di-photon triggers				
HLT_g35_medium_g25_medium_L12EM20VH			✓	✓

Table D.1.: The considered single and di-photon triggers for the different data taking years.

Selections	Baseline photons
p_T	$p_T > 20\,\text{GeV}$
$\lvert\eta\rvert$	$\lvert\eta\rvert < 1.37$ or $1.52 < \lvert\eta\rvert < 2.37$
Identification WP	Loose
Isolation WP	Loose
Overlap removal	Pass

Table D.2.: The photon baseline selections. Definitions of the working points can be found in [81].

Colophon

This thesis was made in LaTeX 2_ε using the "hepthesis" class [110].

Bibliography

[1] M. Thomson, *Modern particle physics*. Cambridge University Press, New York, 10, 2013, 10.1017/CBO9781139525367.

[2] MJ, *The Standard Model of Particle Physics*, .

[3] ALEPH, DELPHI, L3, OPAL collaboration, *Review of LEP results*, *AIP Conf. Proc.* **618** (2001) 32.

[4] G. Bellodi, *Electroweak asymmetries from sld*, *Nuclear Physics B - Proceedings Supplements* **109** (2002) 203.

[5] PARTICLE DATA GROUP collaboration, *Review of particle physics*, *Phys. Rev. D* **110** (2024) 030001.

[6] ATLAS collaboration, *Observation of a new particle in the search for the Standard Model Higgs boson with the ATLAS detector at the LHC*, *Physics Letters B* **716** (2012) 1 .

[7] CMS collaboration, *Observation of a new boson at a mass of 125 GeV with the CMS experiment at the LHC*, *Physics Letters B* **716** (2012) 30 .

[8] ATLAS collaboration, *Standard Model Summary Plots June 2024*, .

[9] ATLAS collaboration, *Combined measurements of Higgs boson production and decay using up to 80 fb^{-1} of proton-proton collision data at $\sqrt{s} = 13$ TeV collected with the ATLAS experiment*, *Phys. Rev. D* **101** (2020) 012002.

[10] A. D. Sakharov, *Violation of CP Invariance, C asymmetry, and baryon asymmetry of the universe*, *Pisma Zh. Eksp. Teor. Fiz.* **5** (1967) 32.

[11] V. C. Rubin, W. K. Ford, Jr. and N. Thonnard, *Rotational properties of 21 SC galaxies with a large range of luminosities and radii, from NGC 4605 (R=4kpc) to UGC 2885 (R=122kpc).*, *apj* **238** (1980) .

[12] K. Freese, *Review of observational evidence for dark matter in the universe and in upcoming searches for dark stars*, *EAS Publications Series* **36** (2009) 113–126.

[13] NASA, "Bullet Cluster (Webb and Chandra Image)." URL: https://sci.esa.int/web/hubble/-/57047-illustration-showing-gravitational-lensing-producing-supernova-images, June, 2025.

[14] ESA and Planck, "Planck's view of the cosmic microwave background." URL: https://www.esa.int/ESA_Multimedia/Images/2018/07/Planck_s_view_of_the_cosmic_microwave_background, 2018.

[15] ESA and Planck, "Planck power spectrum." URL: https://www.esa.int/ESA_Multimedia/Images/2013/03/Planck_Power_Spectrum, 2013.

[16] S. D. M. White, C. S. Frenk and M. Davis, *Clustering in a neutrino-dominated universe*, *The Astrophysical Journal Letters* **274** (1983) L1.

[17] M. Davis, G. Efstathiou, C. S. Frenk and S. D. M. White, *The Evolution of Large Scale Structure in a Universe Dominated by Cold Dark Matter*, *Astrophys. J.* **292** (1985) 371.

[18] ATLAS collaboration, *Constraints on mediator-based dark matter and scalar dark energy models using $\sqrt{s}$ = 13 tev pp collision data collected by the atlas detector*, *Journal of High Energy Physics* **2019** (2019) .

[19] L. Lee, C. Ohm, A. Soffer and T.-T. Yu, *Collider searches for long-lived particles beyond the Standard Model*, *Progress in Particle and Nuclear Physics* **106** (2019) 210–255.

[20] J. Alimena, J. Beacham, M. Borsato, Y. Cheng, X. C. Vidal, G. Cottin et al., *Searching for long-lived particles beyond the standard model at the large hadron collider*, *Journal of Physics G: Nuclear and Particle Physics* **47** (2020) 090501.

[21] V. Silveira and A. Zee, *SCALAR PHANTOMS*, *Phys. Lett. B* **161** (1985) 136.

[22] B. Shuve, "Theory overview of long-lived particles at the lhc." URL: https://indico.cern.ch/event/714087/contributions/2985914/attachments/1650488/2641192/LHC-LLP_Shuve.pdf, 2017.

[23] A. Fradette and M. Pospelov, *BBN for the LHC: Constraints on lifetimes of the Higgs*

portal scalars, *Phys. Rev. D* **96** (2017) 075033 [1706.01920].

[24] ATLAS Collaboration, *A detailed map of Higgs boson interactions by the ATLAS experiment ten years after the discovery*, *Nature* **607** (2022) 52 [2207.00092].

[25] L. Lee, C. Ohm, A. Soffer and T.-T. Yu, *Collider searches for long-lived particles beyond the standard model*, *Progress in Particle and Nuclear Physics* **106** (2019) 210–255.

[26] M. J. Strassler and K. M. Zurek, *Echoes of a hidden valley at hadron colliders*, *Physics Letters B* **651** (2007) 374–379.

[27] M. J. Strassler and K. M. Zurek, *Discovering the higgs through highly-displaced vertices*, *Physics Letters B* **661** (2008) 263–267.

[28] S. Chang, P. J. Fox and N. Weiner, *Naturalness and higgs decays in the mssm with a singlet*, *Journal of High Energy Physics* **2006** (2006) 068–068.

[29] Y. F. Chan, M. Low, D. E. Morrissey and A. P. Spray, *Lhc signatures of a minimal supersymmetric hidden valley*, *Journal of High Energy Physics* **2012** (2012) .

[30] ATLAS collaboration, *Search for long-lived particles produced in pp collisions at $\sqrt{s}$=13 TeV that decay into displaced hadronic jets in the ATLAS muon spectrometer*, *Physical Review D* **99** (2019) .

[31] ATLAS collaboration, *Search for long-lived neutral particles in pp collisions at $\sqrt{s}$ = 13 TeV that decay into displaced hadronic jets in the ATLAS calorimeter*, *The European Physical Journal C* **79** (2019) .

[32] ATLAS collaboration, *Search for long-lived neutral particles produced in pp collisions at $\sqrt{s} = 13$ TeV decaying into displaced hadronic jets in the ATLAS inner detector an muon spectrometer*, *Physical Review D* **101** (2020) .

[33] ATLAS Collaboration, *Search for Light Long-Lived Particles in pp Collisions at $\sqrt{s} = 13$ TeV Using Displaced Vertices in the ATLAS Inner Detector*, *Phys. Rev. Lett.* **133** (2024) 161803 [2403.15332].

[34] ATLAS Collaboration, *Search for neutral long-lived particles that decay into displaced jets in the ATLAS calorimeter in association with leptons or jets using pp collisions at $\sqrt{s} = 13$ TeV*, *JHEP* **11** (2024) 036 [2407.09183].

[35] ATLAS collaboration, *Search for events with one displaced vertex from long-lived*

neutral particles decaying into hadronic jets in the atlas muon spectrometer in pp collisions at $\sqrt{s} = 13$ *tev*, 2025.

[36] ATLAS collaboration, *Combination of searches for invisible Higgs boson decays with the ATLAS experiment*, tech. rep., CERN, Geneva, Oct, 2020.

[37] R. D. Peccei and H. R. Quinn, *Constraints imposed by* CP *conservation in the presence of pseudoparticles*, *Phys. Rev. D* **16** (1977) 1791.

[38] I. Brivio, M. B. Gavela, L. Merlo, K. Mimasu, J. M. No, R. del Rey et al., *Alps effective field theory and collider signatures*, *The European Physical Journal C* **77** (2017) .

[39] L. Evans and P. Bryant, *LHC machine*, *Journal of Instrumentation* **3** (2008) S08001.

[40] ATLAS collaboration, *Luminosity determination in pp collisions at* $\sqrt{s} = 13$ *TeV using the ATLAS detector at the LHC*, *The European Physical Journal C* **83** (2023) .

[41] ATLAS collaboration, *The ATLAS experiment at the CERN large hadron collider*, *Journal of Instrumentation* **3** (2008) S08003.

[42] CMS collaboration, *The CMS experiment at the CERN LHC*, *Journal of Instrumentation* **3** (2008) S08004.

[43] LHCb collaboration, *The LHCb detector at the LHC*, *Journal of Instrumentation* **3** (2008) S08005.

[44] ALICE collaboration, *The ALICE experiment at the CERN LHC*, *Journal of Instrumentation* **3** (2008) S08002.

[45] E. Mobs. The CERN accelerator complex, https://cds.cern.ch/record/2684277, 2019.

[46] K. Schindl, *The Injector Chain for the LHC*, .

[47] *High-Luminosity Large Hadron Collider (HL-LHC): Preliminary Design Report*, Tech. Rep. CERN-2015-005, 12, 2015. 10.5170/CERN-2015-005.

[48] ATLAS collaboration. Luminosity Public Results Run 2, https://twiki.cern.ch/twiki/bin/view/AtlasPublic/LuminosityPublicResultsRun2.

[49] ATLAS collaboration. Luminosity Public Results Run 3, https://twiki.cern.ch/twiki/bin/view/AtlasPublic/LuminosityPublicResultsRun3.

[50] ATLAS collaboration, *ATLAS inner detector: Technical Design Report, 1*, Tech. Rep. CERN-LHCC-97-016. ATLAS-TDR-4, Apr, 1997.

[51] ATLAS collaboration, *ATLAS Insertable B-Layer Technical Design Report*, Tech. Rep. CERN-LHCC-2010-013. ATLAS-TDR-19, Sep, 2010.

[52] ATLAS collaboration, *ATLAS Liquid Argon Calorimeter Phase-I Upgrade Technical Design Report*, Tech. Rep. CERN-LHCC-2013-017. ATLAS-TDR-022, Sep, 2013.

[53] ATLAS collaboration, *ATLAS tile calorimeter: Technical Design Report*, Tech. Rep. CERN-LHCC-96-042. ATLAS-TDR-3, Dec, 1996.

[54] ATLAS collaboration, *ATLAS muon spectrometer: Technical Design Report*, Technical design report. ATLAS. CERN, Geneva, 1997.

[55] *Performance of the atlas muon triggers in run 2*, *Journal of Instrumentation* **15** (2020) P09015.

[56] ATLAS Collaboration, *Standalone vertex finding in the ATLAS muon spectrometer*, *JINST* **9** (2014) P02001 [1311.7070].

[57] ATLAS collaboration, *Operation of the ATLAS trigger system in run 2*, *Journal of Instrumentation* **15** (2020) P10004.

[58] J. Pequenao and P. Schaffner, "How ATLAS detects particles: diagram of particle paths in the detector." 2013.

[59] T. G. Cornelissen, N. Van Eldik, M. Elsing, W. Liebig, E. Moyse, N. Piacquadio et al., *Updates of the ATLAS Tracking Event Data Model (Release 13)*, tech. rep., CERN, Geneva, 2007.

[60] A. Salam and J. Strathdee, *Super-symmetry and non-Abelian gauges*, *Phys. Lett. B* **51** (1974) 353.

[61] ATLAS Collaboration, *Topological cell clustering in the ATLAS calorimeters and its performance in LHC Run 1*, *Eur. Phys. J. C* **77** (2017) 490 [1603.02934].

[62] ATLAS Collaboration, "Properties of jets and inputs to jet reconstruction and calibration with the ATLAS detector using proton–proton collisions at $\sqrt{s} = 13$ TeV." ATL-PHYS-PUB-2015-036, 2015.

[63] ATLAS collaboration, *Muon identification and performance in the ATLAS experiment*, tech. rep., CERN, Geneva, 2018. 10.22323/1.316.0097.

[64] ATLAS Collaboration, *Search for a Light Higgs Boson Decaying to Long-Lived Weakly Interacting Particles in Proton-Proton Collisions at $\sqrt{s} = 7$ TeV with the ATLAS Detector*, *Phys. Rev. Lett.* **108** (2012) 251801 [1203.1303].

[65] ATLAS Collaboration, *Search for long-lived, weakly interacting particles that decay to displaced hadronic jets in proton-proton collisions at $\sqrt{s} = 8$ TeV with the ATLAS detector*, *Phys. Rev. D* **92** (2015) 012010 [1504.03634].

[66] ATLAS collaboration, *Search for events with a pair of displaced vertices from long-lived neutral particles decaying into hadronic jets in the atlas muon spectrometer in pp collisions at $\sqrt{s} = 13$ TeV*, *Phys. Rev. D* **106** (2022) 032005.

[67] ATLAS Collaboration, *Triggers for displaced decays of long-lived neutral particles in the ATLAS detector*, *JINST* **8** (2013) P07015 [1305.2284].

[68] J. Fan, M. Reece and J. T. Ruderman, *Stealth supersymmetry*, *Journal of High Energy Physics* **2011** (2011) .

[69] ATLAS collaboration, *Performance of jet substructure techniques for large-R jets in proton-proton collisions at $\sqrt{s} = 7$ TeV using the ATLAS detector*, *JHEP* **09** (2013) 076 [1306.4945].

[70] LHC Higgs Cross Section Working Group collaboration, *Handbook of LHC Higgs Cross Sections: 4. Deciphering the Nature of the Higgs Sector*, 1610.07922.

[71] ATLAS Collaboration, *The LUCID-2 detector*, *Nucl. Instrum. Meth. A* **936** (2019) 152.

[72] J. Alwall, R. Frederix, S. Frixione, V. Hirschi, F. Maltoni, O. Mattelaer et al., *The automated computation of tree-level and next-to-leading order differential cross sections, and their matching to parton shower simulations*, *JHEP* **7** (2014) 79 [1405.0301].

[73] T. Sjöstrand, S. Ask, J. R. Christiansen, R. Corke, N. Desai, P. Ilten et al., *An introduction to PYTHIA 8.2*, *Comput. Phys. Commun.* **191** (2015) 159 [1410.3012].

[74] ATLAS Collaboration, "ATLAS Pythia 8 tunes to 7 TeV data." ATL-PHYS-PUB-2014-021, 2014.

[75] NNPDF Collaboration, R. D. Ball et al., *Parton distributions with LHC data*, *Nucl. Phys. B* **867** (2013) 244 [1207.1303].

[76] D. J. Lange, *The EvtGen particle decay simulation package*, *Nucl. Instrum. Meth. A*

462 (2001) 152.

[77] S. Agostinelli et al., GEANT4- *a simulation toolkit*, *Nucl. Instrum. Meth. A* **506** (2003) 250.

[78] ATLAS Collaboration, *The ATLAS Simulation Infrastructure*, *Eur. Phys. J. C* **70** (2010) 823 [1005.4568].

[79] T. Sjöstrand, S. Mrenna and P. Skands, *A brief introduction to PYTHIA 8.1*, *Comput. Phys. Commun.* **178** (2008) 852 [0710.3820].

[80] ATLAS Collaboration, "The Pythia 8 A3 tune description of ATLAS minimum bias and inelastic measurements incorporating the Donnachie–Landshoff diffractive model." ATL-PHYS-PUB-2016-017, 2016.

[81] ATLAS Collaboration, *Electron and photon performance measurements with the ATLAS detector using the 2015–2017 LHC proton–proton collision data*, *JINST* **14** (2019) P12006 [1908.00005].

[82] ATLAS Collaboration, *Muon reconstruction and identification efficiency in ATLAS using the full Run 2 pp collision data set at* $\sqrt{s} = 13$ *TeV*, *Eur. Phys. J. C* **81** (2021) 578 [2012.00578].

[83] A. Navlani, "Multi-layer perceptron neural network using python." URL: https://machinelearninggeek.com/multi-layer-perceptron-neural-network-using-python/, Apr, 2021.

[84] Keras, "Keras documentation: The sequential class." URL: https://keras.io/api/models/sequential/.

[85] TensorFlow, "The sequential model." URL: https://www.tensorflow.org/guide/keras/sequential_model.

[86] S. N. et al. (Particle Data Group), *Review of particle physics*, *Phys. Rev. D* **110** (2024) 030001.

[87] M. L. Schott, *Search for long-lived particles decaying into displaced hadronic jets in the muon spectrometer in pp collisions at* $\sqrt{s}$ *= 13 tev with the atlas detector*, 2024.

[88] ATLAS Collaboration, *Luminosity determination in pp collisions at* $\sqrt{s} = 13$ *TeV using the ATLAS detector at the LHC*, *Eur. Phys. J. C* **83** (2023) 982 [2212.09379].

[89] A. L. Read, *Presentation of search results: The* CL_s *technique*, *J. Phys. G* **28** (2002)

2693.

[90] G. Cowan, K. Cranmer, E. Gross and O. Vitells, *Asymptotic formulae for likelihood-based tests of new physics*, *Eur. Phys. J. C* **71** (2011) 1554 [1007.1727].

[91] L. Heinrich, M. Feickert, G. Stark and K. Cranmer, *pyhf: pure-python implementation of histfactory statistical models*, *J. Open Source Softw.* **6** (2021) 2823 [2211.15838].

[92] ATLAS collaboration, *The Phase-II upgrade of the ATLAS muon spectrometer*, tech. rep., CERN, Geneva, 2020. 10.22323/1.364.0149.

[93] ATLAS collaboration, *Technical Design Report for the ATLAS Inner Tracker Pixel Detector*, tech. rep., CERN, Geneva, 2017. 10.17181/CERN.FOZZ.ZP3Q.

[94] ATLAS collaboration, *Overview of the ATLAS High Granularity Timing Detector: project status and results*, tech. rep., CERN, Geneva, 2023. 10.22323/1.449.0525.

[95] ANUBIS collaboration, *2026 ESPPU input from the ANUBIS Collaboration*, 2504.03195.

[96] FASER collaboration, *Technical proposal for faser: Forward search experiment at the lhc*, 2018.

[97] FASER collaboration, *Shining light on the dark sector: Search for axion-like particles and other new physics in photonic final states with faser*, 2024.

[98] M. Bauer, O. Brandt, L. Lee and C. Ohm, *Anubis: Proposal to search for long-lived neutral particles in cern service shafts*, 1909.13022.

[99] A. Shah, *Searches for long-lived particles with the anubis experiment*, in *Proceedings of The European Physical Society Conference on High Energy Physics — PoS(EPS-HEP2023)*, EPS-HEP2023, p. 051, Sissa Medialab, Feb., 2024, DOI.

[100] M. Revering, G. Aielli, O. Brandt, L. Pizzimento, A. Shah and P. Swallow, *Searches for long-lived particles with ANUBIS: first commissioning results from proANUBIS*, *PoS* **ICHEP2024** (2024) 983.

[101] M. Benedikt, F. Zimmermann, W. Bartmann, J.-P. Burnet, C. Carli, A. Chance et al., *FCC Integrated Programme Stage 1: The FCC-ee*, tech. rep., CERN, Geneva, 2025. 10.17181/CERN.SLLK.DA6C.

[102] I. Agapov, M. Benedikt, A. Blondel, M. Boscolo, O. Brunner, M. C. Llatas et al.,

Future circular lepton collider fcc-ee: Overview and status, 2022.

[103] O. Brunner, P. N. Burrows, S. Calatroni, N. C. Lasheras, R. Corsini, G. D'Auria et al., *The clic project*, 2022.

[104] P. Bambade, T. Barklow, T. Behnke, M. Berggren, J. Brau, P. Burrows et al., *The international linear collider: A global project*, 2019.

[105] M. Benedikt, A. Chance, B. Dalena, D. Denisov, M. Giovannozzi, J. Gutleber et al., *Future circular hadron collider fcc-hh: Overview and status*, 2022.

[106] D. Curtin et al., *Exotic decays of the 125 GeV Higgs boson*, *Phys. Rev. D* **90** (2014) 075004 [1312.4992].

[107] Y. Cui and B. Shuve, *Probing baryogenesis with displaced vertices at the LHC*, *JHEP* **02** (2015) 049 [1409.6729].

[108] ATLAS Collaboration, *Measurement of the photon identification efficiencies with the ATLAS detector using LHC Run 2 data collected in 2015 and 2016*, *Eur. Phys. J. C* **79** (2019) 205 [1810.05087].

[109] ATLAS Collaboration, *Electron and photon energy calibration with the ATLAS detector using 2015–2016 LHC proton–proton collision data*, *JINST* **14** (2019) P03017 [1812.03848].

[110] A. Buckley, "The hepthesis LaTeX class."

List of figures

List of tables